UNIVERSITY OF LONDON THESIS

Degree PhD Year 2007 Name of Author HAZEL JOANNA McANDREWS

UNIVERSITY COLLEGE LONDON

Cassini Observations of Low Energy Electrons in and around Saturn's Magnetosphere

Hazel Joanna McAndrews

Mullard Space Science Laboratory
Department of Space and Climate Physics
University College London

A thesis submitted to the University of London
for the degree of Doctor of Philosophy

January 2007

ProQuest LLC
789 East Eisenhower Parkway
P.O. Box 1346
Ann Arbor, MI 48106-1346

I, Hazel Joanna McAndrews, confirm that the work presented in this thesis is my own. Where information has been derived from other sources, I confirm that this has been indicated in the thesis.

Signed...

Abstract

The work in this thesis utilises data from the Cassini spacecraft in the analysis of the Saturnian system. Data from the electron spectrometer (ELS), the ion spectrometer (IMS) and the magnetometer (MAG) gathered during the first two years of the mission have been used in two main areas of research. The first is the investigation of the magnetopause, which forms the boundary between the region of space dominated by the planetary magnetic field and currents, and the interplanetary magnetic field. The second concerns the high energy electrons fluxes in the inner magnetosphere, and the effects caused when the icy moons carve out cavities in these populations.

We find evidence strongly suggestive of reconnection events as observed at Earth at two separate encounters with the magnetopause. The energisation of the plasma, together with the open field configuration provides us with an estimate for the reconnection voltage at Saturn. It is found to, at times, be comparable to the corotation electric field, which is assumed to dominate the dynamics of the system. The large database of ~ 200 crossings of the magnetopause is also used to derive general characteristics of the electron behaviour at this boundary. We find that boundary layer plasma is often present inside the magnetopause of Saturn, although the evidence suggests that internal plasma may play a role in formation of this layer.

The ELS is able to utilise the penetration of high energy electrons directly into the detector to study the 'microsignatures' of the icy moons in the inner magnetosphere. The absorption of the high energy electrons leaves a cavity in the plasma. The subsequent re-filling over time by the surrounding plasma has allowed us to derive diffusion rates at Tethys, Enceladus and Mimas. In general, outward diffusion is faster than inward diffusion, although this varies at Enceladus.

Acknowledgements

There are many people that deserve special thanks for supporting me through my three years. Firstly I would like to acknowledge Dr James Green of NASA who I met in 2001 in a Bier Garten while attending the International Space University. We became friends and later, knowing of my interest in space physics, Jim suggested that I should come and work with him, but I'd need a PhD. "Hang on!" I said...and now here I am. I'm not going to work for Jim now, but who knows what the future holds.

Since Jim, my main driving force has been my two supervisors, Andrew Coates, for providing supervision in the first year and on all things Cassini after that, and Chris Owen. Chris bravely picked up the baton in my second year and managed to provide solid scientific advice on my areas of research, despite his own lying nearly three billion km away.

I would also like to thank the many colleagues and friends at MSSL: Aurélie, Yulia, Nicolas, Jason, Rob W., Yasir, Ilya, 'office' Chris and Claire. Rob F. deserves a special mention for increasing my understanding of plasma processes, cricket and the need to continually rile the French – I cannot thank him enough for the many afternoons of hilarity he provided. To the ELS team, Gethyn and Lin for always being there to answer any IDL query or request, and to 'my' postdoc Abi, may the wine never stop flowing my friend!

My friends have, of course, been particularly understanding, especially throughout the trying time of writing up, "What do you mean you can't come to the pub?!" was often heard being yelled on a Sunday afternoon.

My family have offered wonderful support, or, more accurately, I have offered them wonderful support, with job application letters, GCSE revision and essential big sister guidance, but I wouldn't be where I am today without them. Thanks to my mum, who never hassled me to complete my homework, knowing full well I'd done it already and who did a fantastic job of raising us. To my gran and grandpa, who kick started this whole space obsession by taking me on the trip of a lifetime to KSC when I was 8 and who had such an influence on my outlook on life. Finally, to my husband-to-be, Fraser, who beat me to being a Dr., but who knows I did it with more finesse. He is my life and without him I would never have had the guts to start this, never mind finish it. There is no-one else that I would rather drag to the desert. I can't wait for the rest of our lives together, this is for you.

Table of Contents

List of Figures

List of Tables

1 Introduction

1.1 Introductory concepts in space plasma physics

The study of magnetospheric physics has been at the forefront of space research ever since the first satellites were able to directly measure the Earth's magnetic and particle environment [e.g. Van Allen and Frank, 1959 and references therein]. As instruments became more advanced and our knowledge increased, the interaction between Earth's system of particles and fields and the considerable influence of the Sun became a separate field of physics. With the advent of interplanetary space probes, the space environment around other planets is now being directly explored. The scientific analysis in this thesis describes the data collected by Cassini, which, at the time of writing, is in orbit about Saturn.

As the work in this thesis is almost entirely dedicated to understanding the plasma in the near-Saturn space environment, it is worth highlighting some basic concepts prior to describing this analysis. Firstly, some fundamental expressions explaining the behaviour of a plasma will be introduced. This will be followed by an introduction to plasmas and fields in the space around magnetised planets, and some relevant boundaries and in particular what we know about the plasma environment of Saturn. This latter topic will feature measurements made in the magnetosphere of Saturn prior to, and highlight some new results gained upon the arrival of, the Cassini spacecraft.

1.1.1 Understanding plasma

Firstly, what is a plasma? A plasma is a state of matter in which there is sufficient energy to liberate the electrons from the constituent atoms and molecules by overcoming the atomic potential energy barrier, leaving a collection of effectively 'free' positive and negative charges. On a scale smaller than the Debye length, or the distance over which an individual charge can have an affect, these individual charges can be distinguished. However, over a macroscopic scale, the plasma appears quasi-neutral and will act to maintain this neutrality in response to external influences. This latter

condition is maintained because the constituent charges, although physically separated, exhibit a collective behaviour maintained via electromagnetic forces.

Each charged element in a plasma will be influenced by electric fields, and will in turn, exert its own potential field on the surrounding particles. This occurs via the Coulomb force and results in the Coulomb potential, Φ_C:

$$\Phi_C = \frac{q}{4\pi\varepsilon_0 r},$$

Equation 1.1

where q is the charge on the particle, ε_0 is the permittivity of free space (the ability of a material to polarise in response to an electric field) and r is the distance from the charge. Within a plasma this potential is diminished due to the surrounding charges, which act to provide a shielding effect, modifying the potential to the Debye potential form, Φ_D:

$$\Phi_D = \frac{q}{4\pi\varepsilon_0 r}\exp\left(-\frac{r}{\lambda_D}\right),$$

Equation 1.2

This is dependent on the distance λ_D, which is the distance over which the field due to an individual charge is felt by the other constituent particles. This is known as the Debye length and can be derived by considering the effects of the charges in a plasma. For example, near ions, electrons will cluster and violate charge neutrality, distorting the potential field. We can define a characteristic length scale over which a modified charge density modifies the electrostatic potential:

$$\lambda_D = \left(\frac{\varepsilon_0 k_B T_e}{n_e e^2}\right)^{\frac{1}{2}}, \qquad \text{Debye length}$$

Equation 1.3

where k_B is the Boltzmann constant (1.38×10^{-23} J K^{-1}), T_e (assuming $\approx T_i$, however, the ions will generally be hotter than the electrons, in this case the Debye length will still be dominated by the electrons since they are more mobile than the ions) and n_e are

the electron temperature and density respectively, and e is the electron charge. This length forms the radius of a sphere, known as the Debye sphere, containing the charges that are effectively screening out the charge due to the central particle. For effective screening to occur the Debye length must be much smaller than the characteristic length scale of the plasma defined below. The Debye sphere must contain many particles (i.e. $N_D >> 1$). These are two of the requirements for a charged gas to be considered a plasma.

As already mentioned, the charges in a plasma act in a collective manner, so if some external force should act to disturb the charges, the resultant displacement will generate an electric field. The particles will act instantly to cancel this field, thereby restoring charge neutrality. The electrons, being smaller, and therefore more mobile than the ions, will respond faster, resulting in a natural oscillation of the electrons about the ions. This motion occurs at the plasma frequency, ω_{pe} given by,

$$\omega_{pe} = \left(\frac{n_e e^2}{m_e \varepsilon_0} \right)^{\frac{1}{2}},$$

Equation 1.4

where m_e is the mass of an electron. This parameter provides a benchmark timescale against which processes affecting the system, such as collisions, are measured. Typically, space plasmas are considered collisionless since the collisions between the constituent ions and electrons are rare.

1.1.2 Single particle motion

Much of the understanding behind the behaviour of a plasma, in particular in a magnetosphere, arises from the consideration of how individual particles behave when in the presence of electric and magnetic fields. Note that particles can also generate and modify such fields themselves.

A moving charged particle, subjected to electric and magnetic fields will act under the Lorentz force:

$$\underline{F_L} = q(\underline{E} + \underline{v} \times \underline{B}),$$

Equation 1.5

where $\underline{E}$ and $\underline{B}$ are the electric and magnetic fields and $\underline{v}$ is the particle velocity. This equation governs the motion of charged particles and allows us to predict and understand the movement of plasmas around field lines, particularly relevant in magnetospheres. A further set of relationships between the fields and particles on which they act are represented in a set of four equations known as Maxwell's equations. Here we show Maxwell's equations in their differential form (they can also be represented in an integral form),

$$\nabla \times \underline{B} = \mu_0 \underline{j} + \varepsilon_0 \mu_0 \frac{\partial \underline{E}}{\partial t}, \qquad \text{Ampère-Maxwell equation}$$

Equation 1.6

$$\nabla \times \underline{E} = -\frac{\partial \underline{B}}{\partial t}, \qquad \text{Faraday's law}$$

Equation 1.7

$$\nabla \cdot \underline{E} = \frac{\rho}{\varepsilon_0}, \qquad \text{Gauss' law for electricity}$$

Equation 1.8

$$\nabla \cdot \underline{B} = 0,$$

Equation 1.9

where μ_0 is the permeability of free space and is the magnetic equivalent of ε_0, $\underline{j}$ is the electric current density, and ρ is the net space charge density, $\rho = e(n_i - n_e)$. These equations describe how the presence and motion of particles affect electric and magnetic fields and how the fields are related to their sources and each other. The first of these is Maxwell's modified form of Ampère's original equation and includes the second term on the right called the 'displacement current' which includes the rate of change of the electric field between the plates of a capacitor. This describes how currents produce curls in magnetic fields. The remaining equations represent how changing magnetic fields produce curls in electric fields (Faraday's law of induction),

how electric charges produce divergence in electric fields (Gauss' law for electricity) and the absence of magnetic charges, or the lack of magnetic monopoles. Thus magnetic fields must close on themselves with no net magnetic charge. These equations thus describe the production of curl and divergence in fields, not necessarily fields themselves.

The motion of a charged particle is dependent on the electric and magnetic field strength, orientations and uniformity. The following section describes the different forms of motion executed under different electromagnetic conditions.

a. Uniform magnetic field

In the absence of an electric field and the assumption that the particle is subjected to a uniform magnetic field alone, Equation 1.5 reduces to:

$$\underline{F_L} = q(\underline{v} \times \underline{B}),$$

Equation 1.10

thus, the force is applied perpendicular to both $\underline{v}$ and $\underline{B}$ and the particle gyrates about the magnetic field line. Note that the force on the particle is perpendicular to the field so the parallel speed is not affected. This is known as gyrotropic motion. The radius of the orbit about the field line is the gyroradius.

$$r_g = \frac{mv}{|q|B}.$$

Equation 1.11

As shall be seen later, under ideal conditions, the field and the particle move together, so the particle will continue to gyrate about this particular field line and it is thus referred to as the 'guiding centre' of the particle motion. Note that this expression is dependent on mass and charge polarity so in the same B-field, electrons and ions will circle round the field line in opposite senses (Figure 1.1), with different gyroradii. Of course, although ions have a larger mass than electrons, the charge is also taken into account and this will reduce the radius accordingly if there are higher charge states.

The frequency of this gyration is the gyrofrequency, and occurs about the guiding centre,

$$\omega_g = \frac{qB}{m}.$$

Equation 1.12

The time for one revolution is referred to as the 'gyroperiod'. When there is a component of the particle's velocity parallel to the magnetic field, the motion is not simply circular and instead the particle moves along the field, drawing out helical motion.

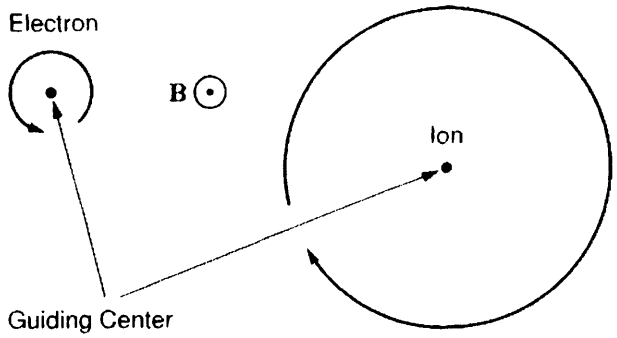

Figure 1.1 The different sense of guiding motion about a field line for positive and negative charges. The B-field is pointing out of the plane of the page. The electrons will travel anti-clockwise about the field line with a small gyroradius while the ion will travel clockwise with a larger radius (assuming a singly charged ion).

The ratio between the perpendicular and parallel velocities defines the tangent of the pitch angle given by,

$$\alpha = \tan^{-1}\left(\frac{\underline{v}_\perp}{\underline{v}_{II}}\right),$$

Equation 1.13

where $\underline{v}_\perp$ and $\underline{v}_{II}$ are the perpendicular and parallel components of the velocity respectively. This parameter is a useful representation of the motion of the particle around a field line and is often important in describing particle effects.

The motion along the field line leads to an additional concept: that of the magnetic mirror point. In converging fields, such as those found close to a planetary surface, the $\underline{v}_{II}$ component will decrease until the motion along the field is eliminated. This is the mirror point and the particle is subsequently reflected from this point to continue back along the field line until such field geometry is encountered again (such as that found at either end of a planetary dipole field line). The period of this 'mirroring' is known as the bounce period, and expresses the time it takes a particle to travel along the field line from the equatorial plane, to each mirror point, and back again and can be expressed as:

$$\tau_b \approx \frac{LR_E}{\sqrt{(W/m)}}\left(3.7 - 1.6\sin\alpha_{eq}\right),$$

Equation 1.14

where W is the particle energy and L is the distance to the field line in the equatorial plane in units of the planetary radius, known as the particle 'L-shell'.

The concept of the magnetic mirror also leads to the definition of *adiabatic invariants*. Which are constants of particle motion. When the v_{para} of the mirroring particle decreases, the v_{perp} component increases to ensure the overall energy of the particle remains constant. The pitch angle will therefore change accordingly with the magnetic field strength. This can be expressed using one of the conserved quantities known as the 'first adiabatic invariant', the magnetic moment, μ, of the particle:

$$\mu = \frac{mv_{perp}^2}{2B},$$

Equation 1.15

which is a constant for a particular particle on a particular magnetic field line providing the magnetic field changes slowly compared with the gyroperiod of the particle about the field line. Other adiabatic invariants include the longitudinal invariant, J, and the perpendicular drift invariant. Both describe properties of the particle which are invariant over the timescales of the associated particle motion, i.e. the longitudinal motion along the field line and the drift period respectively.

b. Static electric field

If an electric field is now re-introduced into Equation 1.10, an additional motion is exhibited. Due to the ease of particle motion along a field line, any parallel electric fields will be cancelled out almost immediately by the fast response of the electrons acting to eliminate the charge separation along the B-field. Therefore, it is the perpendicular component of the field which is of interest here. The resultant motion is orthogonal to the B-field (and the direction of helical motion) and the E-field, and will cause the guiding centre to drift perpendicular to both the magnetic and electric fields. The drift velocity is thus,

$$\underline{v}_E = \frac{\underline{E} \times \underline{B}}{B^2}, \qquad \text{E x B drift}$$

Equation 1.16

and is in the same sense for both positive and negative particles.

c. Non-uniform magnetic field

If a non-homogenous magnetic field is encountered, such as is typically found in a planetary magnetosphere, then at least two additional drift motions result. These are the gradient drift,

$$\underline{v}_\nabla = \frac{m\underline{v}_{perp}^2}{2qB^3}(\underline{B} \times \nabla B), \qquad \text{Gradient drift}$$

Equation 1.17

which acts perpendicular to both the magnetic field and its gradient and acts in opposite directions for electrons and ions, and thus a current is generated, and curvature drift. The latter acts specifically in regions where the field lines are curved, such as in a dipole field. The particles experience a centrifugal force due to the radius of curvature of the field line. The resulting force acts perpendicular to both the magnetic field and its curvature. This force acts in opposite senses for electrons and ions and thus also drives a current.

$$\underline{v}_R = \frac{m\underline{v}_{para}^2}{q} \frac{\underline{R}_C \times \underline{B}}{R_C^2 B^2}, \qquad \text{Curvature drift}$$

Equation 1.18

where $\underline{R}_C$ points away from the centre of curvature of the field and the magnitude equals the local radius of curvature. Note that generally any force will drive a drift motion.

1.1.3 Many particle motion

As mentioned previously, a plasma exhibits collective behaviour. This characteristic can be exploited to treat the particles as a group either using a statistical approach (in kinetic theory) or a fluid approach (in magnetohydrodynamics (MHD)).

1.1.3.1 Kinetic Theory

The position $\underline{x}$, and velocity $\underline{v}$, of each particle at each point in time is used to represent the state of the plasma in what is known as *phase space*. The plasma as a whole is then represented by an average distribution within this six dimensional space (three position and three velocity), $f(\underline{x},\underline{v},t)$. This describes the characteristics of the collection of particles and is a function of position, velocity and time. Collective motion is traced using an equation, such as the Vlasov equation, which describes the continuity of phase space, or the Liouville theorem which allows the motion of the particles to be theoretically predicted. The macroscopic properties of the particles are derived from integrating over phase space to derive different moments of the population, or by fitting the population to an ideal distribution, such as a Maxwellian, and calculating the density and temperature of that distribution. The first of these methods is described in more detail in Appendix B.

1.1.3.2 Magnetohydrodynamics

The collective behaviour can also be represented by considering the plasma over a macroscopic scale and treating it as a magnetised fluid. For this assumption to be valid, processes must occur over large temporal and spatial scales compared with the plasma characteristic scales. For example, the frequency of a process must be higher than the gyration frequency of the particles or spatial lengths must be large compared with the particle gyroradius. This treatment is known as magnetohydrodynamics and applies both Maxwell's equations and the Navier-Stokes equations of fluid dynamics to the plasma.

An important concept in MHD is the '$\underline{j}\times\underline{B}$' force (with no viscous effects). This is the sum of the magnetic pressure,

$$p_B = \frac{B^2}{2\mu_0}, \qquad \text{Magnetic pressure}$$

Equation 1.19

and the magnetic tension in a field line. This term, together with the plasma particle pressure, $P = nk_B T$, can be used to describe the total plasma pressure. An additional parameter can also be defined which gives the ratio of these two pressures, the plasma beta:

$$\beta = \frac{2\mu_0 P}{B^2}. \qquad \text{Plasma Beta}$$

Equation 1.20

This value can indicate whether the plasma or field dominates in a certain region of space and therefore what processes are likely to be observed. For example, the plasma beta can indicate whether a plasma or magnetic wave is supported and whether it will grow or decay in a particular region of the magnetosphere.

1.1.4 Frozen-in theorem and diffusion

The low-energy particle measurements used in this thesis are well described by a simple concept relating the magnetic field and particle motions, known as the 'frozen-in theorem'. Consider the generalised Ohm's law, describing motion of a magnetised plasma,

$$\underline{j} = \sigma_0 (\underline{E} + \underline{v} \times \underline{B}),$$

Equation 1.21

Where σ_0 is the plasma conductivity. Rearranging for $\underline{E}$, then substituting Equation 1.21 into Faraday's law (Equation 1.7) to eliminate the electric field gives,

$$\frac{\partial \underline{B}}{\partial t} = \nabla \times \left(\underline{v} \times \underline{B} - \frac{\underline{j}}{\sigma_0} \right).$$

Equation 1.22

Application of the Ampère-Maxwell equation (Equation 1.6), whilst neglecting the viscous effects represented by the $\frac{\partial \underline{E}}{\partial t}$ term, and noting that $\nabla \cdot \underline{B} = 0$ we get the general induction equation for the magnetic field which describes the change of magnetic field in a plasma with time,

$$\frac{\partial \underline{B}}{\partial t} = \nabla \times (\underline{v} \times \underline{B}) + \frac{1}{\mu_0 \sigma_0} \nabla^2 \underline{B}.$$

Equation 1.23

The magnetic field can therefore be described by the motion of the plasma (the first term on the right, known as the conduction term) and any diffusion of the field through the plasma (the second term on the right). In collisionless plasmas with infinite conductivity, i.e. where the electrical resistivity is low, the second term in Equation 1.23 is negligible and the field and plasma remain 'frozen' together. The field therefore moves with the plasma, until finite resistivity develops in the plasma, such as due to collisions, then, the diffusion term becomes significant.

Diffusion of plasma across the field (and field across plasma) plays an important part in the two topics of this thesis, namely the breakdown in the frozen-in theorem at the magnetopause allowing field lines to reconnect (chapter 3) and the cross-field diffusion that occurs when the magnetospheric plasma acts to fill in the depleted particle wakes left by the Saturnian moons (chapter 5).

1.1.5 Magnetic reconnection

When two magnetic field regions are separated by a narrow current sheet (for example, the magnetopause current layer (MPCL)) and they have an anti-parallel component, such as in the example in Figure 1.2a, it is possible for a region of enhanced resistivity to occur in the current sheet due to the presence of anomalous collisions between the particles, resulting in the breakdown of the frozen-in condition as described above and resulting in a process called 'Magnetic reconnection'. A small 'diffusion region' is created at the centre of the reconnecting fields, and here the field can diffuse with respect to the plasma. This process results in a cancellation of flux from both sides and a null point in the magnetic field strength. At this point, the field can reconfigure across the current sheet to form an 'X' line or separatrix (Figure 1.2b). When the field lines connect they are now highly kinked (Figure 1.2c).

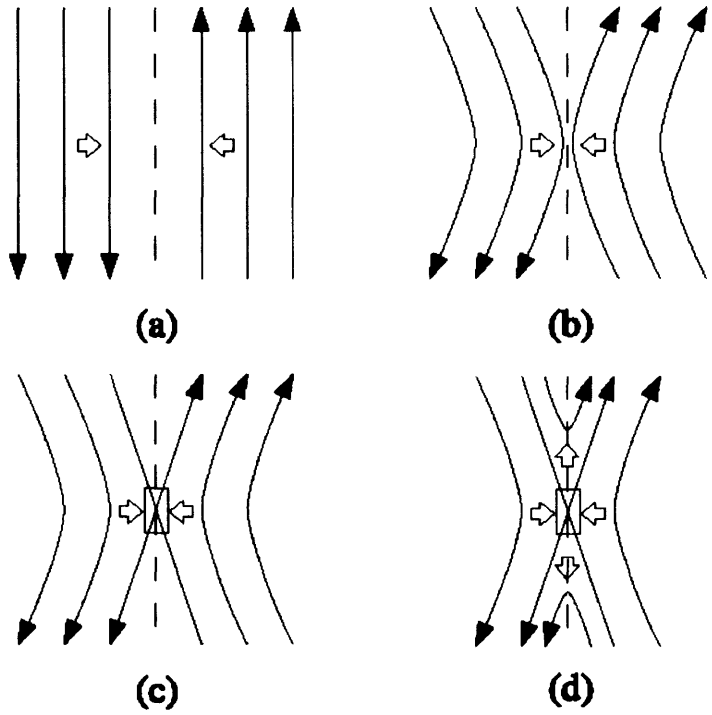

Figure 1.2 A stage by stage outline of the behaviour of the field and plasma during the process of magnetic reconnection Figures a) to d) show schematics of two simple field regions, here assumed to be the IMF (left) which is assumed to be southward, and the planetary field (right) which in this case is northward, in the dayside magnetosphere. a) Initially the fields are anti-parallel either side of the magnetopause current layer (dashed line). As the solar wind and IMF move toward the planet they set-up an electric field known as the convective electric field and when reconnection occurs this field ultimately leads to the driving of the magnetospheric convection. As the field lines encounter the planetary field they are compressed together b) and eventually a diffusive region is created. The size of the diffusion region is defined by the characteristic length over which the field varies. In this region, the fields either side are able to diffuse across the plasma and current layer, becoming independent of the plasma, and annihilate the field the other side of the current layer. c) When this happens the touching fields reconnect and effectively break off from the original field line and join with the oppositely directed field forming an 'X' line or separatrix, d) finally the reformed field lines are subject to magnetic forcing and begin to exit the reconnection site while accelerating the plasma on those field lines away from the 'X' line [i.e. Cowley and Owen, 1989]. The direction of the magnetic field line (or 'flux tube') motion across the magnetopause is defined by the motion of the field line across the surface of the magnetopause due to forcing from the external solar wind and the field line tension [Cowley and Owen, 1989]. The plasma and field are accelerated to the order of the Alfvén speed which is defined by the field magnitude and the plasma density.

This is a crucial process in magnetospheric dynamics since this cycle starts with one interplanetary field line which had no connection to the planet's ionosphere and one planetary field line which had both ends in the ionosphere. The reconnection process reconfigures the field such that two open field lines are created, both with one end in the ionosphere and the other in interplanetary space. This therefore adds open magnetic flux to the system. Prior to reconnection, the magnetic field change across the boundary or discontinuity is known as a tangential discontinuity (TD). A TD is so named because any field rotation occurring at the boundary is purely tangential and there is no component of the field across the boundary to connect the fields ($B_N = 0$) [Neugebauer et al., 1984; Sonnerup and Scheible, 1998]. At a reconnection site, the boundary

becomes a rotational discontinuity (RD) and is defined when the magnetic field has a component across the boundary to connect the fields either side (i.e. $B_N \neq 0$).

This bending of the field lines results in a large magnetic force, $(\underline{j} \times \underline{B})$ which is a combination of the local magnetic pressure gradient and magnetic tension in the field line. This can be re-written as:

$$\underline{j} \times \underline{B} = \frac{1}{\mu_0}(\underline{\nabla} \times \underline{B}) \times \underline{B},$$

Equation 1.24

which equates to:

$$\frac{1}{\mu_0}(\underline{\nabla} \times \underline{B}) \times \underline{B} = \frac{-\underline{\nabla} B^2}{2\mu_0} + \frac{(\underline{B} \cdot \underline{\nabla})\underline{B}}{\mu_0},$$

Equation 1.25

the first term on the right is the magnetic pressure gradient, which acts in a similar way to thermal pressure. The second term consists of a field aligned and a perpendicular component. The former cancels out the field-aligned part of the pressure gradient, leaving only the perpendicular part of the magnetic pressure. The second term's perpendicular component is known as the curvature force or magnetic tension. These resultant forces act to straighten the field lines and thereby accelerate and heat the plasma on the field lines recoiling away from the reconnection site (Figure 1.2d). The acceleration of the particles on a particular field line is that required to balance the magnetic force and is such that the plasma emerges approximately at the Alfvén speed. The Alfvén speed is a characteristic of the reconnection process and depends upon the local field strength, plasma density and the mass of the particles. In the case of a proton dominated plasma,

$$v_A = \sqrt{\frac{B^2}{\mu_0 n m_i}},$$

Equation 1.26

where B is the local field strength and n and m_i are the proton density and mass respectively. The detection of the accelerated 'outflow' is one diagnostic of the presence of reconnection, as is the detection of kinked magnetic field lines [e.g., Paschmann et al., 1979; Sonnerup et al., 1981; Paschmann et al., 1986]. The field component across the magnetopause now allows plasma to flow in and out of the magnetosphere [e.g. Scholer et al., 1981; Gosling et al., 1990]. Although reconnection is a common process

throughout the universe, it is of particular interest at the magnetopause of a planet as it joins the IMF and planetary fields. This allows the transfer of energy and, especially in the case of the Earth, the driving of magnetospheric dynamics.

1.2 Saturn's magnetosphere

Saturn is the sixth planet from the Sun and on average orbits at a distance of 9.54 AU (Astronomical Unit = 1.5 x 10^8 km), i.e. nearly 10 times further from the Sun than the Earth. Its orbital plane is inclined at 2° from the ecliptic and the planet completes one revolution about the Sun in 29 Earth years. It is the second largest planet (after Jupiter) with a radius of 60,268 km (defined by the 1 bar level at the equator[1]) and, like Jupiter; it has a fast rotation rate, spinning about its axis once every ~ 10 hours 45 minutes [Gurnett et al., 2005]. Because of the rapid rotation, Saturn is oblate and thus the equatorial and polar radii vary by up to 10%.

With its plethora of rings and moons, the Saturnian system is unique in the solar system. In addition to the scientific interest surrounding each of these bodies in their own right, they also all interact with the magnetosphere as either a source or a sink for plasma. They thus play a very important role in Saturnian magnetospheric dynamics.

1.2.1 Previous missions to Saturn

The Cassini-Huygens mission is dedicated to exploring the planet Saturn and its environment. Just as Cassini made gravity assist detours via Earth and Jupiter on the way to its target destination, so a number of previous missions visited Saturn on their way to the outer solar system. These missions afforded only brief, but tantalising glimpses of Saturn's field and particle environment, but paved the way for the specific and dedicated measurements being made in Saturn orbit by Cassini instruments from Saturn orbit insertion in June 2004.

1.2.1.1 Pioneer 11

Pioneer 11 left Earth for the outer solar system in 1972. The last signal from this spacecraft from over 8 billion km away was detected at Earth in 2003. It was the first

[1] http://nssdc.gsfc.nasa.gov/planetary/factsheet/saturnfact.html

spacecraft to reach the outer solar system, visiting Jupiter in 1973 and Saturn in 1979. Its in situ measurements of the magnetospheric environment around Saturn confirmed the presence of a planetary magnetic field [Acuña and Ness 1980; Smith et al, 1980]. This was evidenced by the detection of a bow shock at 24 R_S (where 1 R_S = 60,330 km during the Pioneer 11 mission) upstream of the planet near local noon, and the magnetopause at 17.2 R_S [Smith et al., 1980]. The encounter lasted 8 days and Pioneer 11 remained close to the equatorial plane throughout. It finally exited the magnetosphere at a distance of 39.8 R_S from Saturn on the dawn magnetopause (Figure 1.3 and Figure 1.4). The magnetospheric instruments carried on board included a plasma analyser (for solar wind measurements), a charged particle instrument (for electrons > 40 keV and protons 0.61 to 3.41 MeV and > 5 MeV) and a vector helium/fluxgate magnetometer.

1.2.1.2 Voyagers 1 and 2

Voyager 1 encountered Saturn in 1980 and Voyager 2 followed a year later after their 3 and 4 year voyages respectively. They both entered the magnetosphere of Saturn near noon, with Voyager 2 exiting on the dawn flank and Voyager 1 leaving further downtail at a local time of 04:00 on the dawnside of the planet (see Figure 1.3 and Figure 1.4). Voyager 1 remained close to the equatorial plane with Voyager 2 reaching higher latitudes of ~ ± 30°.

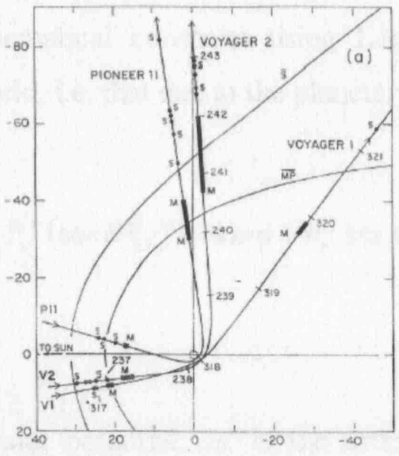

Figure 1.3 Encounter trajectories for the Pioneer 11 and Voyager spacecraft shown projected onto the equatorial plane. The highlighted sections of the trajectory show the range of magnetopause crossings [reproduced from Blanc et al., 2002]

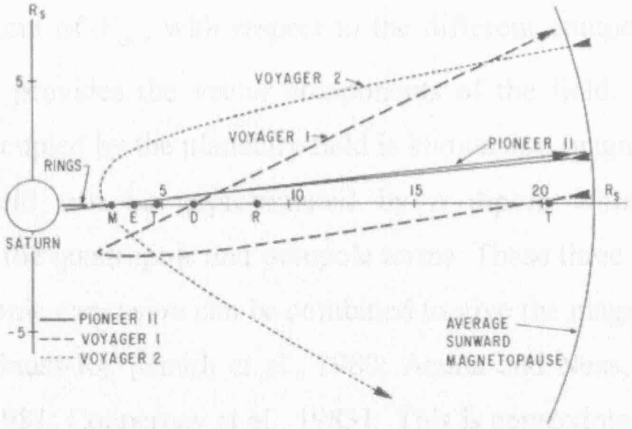

Figure 1.4 Meridional projection of the encounter trajectories for Pioneer 11 and the two Voyager spacecraft (reproduced from Schardt et al., [1984])

1.2.2 Saturn's intrinsic magnetic field

A number of planets in the solar system have an intrinsic magnetic field generated by a dynamo in the core of the planet [Bagenal, 1992; Connerney, 1993]. This process involves the generation of a current via convection of a fluid core which, in turn, induces a magnetic field. The convective motion is driven by the planetary rotation and internal heating. The magnetic field can be represented as the gradient of a scalar potential [Stevenson, 1983; Connerney, 1993; Russell and Luhmann, 1997]. This potential can describe the contributions from sources (internal and external to the planet) and for ease is often expanded into spherical harmonic terms [Connerney, 1993]. It forms an idealised mathematical construct using Legendre functions. The total internal contribution to the field, i.e. that due to the planetary dipole is:

$$V_{\text{int}} = \frac{4\pi}{\mu_0} a \sum_{n=0}^{\infty} \left(\frac{a}{r}\right)^{n+1} \sum_{m=0}^{n} P_n^m(\cos\theta)\left[g_n^m \cos m\phi + h_n^m \sin m\phi\right]$$

Equation 1.27

where V_{int} represents a scalar potential, m is the order and n the degree of the Legendre functions, P_n^m, θ and ϕ are the polar and azimuthal angles and a is the equatorial radius of the planet. The Gauss coefficients, g_n^m and h_n^m, are determined from observational data and are often presented in units of nanoteslas. There is an equivalent expression for the external terms due to the different current systems in the

magnetosphere such as those induced by the solar wind and magnetospheric plasma motions. The gradient of V_{int}, with respect to the different components of a spherical coordinate system, provides the vector components of the field, B_r, B_θ and B_Φ. The volume in space occupied by the planetary field is known as a magnetosphere.

Saturn's field can be approximated by a dipole with further high-order contributions from the quadrupole and octupole terms. These three first-degree terms in the spherical harmonic expansion can be combined to give the magnetic moment, which at Saturn is 0.21 Gauss-R_S^3 [Smith et al., 1980; Acuña and Ness, 1980; Acuña et al., 1980; Ness et al., 1981; Connerney et al., 1983]. This is approximately 600 times larger than the Earth's and ~ 30 times smaller than Jupiter's [Russell, 1991; Bagenal, 1992]. One unique aspect to Saturn's field compared with other magnetised planets is the close alignment of the magnetic and spin axes. At Saturn this is ~ 0.17° [Giampieri and Dougherty, 2004], whereas Earth and Jupiter have dipole tilts of + 11.3° and - 9.6° respectively. The field is axisymmetric [Ness, 1981] and the polarity is aligned opposite to that of Earth, i.e. Saturn's northern hemisphere contains a north magnetic pole.

Magnetic field models for Saturn were constructed using data from the Pioneer and Voyager data: the Z_3 model [Acuna et al., 1983] and the Saturn-Pioneer-Voyager (SPV) model [Davis and Smith, 1990]. These included no external sources such as those generated due to currents in the magnetosphere [Connerney et al., 1983; Connerney, 1993] and were found to be insufficient models of the field observations made during the first fly through of the magnetosphere during Saturn orbit insertion [Dougherty et al., 2005].

Dougherty et al. [2005] adapted the Connerney model [Connerney et al., 1983] to produce a new "Cassini" model to include an updated representation of the fields produced by the magnetospheric plasma motions (e.g. the ring current) and the magnetopause currents. This model includes updated g_{10}, g_{20} and g_{30} terms. More recent work further refines the contribution from the ring current and the magnetopause currents [Arridge et al. 2006a]. The field at Saturn remains approximately dipolar within ~ 10 R_S of the planet, after which the field lines start to lag corotation and an azimuthal field component becomes more significant [Arridge et al., 2006b].

1.2.3 The solar wind at ~ 9 AU

All objects in the solar system are subject to impact by the constant outflow of plasma and magnetic field from the Sun, thus it is important for us to understand how these properties develop by the time they reach the orbit of Saturn.

In the outermost layer of the Sun, the corona, the temperature of the plasma is so hot that the thermal pressure is able to balance the gravitational force of the sun and the plasma can escape from the solar surface [Parker, 1958]. This outwards-streaming plasma is known as the solar wind. The plasma flows radially outwards, accelerating and expanding into interplanetary space. At the orbit of Saturn, the density and temperature of the solar wind plasma has therefore reduced compared with values found upstream of Earth. Typical values at 9 AU are $n \sim 1x10^4$ m^{-3} and $T \sim 30$ eV.

Due to the high plasma conductivity, the solar field lines are frozen to the radial outflow of plasma. However, the end of the field line remains routed in the Sun's interior and therefore as the Sun rotates, the field rotates with it. This is demonstrated in the sketch in Figure 1.5.

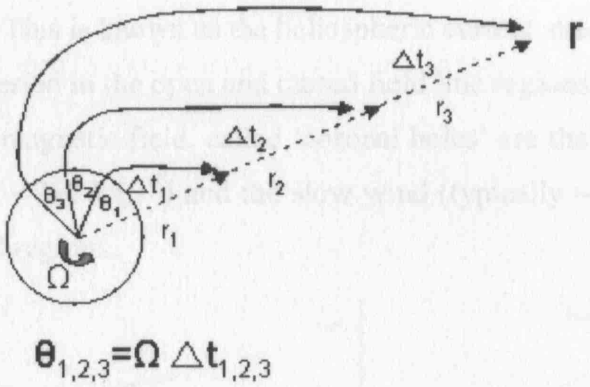

Figure 1.5 Evolution of the plasma and magnetic field emanating from the Sun's surface during a rotation. As the plasma expands radially outwards (dashed lines) the field-lines (solid lines) remain frozen to the Sun's surface resulting in the Parker spiral.

As the sun rotates with an angular speed Ω, in one time step, Δt, the plasma will have moved outwards a distance r, carrying with it the end of the field line. The footprint of the field line will, however, have rotated a distance $\Omega\Delta t$. As the field propagates outwards (where it becomes the Interplanetary Magnetic Field (IMF)) it becomes 'wound' and forms a spiral [Parker, 1958]. Thus we can see that at r, the angle formed in the IMF is $\theta = \tan^{-1}(\Omega r)$ which at Saturn's orbit is $\sim 90°$ to the Sun-Saturn line. This indicates the importance of the azimuthal component of the IMF at ~ 9 AU.

The Sun demonstrates an inherent ~ 11 year periodicity in its activity known as the 'solar cycle'. During the Pioneer 11 and Voyager encounters with Saturn, the Sun was approaching solar maximum. However, during Cassini-approach the cycle was nearing solar minimum. This cycle results in a variation of the characteristics of the solar wind and magnetic field that originate from the Sun, which in turn alters the plasma and field structure which develops throughout the solar system. At solar minimum, for example, when the Sun is in its most quiescent state, the Sun's activity becomes more predictable and the magnetic configuration stabilises and approximates a dipole field. Thus, open field lines emanate from the polar regions in each hemisphere. When the cycle approaches solar maximum, magnetic activity on the surface increases and disturbs the underlying dipole field and the source regions of the open field are shifted.

Since the field is frozen to the radially outflowing plasma, the field adopts a stretched, almost radial field configuration in the Sun's equatorial plane. This radial stretching results in a region separating 'inward' and 'outward' field (shown for the simplest case at solar minimum in the left hand side of Figure 1.6), and therefore a current sheet forms. This is known as the heliospheric current sheet (HCS).

We are interested in the open and closed field line regions since it is thought that the regions of open magnetic field, called 'coronal holes' are the source regions for the fast wind (typically ~ 750 kms^{-1}) and the slow wind (typically ~ 400 kms^{-1}) is emitted from the closed field regions.

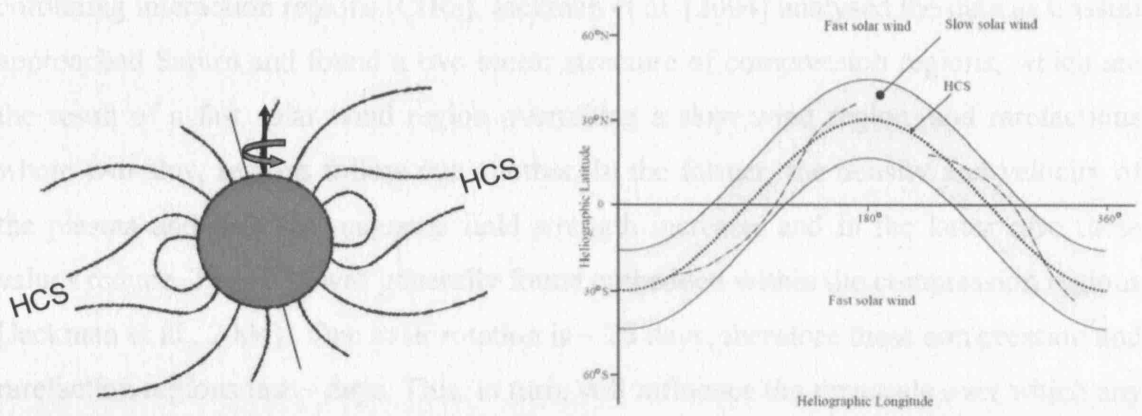

Figure 1.6 Schematic showing (left) the solar field during solar minimum The dipole field results in regions of open and closed field lines at high and low latitudes respectively. The field lines of opposite orientation at the magnetic equator are separated by the HCS. (Right) The two-sector structure of the solar wind which threads out into interplanetary space along with the HCS.

At solar minimum, when the Sun's field is approximately dipolar, the fast wind streams out from high magnetic latitudes, while the slow wind emanates from lower

latitudes. This is demonstrated in Figure 1.7 which shows the field configuration and associated fast and slow wind speeds at solar minimum. If we consider that the dipole magnetic pole is tilted with respect to the rotational axis (~8°), then as the Sun rotates, alternate fast- and slow-wind regions are emitted either side of the HCS.

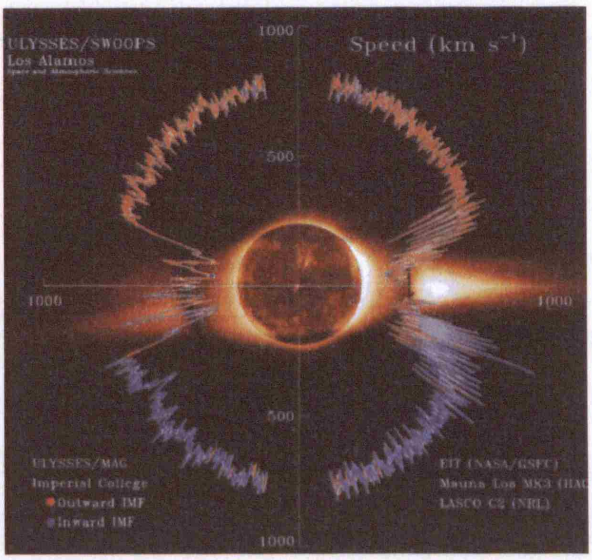

Figure 1.7 The solar wind speed, magnetic polarity, and coronal brightness as a function of time and heliolatitude [McComas et al., 1998]. Clearly, the polar regions, where we expect open field lines, correspond to high solar wind speed while the slow solar wind emanates from the closed-field, equatorial regions. Finally, the magnetic field orientation shows the expected change in polarity expected at the heliospheric current sheet.

These regions of slow wind and fast wind can interact with each other to form corotating interaction regions (CIRs). Jackman et al. [2004] analysed the data as Cassini approached Saturn and found a two sector structure of compression regions, which are the result of a fast solar wind region overtaking a slow wind region, and rarefactions where two slow regions follow one another. In the former, the density and velocity of the plasma and thus the magnetic field strength increase, and in the latter case these values reduce. The HCS was generally found embedded within the compression regions [Jackman et al., 2004]. One solar rotation is ~ 26 days; therefore these compression and rarefaction regions last ~ days. This, in turn, will influence the timescale over which any interactions occur with the magnetoshere.

The characteristics of the solar wind and IMF that impact Saturn's magnetosphere are clearly variable and these must be considered when analysing the magnetospheric response and processes observed. However, without an upstream solar wind monitor for Saturn, it is crucial to establish alternate means to understand the

conditions impacting on the magnetosphere of Saturn. This is discussed in more detail in Chapters 3 and 4.

1.2.4 The bow shock and magnetosheath

The solar wind is super-magnetosonic, i.e. the solar wind has an associated magnetosonic Mach number, $M_{MS} > 1$, where

$$M_{MS} = \frac{v}{C_{MS}}$$

Equation 1.28

the magnetosonic speed, C_{MS} is the square-root of the sum of the squares of the local sound speed C_S, and the Alfvén speed, v_A. Consequently, as the solar wind flow encounters an obstacle in its path, a plasma shock forms upstream. This shock wave, known as the 'bow shock' develops because the information needed to deflect the solar wind plasma around the obstacle travels at a velocity that is less than that of the solar wind flow. The transition from super-magnetosonic (upstream of the bow shock, Mach number $M_{MS}>1$) to sub-magnetosonic (downstream of the bow shock, $M_{MS}<1$) flow causes dramatic changes in the plasma and field. Since the solar wind expands into interplanetary space, Mach numbers tend to be higher at Saturn than in the inner solar system.

Downstream of the bow shock, the solar wind plasma is slowed, heated and deflected as the kinetic energy of the solar wind flow is dissipated into thermal and magnetic energy. This causes the density and temperature of the solar wind particles to increase. This region downstream of the bow shock and bounding the outer boundary of the magnetosphere, is known as the magnetosheath. The thickness of this layer is variable and depends upon the solar wind pressure and the size of the obstacle.

The magnetosheath borders the region of space dominated almost entirely by the planetary magnetic field, the magnetosphere. The magnetosheath, therefore, plays an important role since it strongly influences the eventual configuration of the IMF reaching the magnetic cavity of the planet [Crooker et al., 1985]. As the solar wind flow is deflected around the magnetosphere, it compresses the dayside magnetospheric field and stretches out the field on the night-side forming a shape very much like that of a cometary tail. This tail can extend many hundreds of planetary radii downstream [Russell, 1991].

1.3 The magnetopause

The nature of the field and plasma processes occurring at the Earth's magnetopause have been the subject of numerous studies since the advent of the first space-based plasma and field instruments [e.g. Sonnerup and Cahill, 1967; Ogilvie et al., 1971; Sonnerup and Ledley, 1979; Haerendel et al., 1978; Sibeck et al., 1991; Sibeck et al., 1999].

The magnetopause defines the outermost edge of the planetary field and is a crucial boundary for energy and momentum exchange between the planetary fields and plasma sources and the Sun's field and particles [Eastman et al., 1976; Eastman and Hones, 1979]. Its existence was first proposed by Chapman and Ferraro [1931] in a paper which described how the solar wind could not penetrate the Earth's field due to a shielding current that is formed between the two regions. The formation of a current layer between the planetary magnetic field and that of the IMF is a result of the field regimes remaining separate by the frozen-in field condition.

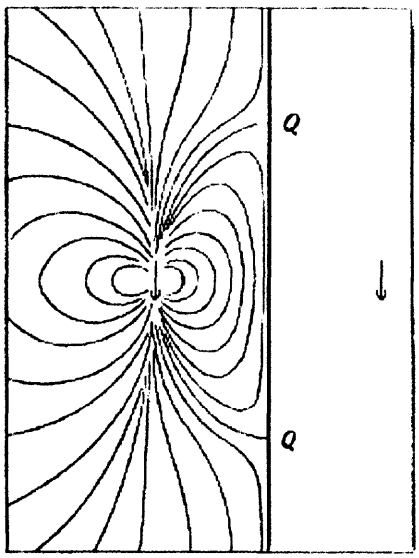

Figure 1.8 The Earth's dipole field (left), flattened by the addition of the field of an image dipole (right), as proposed by Chapman and Ferraro [1931].

In the simple Chapman and Ferraro [1931] picture of the interaction (Figure 1.8), the solar wind field and the magnetospheric plasma are neglected. The current at the magnetopause is carried predominately by the ions arriving from the solar wind/magnetosheath. Particles can enter the current layer and find themselves subjected to the relatively intense planetary field: the particles respond to the resultant Lorentz

force and rotate halfway about the field (executing half a gyration) before they are reflected back, the example for Earth is shown in Figure 1.9.

The thickness of this current layer is thus approximated by the gyroradius of the positively charged particles. The opposite direction of the rotational motion for positive and negative charges generate the current. This is, of course, a very simplified picture and relies on several assumptions about the plasma. In addition, a more advanced treatment of the magnetopause takes into account the solar wind magnetic field and thus the particle motion in the magnetopause current layer behaves according to the magnetic field gradient. These descriptions shall not be discussed further here, but are detailed in Cowley [1995].

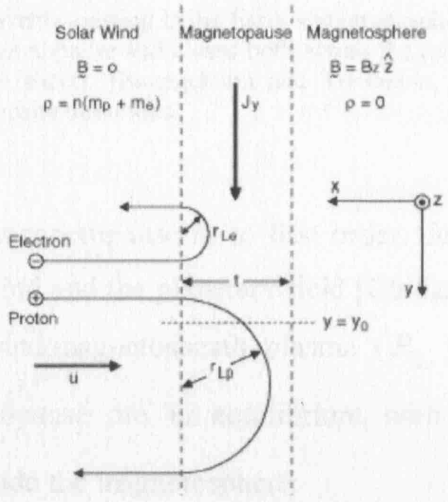

Figure 1.9 Classic Chapman and Ferraro schematic of the magnetopause current layer at Earth. It shows how the charge separation occurs under the influence of the magnetospheric field resulting in a layer ~ one gyroradius thick [reproduced from Russell, 2003].

The magnetic field generated by this current produces a diamagnetic effect and confines the magnetospheric field within the magnetopause [Cowley 1995; Baumjohann and Treumann, 1997], preventing it from penetrating the magnetosheath. At Saturn, whose dipole is directed opposite to that of the Earth, the sense of this current is from dusk to dawn and it closes on the nightside magnetopause via the tail magnetopause. Here it is redirected northwards and southwards across the magnetopause surface and via the cross-tail current located in the central plasma sheet between the magnetospheric tail lobes (Figure 1.10).

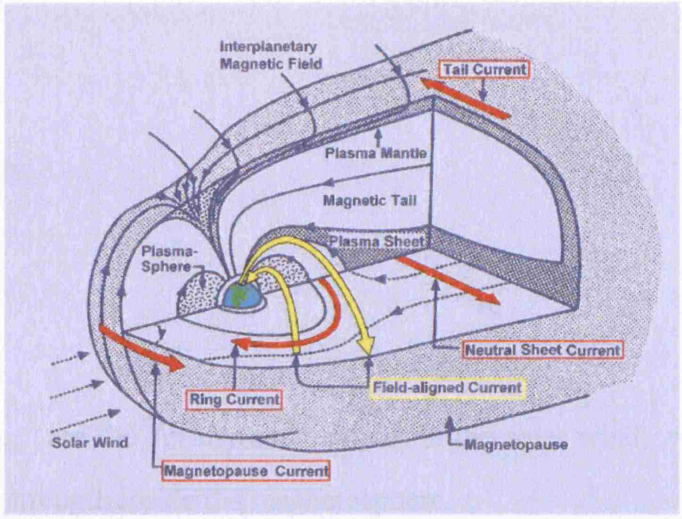

Figure 1.10 Sketch of the main currents existing in the Earth's magnetosphere. The magnetopause current runs across the surface of the magnetopause and closes both across the tail magnetopause and in the tail current sheet (the neutral current sheet). [Baumjohann and Treumann, 1997]. The main currents in Saturn's magnetosphere are of opposite directions.

The position of the magnetopause is, to first order, determined by the pressure balance between the solar wind and the planetary field [Cowley, 1995; Stern, 1995]. At this boundary, the solar wind/magnetosheath plasma ($P_{P_{SW}}$) and magnetic pressure ($P_{B_{SW}}$) outside the magnetopause are in equilibrium with the plasma ($P_{P_{MS}}$) and magnetic pressure ($P_{B_{MS}}$) inside the magnetosphere:

$$P_{P_{SW}} + P_{B_{SW}} = P_{P_{MS}} + P_{B_{MS}},$$

Equation 1.29

and as we have seen in section 1.2.3, the solar wind pressure is highly variable and therefore will, in turn, cause compressions and expansions of the magnetosphere. To a first approximation, the magnetic pressure in the solar wind field can be considered insignificant, and the plasma term dominates. This is a summation of the thermal and dynamic pressures, and since the majority of the energy of the solar wind is in the bulk flow [Baumjohann and Treumann, 1997], only the dynamic pressure is considered. In addition, the plasma pressure in the outer magnetosphere is assumed to be negligible relative to the planetary field pressure, so only the latter term is included. Thus, a simple condition for magnetopause pressure balance is:

$$P_{dyn_{SW}} = P_{B_{MS}},$$

Equation 1.30

or more specifically;

$$n_{SW} m_i \underline{v}_{SW}^2 = \frac{B^2}{2\mu_0},$$

Equation 1.31

where n_{SW} and $\underline{v}_{SW}$ are the density and velocity in the solar wind, m_i is the ion mass and B is the field strength inside the magnetosphere.

At Earth these upstream conditions have been monitored over recent years allowing comparisons between expected and observed phenomena [e.g. Stone et al., 1998]. Note that the actual characteristics of the IMF impacting the magnetopause, i.e. its strength and direction, are modified as a result of the traversal through the bow shock and magnetosheath and draping around the magnetosphere [Crooker et al., 1985; Longmore et al., 2006].

1.3.1 Reconnection at the magnetopause

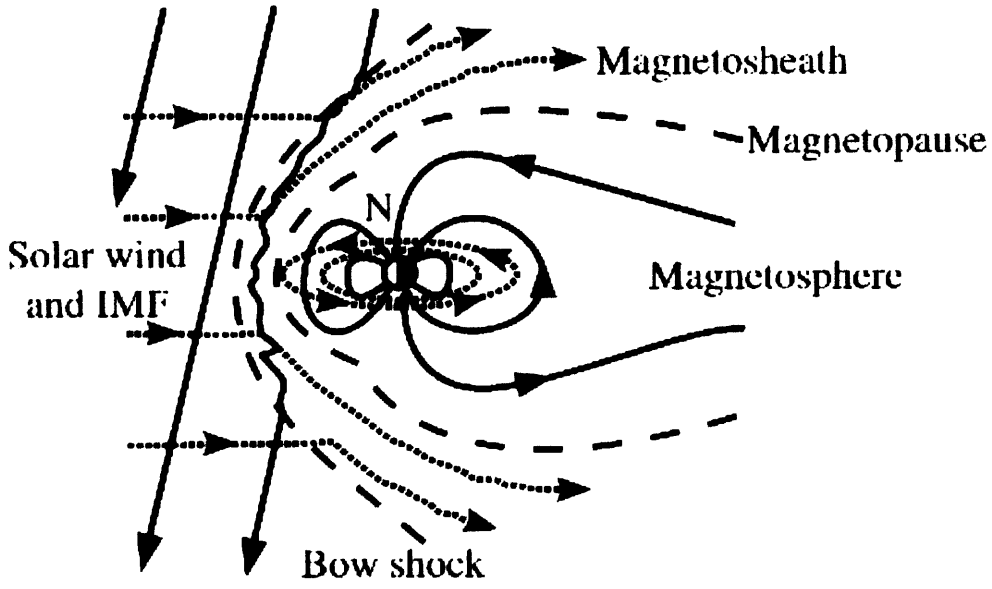

Figure 1.11 Example of a 'closed' magnetosphere at Earth. The solid lines are the magnetic field lines and the dotted lines are flow stream lines. The incoming solar wind is approaching from the left, carrying the IMF. Upstream of the Earth's magnetic cavity the solar wind and associated field are slowed and deflected round the magnetosphere by the bow shock. Downstream of the bow shock the magnetosheath consists of heated and slowed solar wind plasma and the modified IMF. This region is bounded by the magnetopause. In this closed configuration the fields and plasma in the magnetosphere and solar wind remain separate

The magnetopause is, in its simplest form, an impenetrable layer bounding the magnetosphere. In this case, the magnetosphere is 'closed' (the example in the case of Earth is in Figure 1.11) and the field and plasma from the planetary and solar regions remain separated. In regions where the external and magnetospheric fields have an antiparallel component, reconnection can occur.

Two such locations are shown for a northward and a southward IMF for the case of Earth in Figure 1.12. The first shows where reconnection is likely to occur under southward IMF. In this case a field line in the solar wind reconnects on the dayside (where the fields are antiparallel), resulting in two open field lines, with one end connected to the planet and the other in the solar wind. If reconnection occurs under northwards IMF, the most likely place where anti-parallel fields will be found is tailward of the cusps. The cusps are funnel shaped field regions at high latitudes that separate the dayside and nightside fields in both the northern and southern hemispheres.

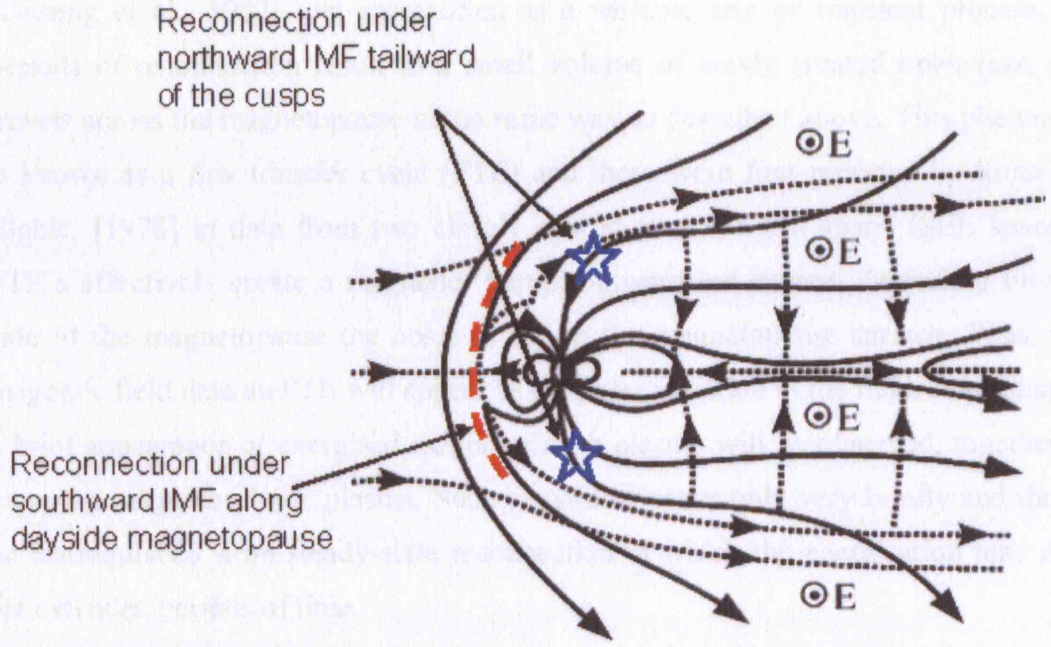

Figure 1.12 Example of an 'open' magnetosphere at Earth. The solid lines are the magnetic field lines and the dotted lines flow stream lines. The incoming solar wind is approaching from the left, carrying the IMF and the convective electric field which ultimately drives the convection in the magnetosphere. Upon reaching the bow shock, the field and plasma are deflected round the magnetosphere, but this time the fields of the IMF and magnetosphere are in a favourable configuration on the dayside to reconnect across the magnetopause. The red dashed lines indicate reconnection for a southward IMF and the blue stars indicate the location of reconnection for a northward IMF. The dotted flow streamlines originating in the solar wind are now able to enter the magnetosphere and plasma is transported into the magnetic cavity to mix with the magnetospheric plasma. As the now-open field lines are dragged tailward by the solar wind forcing they convect over the polar cap and build-up in the tail. They eventually return to the dayside via the flank equatorial regions and a dawn-dusk electric field is set up (due to the presence of $\underline{v} \times \underline{B}$) as shown in the tail [Cowley, 1996].

In this case, an IMF field line will reconnect with an open field line (in the magnetospheric 'lobes', see Figure 1.12) and no extra flux is added or taken away. In addition, as has been discussed, due to the Parker spiral, there is a significant B_Y component of the IMF once Saturn's orbit is reached. If Figure 1.11 is imagined in three dimensions we might expect the reconnection line to lie along the equatorial region of the magnetopause. With a significant IMF B_Y we expect the reconnection line to 'tilt' [Marcucci, et al., 2001] although we have not explored the effects of this in this work.

Once reconnected, an open field line will be subject to forcing from the magnetosheath flow and the magnetic tension force and will convect across the magnetopause surface as the flow moves tailward, since the field lines are frozen to the solar wind plasma. They then reconnect in the tail in a process known as a substorm, and return in the low-latitude regions to the dayside where the process begins again.

At Earth, reconnection between IMF and planetary field lines is common [Sonnerup et al., 1981; Paschmann et al., 1986] and may occur as a steady-state process [Gosling et al., 1982], but more often as a variable rate or transient process. Brief periods of reconnection result in a small volume of newly created open flux, which travels across the magnetopause in the same way as described above. This phenomenon is known as a flux transfer event (FTE) and these were first reported by Russell and Elphic, [1978] in data from two closely spaced (~ 100's km apart) ISEE spacecraft. FTE's effectively create a magnetic 'bump' outward (or inward, depending on which side of the magnetopause the observer is) on the magnetopause surface. Thus, in the magnetic field data an FTE will appear as a bipolar variation in the field. In plasma data, a brief appearance of energised magnetosheath plasma will be observed, together with escaping magnetospheric plasma. Such signatures occur only very briefly and thus can be distinguished from steady-state reconnection in which the energisation may appear for extended periods of time.

FTEs have also been observed at Mercury [Russell and Walker, 1985; Russell, 1995] and Jupiter [Walker and Russell, 1985, Russell, 1995]. These observations are based on the FTE model as proposed by Russell and Elphic [1978], alternative models exist which, for example, describe an FTE as being due to a transient increase in the reconnection rate and therefore the separatrix layer alternates in thickness [e.g. Southwood et al., 1988; Scholer, 1988]. Lee and Fu [1985] also proposed that multiple X-lines on the magnetopause could result in FTE signatures. There are also examples of non-reconnection generated FTE theories, one such model was proposed by Sibeck et

al. [1989] who cite waves along the magnetopause as causing the observed bipolar signatures.

1.3.2 Global plasma circulation at Saturn

As described above, reconnection of solar and magnetospheric fields drives a convection cycle in the magnetosphere known as the 'Dungey cycle' [Dungey, 1961, 1963]. At Earth, this cycle dominates the magnetospheric dynamics. At Jupiter, the fast rotation of the large, mass-laden magnetosphere results in an internally-driven system. The same internally-driven characteristics may be seen at Saturn since it is also a fast rotator, and there are also significant plasma sources in the rings and moons which continually 'feed' new plasma into the system [Gombosi and Hansen, 2005; Hansen et al., 2005]. The fast rotation of Saturn results in a centrifugal force which acts on the plasma, confining it to the equatorial plane [Gombosi and Hansen, 2005]. The magnetic field is therefore stressed in these regions and also the ring current has the magnetic effect of 'stretching' the field, resulting in a predominately radial field orientation. This is known as 'ballooning' of the field [Kivelson and Southwood, 2005]. At some threshold the field line will not be able to confine this plasma any longer and the ionosphere will not be able to enforce rotation and the mass-laden bubble will detach from the closed field line and will be released outward [Kivelson and Southwood, 2005]. The release of plasma will result in a dipolarisation of the field and an acceleration of the field line to the corotation velocity. Due to the lack of external forcing, this plasma release preferentially occurs in the tail regions via a 'planetary wind'. This process results in reconnection of stretched fields in the tail, and forms the basis of the 'Vasyliunas cycle' [Vasyliunas, 1983].

Since Saturn is intermediate in size between Earth and Jupiter we may have expected the magnetospheric dynamics to fall somewhere in the middle of the two extremes: externally or internally driven dynamics? Theoretical consideration of the large-scale magnetospheric flows at Saturn was carried out by Cowley et al., [2004] who considered the pattern formed by both solar wind and rotation-driven flows, and suggested the picture in Figure 1.13.

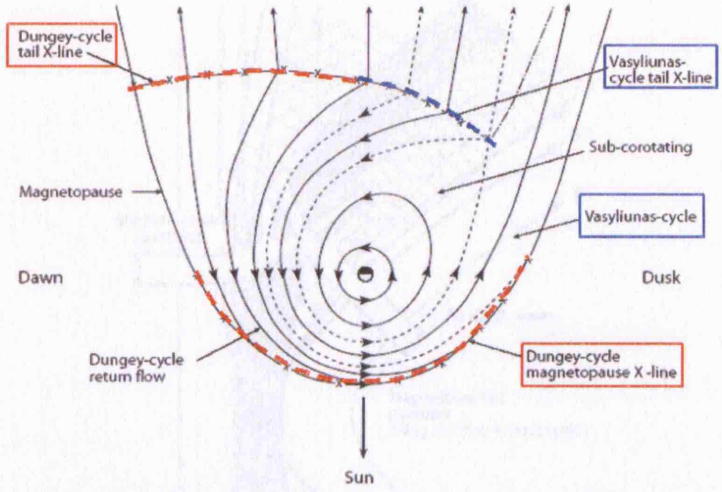

Figure 1.13 Sketch of the plasma flow in the equatorial plane of Saturn's magnetosphere. Arrowed solid lines show plasma streamlines, the short dashed lines the boundaries between regions. The Dungey and Vasyliunas cycle reconnection lines are indicated by the red and blue lines respectively, [Cowley et al., 2004].

The internal magnetospheric plasma corotates, while in the outer regions the plasma slows due to the mass-loading by the rings and moons. The Dungey and Vasyliunas cycles are indicated, together with their associated reconnection or 'X-lines'. From this picture we expect that both cycles occur at Saturn, but without knowing which is dominant. The motional electric field of the solar wind driving the Dungey cycle can be compared with the electric field due to the corotation of the magnetospheric plasma. Since the latter will weaken with radial distance, there is a point at which these two fields cancel (known as the 'stagnation point'). It is known that at Jupiter this point occurs *outside* the magnetopause and thus the magnetospheric flows are dominated by the internal dynamics. However, at Saturn the balance of these two cycles and associated flows are currently being investigated by data from the Cassini spacecraft and we aim to establish this balance for two particular magnetopause encounters in Chapter 3.

1.3.3 The particle picture of reconnection

A closer look at the reconfiguration of the magnetopause due to reconnection is shown in Figure 1.14. In addition to particles being transmitted through the current layer, there may also be a reflected portion of each population. These mixed populations combine to populate the low-latitude boundary layer (LLBL) and the magnetosheath boundary layer (MSBL). These are discussed in more detail later.

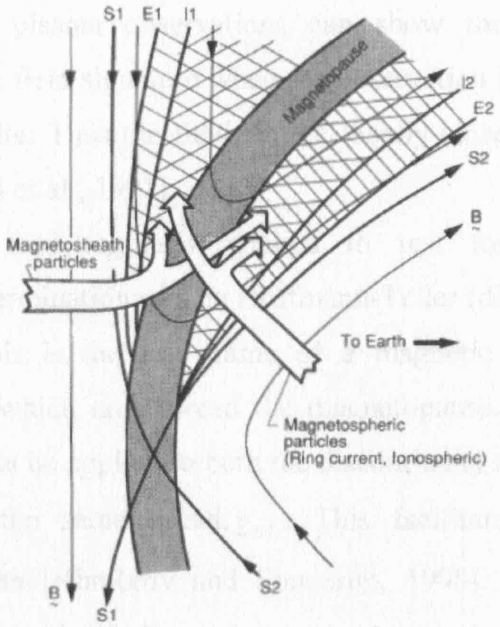

Figure 1.14 Reconnection geometry from Gosling et al., [1990]. The left hand side shows a southward magnetosheath field and the right hand side the northward magnetospheric field. The current layer is shown as the shaded boundary in the centre of these two regions. As the fields reconnect (where the two separatrices, S1 and S2 cross) and thread the magnetopause, a region of 'open' field allows the entry of magnetosheath particles into the magnetosphere. Additionally, a portion of the population is reflected. Both populations are heated by the process of interacting with the current sheet. On the right the magnetospheric counterpart is transmitted through the boundary and a population is again reflected, again both are heated. As the reconnection continues the fields convect away from the site (up in this figure), carrying the plasma with them. Due to the velocity filter effect a layer of electrons is seen further away from the magnetopause on both sides (between E1 and I1 and I2 and E2). Once the ions 'catch up', a layer of both electrons and ions is then seen (within I1 and I2).

As heated and accelerated plasma streams away from a reconnection site there is dispersion in the appearance of the electrons and ions. This is the 'velocity filter effect' and is a consequence of the greater speeds of the light electrons compared with the heavy ions [Gosling et al., 1990; Song and Russell, 1992]. The electrons are therefore able to travel further from a reconnection site in a finite time compared with the ions, thus an observer will detect accelerated electrons before the accelerated ions. The signature of reconnection therefore includes:

- Increase or decrease in the bulk speed (depending on the direction of boundary layer plasma flow relative to the magnetosheath bulk flow) or a velocity deflection of plasma at and immediately surrounding the magnetopause;
- An increase in plasma temperature;
- Evidence of an open field [Paschmann et al., 1979, 1986; Gosling et al., 1982].

Note also, that plasma observations can show the traits associated with reconnection without the field signature when the observation is made at some distance from the reconnection site. Thus the field can be locally closed, but accelerated flows may still be present [Hall et al., 1991].

One analytical tool regularly applied to test for reconnection on the magnetopause is the determination of a de Hoffmann-Teller (dHT) frame [de Hoffmann and Teller, 1950]. This is the rest frame of a magnetic field line, such as the reconnected field lines which now thread the magnetopause. Thus, a single velocity space reference frame can be applied to both the discontinuity and the fields either side, as they all move at the same speed, $\underline{v}_{HT}$. This facilitates further analysis and interpretation of the data [Khrabrov and Sonnerup, 1998]. The de Hoffman-Teller velocity ($\underline{v}_{HT}$) is determined by finding a frame of reference in which the velocity of the plasma and field, $\underline{v}$ is parallel to $\underline{B}$, as in this frame the convection electric field is zero. The velocity of the accelerated plasma is therefore the Alfvén speed in this frame, i.e. $\underline{v} - \underline{v}_{HT} = \pm \underline{v}_A$. This is known as the Walén relation, which can provide information on which side of the X-line the observations are made and indeed whether the magnetopause is in fact a rotational discontinuity at the observation site [Sibeck et al., 1999].

The location of the reconnection site relative to the spacecraft can also be determined via analysis of the pitch angles of particles, which give their direction of motion with respect to a field line. To give an example, consider Figure 1.15. If an observer crosses the Earth's magnetopause outbound near the subsolar point into a southward magnetosheath magnetic field when reconnection is occurring and observes heated electrons with anti-parallel pitch angles, the spacecraft must be northward of the reconnection site. If heated parallel pitch angles are observed, the spacecraft must be southward of the reconnection site. By taking account of the field geometry and the pitch angles of the heated and un-heated populations at the site of an observer, the relative location of the reconnection site can be inferred [Fuselier et al., 1995].

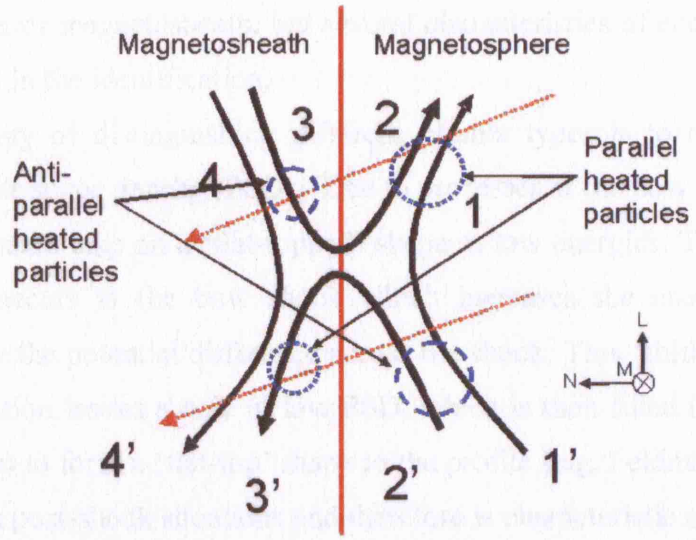

Figure 1.15 Schematic of the field line geometry for a model reconnection site looking tangentially along the dayside magnetopause. The coordinate system is the 'boundary normal coordinates' where $\underline{L}$ and $\underline{M}$ form the plane of the magnetopause and $\underline{N}$ is the normal (Appendix B). On the left is a southward pointing magnetosheath magnetic field and a northward planetary field is on the right. Above and below the central point where reconnection has occurred, the newly reconnected, bent field line, will now thread the magnetopause (the vertical red line). Consider the particle flows seen by a spacecraft as it leaves the magnetosphere passing either above or below the x-line. If the spacecraft trajectory (red dotted line) passes northward of the x-line it will first see bi-directional trapped plasma population (field line 1), upon crossing the first open field line (2) it will observe parallel heated magnetosheath particles streaming away from the reconnection site and un-heated anti-parallel magnetospheric particles exiting the magnetosphere, so there is no change in the magnetospheric population. However, reconnection can also cut-off the supply of anti-parallel moving magnetospheric particles. Eventually it can also cut-off the parallel magnetospheric population, so a 'hole' in the population may be observed. The magnetopause current layer is then crossed and the external part of the open field line (3) will contain anti-parallel streaming heated particles plus parallel un-heated magnetosheath plasma entering the magnetopause and finally upon crossing (4) it will observe un-heated magnetosheath plasma. If we now consider the second trajectory passing below the reconnection site, first trapped magnetospheric plasma will be observed on (1'), then (2') will contain anti-parallel heated particles streaming away from the reconnection site and un-heated parallel magnetospheric particles exiting the magnetosphere and crossing the magnetopause. Upon leaving the magnetosphere (3'), parallel heated plasma plus un-heated, anti-parallel magnetosheath plasma will be observed, before finally crossing an open field line with un-heated magnetosheath plasma (4').

1.3.4 Boundary layer plasma

The analysis of the plasma characteristics and behaviour in the internal and external magnetopause boundary layers allows a more detailed look at the formation and evolution of plasma mixing processes at the magnetopause [Eastman et al., 1976; Ogilvie et al., 1971; Eastman and Hones, 1979]. Eastman et al. [1976] first noted that the plasma in the internal boundary layer is a combination of magnetosheath and magnetospheric plasmas with a field orientation akin to that in the magnetosphere. There is no strict definition of the distinction between plasmas in the boundary layer,

magnetosphere or magnetosheath, but several characteristics of each population can be outlined to aid in the identification.

One way of distinguishing different plasma types is to observe the electron spectra in phase space density (PSD). Due to processes at the bow shock, the spectra in the magnetosheath take on a 'flat-topped' shape at low energies. This arises due to the heating that occurs at the bow shock which increases the energy of the electron distribution by the potential difference across the shock. This 'shift' upwards in energy of the distribution leaves a hole at low PSD, which is then filled (via mechanisms not discussed here) to form a 'flat-top' shape to the profile [e.g. Feldman et al., 1982]. This is only seen in post-shock situations and therefore is characteristic of the magnetosheath population. Once the population mixes with the different magnetospheric populations to form boundary layers this characteristic shape will be altered [Scudder et al., 1973].

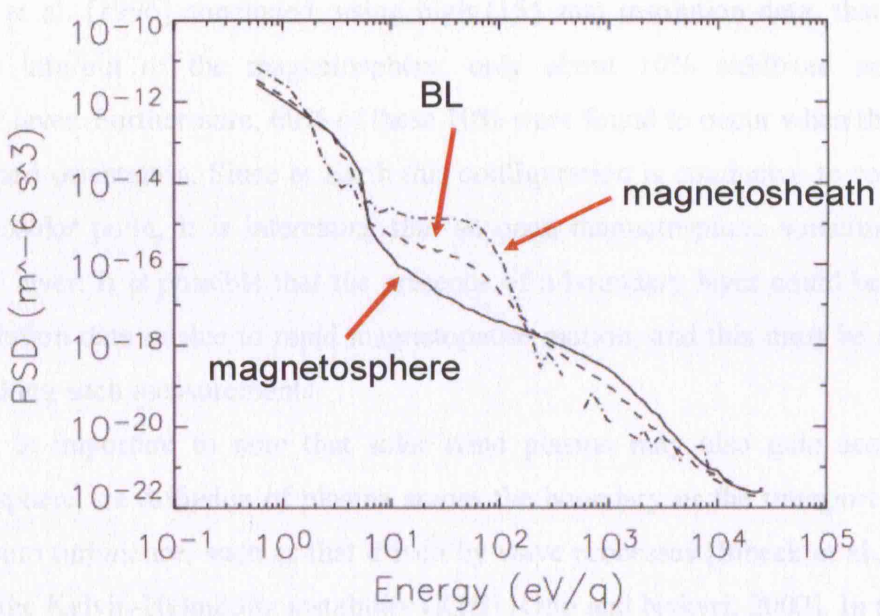

Figure 1.16 PSD electron distribution spectra with PSD on the vertical-axis and $\log_{10}$ energy on the horizontal axis demonstrating the differences between three separate populations in Saturn's magnetosphere (solid line), boundary layer (dashed line) and magnetosheath (dot-dash line) for 17 April 2005 at 17:31 UT, 18:07 UT and 18:58 UT respectively. The boundary layer distribution is bounded by the magnetosheath and magnetospheric populations indicating that it is formed from the two plasma types. The characteristic 'flat-top' shape of the magnetosheath population between ~ 10 eV and ~ 60 eV is evident.

The change in shape of the electron spectra in PSD for Saturn is demonstrated in Figure 1.16 which shows typical PSD distributions for magnetosphere, boundary layer and magnetosheath populations and the distinction between them. The magnetospheric population has the largest PSD at higher energies. In the boundary layer, the high energy PSD is depleted and the lower energy population starts to increase relative to the

magnetospheric population. Finally, the magnetosheath population shows a clear 'flat-topped' distribution between ~ 10 - 60 eV with a significant PSD at these energies. Note the boundary layer sits in between these populations demonstrating that it is indeed a mix of these two populations.

At Earth an internal boundary layer is prevalent. The main example of this is the 'Low-Latitude Boundary Layer' (LLBL) [Eastman et al., 1976; Eastman and Hones, 1979; Haerendel et al., 1978; Sckopke et al., 1981; Mitchell et al., 1987; Song and Russell, 1992]. Some studies have separated this boundary layer further [Sckopke et al., 1981; Hall et al., 1991; Song and Russell, 1992] into regions with different density and temperature characteristics. This can be a means of testing differing theories behind the formation of the layer, e.g. diffusive entry across the boundary or reconnection. At Earth this boundary layer is almost always present, as found in a survey of magnetopause crossings at all local times [Haerendel et al., 1978; Eastman et al., 1996]. Eastman et al. [1996] concluded, using high (155 ms) resolution data, that of all the crossings into/out of the magnetosphere, only about 10% exhibited no apparent boundary layer. Furthermore, 60% of these 10% were found to occur when the IMF had a southward orientation. Since at Earth this configuration is conducive to reconnection at the subsolar point, it is interesting that an open magnetosphere sometimes has no boundary layer. It is possible that the presence of a boundary layer could be missed in low resolution data or due to rapid magnetopause motion, and this must be considered when making such measurements.

It is important to note that solar wind plasma may also gain access to the magnetosphere via diffusion of plasma across the boundary or the transport of plasma arising from turbulence, such as that driven by wave processes [Sibeck et al., 1999] for instance the Kelvin-Helmholtz instability (KHI) [Otto and Nykyri, 2002]. In these latter cases, the plasma may not show signs of energisation and will not satisfy the Walén test. This allows for a distinction between the formation of such layers from those formed due to reconnection [Paschmann et al, 1993; Song et al, 1990]. However, recent observations supported by simulations suggest that magnetic reconnection could occur within rolled-up KHI vortices [Nykyri et al., 2006].

The external counterpart to an internal boundary layer is known as the magnetosheath boundary layer (MSBL) [Fuselier et al., 1995; Onsager et al., 2001]. This refers to plasma in the magnetosheath which is on field lines connected to the planet. By understanding the plasma flow directions, together with any heating adjacent,

but external to the magnetopause, unambiguous signs of reconnection can be identified [Lavraud et al., 2005].

Another type of layer external to the magnetopause can form when the solar wind faces an apparently impenetrable obstacle, such as with a locally closed magnetosphere. The IMF lines drape around the magnetosphere and create a build up of flux on the dayside. This causes an increase in the magnetic pressure and forces plasma away from the strong field region, effectively 'squeezing' the plasma out along the field lines and resulting in a plasma depletion layer (PDL) [Zwan and Wolf, 1976; Crooker et al., 1979; Paschmann et al., 1993; Phan et al., 1994]. However, Maynard et al. [2004] also reported the presence of a PDL in the case of an open magnetosphere, indicating that the flux build up can occur even when reconnection is occurring. In such cases the incoming flow adds magnetic flux faster than the rate of reconnection can remove it.

1.3.5 Previous findings at Saturn's magnetopause

The three previous flybys of Saturn (Pioneer 11 and Voyagers 1 and 2) found the magnetopause to be located at a range of distances, indicating a variable magnetosphere driven either by external forcing from the solar wind pressure or internal plasma and field effects. On Pioneer 11's inbound trajectory, Wolfe et al. [1980] reported the solar wind pressure upstream of the bow shock to be 0.15 nPa which was high compared with the predicted average dynamic pressure of < 0.02 nPa (P_{dyn}) at this heliocentric distance. This was due to the arrival of a corotating interaction region (CIR) at Saturn. The outbound crossing locations suggested that there had been a reduction in P_{dyn} while the spacecraft was within the magnetosphere [Wolfe et al., 1980; Smith et al., 1980]. Overall, the magnetopause positions observed by Pioneer 11 are now known to indicate a compressed magnetosphere [Smith et al., 1980] and are listed in Table 1-1.

Voyager 1 observed five magnetopause crossings inbound and outbound [Bridge et al., 1981; Ness et al., 1981; Maclennan et al., 1983]. The relative stationarity of the magnetopause during this flyby allowed the identification of surface waves in the inbound crossing data [Lepping et al., 1981, 1992; Huddleston et al., 1997]. The regular spacing (~ 4 to 20 minutes) of the crossings and the alternating directions of the magnetopause normals suggested that the variations were associated with a wave such as the Kelvin-Helmholtz instability, driven by velocity shear between the

magnetospheric and magnetosheath flow, rather than global magnetopause inflation and compression.

Voyager 2 made just one crossing of the magnetopause on its inbound trajectory [Bridge et al., 1982; Ness et al., 1982] at a distance of 18.5 R_S, indicating a compressed magnetosphere relative to that seen by Voyager 1 but more inflated than the Pioneer 11 case. However, the outbound crossing locations suggested a much more inflated magnetosphere. Such an expansion is expected only rarely and was eventually explained as the effect of the immersion of Saturn in Jupiter's magnetotail, resulting in a much reduced solar wind pressure [Bridge et al.,1981; Ness et al., 1982; Behannon et al., 1983]. The large number of crossings outbound was attributed to boundary waves causing large-scale motion of the boundary over the spacecraft [Bridge et al., 1982; Lepping et al., 1992].

Table 1-1 Magnetopause crossing times and distances from Pioneer 11 [Wolfe et al., 1980], Voyager 1 [Bridge et al., 1981] and Voyager 2 data [Bridge et al., 1982]

Date	**Time**	**Radial distance***	**Date**	**Time**	**Radial distance***
Pioneer 11			**Voyager 2**		
inbound			*inbound*		
31 Aug 1979	2208	17.3	25 Aug 1981	0703	18.5
outbound			*outbound*		
03 Sep 1979	0916 – 0927	30.25	28 Aug 1981	1620 to 1626	-
03 Sep 1979	1406-1412	33.24		1644	
03 Sep 1979	1828	35.9		1648	-
03 Sep 1979	2334-2335	39.0		1650	-
04 Sep 1979	0048-0103	39.81		1652 to 1700	48.6
				1743 to 1809	49.1
Voyager 1				2138	-
inbound				2148	-
12 Nov 1980	0154	23.6		2156	52.0
12 Nov 1980	0213	23.4		2255	52.7
12 Nov 1980	0228	23.2	29 Aug 1981	0421 to 0453	56.9
12 Nov 1980	0242	22.9		0620	57.9
12 Nov 1980	0248	22.7		0721	58.5
outbound				1620	64.8
14 Nov 1980	1729	42.7		1641	65.1
14 Nov 1980	1806	43.4		1814 to 1833	66.3
14 Nov 1980	2034	45.7	30 Aug 1981	0031	70.4
14 Nov 1980	2115	46.1			
14 Nov 1980	2140	46.9			

* Where 1 R_S = 60,330 km

During the Voyager 1 outbound pass, the detection of plasma adjacent to the boundary that was unlike that of the magnetosheath or interior magnetospheric lobe was identified as boundary layer [Behannon et al., 1983]. In this layer there was a noticeable increase in the ion flux and temperature in an anti-sunward streaming population. This

boundary layer was encountered a number of times and Behannon et al. [1983] suggested that the irregular spacing of the encounters were due to the bulk motion of the magnetopause, rather than surface waves. The magnetic field fluctuations were also seen to increase in the boundary layer relative to that observed in the magnetosphere proper [Behannon et al., 1983] and lessen with respect to those seen in the magnetosheath. This may also provide an aid in identifying boundary layers where the plasma data is ambiguous.

The only study to address kinetics of reconnection at Saturn using the Pioneer 11 and Voyager data is Huddleston et al., [1997], who reported an open magnetospheric configuration based on the finite normal component of the magnetic field across the magnetopause boundary and the presence of accelerated and heated plasma flows. However, the inferred electric field due to the solar wind flow (~0.2 mVm^{-1}) was found to be insignificant compared with their estimates of the corotational electric field at 23 R_S (~1.4 mVm^{-1}), suggesting that reconnection should not be a dominant process at Saturn. The lack of reported observations suggesting bursty reconnection [Russell, 1995; Huddleston et al., 1997] in the form of flux transfer events (FTEs) which are prevalent at Earth [Rijnbeek et al., 1984; Russell et al., 1985, 1996] also suggests that reconnection is not a significant mechanism at Saturn. However, the observations of transient reconnection at Jupiter [Walker and Russell, 1985] is worth highlighting since it is also a large, rapidly rotating magnetosphere with significant internal effects, yet still shows evidence of interaction with the solar wind and IMF.

In addition to searching for reconnection driven by the IMF and solar wind, Saturn's unique magnetospheric system provides another possibility for reconnection at the magnetopause, driven by internal processes. As described in section 1.3.2, the build-up of magnetospheric plasma will eventually result in the release of plasma 'bubbles'. If these impact the magnetopause with enough momentum to break out through the magnetopause, they will ultimately reconnect with the magnetosheath field, resulting in similar signatures of reconnection at the magnetopause [Southwood and Kivelson, 2005; Southwood, 2006, *private communication*].

1.3.6 Saturnian magnetopause models

There are currently three models of Saturn's magnetopause available. Slavin et al., [1983, 1985] generated an empirical model based on Voyager 1 and 2 data. A

symmetric, conic surface was fitted to the observed magnetopause locations and then scaled for upstream dynamic pressure variations. The scaling was achieved by inferring the upstream pressure based on the assumption of pressure balance with the magnetic pressure recorded just inside the magnetopause.

The magnetopause model of Maurice et al., [1996] was generated as a consequence of the creation of their theoretical global model. The generated magnetopause surface was fitted to a conic section through least-squares fitting and provided a model geometry that is a function of the magnetopause stand-off distance. This was found to be very different from the Slavin et al., [1985] model, particularly at the flanks [Arridge et al., 2006a].

Most recently Arridge et al. [2006a] have used a new technique based on a functional form for the magnetopause based on a model applied at Earth [Shue et al., 1997] which they make pressure-dependent. The geometry is significantly different to the previous models. The resultant model also indicates that plasma pressure as well as magnetic pressure internal to the magnetosphere are key to the pressure balance. The flaring of the magnetopause also decreases with increasing solar wind dynamic pressure, which is opposite to the situation at Earth. This model is used in this study due to increased accuracy compared with previous models.

1.3.7 Inferring upstream conditions

Observations at Earth are the result of the integration of a large set of coordinated measurements of solar activity, the resultant solar wind parameters and the various ground-based measurements which allow a thorough investigation of the response of the magnetosphere and ionosphere to changes in the solar wind conditions.

It is an unfortunate by-product of the nature of exploratory missions such as Cassini that there is no analogous set of measurements to monitor the upstream particle and field conditions out at 9 AU. This limits the ability to be certain about the conditions of the solar wind when the spacecraft is inside the magnetopause, and hence determine the correlation of the boundary conditions with upstream conditions. All that can be reported are the conditions observed just prior to the crossing inbound (or just after an outbound crossing).

There are methods available to try and better understand the nature of the solar wind out at the distance of Saturn. The numerous spacecraft situated at or near 1 AU

could allow propagation of the solar wind out to 9 AU. However, this is known to be inaccurate [Prangé et al., 2004].

There have been links made between Saturn's auroral activity and the solar wind pressure [Cowley et al., 2005; Crary et al., 2005]. However the auroral activity is not monitored continually and the exact relationship is not understood enough to use it as a proxy for upstream conditions. Another option is to apply a magnetopause model that uses the scaling of the magnetopause position with solar wind dynamic pressure and simply work backward from observed positions to infer solar wind pressure [Arridge et al., 2006a].

1.4 Moon-magnetosphere interactions

1.4.1 Plasma interactions with moon-like bodies

In general, the moons orbiting inside Saturn's magnetosphere do not have intrinsic magnetic fields and are considered to be insulating bodies. In this case, the moons will simply absorb any incident plasma particles, leaving a cavity or wake in the corotating plasma. The obstacle presented to the plasma flow inside Saturn's magnetosphere is thus approximately equal to the moon diameter. The form of the downstream wake is dependent solely on the upstream plasma flow. For example, if the incident flow velocity is slow relative to the thermal speed of the particles, then the perpendicular motions of the particles can refill the wake in a short time. This may likely be the case for electrons at Tethys since $v_{corotation} - v_{moon} \sim 10$'s kms^{-1} compared with $v_{thermal} \sim 1000$'s kms^{-1}.

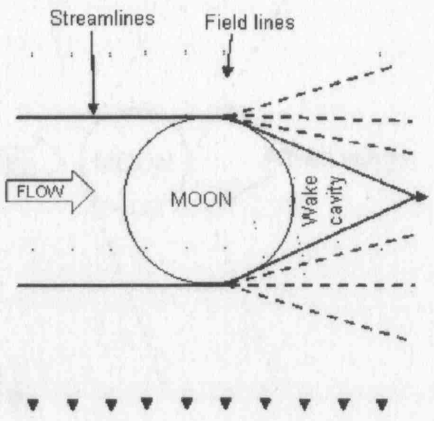

Figure 1.17 Sketch showing the interaction of a non-magnetised, insulating, atmospheric-less moon with the magnetospheric plasma and field flow [after Kivelson and Russell, 1995].

In the presence of a perpendicular magnetic field, as will be the case with moons inside the magnetosphere, particles will refill along the field lines in two preferential directions [Ogilvie et al., 1996]. A sketch of the wake is shown in Figure 1.17. The magnetic field will be slightly perturbed due to the resultant plasma void behind the moon.

1.4.2 Plasma interactions with bodies with atmospheres

Prior to the arrival of Cassini, it was well known that Titan had an atmosphere [Hartle et al., 2006]. However, the Cassini data have also revealed an atmospheric signature in the vicinity of Enceladus [Dougherty et al., 2006]. Therefore, in considering the moon interactions we must also take into account the effect of the atmosphere. One difference between the interaction with bodies with and without atmospheres is the additional mass-loading or plasma generation arising due to sputtering and ionisation of the atmospheric particles. In addition there is ionisation of the atmosphere by sunlight which forms a conducting layer upstream of the moon. The atmospheric neutrals can also get 'picked up' and added to the magnetospheric plasma populations. This is a process whereby a neutral acquires charge, through either particle-impact ionisation or charge-exchange, and is then subject to the magnetospheric electric fields.

Since the magnetospheric field is steady, it will eventually penetrate the body. Absorption of the incident plasma can still occur, but this time the magnetic field drapes around the body. This sort of disturbance takes the form of Alfvén wings which occur when the field disturbance caused by the moon travels up the field lines. This interaction is illustrated in Figure 1.18.

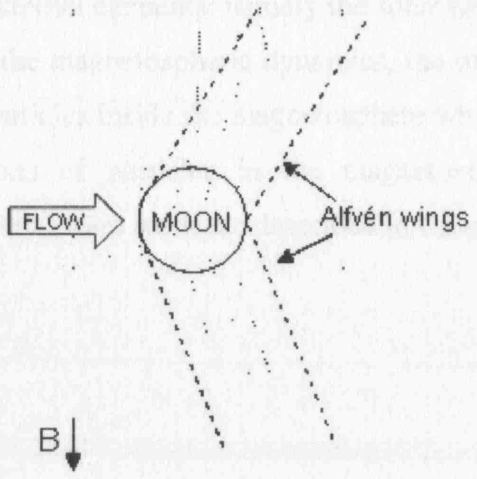

Figure 1.18 Sketch illustrating the concept of Alfvén wings and the effect on the field lines in the vicinity of e.g. Titan.

1.5 This thesis

The work in this thesis uses the data from the Cassini Plasma Spectrometer (CAPS) instrument suite and the magnetometer on board the Cassini spacecraft. Chapter 2 outlines the Cassini-Huygens mission and instrumentation, detailing the methods of operation of CAPS, reviewing the supporting measurements and describing the datasets produced.

The scientific analysis covers two topics of particular interest in the Saturnian magnetospheric system. The first is the dynamics of the magnetopause and Chapter 3 concentrates on the plasma dynamics and characteristics at two separate encounters with the Saturnian magnetopause, providing insight into the behaviour of the magnetopause over two specific intervals. The plasma and magnetic field data is analysed in detail and the processes occurring are interpreted. Chapter 4 is a survey of magnetopause crossings over an 18 month time period including over 200 events. This allows a more general understanding of the behaviour of the magnetopause and its interaction with the solar wind particles and fields, specifically the formation and characterisation of an internal boundary layer.

The second topic addresses the impact of the icy satellites on the inner magnetospheric plasma, specifically, the absorption of high energy electrons throughout the orbit of three of the moons. The depleted electron cavities are replenished by the surrounding plasma and we can derive information on the plasma in those regions by understanding the refilling process.

These are clearly two very different subjects, yet both have significant implications for the dynamics of the magnetosphere. One can provide a diagnostic for the influences of the external elements; namely the solar wind, and the characteristics of a crucial boundary to the magnetospheric dynamics, the other gives an insight into the sources and sinks of particles inside the magnetosphere which ultimately determines the motion and populations of particles in the magnetosphere. The summary, main conclusions and expected future work are described in Chapter 6.

2 Instrumentation and Dataset

2.1 The Cassini-Huygens Mission

The Cassini-Huygens orbiter and Titan lander pair is an international mission involving scientists from both the USA and Europe and were designed to improve upon and extend the previous datasets gathered in the Saturnian system. The orbiter was built by NASA's Jet Propulsion Laboratory, with the Italian Space Agency (ASI) contributing its high-gain antenna and other radio subsystem equipment. Huygens, the lander for Saturn's largest moon, Titan, and the required communications equipment on the orbiter, was built by the European Space Agency. The Cassini orbiter was so named after Giovanni -Domenico Cassini, an Italian-born French scientist, who, because of his ties to France renamed himself Jean-Dominique Cassini. During his time at the Observatiore de Paris, Cassini discovered the Saturnian satellites Iapetus in 1671, Rhea in 1672, and both Tethys and Dione in 1684. He also correctly postulated the nature of the rings as swarms of individual particles and made the first observation of the 4,700 km gap between the A and B rings, which eventually became known as the Cassini Division.

Christiaan Huygens was born in 1629 in Holland. As well as being a competent mathematician he applied himself to the manufacture of telescopes and soon developed improved techniques for lens polishing. In 1655, he pointed one of his new telescopes, of far better quality than that used by Galileo, towards Saturn with the intention of studying its rings. Instead, he made the discovery that secured his name in the history books of planetary exploration, and 350 years later would result in him being the namesake of one of the most significant interplanetary missions of its time, the sighting of Titan, Saturn's largest and most enigmatic moon.

The Cassini-Huygens mission is one of the most eagerly-awaited and exciting missions for space and planetary physicists alike. After the culmination of many years planning and preparation, it proved to be a feat of both modern technological prowess and international collaboration when it was finally launched on October 15, 1997 on a Titan IV rocket. At 6000 kg the Cassini-Huygens spacecraft was too massive to send on a direct trajectory to Saturn. In order to meet the energy demands of the trip, a number of gravity assist manoeuvres were required. First, it completed an orbit around the Sun and the planet Venus. This allowed it to use the planet's angular momentum and thus

gain valuable extra energy. The next two gravity assists took Cassini-Huygens past Earth, on 18 August 1999, and Jupiter at the end of 2000. Shown schematically in Figure 2.1, these additional planetary encounters provided enough momentum to allow Cassini to cover the 9 AU from Earth to Saturn in 7 years.

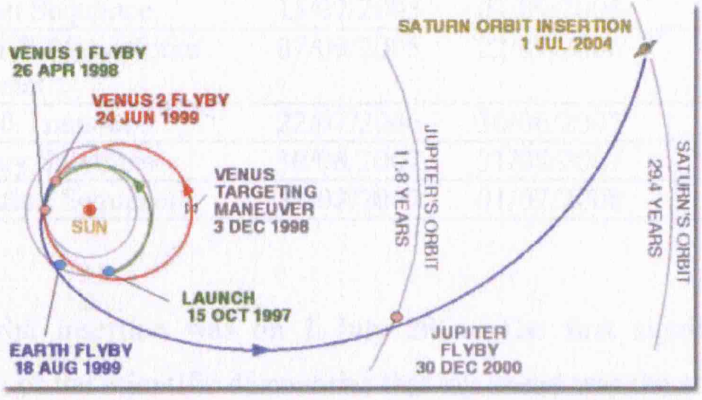

Figure 2.1 The route taken by Cassini-Huygens to reach Saturn. It included four planetary flybys and took 7 years.

The Cassini mission tour was designed with maximum scientific return in mind. It comprises several stages, each of which is targeted to provide a thorough inspection of one or multiple aspects of the Saturnian system. Figure 2.2 shows the orbits planned for the nominal four year tour.

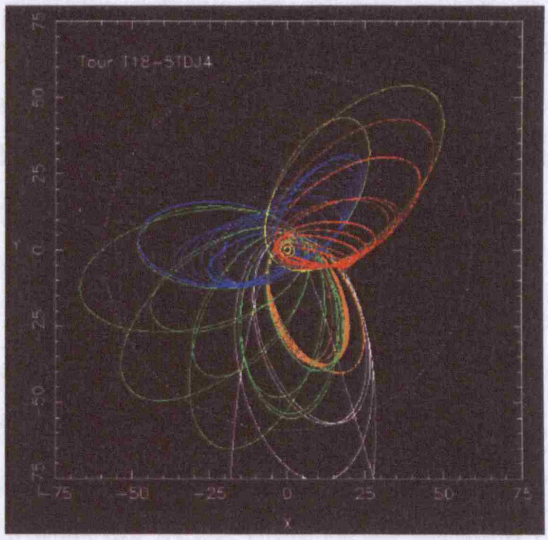

Figure 2.2 The Cassini orbiter's nominal four year tour of Saturn,shown projected onto the x-y plane of the Saturnian ecliptic. Note that some of these orbits are inclined to this plane. Iapetus orbits at ~ 60 R_S from Saturn (dotted outer ring) and Titan at 20R_S (dotted inner ring).

Table 2-1 shows the planned stages drawn schematically in Figure 2.2. The data used in this thesis was collected during the first three of these stages.

Table 2-1 The nominal stages of the Saturn tour and the main mission aims of each orbit

Orbit section (petal)	Date from	Date to	Colour in Figure 2.2
Saturn Orbit Insertion and Probe Release	01/07/2004	15/02/2005	White Petal
Occultation Sequence	15/02/2005	07/09/2005	Orange Petal
Petal Rotation & Magnetotail Petal	07/09/2005	22/07/2006	Green Petal
Titan 180 Transfer	22/07/2006	30/06/2007	Blue Petal
Rotation/Icy Satellites	30/06/2007	31/08/2007	Yellow Petal
High Inclination Sequence	31/08/2007	01/07/2008	Red Petal

Saturn orbit insertion was on 1 July 2004. The first significant event that signalled the start of the scientific discoveries that lay ahead was the scheduled flyby of one of Saturn's outmost moons: Phoebe, at a distance of 215 R_S from Saturn (1 R_S = 60,268 km). The next event of note was the crossing of the bow shock at ~ 49 R_S upstream of Saturn at 09:47 UT on June 27. After passing through the magnetosheath region containing the post-shock, compressed solar wind plasma, Cassini crossed the magnetopause of Saturn. There, Cassini was finally in the region of space under the influence of Saturn's internal field. This occurred on 28 June at 18:43 UT at a distance of 34 R_S from the planetary centre. The inbound orbit took Cassini across the magnetopause at a Magnetic Local Time (MLat) of ~ 08:00 and a magnetic latitude of ~ -15°. For the final stage of orbit insertion, Cassini-Huygens needed to cross through the ring plane of Saturn. This was a risky manoeuvre and required the spacecraft to rotate so that its large, high-gain antenna faced the ram direction. It was hoped that this would bear the brunt of any ring particle impacts during the crossing.

On the 1 July 2004, Saturn orbit was finally achieved via a firing of the thrusters. During this burn, many instruments were switched off to avoid contamination by the thruster products. For a portion of this time Cassini flew very low over the equatorial B and A rings, at a minimum distance from the ring plane of ~ 1.5 R_S, the closest that Cassini will ever get to the rings in the nominal tour. Cassini exited the magnetosphere a few days later. It would be another three months before it returned to the magnetosphere to continue its tour.

At the time of writing, Cassini has been in orbit around Saturn for over 2 years, completing over 20 orbits, and the Huygens probe descent mission was successfully completed.

2.2 The Cassini Orbiter

The Cassini orbiter is the largest and most complex spacecraft ever to travel into interplanetary space. At a distance of ~ 9 AU from Earth, it is the furthest we have ever sent a dedicated planetary orbiter. It is equipped with a host of sophisticated instruments, designed to probe Saturn and its system with precision and detail. The orbiter instruments, hosting 27 experiments in all, are listed in Table 2-2. They fall broadly into three categories:

- optical imaging
- fields, particles and waves
- microwave imaging

In order to truly appreciate and understand processes in the magnetosphere of Saturn, Cassini is equipped with a host of instruments that fall under the category of MAPS; Magnetospheric and Particle Science [Blanc et al., 2002]. These have been designed to complement each other in all particles and fields measurements. Hence, wherever possible, this thesis has attempted to use, or at least consider, results from other instruments and collaborative teams also in the MAPS working group.

Throughout this thesis, the examination of low-energy plasma data from the Cassini Plasma Spectrometer (CAPS) forms the core of most of the analysis. This comprises three individual experiments; the Electron Spectrometer (ELS), the Ion Mass Spectrometer (IMS) and the Ion Beam Spectrometer (IBS). The ELS supplies the key data product, with some consideration of the IMS data. In addition, magnetic field data from the dual-technique Magnetometer (MAG) instrument is often used to enhance or support the analyses. Data from other instruments are used to place the low energy electron data in context, or provide additional results which can help with the scientific interpretation. Primarily these are the high energy electron and ion instrument suite: the Magnetospheric Imaging Instrument (MIMI) and the Radio and Plasma Wave Science (RPWS) experiment. Details of these have also been provided in this chapter.

In addition to the orbiter, the mission included a lander; the Huygens probe, which was designed to be released into the atmosphere of Titan, Saturn's largest moon, with the ultimate aim of landing on the surface. Huygens had a suite of instruments designed to sample the atmosphere and the moon surface upon impact. For those studies concerned with the impact of Titan upon the magnetosphere of Saturn, the instruments on board Huygens can provide a valuable resource. However, this thesis

will not address those issues and therefore does not use the results from the probe instruments.

Table 2-2 List of the instruments on board the Cassini orbiter

Suite	Instrument	Purpose
Optical Remote Sensing		
	Composite Infrared Spectrometer (CIRS)	Measure infrared emission from atmospheres, rings, and surfaces over wavelengths from 7 to 1000 μm to determine their composition and temperatures.
	Imaging Science Subsystems (ISS)	Wide and narrow angle (60 and 6 $\mu rads^{-1}$) cameras to make observations of atmosphere, rings, satellites and surface features.
	Ultraviolet Imaging Spectrograph (UVIS)	Measure ultraviolet light reflected or emitted from atmospheres, rings, and surfaces over wavelengths from 55.8 to 190 nm to determine their compositions, distribution, aerosol content, and temperatures.
	Visual and Infrared Mapping Spectrometer (VIMS)	Measure reflected and emitted radiation from atmospheres, rings, and surfaces over wavelengths from 0.35 to 5.1 μm to determine their compositions, temperatures, and structures.
Microwave Remote Sensing		
	Cassini Radar (RADAR)	Identify if and where water exists on Titan and map Titan surface. Map surfaces of satellites.
	Radio Science Subsystem (RSS)	Search for gravitational waves. Study solar corona and general relativity when Cassini is behind the Sun. Improve Saturnian mass estimates. Study ring structure. Study Saturn and Titan atmospheres and ionospheres.
Fields, Particles, and Waves		
	Cassini Plasma Spectrometer (CAPS)	In situ measurements of the flux of ions as a function of mass per charge, and the flux of ions and electrons as a function of energy per charge and angle of arrival relative to CAPS.
	Cosmic Dust Analyser (CDA)	Observe particulate matter in the Saturnian system, to investigate the physical, chemical, and dynamical properties of these particles, and to study their interactions with the rings, icy satellites, and magnetosphere of Saturn.
	Ion and Neutral Mass Spectrometer (INMS)	Measure positive ion and neutral species composition and structure in the upper atmosphere of Titan and magnetosphere of Saturn, and to measure the positive ion and neutral environments of Saturn's icy satellites and rings.
	Dual Technique Magnetometer (MAG)	Determine the planetary magnetic fields and the dynamic interactions in the planetary environment.
	Magnetospheric Imaging Instrument (MIMI)	Measure the composition, charge state and energy distribution of energetic ions and electrons, detect fast neutral species and conduct remote imaging of the Saturn's magnetosphere.
	Radio & Plasma Wave Science (RPWS)	Measure the electric and magnetic fields and electron density and temperature in the interplanetary medium and planetary magnetospheres.

2.3 The Cassini Plasma Spectrometer (CAPS)

In order to make the required plasma measurements in the distant solar wind and the demanding regime of the Saturnian magnetosphere, the Cassini Plasma

Spectrometer (CAPS) [Young et al., 2004] is made up of three individual instruments; the electron spectrometer and two ion instruments. Each has a particular remit chosen specifically to meet the scientific goals identified after the Pioneer and Voyager missions. Of particular importance was the need to ensure that there was complete coverage of electron and ion velocity distributions over the ranges not covered by Voyager. In particular, the gaps fell between the energy ranges of the Voyager plasma spectrometer instrument (PLS) [Bridge et al., 1977] and the low energy charged particle instrument (LECP) [Krimigis et al., 1977] between 6 to 14 keV for electrons and 6 to 30 keV for ions. Figure 2.3 shows the placement of the instruments on the main body of the spacecraft.

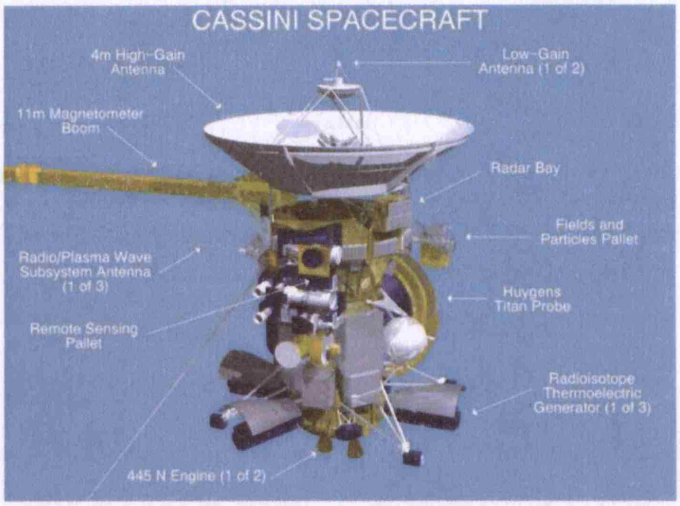

Figure 2.3 An overview of many of the key components of the Cassini spacecraft, including the high-gain antenna at the 'top' and the magnetometer boom. The CAPS instrument is on the field and particles pallet, placed well away from the engines to avoid contamination.

CAPS is placed on the underside of the field and particles pallet on the orbiter to minimise contamination from the main engines and thrusters. This is apparent in Figure 2.4 which shows the position and pointing of CAPS relative to the other instruments on the field and particle pallet. The field of view of the three elements of CAPS are sketched for clarity. The azimuthal coverage (in the spacecraft X-Y plane) and the elevation (Z) are indicated. As Cassini is a non-spinning spacecraft, the only way to achieve a practical azimuthal field of view was to place the instruments on a rotating platform. The platform uses a motorised actuator, moving at ~ 1° per second, to sweep the platform through ±104° about the spacecraft's Z-axis (through the longest axis of the spacecraft, negative towards the high-gain antenna shown in Figure 2.3) when operating at full range.

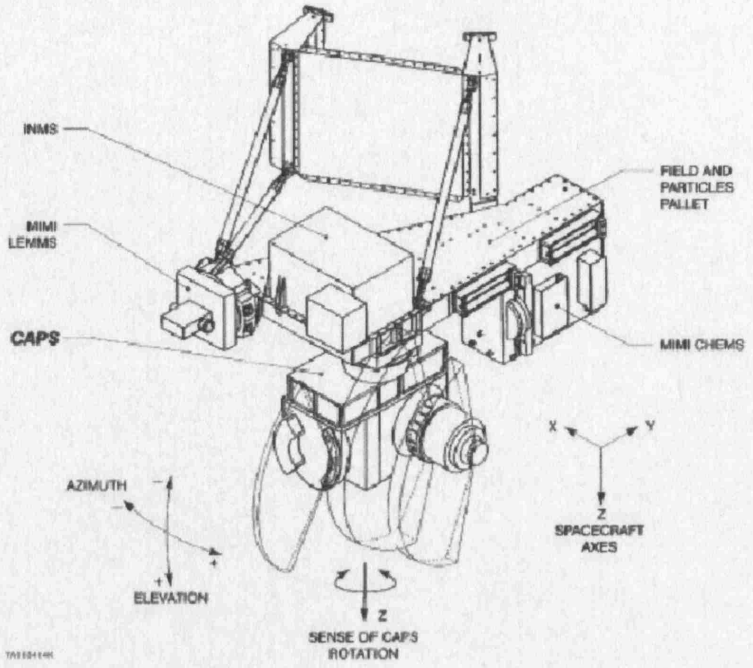

Figure 2.4 Location and orientation of CAPS on the fields and particle pallet. The three field of view fans of ELS, IMS and IBS are traced on and shown pointing towards –Y). Instrument azimuth is shown as lying in the spacecraft X-Y plane and the elevation is parallel to the spacecraft Z axis.

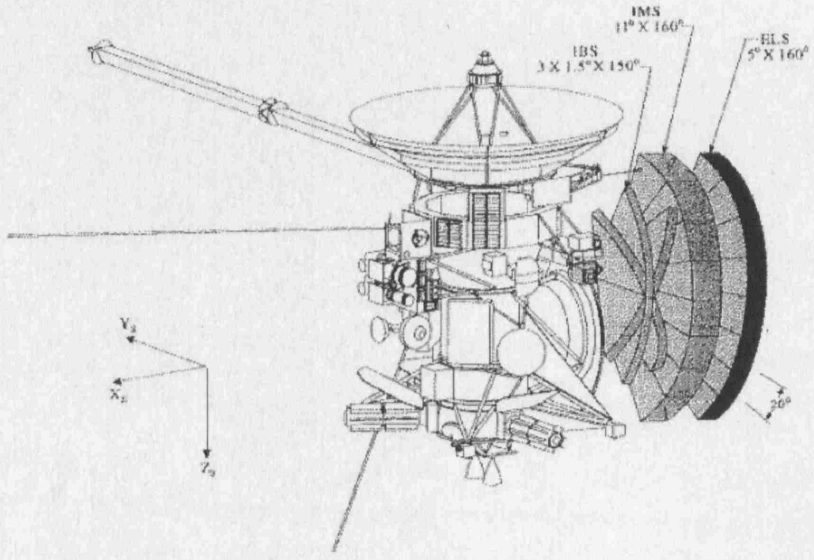

Figure 2.5 Sketch of the Cassini spacecraft with the field of view of each of the CAPS instruments is drawn on. The spacecraft frame is marked showing that the high gain antenna points along the spacecraft –Z axis and the CAPS instruments point outwards along –Y. The actuator sweeps the instrument field of view between –X and +X.

The actuator angle is at a position of 0° when it is pointing along the spacecraft negative Y-axis and this is also shown in Figure 2.5 which shows the CAPS instrument fans (exaggerated for clarity) pointing along the spacecraft –Y axis. During data downlinks, when the spacecraft performs a roll manoeuvre about its Z axis, up to 360° coverage of the sky can be obtained. Despite the actuator, there are still regions of the

instrument field of view that are obscured by other parts of the main spacecraft body. This has an effect on the measurements, as described later in this chapter.

2.3.1 The Electron Spectrometer (ELS)

2.3.1.1 Introduction

The ELS [Linder et al., 1998; Coates et al., 1992] is a hemispherical 'top-hat' electrostatic analyser (ESA) and its design is based on an improved version of the High Energy Electron Analyser (HEEA) sensor of the Cluster Plasma Electron and Current Experiment (PEACE) [Johnstone et al., 1997]. Figure 2.6 shows a cross-section, in the spacecraft X-Y plane, of the entire CAPS instrument suite and the relative placement of the three experiments, ELS, IMS and IBS.

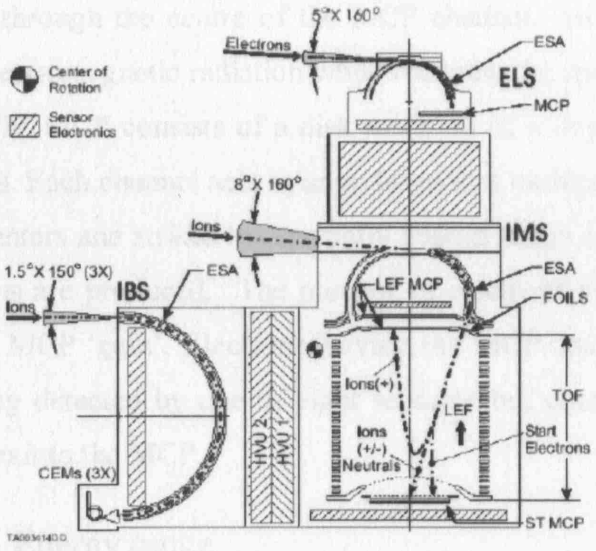

Figure 2.6 Cross-section of the CAPS instrument in the spacecraft X-Y plane showing all three of the detectors and their relative positions. The key sensor components are indicated, such as the hemispherical plates used for energy selection on the ELS. The path that incoming particles take is indicated and the detection mechanism, i.e. the Multi-Channel Plate (MCP) is labelled. Cross-hatched areas indicate the sensor electronics subsystems. The entrance fan for each instrument is indicated and shown to be bore-sighted with each other along the spacecraft –Y axis.

The key sensor subsystems are shown for each, including the ESA and detector. The incoming particle trajectories and acceptance cones for each instrument are also marked in the figure and it is clear that the three are bore-sighted. Cross-hatched areas indicate the sensor electronics subsystems.

2.3.1.2 Principles of operation

Incident electrons enter through a baffled opening in the top of the ELS instrument. The baffle, together with a special black coating which is applied to most of the internal surfaces of the instrument, is designed to reduce scattering of particles and sunlight and to absorb and scatter UV photons. The electrons then pass between concentric hemispherical electrostatic plates. The outer plate is grounded while the inner plate has a positive variable voltage. At each voltage level, the resultant potential difference between the plates will allow only electrons of certain energies to pass between the plates without impacting these surfaces. When the selected electrons exit the plates, they pass through a grid placed at the focus of the ELS optics which confines the field across the plates and impact one of two 90-degree curved microchannel plates (MCPs) arranged in a 'chevron pair' stack. The back-to-back arrangement of two 'slanted' MCPs maximises the chance of electrons striking the inside of the tube and not just passing directly through the centre of the MCP channel. An MCP multiplies the incident particle or electromagnetic radiation while retaining the spatial resolution of the incident radiation. The MCP consists of a disk made up of a large number of closely packed glass channels. Each channel acts as an independent multiplier so that each time an incident electron enters and strikes the specially coated inside of the tube, a cascade of secondary electrons are produced. The number of electrons produced per incident electron is called the MCP 'gain'. Electrons leaving the MCP channel cross a 500 μm wide gap before being detected by one of eight separate but contiguous electrodes or anodes placed at the exit to the MCP.

2.3.1.3 Energy range

The ELS measures electrons with energies between 0.6 eV to 28,250 eV with an energy passband of $\Delta E/E=16.7$ %. This is the energy resolution of the instrument. Due to the design of the analyser, the lower energy bands are more closely spaced, and thus the instrument has better energy resolution at these lower energies.

2.3.1.4 Voltage sweep

At each step during the voltage sweep, the selected potential difference is maintained for a set accumulation time (31.25 ms) while electrons enter the analyser.

This accumulation time includes 25% of 'dead time', during which no electrons are counted; it is simply to allow the voltage to settle before it is stepped down to the next level. Thus the actual measurement time is 23.44 ms. The spacing of the steps is designed to match the intrinsic analyser resolution over most of the energy range to provide continuous energy coverage.

2.3.1.5 MCP Gain

Particle amplification in the MCP is defined by the inner coating, the chevron arrangement and applied voltage. It is designed such that ~ 2 x 10^6 electrons are produced for each incident electron [Johnstone et al., 1997; Linder et al, 1998]. Each MCP has a sensitive interior surface coating, prone to degradation and this limits the lifetime of an MCP and hence the instrument. During the mission, the MCP operating voltage is increased periodically to counteract the degradation of the plates. In order to increase the instrument lifetime and the gain for a particular voltage, a 66μm gold-coated copper spacer is placed between the two chevron MCPs [Linder et al, 1998]. This acts to reduce the voltage required for a particular gain and therefore, if required, higher gains can be attained later on in the mission. Electrons leaving the MCP channel cross a 500 μm wide gap before being detected by the anodes. These anodes are biased at ~ +150V with respect to the rear of the MCP, and they register one count for a threshold of ~ 400,000 electrons. The maximum count rate that can be measured without saturation is ~ 10^6 incident electrons per anode per second.

2.3.1.6 Electronics

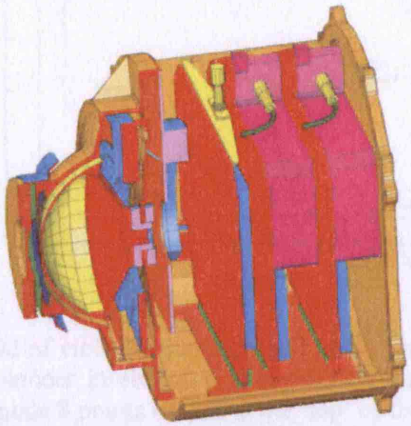

Figure 2.7 Cut away diagram of the ELS instrument demonstrating the overall structure of the instrument. The top-hat ESA is on the left with the instrument electrons on the right.

The response of the anodes determines the direction of the incident electrons. The output pulses from the anodes are then collected and read out by the instrument electronics. Ultimately, the data is passed to the data processing unit (DPU) for processing and transmission. A schematic of the instrument is provided in Figure 2.7, showing the analyser head and detectors relative to the back end electronics. Note that no higher-level data processing is carried out on-board, the only processing of the data is for compression purposes and may involve the summation across any of the dimensions measured (i.e. energy, angle or time). The resulting data products to result from this compression are discussed below.

2.3.1.7 Field of view

The instrument field of view is sketched in Figure 2.8. The coverage is produced using eight anodes, each covering 20° x 5° of sky, providing a total of 160° in the polar direction. With the actuator functioning at maximum sweep the azimuthal field of view is 208°. In total this provides coverage of 56% of the sky, although this is not ideal for plasma measurements since the instrument cannot sample all directions simultaneously. This is particularly disadvantageous when trying to determine whether the ion flow is isotropic, or trying to continuously sample a full range of pitch angles of the electrons, for example. In addition, the main body of the spacecraft and other instruments cause obscurations which reduce the field of view to a useable coverage of ~ 45%.

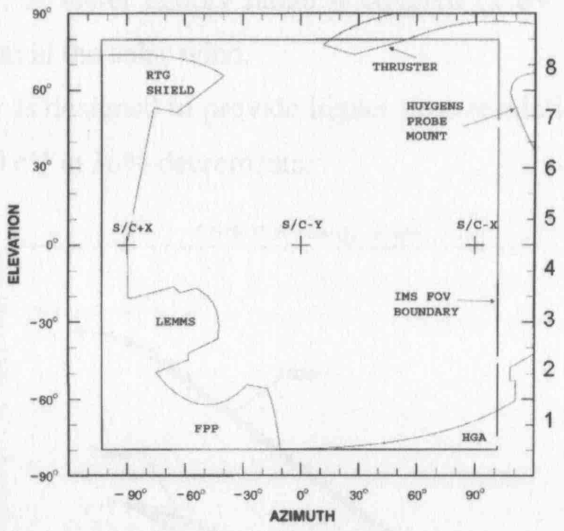

Figure 2.8 The approximate field of view for the IMS (and ELS) instruments looking outward from the spacecraft. The spacing of the anodes in elevation is marked on the right hand side of the plot going upward from 1 to 8. Note that anode 8 points toward at the 'top' of the spacecraft (- Z), so the instrument is effectively placed upside down on Cassini. The range of the azimuthal coverage, provided by the actuating platform, is indicated on the bottom of the figure. The protrusion of elements of the spacecraft such as the FPP (Fields and Particles Palette), the HGA (High Gain Antenna) and the RTG (Radio Thermo Isotope Generator) shield is outlined.

2.3.1.8 Sampling time

The energy is swept through 0.6 eV up to 28,250 keV in 2 seconds, each being held for a fixed accumulation time of 31.25 ms (23.44 ms not including the dead-time). The energy range is split into 63 bins (see Appendix A) with the 64th level being the voltage flyback step, needed to prepare for the next downward voltage sweep. Thus, as the instrument cycles through each of the 64 steps, each one of 31.25 ms, an energy spectrum is built up in 2 s, before the voltage resets and the process begins again.

2.3.1.9 Modes of operation and telemetry

There are alternate modes of operation for different scientific requirements; these use different voltage tables (Figure 2.9), which affect the resultant energy spectrum:

Sweep table 1: In normal operation, a 64 point energy spectrum between 0.6 and 28,250 eV is generated in 2 s. Alternatively, a subset of 32 of the 64 energy bins can be selected, starting with any one of the top 32 bins, to be sampled twice in 2 s.

Sweep table 2: A lower energy range is covered (1 eV to 1,000 eV) which is suited to measurements in the solar wind.

Sweep table 3: Is designed to provide higher time resolution and covers energies from 1.8 eV to 22,000 eV in 36% decrements.

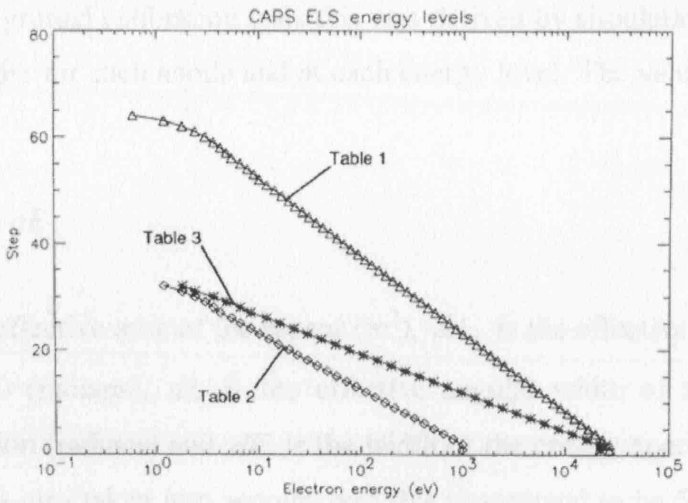

Figure 2.9 Energy versus sweep steps for the three different voltage tables [Linder et al., 1998].

There is also a fixed energy mode for ground calibration and, if required, fast time resolution for a single energy. All these modes have been tested on the ground but only table 1 has been used in flight, and for this reason the hardware is optimised for that configuration. The final data product consists of an array containing (a maximum of) 63 energies for each of 8 anodes, for each azimuthal angle provided by the actuator motion. The data are stored in an 'A-cycle', defined as 16 energy sweeps. Thus for a standard sweep of 2 s, an A-cycle is 32 s long. The instruments on board Cassini share a limited telemetry bandwidth due to constraints on the downlink via the high gain antenna. Therefore, the ELS cannot operate in its highest resolution mode all the time. Instead it has a number of different modes which control the way the data is stored (i.e. via summing or averaging) to reduce the amount of data while preserving scientific information.

For highest resolution data, adopted for the scientifically key periods such as moon flybys, the telemetry rate is 16kbps (kilobits per second); this allows telemetry of the full resolution, non-averaged data and is known as data format 1. Appendix A summarises the telemetry modes and the resultant time resolution of the summed energy bins. In addition to the electron energy spectra, the ELS data file contains the actuator position, data type, the spacecraft position, attitude, and velocity and the MCP levels as well as a range of housekeeping data used for monitoring the instrument performance.

2.3.1.10 Geometric factor

In order to accurately transform the number of raw electron counts entering the instrument to a meaningful, calibrated unit, the geometric factor (G) of the instrument is required. Prior to ground calibration tests this was derived by simulation, giving a range of geometric factors for each anode and at each energy level. The value is calculated as in Equation 2.1:

$$G = dA \cdot dA_Z \cdot dL \cdot dE$$

Equation 2.1

where dA is the effective area of the sensor (m^2), dA_Z is the effective angular width of the sensor in 1-D (radians), dL is the effective angular width of the sensor in the orthogonal direction (radians) and dE is the width of the energy aperture, ($\Delta E/E$). The MCP efficiency is also taken into account and this is assumed to be 50% for the ideal,

simulated value [Linder et al., 1998]. More accurate, energy dependent values are determined from ground calibration and in-flight cross calibration.

2.3.2 Factors affecting electron measurements

2.3.2.1 Spacecraft potential

When immersed in a plasma, a spacecraft is subject to a constant particle flux. In addition, any sunlit surface will release electrons. Both mechanisms will result in a spacecraft becoming charged relative to the surrounding population. The sign and magnitude of this charge depends upon the ambient plasma and sunlight environment. In equilibrium, the net flow of charge to and from the spacecraft must be zero. This can be expressed by the current relationship:

$$I_i + I_e + I_{pe} + I_{se} = 0$$

Equation 2.2

where I_i and I_e are the ambient ion and electron currents respectively, I_{pe} is the photoelectron current and I_{se} is the secondary electron current. Generally, the combination of the release of photoelectrons, plus the large thermal velocity of the electrons compared with that of the ions, will result in a positive charge on the spacecraft. However, the balance of these generating mechanisms is highly variable and is affected by the plasma environment and the solar illumination, both of which change significantly and often rapidly during Cassini's passage through the different plasma regimes encountered. For example, in very dense plasma regions or where there is a reduction in the photoelectrons produced, (such as in eclipse), electrons are attracted to the positive spacecraft at a greater rate than photoelectrons are produced. A negative charge is thus built up on the spacecraft surface which will decelerate and, in some cases, repel incoming electrons.

The photoelectrons are produced by incident UV solar radiation and occur when a high energy eV photon collides with an atom in the surface of the spacecraft and frees an electron. The energy of the newly formed electrons are related to the work function of the surface from which they are being generated and the frequency of the incident light. The material on the surface of Cassini is multi-layer insulation, and the incident light is UV, therefore, electrons of energies ~ 10s eV are produced. The same

mechanisms act on the instrument internal surfaces, but these can be mitigated via specialist coatings and using baffles on the entrance aperture. Secondary electrons may also be produced when a higher energy electron in the surrounding plasma strikes the surface of the spacecraft and releases a low energy secondary electron.

For the usual case of a positive potential (the spacecraft is positively charged) the newly created photo- and secondary electrons are attracted to, and surround, the spacecraft and form a negatively charged sheath. The resulting charge separation around the spacecraft creates a potential difference between the spacecraft and the surrounding plasma and will thus modify the energy of any particles approaching the spacecraft. These effects are of particular interest due to the low energy sensitivity of the ELS, and as a result all measurements are susceptible to contamination by these spurious electrons generated on the spacecraft surface and within the instrument itself.

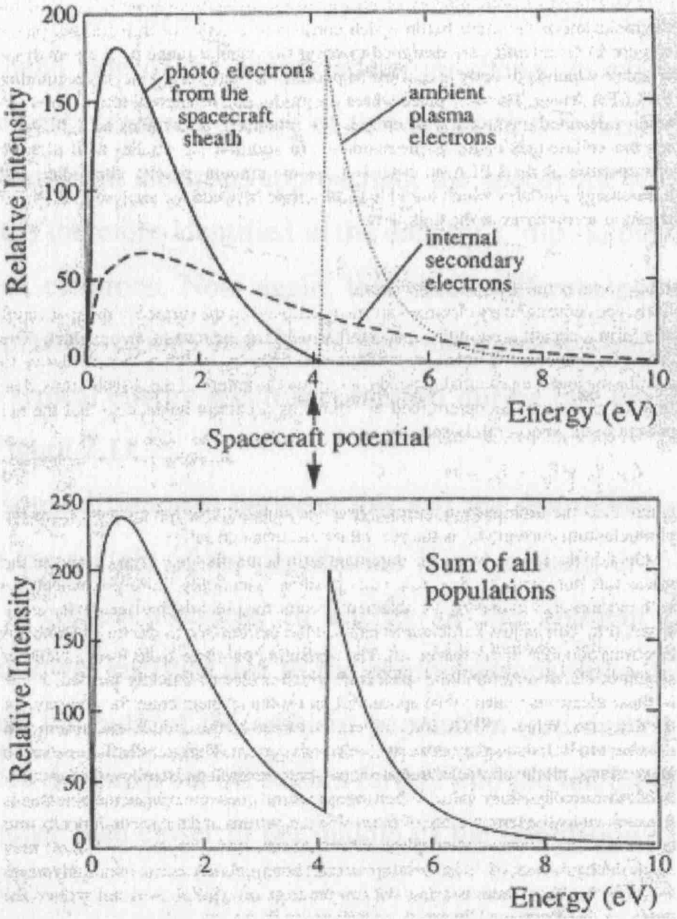

Figure 2.10 Theoretical example of the low energy electron populations (top) and how they effect the total distribution seen at the analyser (bottom). [Johnstone et al., 1997]

Determining the potential difference is therefore imperative to the accuracy of the ELS measurements, since it affects the energy of any incoming particles to the analyser. If a spacecraft generated electron has an energy greater than the potential difference of the spacecraft, then it may escape the spacecraft sheath and avoid entering

the ELS. Thus, we do not expect to observe photoelectrons at energies higher than the spacecraft potential.

Conversely, there are no ambient electrons with energy below the spacecraft potential, since they have gained energy equal to the spacecraft potential. This fact can aid in identifying the value of the potential, since at this value, the number of spacecraft-sheath electrons is zero. This is summarised schematically in Figure 2.10 [Johnstone et al., 1997] which contains two example energy spectrograms showing the different components of the electron population measured (top) and the resultant spectrum observed (bottom). The secondary and photoelectron populations peak at the lower end of the energy range and are, in effect, noise that must be removed from the raw measurements. This must be carried out before moments of the ambient plasma can be calculated, since they will cause significant error in the results due to their high density.

The right hand side of the energy spectrum shows an example 'real' electron population. The lowest measured energy of this population is limited by the spacecraft potential, since all ambient electrons approaching the spacecraft will be accelerated up to that potential. It is therefore identified in the data by a 'dip' in the counts between the photo- and ambient electrons. Note again, that these different populations are highly variable between plasma regions and this is just one possible configuration [Johnstone et al., 1997]. A typical energy spectrum obtained during one energy sweep from the ELS is shown in Figure 2.11.

There are some differences between this and the theoretical spectrum in Figure 2.10. The 'dip' in the middle of the distribution is not a sharp drop-off in counts, but exhibits a more a gradual decrease in energy of the ambient population, before increasing again at lower energies due to the photoelectrons (blue dashed line). This is most likely because the bulk of the ambient population (red dashed line) is of higher energy and therefore the sharp cut off occurs further into the tail on the left hand side of the distribution (rather than closer to the middle of the population as in the right hand side of Figure 2.10).

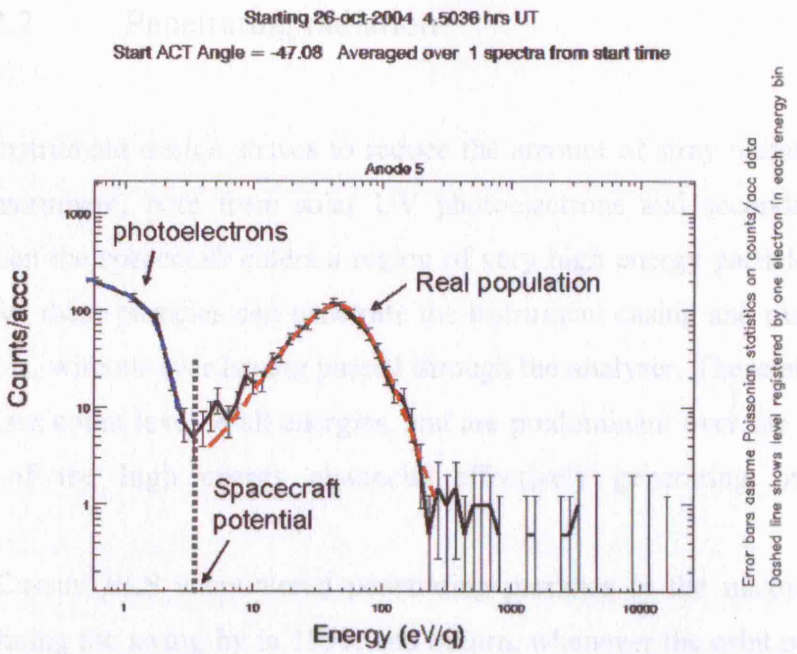

Figure 2.11 An example electron spectra from the magnetosheath, taken on 26 October 2004 at 04.30 UT. The high counts of photoelectrons can be seen on the left, over plotted with the blue dashed line, with the ambient, 'real' population on the right, over plotted with the red dashed line. The spacecraft potential has been marked on as the 'dip' between the two populations as explained in the text.

In Figure 2.11, there is a clear dip at ~ 3.5 eV, however, this is an ideal case taken from the magnetosheath. The separation of the populations is rarely this pronounced, which makes it difficult to extract the 'useful' population using automated algorithms. This is discussed further in Appendix B. Note that the method described above is assuming the usual case of a positive spacecraft potential. When the spacecraft enters a region where the ambient plasma is very dense and energetic, then the spacecraft potential may be forced negative and this is much more difficult to determine, since the spacecraft potential is now below the limit of the instrument's range. Thus, there will be a portion of the low energy, ambient population that the instrument will no longer be able to detect. In cases like this, such as the inner magnetosphere, the Langmuir probe instrument, part of the Radio and Plasma Wave Science (RPWS) instrument can determine the potential. In addition to the above factors, other complications can influence the low energy electron measurements. Escaping secondary electrons with energy greater than the spacecraft potential can encounter other parts of the spacecraft surface. In this case they can rebound back into the instrument or generate another secondary electron. The spacecraft-sheath electric field can also alter the trajectory of incoming particles, resulting in erroneous directionality information.

2.3.2.2 Penetrating radiation

The instrument design strives to reduce the amount of stray radiation produced inside the instrument, both from solar UV photoelectrons and secondary electrons. However, when the spacecraft enters a region of very high energy particles (~MeV), it is possible that these particles can penetrate the instrument casing and make it through to the detectors, without ever having passed through the analyser. These electrons show up as a constant count level at all energies, and are predominant over the normally low background of the high energy channels, effectively generating 'noise' in the instrument.

The Cassini ELS encountered penetrating particles in the magnetospheres of both Earth, during the swing-by in 1999, and Saturn, whenever the orbit periapsis takes the spacecraft inside the radiation belts. In addition, MeV particles were detected throughout the January portion of the Jupiter flyby in 2001, when energetic particles were believed to be leaking from the Jovian magnetosphere [Krupp et al., 2004]. Rymer et al. [2001], estimated the minimum energy of these particles by considering the stopping power of the instrument shielding, arriving at a figure of ~ 0.8 MeV. This is discussed further in Chapter 5. As usually there is a need to observe the uncontaminated ambient low energy electrons, these particles are often removed from the raw data.

The magnetospheric imaging instrument on Cassini (MIMI) was designed to measure particles of these higher energies and above, which contaminate the ELS measurements. The electron instrument on MIMI; LEMMS (Low Energy Magnetospheric Measurement System) can not only detect these particles, but they also pass through the instrument analyser where pitch angles and differential energy flux can be derived. In certain, cases cross-calibration between the two instruments can identify the maximum energy of particles penetrating into the ELS.

2.3.2.3 Obscuration of the field of view

The actuator motion aims to increase the possible field of view of the CAPS instruments. However, at the extremities of the sweep (close to ±104°) the instrument fan points closely along the surface of the spacecraft. This results in obstructions of the field of view due to the spacecraft itself. The various instruments and, prior to its release, the Huygens probe, block the analyser's view of the sky. In addition, these obstacles themselves are a source of secondary electrons, which can enter the analyser

and contaminate the measurements. Figure 2.8 shows how the field of view of the IMS and the ELS is obscured by different parts of the spacecraft. This effect is not specifically corrected for during the analysis, but care must be taken when analysing data from anodes 1 and 8 and when the actuator angle is close to its limits and has a field of view tangential to the spacecraft surface.

2.3.3 The Ion Beam Spectrometer (IBS)

The ion beam spectrometer (IBS) is designed to measure beams of ions in the solar wind and magnetosphere. It is an ESA and again consists of two hemispherical plates, with a larger radius than the ELS, between which an electric field is applied. This guides ions of the required energies to the detectors with an energy range of 0.95 eV to 49,800 eV.

High angular resolution of 3D velocity space measurements is obtained using a crossed-fan technique [Bame et al. 1978]. The middle fan is placed so that its polar dimension is parallel to the azimuthal (Z) axis of the CAPS actuator (see Figure 2.3 to Figure 2.5) and then two identical fans are tilted 30° relative to the central fan. They each utilise a single, non-imaging channel electron multiplier (CEM) detector which are placed at the focus of the analyser and provide an instantaneous 1-D view of the ion distribution.

The CEM's are analogous to the MCP's in the ELS, as they act to multiply each incoming particle for eventual detection at the anodes. A 3D distribution is thus built up from stepping through the energy levels and using the actuator motion in each detector. These data are then combined to provide the high angular resolution. The resolution degrades at the extreme ends of the fan due to the broadening of the azimuthal acceptance angle with increasing polar angle. The data product consists of 255 energies for each of the three detectors for 16 azimuthal bins.

2.3.4 The Ion Mass Spectrometer (IMS)

The ion mass spectrometer (IMS) is used to gather compositional information about the major ion species in the magnetosphere, with energies up to 50 keV. The instrument combines both a toroidal ESA and a carbon-foil based time-of-flight (TOF)

analyser utilising a linear electric field (LEF) timing region as shown in Figure 2.6. The toroidal geometry has two radii of curvature that allow independent control of the ion focussing. Incoming ions are formed into a beam by the entrance collimator before entering the curved electrode plates in the ESA. Here they encounter a variable electric field which deflects the ions into the toroid.

Like the ELS and IMS there is a range of particles accepted based on their energy, charge and incoming direction, depending on the electric field across the plates. The successful candidates leave the plates and are then accelerated by a voltage through one of eight ultra-thin carbon foils placed around the entrance to the TOF analyser. For the simplest case, an ion that does not break up upon impacting the foil, a single spectra peak is produced from the TOF measurements; this gives the parent ion's specific mass to charge ratio. It is a more complicated, multi-step process to identify the parent molecular species since patterns of identifiable peaks plus their relative abundances are needed.

Mass resolution is determined by the time resolution of the LEF encountered by the products once they leave the foil. For ions with E/Q < ~ 15.5 kV they are sufficiently retarded and their trajectories curve so they strike the LEF detector at the top of the instrument (Figure 2.6). For ions with E/Q > ~ 15.5 kV, their path is retarded by the LEF, however, they have enough velocity to carry on to strike the 'straight-through' (ST) detector (at the base of the instrument). The detection limit of the IMS is ~ 10^3 m^{-3} [Young et al., 2005].

The compositional identification of species is a complex and intricate task as each species will exhibit different behaviour upon hitting the foils, although most positive ions leave the foil as a neutral (i.e. having collected an electron). If an ion leaves the foil it will eject a secondary electron, this will travel to the ST detector where it starts the TOF timer. In the case of a single atomic species, a daughter product will stop the timer upon striking either the LEF or ST detectors. Molecular species are broken up during passage through the foils and the fragments can be measured at either or both of the detectors. The time of flight plus other relevant information about the fragment detection are then used to identify the incoming molecule by use of a look-up table which stores a targeted list of species and their typical parameters. In normal operation the data product consists of 16 TOF bins for each of the 8 elevation sectors for each of the two detectors, LEF and ST. The data can also give ion velocities when the instrument pointing is favourable. The data product from the IMS, the ion counts are called IMS singles data (SNG).

2.4 The Fluxgate Magnetometer (FGM)

The fluxgate magnetometer [Dougherty et al., 2004] provides the magnetic field measurements essential to understanding the magnetic environment surrounding Saturn. The magnetometer on Cassini is a dual technique instrument and consists of a fluxgate magnetometer (FGM) and a vector helium magnetometer which can operate in both a vector (VHM) and a scalar (SHM) mode. The instrument design has been driven by the need for a large dynamic range and high sensitivity needed to determine the interior field of the planet. In addition, having two sensors provides redundancy and a means to cross-calibrate results. The V/SHM is placed at the end of an 11-metre boom attached to the side of the orbiter and the FGM is halfway along. This minimises the disruption to the measurements by the spacecraft itself. Each of the magnetometers can measure the three perpendicular magnetic field components. Furthermore when the SHM mode is used it can very accurately measure the magnitude of the magnetic field. The wide dynamic range is required to measure the very large field strength, to tens of thousands of nanotesla (nT), encountered during the Earth swing-by in 1999 through to the very low field magnitude in the solar wind (tenths of a nT). The data is collected at a resolution of 32 vectors per second and this thesis uses 1 s averaged data in a range of coordinate systems. These data are provided by Imperial College London.

2.5 Magnetospheric Imaging Instrument (MIMI)

The magnetospheric imaging instrument (MIMI) suite is designed to be the energetic counterpart to CAPS [Krimigis et al., 2004]. It measures energetic electrons, ions and neutrals according to charge, energy and composition and operates remotely to image neutrals in the magnetosphere. It consists of three experiments: the low-energy magnetospheric measurement system (LEMMS), the charge-energy-mass spectrometer (CHEMS) and the ion and neutral camera (INCA). LEMMS measures the 3d distribution of high-energy ions and electrons with an energy range that overlaps the higher end of the CAPS energy range (i.e. 20 keV to ~130 MeV), making it possible to perform cross-calibration between these two instruments. The LEMMS is located on a rotating platform akin to the CAPS actuating platform and rotates the instrument about the –y axis of the spacecraft in order to increase the instrument field of view. It is a double-ended telescope (a low and a high energy end) which is bore-sighted orthogonal

to the –y axis of the spacecraft and thus scans across the x-z plane in spacecraft coordinates. The low energy end is designed to measure ions ($E \geq 30$ keV) and electrons (15 keV – 1 MeV) and the high energy is sensitive to ions (1.5–160 MeV/nucleon) and electrons (0.1–5 MeV).

CHEMS measures the 3d distributions of atomic and molecular ions over an energy per charge range of 3 – 220 keV/q. It measures ion species with masses from H to Fe. The INCA detector analyses both the composition and direction of incidence of incoming energetic neutral atoms within energies of < 7 keV to 3 MeV/nucleon. It is also uniquely able to image the global distribution of the energetic neutral emission of hot plasmas in the Saturnian magnetosphere, measuring the composition and energy spectra of those energetic neutrals for each image pixel.

3 Low Energy Plasma Investigations of Saturn's Magnetopause

3.1 The aim of the chapter

The aim of this chapter, is to provide a description of the nature of Saturn's magnetopause and to infer the importance of the interaction of the particle and fields of the solar wind with those of the outer magnetospheric boundary. Does the input from the solar wind drive the magnetospheric dynamics, as at Earth [Dungey, 1961], or is the solar wind influence minimal in the face of the internal rotational forces, as at Jupiter [Hill et al., 1983]? The results of this work contribute to the understanding of the relative importance of internally- versus externally-driven processes on the magnetospheric dynamics of this large, rapidly-rotating planet. Another important result of this work is the comparison between observed processes occurring at the magnetopause with the predicted activity. Observations of auroral activity at Saturn have been used to infer magnetospheric processes occurring in the regions mapping to the auroral oval [Cowley et al., 2005]. Considerations of the plasma and magnetic field behaviour at the dayside magnetopause allow previous assumptions about the presence and conditions under which reconnection occurs at Saturn to be tested. These are based on studies of upstream solar wind [Jackman et al., 2004] and the auroral signatures [Badman et al., 2005; Cowley et al., 2005]

This chapter first outlines the method we apply in looking for evidence of reconnection at Saturn's magnetopause, before detailing two examples of magnetopause crossing events observed during Cassini's first 18 months in orbit about Saturn. The inferred processes occurring at each boundary crossing are described, based on electron, ion and magnetic field data. Observations and characteristics of any boundary layers are outlined with the aim of understanding the mechanism behind their generation. A lack of observations of such interactions will also allow some interesting conclusions to be drawn.

3.2 Looking for evidence of reconnection at Saturn's magnetopause in plasma and magnetic field data

Here we define the criteria used in this study to distinguish between the different plasma and magnetic field regions encountered during the chosen magnetopause traversal events. Firstly, we outline the typical characteristics of the different plasma regimes, starting with magnetospheric plasma. Studies suggest that at different times and latitudes the plasma inside the magnetopause can have very different characteristics [Wolfe et al., 1980; Sittler et al., 1983; Young et al., 2005]. However, most of the crossings used in this study occur on the dawn flank magnetopause at low latitudes. Thus, based on our observations to date, the spacecraft encounters a population which is rare and hot compared with the magnetosheath plasma. The magnetic field orientation points predominately southward [Ness et al., 1981; Dougherty et al., 2005].

Another class of plasma encountered is magnetosheath plasma. From our observations of the electrons in this region, we expect the plasma here to have typical densities of the order ~ 10^5 m^{-3} and temperatures of ~ 70 eV. In addition, we find the electron distribution in the post-shock region is flat-topped [e.g. Feldman et al., 1982], in the energy range ~ 10 – 70 eV when plotted in phase space density (PSD). This particular magnetosheath distribution profile arises due to processes at the bow shock as mentioned in Chapter 1.

The final, most ambiguous, class of plasma is that found in boundary layers. As discussed in Chapter 1, boundary layer plasma can consist of a mix of populations from both the magnetosphere and magnetosheath and care must therefore be taken to avoid misidentifying boundary layer as one or other of these regions. Together with previous magnetosheath and magnetopause studies [e.g. Haerendel et al., 1978; Scudder et al. 1973] we use this understanding to outline a set of 'rules' for distinguishing the different plasma regimes. Note that not all the following pieces of evidence are needed to categorise (or eliminate) the plasma region being sampled. However, together with a clear understanding of the data, these can aid in positive identification:

1. Plasma inside the magnetopause with a density greater than 25% of the magnetosheath density is boundary layer;
2. Magnetosheath plasma has a clear 'flat-topped' distribution in phase space density, allowing it to be distinguished from plasma that is a mix of magnetosheath and magnetospheric plasma;

3. If the magnetosphere is magnetically open there will be a finite B_N component at the magnetopause;
4. The magnitude of the magnetic field component across the magnetopause (B_N) relative to the (largest) total field strength |B| either side of the MPCL should have a ratio of $\geq$ 0.4 if it is a rotational discontinuity (RD) [Neugebauer et al., 1984];
5. The change in the magnetic field magnitude ([|B|], where '[]' denotes the difference in the values either side of the discontinuity) across the magnetopause relative to the total field strength |B| either side of the magnetopause current layer should have a ratio of < 0.2 if it is a RD [Neugebauer et al., 1984];
6. If the boundary layer plasma has passed through a reconnection site the acceleration of plasma in the boundary layer will be expected to be of the order of twice the Alfvén velocity [e.g. Cowley and Owen, 1989];
7. The Walén relation [Sibeck et al., 1999] is satisfied if boundary layer is formed on open field lines by reconnection;
8. The pitch angles of any heated electrons will indicate the direction of origin of the plasma and indicate if it has come from a reconnection site. In addition, the location of the reconnection site relative to the spacecraft can be inferred.

Note that for points 3 and 4 the success of these criteria depends on the confidence in the derived or assumed magnetopause normal direction. As discussed in Chapter 1, the use of the de Hoffmann-Teller frame and the Walén relation can also provide a quantitative method of interpreting the data at the magnetopause.

3.3 Data Overview

The two crossings investigated here took place during Cassini's nominal tour of Saturn on 17 April 2005 and 21 September 2005. The encounters both occurred close to Saturn's equatorial plane at local times of 06:00 and 09:00 respectively. Electron and magnetic field data are used throughout the analysis with ion data being used where available but, due to the restricted pointing, the instrument was not always able to view the relevant ion populations. The identification of the magnetopause was based on the

changes from typical magnetospheric to magnetosheath conditions in both the low energy electrons and ions (where available) and the magnetic field.

3.4 17 April 2005

This magnetopause crossing event occurred on 17 April 2005 as Cassini was leaving the magnetosphere at 05:51 LT at a distance of 26 R_S and a latitude of ~ -3°. Kronocentric Solar Magnetic (KSM) coordinates are used where X points from Saturn to the Sun, Y is perpendicular to the rotation axis towards dusk and the Z axis is chosen so that the rotation axis lies in the X-Z plane. Cassini's location relative to the planet is sketched in Figure 3.1.

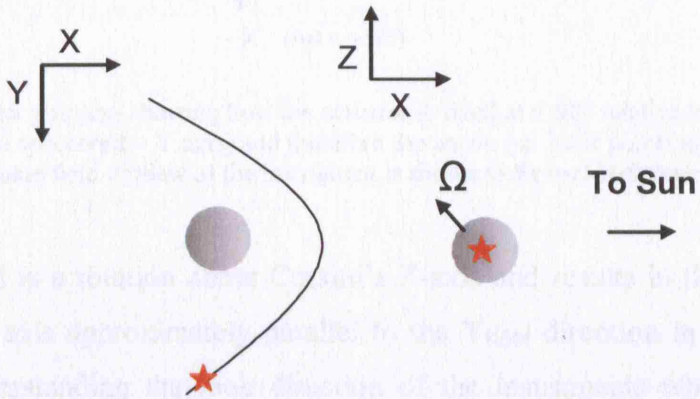

Figure 3.1 Location of Cassini relative to the planet on 17 April 2005. Left: the view in the X-Y_{KSM} plane with the magnetopause indicated by the solid line. Right: the view in the X-Z_{KSM} plane with the rotation, Ω (and magnetic) axis tilted by ~ 21° for this period. In both cases, Cassini's position is indicated by the red star and the Sun is to the right.

In order to interpret this event and even before the plasma data is considered, it is important to have a clear understanding of the field of view of the electron (ELS) and ion (IMS) instruments throughout this event.

3.4.1 Spacecraft motion and instrument pointing

Both the instruments are situated on the actuating platform as described in Chapter 2. At 0° pointing they face outward along the spacecraft –Y axis. However, during this interval the actuating platform was fixed at + 90° and therefore the anode fan points along the spacecraft –X axis as shown in Figure 3.2.

The other key consideration is the motion of the spacecraft, which is especially important for this event as the spacecraft was performing a roll manoeuvre throughout. This effectively provided a slowly spinning spacecraft with, in this case, a period of 27

minutes. This is not an ideal sampling rate for taking measurements pertinent to plasma dynamics in the magnetosheath and magnetosphere, since processes generally act over faster time scales than this, but can provide additional information about the particle flows even with the limited pointing of the instrument.

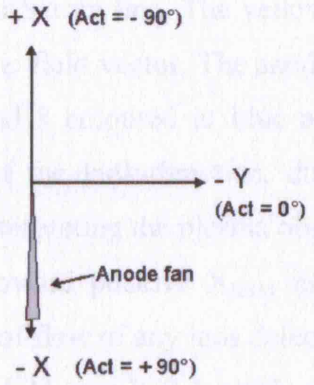

Figure 3.2 Actuator pointing showing how the actuator is fixed at + 90° relative to its null position at 0° (pointing along the spacecraft – Y axis) and therefore the anode fan itself points along the spacecraft – X axis. The approximate field of view of the instrument is shown in **Error! Reference source not found.**.

The roll is a rotation about Cassini's Z-axis and results in the anode fan being spun about an axis approximately parallel to the Y_{KSM} direction in the anti-clockwise direction. Understanding the look direction of the instruments when a population is viewed is vital for understanding the flow directions.

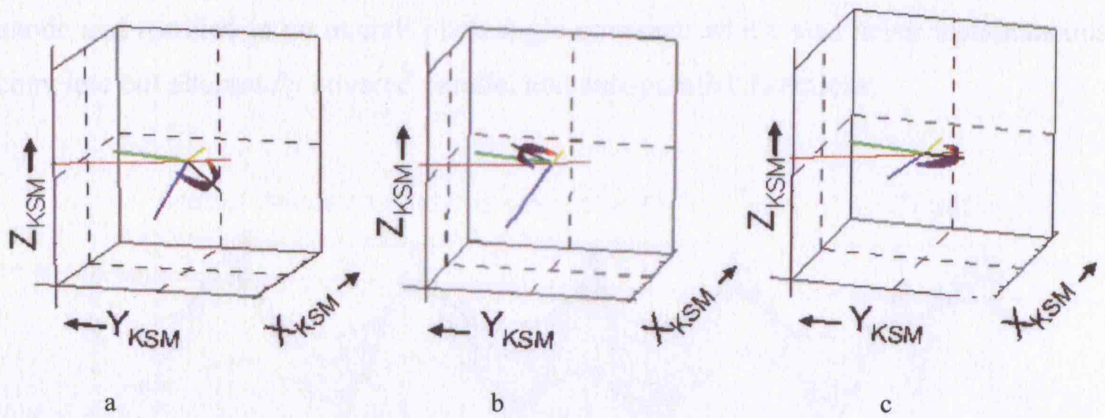

Figure 3.3 Plots showing the relative pointing of the ELS and IMS anodes fans at a) 18:00 UT, b)18:15 UT and c) 18:30 UT on 17 April 2005 in KSM coordinates. The spacecraft trajectory for the whole day is marked in red. The planet and Sun directional vectors are in green and yellow respectively and the magnetic field direction is shown in blue. The roll manoeuvre is about the spacecraft Z-axis. The anode fan is also drawn on with anodes 1 and 8 coloured in blue and red respectively.

This is especially critical for understanding the ion observations which are highly-directional. If the instrument does not look at or near the direction of the bulk

flow, it will not detect the bulk of the ion population. However, this can be useful in eliminating possible flow directions (assuming the density is above the detector threshold). Figure 3.3 contains three plots which demonstrate the pointing of the anode fan at 18:00 UT, 18:15 UT and 18:30 UT in KSM coordinates. The red line shows Cassini's trajectory as it left the magnetosphere moving away from the planet. The green line indicates the Cassini-Saturn line. The yellow line is the direction vector for the Sun and blue is the magnetic field vector. The anode fan is shown looking outward, with the extreme anodes 1 and 8 coloured in blue and red respectively. The figure demonstrates the variability of the look-direction, during a portion of this interval, highlighting the subtleties in interpreting the plasma observations. For example, anode 7 was pointing predominately toward positive X_{KSM} in the view in Figure 3.3 which allows us to infer the direction of flow of any ions detected in anode 7 of IMS.

At 18:00 UT (~ 05:51 LT), anode 7 looked outward from the planet and was pointing slightly southward. By 18:15 UT there had been a rotation, predominately about the Y_{KSM} direction, resulting in anode 7 pointing toward the planet and now slightly northward. By 18:30 UT the fan had rotated to look away from the planet once more. It is therefore clear that each of these rotations changes the field of view significantly. This is also apparent when the pitch angle of any particle entering a given anode of the detector is calculated. Figure 3.4 shows a time series plot of the pitch angle of particles entering the centre of the field of view of each anode of the ELS from 17:30 UT to 19:30 UT on 17 April 2005. The view of pitch angles was periodic for each anode and resulted in an overall pitch angle coverage which was never instantaneously complete but alternately covered parallel and anti-parallel directions.

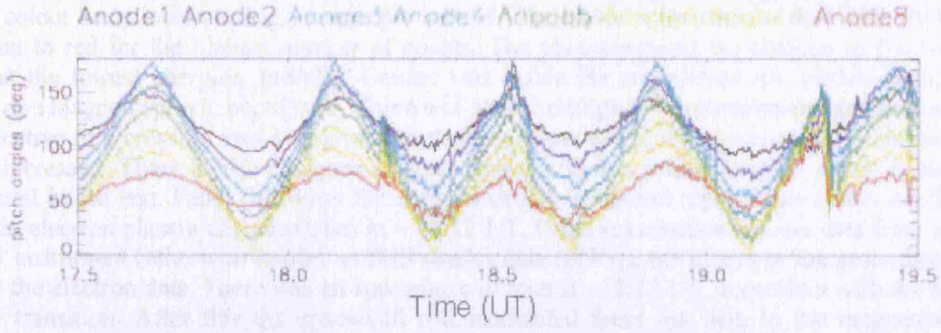

Figure 3.4 The time variation of pitch angle of particles entering a given anode. Each anode is plotted in a different colour (as listed at the top of the plot) with pitch angle on the vertical axis and time along the horizontal axis. This shows that during this interval anode 7 of the ELS (and the IMS) viewed particles with minimum pitch angles of ~ 0° up to a maximum of 100° over a 27 minute period.

3.4.2 Overview of the magnetopause encounter

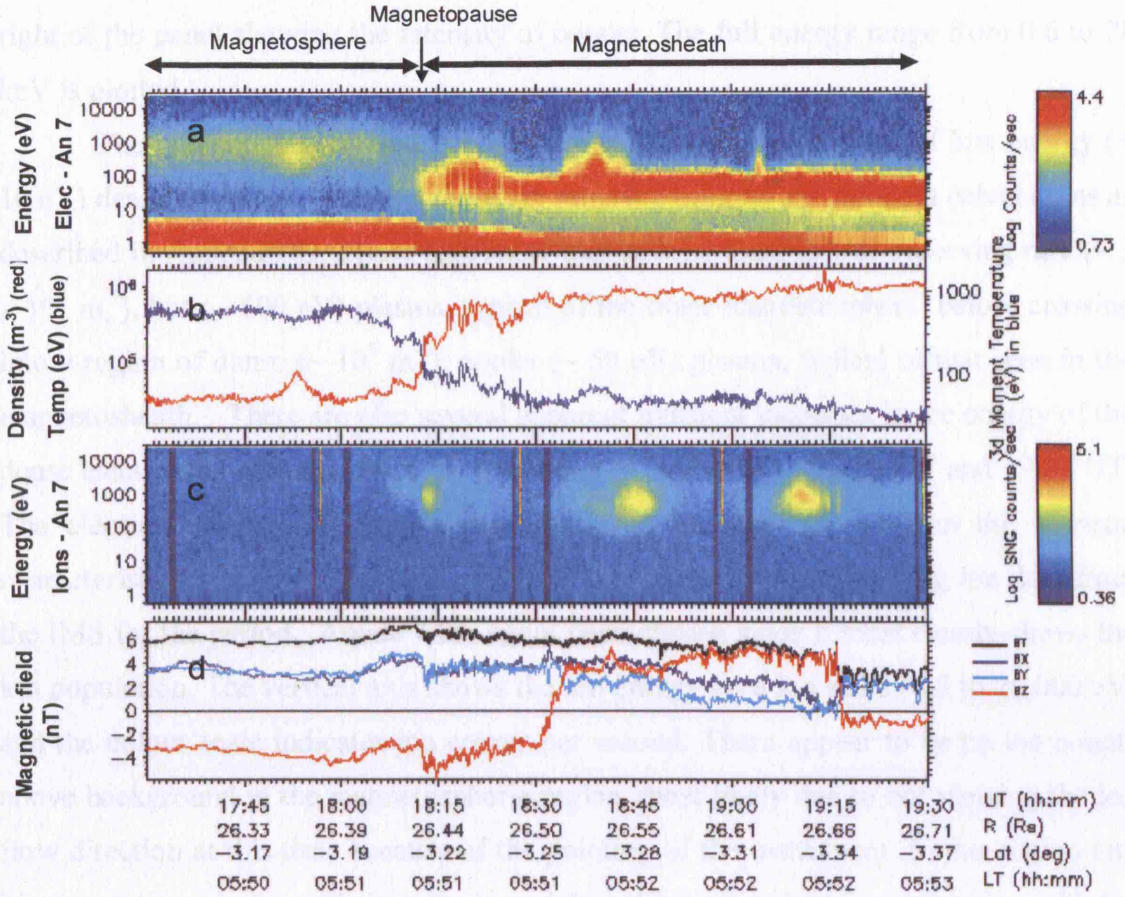

Figure 3.5 Data from the 17 April 2005 17:30 UT to 19:30 UT when Cassini was exiting the magnetosphere on the equatorial dawn flank. The CAPS actuator was fixed at + 90° during this period and the spacecraft was performing a roll manoeuvre. Panel (a) shows the electron spectrogram for anode 7 of the ELS where time is along the horizontal axis, electron energy is in $\log_{10}$ eV on the vertical axis and the colour scale indicates $\log_{10}$ counts per second. The colour scale starts at dark blue for the lowest counts up to red for the highest number of counts. The photoelectrons are obvious as the red band of counts at the lowest energies. Initially, Cassini was inside the magnetosphere, evidenced by the high energy, rare magnetospheric population. There was a clear change in the electron characteristics at ~18:12 UT indicative of a crossing into a magnetosheath-like regime where the electron energy reduced and the density increased. There is also evidence of heated plasma in this external region which is discussed in more detail in the text. Panel (b) shows the electron density (red) and temperature (blue) confirming the change in electron plasma characteristics at ~ 18:12 UT. Panel (c) contains the ion data from anode 7 of the IMS instrument (otherwise known as IMS singles data (SNG)), the plot is in the same format as that used for the electron data. There was an appearance of ions at ~18:12 UT, coincident with the time of the electron transition. After this the spacecraft roll modulated these ion data in the magnetosheath-like region as is explained later in this section and Figure 3.13. Panel (d) contains the three magnetic field vectors, BX_{KSM} (dark blue), BY_{KSM} (light blue) and BZ_{KSM} (red) and the field magnitude, |B| (black). There were three significant magnetic field rotations at 18:12 UT, 18:32 UT and 19:16 UT.

Figure 3.5 shows the electron and ion plasma and magnetic field data from the outbound magnetopause crossing at ~ 18:12 UT on 17 April 2005. The spectrogram in panel (a) contains electron data from anode 7 of the ELS instrument, chosen since it detects the clearest signature of heating. The plot shows the time series of electron counts with electron energy in $\log_{10}$ eV on the vertical axis and the colour scale on the right of the panel showing the intensity of counts. The full energy range from 0.6 to 28 keV is plotted.

The spacecraft generated photoelectrons are visible as a band of low energy (< 10 eV) dense electrons. Note that these are removed prior to any moment calculations as described in Appendix B. These data show that initially Cassini was observing rare (~ 3 x 10^4 m^{-3}), hot (~ 600 eV) plasma, typical of the outer magnetosphere, before crossing into a region of dense (~ 10^5 m^{-3}), cooler (~ 50 eV) plasma, typical of that seen in the magnetosheath. There are also several apparent transient increases in the energy of the dense electron population, observed starting at ~ 18:16 UT, ~ 18:32 UT and 19:04 UT. The electron density and temperature displayed in panel (b) confirm the electron characteristics change at 18:12 UT. Panel (c) contains the corresponding ion data from the IMS for the period. Anode 7 has again been chosen since it most clearly shows the ion population. The vertical axis shows the ion energy on a log scale (0.5 to 26,000 eV) and the colour scale indicates ion counts per second. There appear to be no ion counts above background in the magnetospheric region, most likely due to not viewing the ion flow direction at this time because of the pointing of the instrument. In this region any ion population present will either be in an internal boundary layer or corotating with the magnetospheric plasma.

The ion data contains an obvious periodicity in the count rate after ~ 18:12 UT, when Cassini enters the magnetosheath. This modulation is a consequence of the spacecraft's roll during this period. This is most marked in the ions due to the strong directional dependence of the ion fluxes, i.e. $V_{ION\_BULK} \geq V_{ION\_THERMAL}$ (Compared with the electrons $V_{ELEC\_BULK} \leq V_{ELEC\_THERMAL}$). The ion observations resulting from the spacecraft motion are described in more detail later.

The final panel in Figure 3.5 shows the magnetic field vectors (in KSM coordinates) and field magnitude. During this two hour period there are three significant field rotations, at 18:12 UT, 18:32 UT and 19:16 UT. Initially the field has a Sunward, duskward and southward orientation inside the magnetosphere. This is consistent with expectations as Cassini is located just below the magnetic equator and in the outer magnetosphere at dawn. The field in this region lags rigid corotation [Arridge et al.,

2006b] thus is swept tailward. These factors result in the positive B_X and B_Y components observed.

3.4.3 Identifying the Magnetopause Current Layer (MPCL)

It is critical to accurately determine the time of the magnetopause crossing since this allows us to understand the plasma populations observed and properly order the data. There are three significant field rotations evident in Figure 3.5, at 18:12 UT, 18:32 UT and 19:16 UT, which are all candidates for the magnetopause crossing. The 18:12 UT rotation involved all three magnetic field components, while the later two were both predominately confined to the B_Z component and had a larger shear than at 18:12 UT. In order to determine which rotation marks the traverse of the magnetopause current layer, a Minimum Variance Analysis (MVA - see Appendix B) was applied to each rotation.

The 18:12 UT rotation coincided most clearly with the change in the electron characteristics. MVA on this event over 18:12:15 UT to 18:13:00 UT gives a minimum variance (normal) vector of $\underline{N}$ = [0.828,-0.551, -0.101] and (λ_2/λ_3 = 5.45) which points in a sunward and dawnward direction. Comparing this with the expectation of the Arridge et al., [2006a] model normal ($\underline{N}$ = [0.529, -0.847, -0.056]) reveals the observed and model normals agree to within 25°. Applying the error analysis in Sonnerup and Scheible [1998], the angular error on the normal component is 4.6°. The normal component, B_N of the field is ~ + 1.2 nT ± 0.34 nT, indicating that this magnetopause could have been locally open. However, applying the criteria for distinguishing between RD's and TD's as defined in Neugebauer et al., [1984] (see section 3.2, criteria 4 and 5), $B_N/|B|$ = 0.167, below the threshold of 0.4 and considered too low for an RD. It is clear that there was very little change in the field strength, thus the second condition ($[|B|]/B_N$ <0.2) is satisfied.

The second field rotation at 18:32 UT was a large rotation in B_Z from southward to northward. The MVA gives a poorly determined (λ_2/λ_3 = 1.72) normal component of $\underline{N}$ = [0.990, 0.143, -0.006] with an angular error of 6.08°. Since Cassini was on the dawn flank (05:50 LT), the expected magnetopause normal should point predominately in the X_{KSM} and $-Y_{KSM}$ directions as shown from the Arridge et al., [2006a] model normal at this location $\underline{N}$ = [0.531, -0.845, -0.06]. The MVA determined normal for this discontinuity is more sunward, with a 66° disagreement with the model normal direction. Even taking into account the angular error, this is a large discrepancy between

the data and the model. The MVA derived field component across this discontinuity, ($|B_N|$), has a magnitude of ~ 4 nT ± 0.13 nT, compared with the total field strength of 6 nT. Using the criteria from Neugebauer et al., [1984] (see section 3.2) $B_N/|B| = 0.67$ and $[|B|]/B_N < 0.2$ hence this rotation meets the criteria for a RD, however, without a high confidence in the calculated normal these results are unconvincing.

The final field rotation of note was observed at 19:16 UT, ~ one hour after the main change in the plasma, and was again predominately confined within the B_Z component. MVA produces a normal vector of $\underline{N}$ = [0.814,-0.534, -0.229] with a good confidence, $\lambda_2/\lambda_3 = 20$. The analysis also suggests that at this location the magnetopause was a tangential discontinuity, with the value of $|B_N|$ varying between 0.0 and 0.5 nT ± 0.08 nT. Applying conditions 4 and 5 from section 3.2 gives a maximum value of $B_N/|B|$ ~ 0.1 and $[|B|]/B_N$ ~ 0.27 neither of which meet the criteria for an RD. Comparing the normal with the Arridge model normal, $\underline{N}$ = [0.535, -0.843, -0.055], (which has an angular error of 1.49°) gives a 26° angular difference between the predicted normal for this position on the magnetopause. This disagreement with the model normal is similar to that found for the first field rotation at 18:12 UT.

In considering all three of these rotations, the first rotation at 18:12 UT is identified as the magnetopause current layer for several reasons:

1. The rotation at 18:12 UT is coincident with the increase in the electron density and the decrease in the electron temperature suggestive of Cassini crossing into a region of magnetosheath-like plasma;
2. The ion population appears abruptly at the same time as this rotation, indicative of the spacecraft having crossed into a new plasma regime, rather than the population gradually rotating into the field of view;
3. The magnetic field normal vector at this rotation is reasonably well aligned with the model normal vector;
4. The two later rotations at 18:32 UT and 19:16 UT occur when there is no corresponding change in the plasma to suggest that a boundary has been crossed. In fact, the last rotation at 19:16 UT occurs ~ one hour after the change in the plasma;
5. There is a large difference between the normal derived from the rotation at 18:32 UT compared with the model normal at that location;
6. The plasma observed in the anti-parallel direction prior to the crossing at 18:32 UT (and 19:16 UT) is identical to that observed later in the magnetosheath.

Based on these findings, it is concluded that the first rotation in the field at 18:12 UT is the magnetopause and the latter two rotations are likely due to structure in the exterior magnetosheath field. Using this identification, the plasma behaviour can be ordered.

3.4.4 Plasma observations

From the data in Figure 3.5 and the identification of the MPCL, it is clear that heated magnetosheath plasma was seen outside, yet close to, the inferred magnetopause position. In order to understand the geometry of this event and interpret the data with respect to the field of view of the instruments, we examine the pitch angle coverage of the data. Figure 3.6 shows the electron observations for each anode together with the extent and variation of the pitch angle coverage over the same time range shown in Figure 3.5. By studying the data from all anodes additional details can be identified.

The first seven panels (a – g) contain energy-time spectrograms for anodes 1 to 7 of the ELS. The data from anode 8 is not included in the analysis as its obstructed field of view rendered the counts artificially low. Panel (i) contains the magnetic field vectors. Panel (h) contains an orientation plot for the anodes as a time series. The anodes are labelled from 1 to 8 on the vertical axis and the colour scale indicates the pitch angle range sampled by each anode with red indicating ~ 0° and black ~ 180°. The sinusoidal variation in the pitch angle coverage for each anode is apparent.

The first population encountered in this interval is the hot, magnetospheric population which is apparent in the left hand side of Figure 3.6 in all anodes. This population remains constant in all anodes until ~ 17:35 UT when an increase in the count rate at energies of ~ 500 eV is observed in anodes 2 and 3 lasting for ~ 5 minutes. From the orientation plot in Figure 3.6, this 5 minute interval is when these anodes are sampling particles travelling approximately anti-parallel to the magnetic field direction, i.e. with anti-parallel pitch angles. The population then returns to the previous levels with a constant count rate in all anodes.

A second count rate increase in the ~ 500 eV electrons occurred at ~ 17:51 UT, this time in anodes 5 and 6, again lasting for 5 minutes. The orientation plot in Figure 3.6 panel (h) shows that these anodes were viewing electrons with near- parallel pitch angles at this time. The flux then returned to nominal magnetospheric values before the final flux increase was seen during this interval at ~ 18:03 UT in anodes 2-4, which

indicates that this enhancement was in the near anti-parallel population. We also note that we do not see the other field-aligned direction simultaneously, i.e. ~180° pitch angles, so we cannot rule out the possibility of bi-directional enhancements.

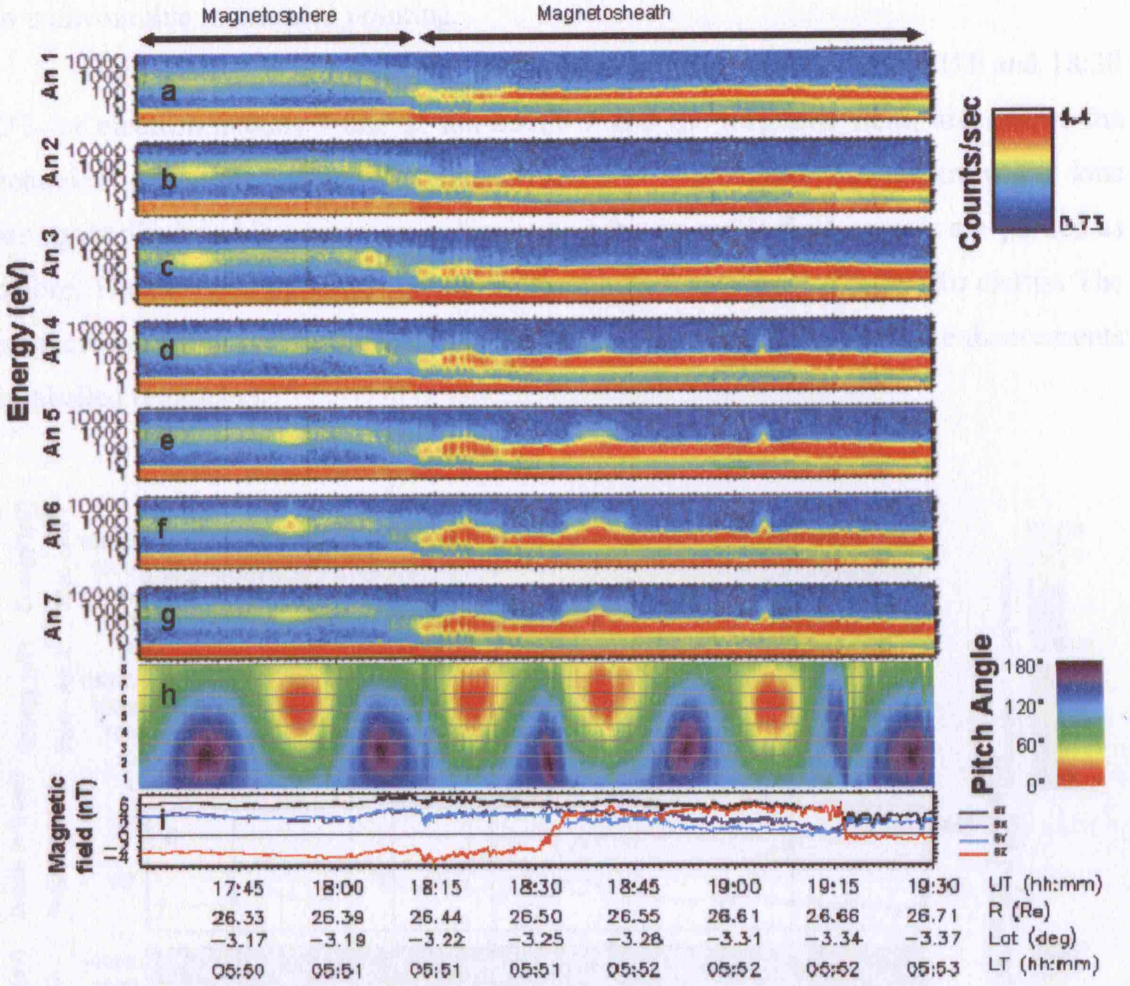

Figure 3.6 Panels (a - g) contain energy-time spectrograms for each anode of the ELS (excluding anode 8 which is omitted due to poor count rates), with time along the horizontal axis from 17:30 UT to 19:30 UT, the vertical axis shows the energy in eV and the colour scale indicates the count rate. The photoelectrons are evident along the bottom of the plots as the red band at low energies. The three heated populations are evident at 18:16 UT, 18:39 UT and 19:04 UT. Panel (h) contains the pitch angle coverage for each anode as a time series. The anodes are labelled from 1 to 8 on the vertical axis and the colour scale indicates the pitch angle range with red indicating ~ 0° and black ~ 180°. Panel (i) contains the 3 magnetic field vectors, BX_{KSM} (dark blue), BY_{KSM} (light blue) and BZ_{KSM} (red) and the field magnitude, |B| (black). Note the variation in the pitch angle coverage due to the spacecraft roll. It is clear that ELS could not see all pitch anodes at the same time. Therefore, the parallel and anti-parallel flows cannot be compared simultaneously. Note that the heated electron populations were seen predominately in anodes 4-7 and occurred when these anodes were sampling particles with mainly parallel pitch angles. These field aligned flows were seen when the field was orientated both northward prior to the large rotation at 18:32 UT and southward after this time.

During the period when the spacecraft was located inside the outer magnetosphere-proper, the field was directed southward, Sunward and duskward, and there was no significant change in the magnetic field configuration during this time as

shown in Panel (i). Note that there were no significant fluxes of ions detected inside the magnetosphere, which might be expected due to a corotating ion population or the presence of any boundary layers (Figure 3.5 panel c), this could be due to the plasma densities being below the detection limits of the IMS (~ 10^3 m^{-3} [Young et al., 2005]) or to unfavourable instrument pointing.

Figure 3.7 contains a subset of the data recorded between 18:05 UT and 18:30 UT for electron anodes 7 and 2, ion anode 7 and the magnetic field, and shows the behaviour of the plasma as the magnetopause was approached. The electrons and ions are again displayed in spectrogram format and the magnetic field vectors are plotted as before. The different plasma populations encountered have been labelled for clarity. The magnetospheric population, including the final of the three field-aligned enhancements is labelled region (1).

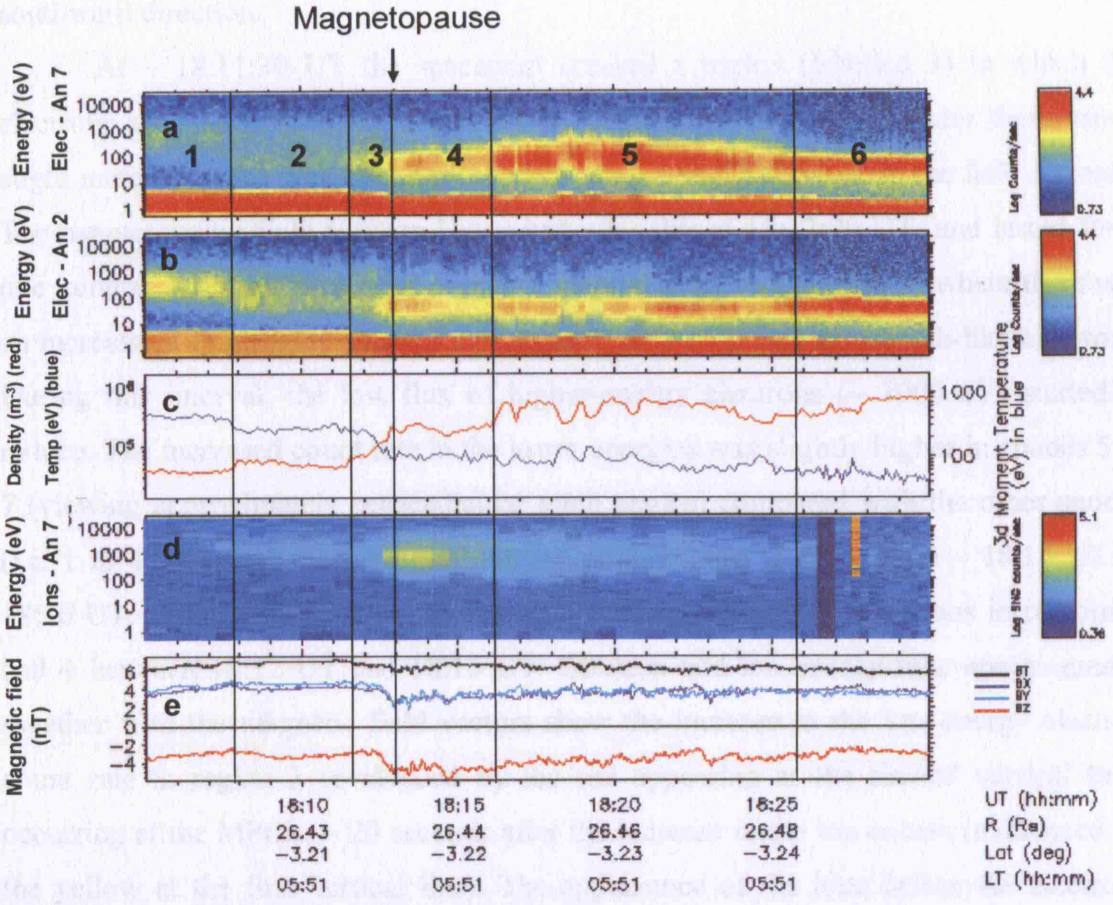

Figure 3.7 A subset of the data from Figure 3.5 on the 17 April 2005 from 18:05 to 18:30 UT. Panel (a) shows the electron spectrogram for anode 7 with different regions of interest labelled from 1 to 6 (see text). The heated population in the magnetosheath is apparent between ~ 18:16 UT and 18:26 UT (region 5). In panel (b) the electron spectrogram from anode 2 shows no evidence of the heated population. Panel (c) contains the electron density and temperature showing the gradual change as the boundary is approached. In panel (d) the ion spectrogram for anode 7 shows the first appearance of the ions upon crossing the magnetopause. The orange feature at ~ 18:28 UT is a data glitch. Panel (e) contains the three magnetic field vectors, BX_{KSM} (dark blue), BY_{KSM} (light blue) and BZ_{KSM} (red) and the field magnitude, |B| (black).

The first change in the electrons was at 18:08 UT when an additional, lower-energy, population (~ 100 eV) appeared alongside the higher-energy magnetospheric electrons (see region labelled 2). The magnetic field remained largely in the same configuration as that in region 1. The electron density increased slightly and the temperature decreased slightly (panel c). The low energy population has energies similar to typical magnetosheath plasma, but is rarer. Simultaneously, very low ion count rates (but above the background) were observed predominately in anode 7 of the IMS. The lack of counts suggests the bulk flow (of any boundary layer or corotating magnetospheric population) was outside the instrument field of view. The remaining anodes detected even weaker fluxes, suggesting that anodes 6 and 7 were looking closest to the flow direction. As will be shown later, this is in a dawnward and slightly southward direction.

At ~ 18:11:30 UT the spacecraft entered a region (labelled 3) in which the electrons showed an increase in density. Approximately 30 seconds later there was a slight increase in the ion count rate, together with a slight decrease in the field strength. The magnetopause field rotation began just after this at 18:12:20 UT, and lasted for ~ one minute. After this time, the spacecraft entered a region (labelled 4) where there was an increase in the density of the low-energy (~ 100 eV), magnetosheath-like electrons. During this interval, the low flux of higher-energy electrons (~ 1000 eV) started to reduce. The increased count rate in the lower energies was slightly higher in anodes 5 to 7 (viewing approximately perpendicular pitch angles) compared with the other anodes (i.e. 1 to 4, sampling electrons with higher pitch angles, $\geq 120°$) from ~ 18:14 UT to 18:16 UT. Figure 3.8 shows a shorter time period covering observations in regions 3 and 4 between 18:12 UT and 18:15 UT. Electron and ion energy-time spectrograms, together with the magnetic field vectors show the increase in the low-energy electron count rate in region 3 (evidenced by the red appearing at the second vertical line) occurring at the MPCL, ~ 20 seconds after the increase in the ion counts (evidenced by the yellow at the first vertical line). The appearance of the ions before the electrons suggests that the ions are seen closer to the field rotation than the electrons and thus the magnetosheath ions are penetrating further into the magnetopause than the electrons due to their larger gyroradii as shown in Figure 1.9.

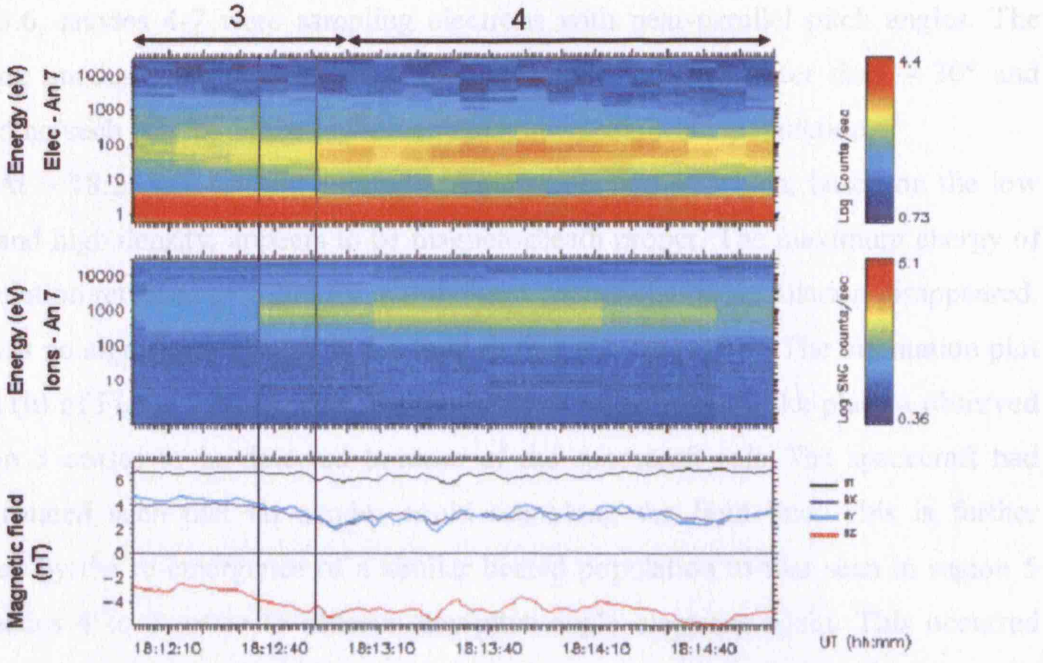

Figure 3.8 Panel (a) The electron spectrogram from anode 7 with time along the horizontal axis from 18:12 UT to 18:15 UT, energy along the vertical axis and the colour scale indicating the number of counts, (b) the ion spectrogram from anode 7 in the same format as above; (c) the three magnetic field vectors, BX_{KSM} (dark blue), BY_{KSM} (light blue) and BZ_{KSM} (red) and the field magnitude, |B| (black). This three minute interval shows the data as the MPCL was encountered. The rotation in the field began at ~18:12:20 UT and the sharp increase in the ion count rate followed a short while later at 18:12:25 UT. The increase in the electron count rate was not seen until 18:12:52 UT.

The ions appeared relatively abruptly (compared, for example, with the two later beams at ~ 18:45 UT and 19:10 UT which appeared more gradually as the field of view of the instrument rotated). This indicates that the crossing of the current layer has allowed the spacecraft to view a population which was not present inside the magnetopause. The direction of flow of this population was also deflected with respect to the magnetosheath ion population observed at ~ 18:45 and 19:10 UT. As the spacecraft continues to rotate the ion count rate gradually decreased, consistent with the population leaving the IMS field of view.

From 18:16:28 UT Cassini encountered a region (labelled 5 in Figure 3.7) of denser electrons with the density increasing from 2 x 10^5 m^{-3} to 4 x 10^5 m^{-3} at lower energies (~ 100 eV). However, this population also showed evidence of being energised, as the maximum energy of this population increased from ~ 200 eV in region 4 to 500 eV in region 5. A low flux of electrons with energies ~ 500 eV to ~ 1000 eV is also present. This change in the electrons in region 5 was not accompanied by any measured change in the ions or magnetic field. Note that this heating only appeared in electrons detected by anodes 4 to 7, with the strongest presence in anode 7; note the lack of such a signature in anode 2 in Figure 3.7. From the orientation plot in panel (h) of

Figure 3.6, anodes 4-7 were sampling electrons with near-parallel pitch angles. The remaining anodes viewed electrons with pitch angle values greater than ~ 30° and observed no such heating in the low-energy magnetosheath-like population.

At ~ 18:25 UT Cassini entered a region (labelled 6) which, based on the low energy and high density, appears to be magnetosheath proper. The maximum energy of the population returned to ~ 200 eV and the rare, higher energy population disappeared. There was no significant change in the field during this transition. The orientation plot in panel (h) of Figure 3.6 suggests that the heated magnetosheath-like plasma observed in region 5 ceases to be detected because of the spacecraft roll. The spacecraft had simply rotated such that no anodes could see along the field line. This is further supported by the re-emergence of a similar heated population to that seen in region 5 once anodes 4 to 7 rotate to observe low-pitch-angle electrons again. This occurred between 18:34 UT and 18:44 UT and from 19:03 UT to 19:06 UT. The third time the heated population was observed, the duration was noticeably shorter than the observations of the heated populations seen previously. The population was not present for the period when Cassini was able to view low-pitch-angle electrons (~ 10 minutes for the populations starting at 18:16 UT and 18:34 UT).

Further inspection of these heated populations can be carried out by looking at a pitch angle plot, which divides the energy scale on a standard spectrogram into individual pitch angle bins. Hence the flux of electrons at each pitch angle can be seen for a particular energy bin. Figure 3.9 contains the pitch angle plot for 18:00 UT to 19:10 UT on 17 April 2005. Electron energy in $\log_{10}$ keV is on the vertical axis. Only energies from 100 eV to 2 keV have been plotted in order to best show the heated populations. Between each tick mark (logarithmic energy bin) are 12° pitch angle bins, the colour scale represents the $\log_{10}$ average counts per cm^{-2} per second. The heated electron fluxes discussed above appear to be closely field-aligned, which shows in the pitch angle plot as an enhanced flux toward the bottom of each 0° pitch angle energy bin for the three intervals discussed above. Note that we do not view the anti-parallel pitch angle electrons at the same time, so we are unable to comment on the fluxes at high pitch angles. This method of plotting these data also shows an effect not previously apparent from the individual spectrograms.

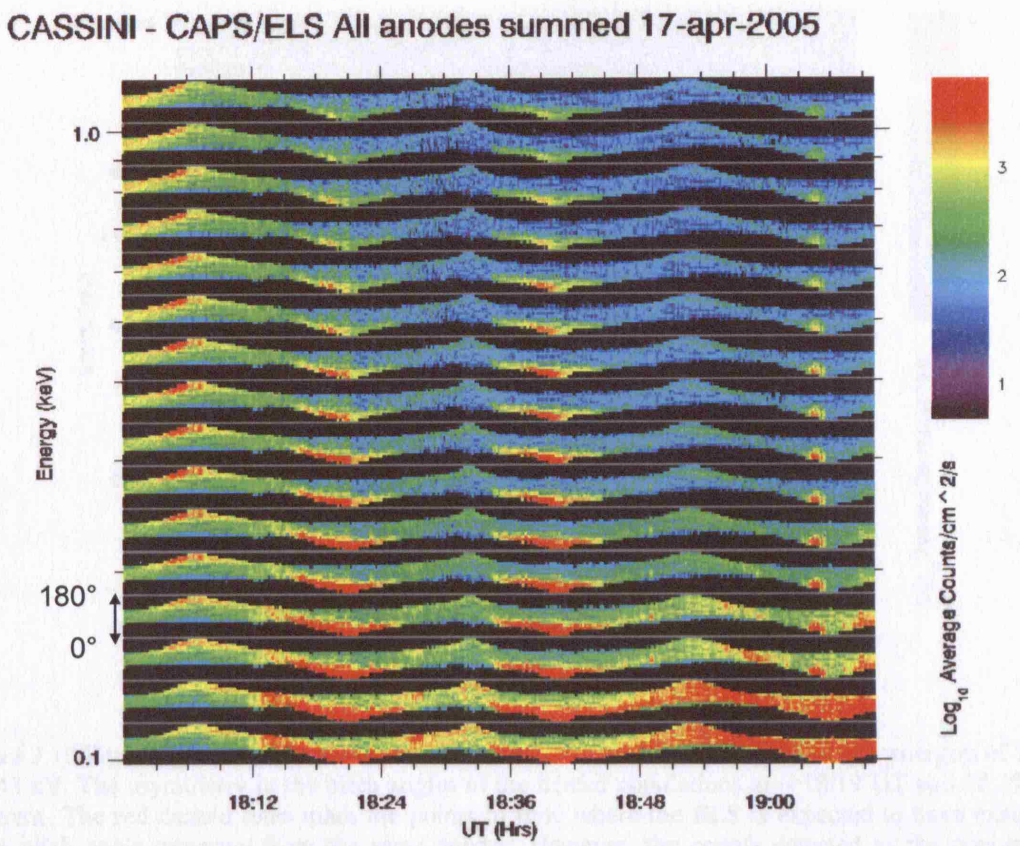

Figure 3.9 Savaud plot for 18:00 UT to 19:10 UT on 17 April 2005.Time is along the horizontal axis, energy is on the vertical axis in keV and the colour scale indicates the number of counts. Each of the energy bins are divided into 15 pitch angle bins (with 12° per division) to show the number of counts at each pitch angle with 0° at the bottom of the bin and 180° at the top. The three heated populations start at ~ 18:16 UT, 18:34 UT and ~ 19:03 UT are apparent as the high counts at low pitch angles, indicating their field-aligned nature.

Figure 3.10 shows a closer look at the first two of the heated populations spanning a time range of ~ 18:12 to 18:45 UT and energies 135 eV to 343 eV. The two observations of heated populations are shown by the high flux at energies ~ 100 eV to 400 eV and are bounded by two pairs of red lines. The first population (from ~ 18:16 UT to ~ 18:25 UT) contains a noticeable asymmetry, with an increased number of counts per cm^2 per second at pitch angles of ~ 50° - 70° as the population entered the field of view (~18:16 UT) compared with the number of counts at the same pitch angles as the population left the field of view (~18:25 UT). The same can be seen for the second population between 18:36 UT and 18:44 UT.

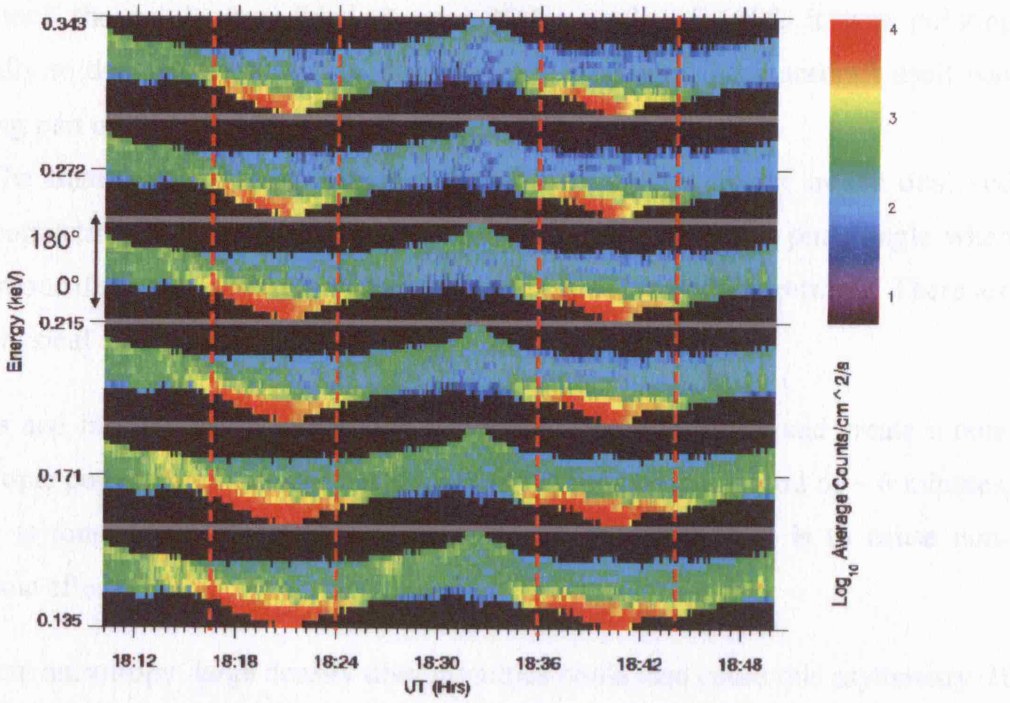

Figure 3.10 Pitch angle plot from Figure 3.9 from 18:10 UT to 18:50 UT and between energies of 135 eV to 343 eV. The asymmetry in the pitch angles of the heated populations at ~ 18:19 UT and 18:39 UT is apparent. The red dashed lines mark the points in time where the ELS is expected to have exactly the same pitch angle coverage from the same anodes. However, the counts detected as the population is entered at ~ 18:16 UT and ~ 18:36 UT are higher at pitch angles of ~ 50° - 70° compared with the counts observed as the population is exited at ~ 18:25 UT and ~ 18:44 UT at the same pitch angle range.

The asymmetry in the counts observed during the spacecraft roll could be caused if a section of the spacecraft body had shadowed part of the population during a section of the roll. As discussed earlier and shown in Figure 3.2, the actuator was fixed at + 90° during this period. Therefore, this difference cannot be explained by some effect due to the change in the instrument pointing with respect to the spacecraft body. In addition, a variation in response of one anode above another cannot explain this effect since, from the pitch angle plot in Figure 3.4, it is the same anodes (4 and 5) viewing the pitch-angle range of interest (~ 50° - 70°) as the spacecraft rotates into and out of a direction that allows the ELS to view the population.

However, it is possible that as the spacecraft itself rotated, different sections of the structure of the spacecraft became relevant with respect to the magnetic field direction and stopped some electrons from reaching the detector. Thus, the orientation of the anode fan (and spacecraft) is compared at the start and end of the appearance of the low-pitch angle population. The orientation of the instrument with respect to the magnetic field was similar at both times coinciding with the appearance of the populations (at ~ 18:16 and 18:34 UT) and when the population left the field of view (~ 18:25 UT and ~18:44 UT). Thus any shadowing effects would be the same at these

times. Since the anode was fixed at an actuator angle of +90°, it was pointing tangentially to the spacecraft body and it may have been that the spacecraft itself was shadowing part of the population at these times.

The final option is that there was some inherent asymmetry in the observed plasma population resulting in a higher flux of electrons at a given pitch angle when viewed in one direction and not the other, i.e. the plasma was non-gyrotropic. There are several physical effects that could cause this:

a) Waves and instabilities in the plasma can modify the population and create a non-gyrotropic population; however, the asymmetry is seen over a period of ~ 6 minutes, which is longer than the typical wave frequency expected if it is to cause non-gyrotroic effects.

b) Gradient anisotropy: large density discontinuities could also cause this asymmetry. If the observation being made is within a gyroradius of the discontinuity there would be a lack of particles with a given pitch angle from the rare region compared with the denser region. However, this discontinuity is not seen at the time of these asymmetric populations and it would require a stable spacecraft trajectory along the discontinuity for a ~ 6 minute duration.

c) High-energy electron depletion by moon absorption can result in asymmetric distributions [e.g. Mauk et al., 2001] but this is not considered here since we are not looking in regions where such moon wakes are evident. Note that although Titan orbits close to the magnetopause, it is not in the vicinity at the time of these two crossings.

The heated populations are further investigated by comparing their distributions in PSD as outlined in Chapter 1. Figure 3.11 contains plots of time slices through the ELS spectrograms for each of the different regions labelled in Figure 3.7. Thus, $\log_{10}$ of the energy is now on the horizontal axis and PSD is on the vertical axis. The spectrograms used in this analysis so far have used units of counts per second. In order to demonstrate the difference in the shape of the populations, the phase space density (PSD, as discussed in Appendix B) is used instead of count rate.

A time slice of PSD has been plotted for the central region of each of the electron populations seen in anode 7. The central times for these populations are at 17:53 UT (in the magnetosphere, region 1), 18:10 UT (region 2), 18:12 UT (region 3),

18:14:30 UT (region 4), 18:19 UT in the heated population (region 5) and 18:27 UT in the magnetosheath.

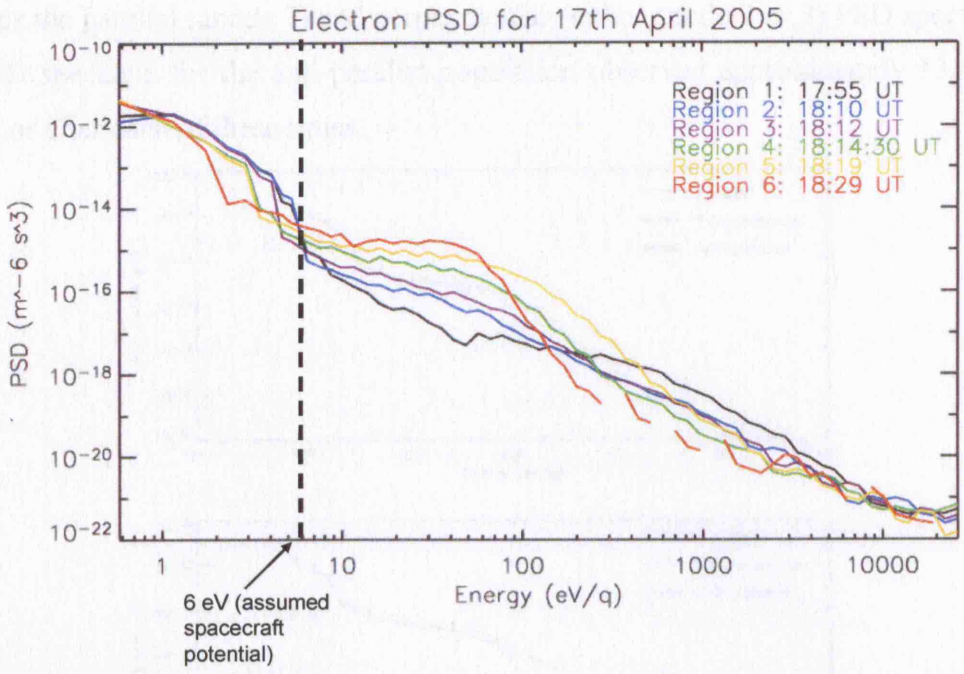

Figure 3.11 PSD distribution spectra of the different plasma regimes encountered across the magnetopause on 17 April 2005 in anode 7 at 17:53 UT (solid), 18:10 UT (dotted), 18:14:30 UT (dash dot), 18:19 UT (long dash) and 18:27 UT (dash dot dot). PSD is on the vertical axis and $\log_{10}$ energy is on the horizontal axis. The peak PSD for each population occur at the very lowest energies and these are the photoelectrons which are omitted from any moment calculations. Therefore the spectra can be ignored below ~ 6 eV in this case (see vertical line). There is a noticeable transition from the magnetospheric population at ~ 17:53 UT with a large PSD at high-energies through to the magnetosheath population at ~ 18:27 UT which has the highest PSD in the mid-energy range. Note the characteristic flat-top shape to the magnetosheath spectra in these mid-energies. All of the intermediate populations sit within the bounds of the magnetospheric and magnetosheath population distributions, apart from a departure in the population observed at ~ 18:19 UT between ~ 60 eV to ~ 400 eV which is where the heating is observed.

From the plot it is clear that the bounding populations are those from the magnetosphere (region 1) and the magnetosheath (region 6), with all the other populations, except one, sitting in between these curves. The exception is the spectrum from 18:19 UT which is taken from the heated region (region 5) which shows an enhancement in the PSD from ~ 50 eV to ~ 400 eV.

To establish any asymmetry within this population, we need to compare the parallel and anti-parallel flows simultaneously, but, during this interval the instrument was not able to see both directions along the field simultaneously. Hence it is only possible to compare it with the instantaneous perpendicular population. However, the (apparently unheated) anti-parallel population was seen within approximately half a spacecraft roll period (~ 13 minutes) before or after the central peak of the heated population. Thus, the PSD distribution at the time the heated parallel population was seen is compared with the closest time the anti-parallel population was viewed.

When the heated population came into view, the PSD distribution at the central time of each region (18:19 UT, 18:39 UT and 19:04:30 UT) is plotted. Figure 3.12 contains the parallel (anode 7) and perpendicular (either anode 2 or 3) PSD spectra, plus the PSD spectrum for the anti-parallel population observed approximately 13 minutes before or after each of these times.

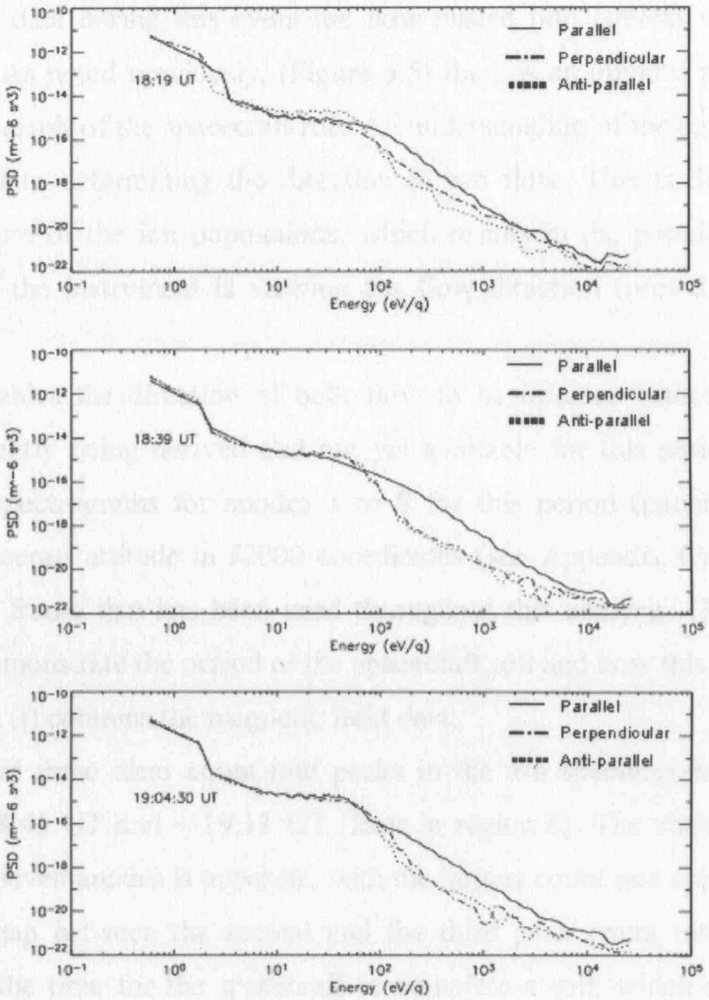

Figure 3.12 PSD distribution spectra with PSD on the vertical axis and energy in $\log_{10}$ eV on the horizontal axis from each of the three heated populations in the parallel (solid line) and perpendicular (dash-dot line) populations plus an anti-parallel (dotted line) component when visible. Top: parallel and perpendicular at 18:19 UT, anti-parallel at 18:32 UT, middle: parallel and perpendicular at 18:39 UT, anti-parallel at 18:32 UT, bottom: parallel and perpendicular at 19:04:30 UT, anti-parallel at 18:53 UT. The heating in the parallel direction for all three times is evident. The anti-parallel and perpendicular components are generally very similar apart from the perpendicular component at 18:19 UT which has a slightly higher flux at the higher energies compared with the anti-parallel flux. All have the characteristic 'flat-top' shape in the intermediate (~ 6 – 70 eV) energy range, although this is slightly less 'flat' for the parallel population.

The heating in the parallel direction above the perpendicular and anti-parallel populations at all three times is evident as a higher flux at energies > ~ 100 eV. The anti-parallel and perpendicular components are very similar apart from the perpendicular component at 18:19 UT which has a slightly higher flux above 100 eV

compared with the anti-parallel flux. This asymmetry in heated electrons outside the magnetopause is a signature of reconnection somewhere along the field line, producing a heated population in the direction outwards from the magnetopause. All populations exhibit a characteristic flat-top shape in the mid-energy range (~ 6 to 70 eV), but this is slightly modified in heated magnetosheath or mixed populations.

The ion data during this event are now placed into context with the electron measurements. As noted previously, (Figure 3.5) there is an obvious periodicity in the ions which is a result of the spacecraft roll. An understanding of the spacecraft pointing is again critical to determining the direction of ion flow. This is due to the highly anisotropic nature of the ion populations, which results in the population only being observed when the instrument is viewing the flow direction (providing $V_{ION\_BULK} \geq V_{ION\_THERMAL}$).

This enables the direction of bulk flow to be inferred without ion moments, which are currently being derived and not yet available for this period. Figure 3.13 contains IMS spectrograms for anodes 1 to 8 for this period (panels a-h). Panel (i) shows the spacecraft attitude in J2000 coordinates (see Appendix C). This is not the same reference frame that has been used throughout this analysis. However, its only purpose is to demonstrate the period of the spacecraft roll and how this controls the ions observed. Panel (j) contains the magnetic field data.

There are three clear count rate peaks in the ion spectrograms at ~18:12 UT (region 4), ~ 18:45 UT and ~ 19:13 UT (later in region 6). The variation in intensity detected in the seven anodes is apparent, with the largest count rate appearing in anodes 6 and 7. The gap between the second and the third peak count rate is 25 minutes, approximately the time for the spacecraft to complete a roll, which suggests that the flows were coming from the same direction. This implies that the latter two enhancements were manifestations of the same plasma population. In fact, if the spectrogram in Figure 3.13 is extended to include the next 1.5 hours, this repetition in the spacecraft roll and the ion modulation does not change (not shown).

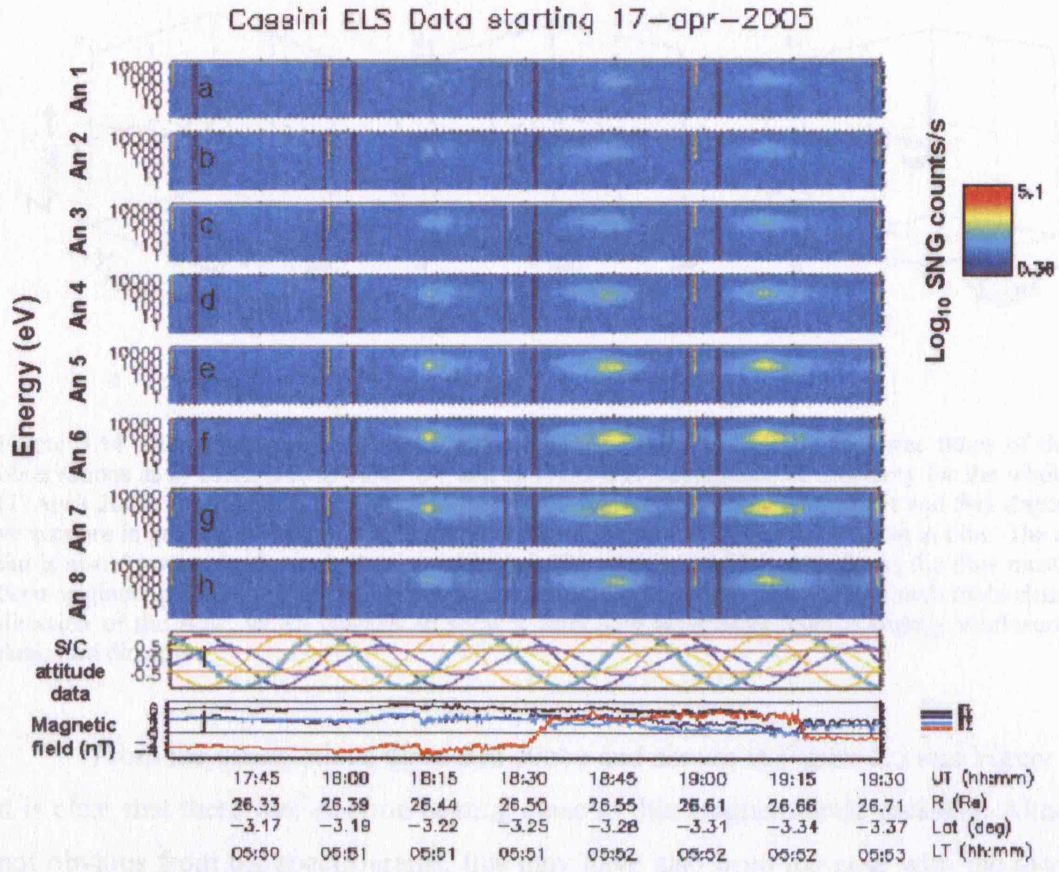

Figure 3.13 Ion spectrograms are plotted for anodes 1-8 in panels (a-h). Time is along the horizontal axis and is plotted from 17:30 UT to 19:30 UT; energy is on the vertical axes and the colour scale indicates the number of counts. The peak count rate appears in anodes 6 and 7. Panel i) shows the spacecraft attitude data for each of the spacecraft X, Y and Z axes in the J2000 coordinate frame. The labels for this plot have not been included since the quantitative values are not of concern here, only a qualitative appreciation of the period of the spacecraft roll. Panel (j) contains the three magnetic field vectors, BX_{KSM} (dark blue), BY_{KSM} (light blue) and BZ_{KSM} (red) and the field magnitude, |B| (black).

However, the first peak at 18:12 UT is separated from the second peak by 33 minutes and this flow was thus deflected compared with the flow direction of the later populations. From knowledge of the instrument pointing discussed in section 3.4.1, these directions can be inferred and some measure of the deflection obtained. The orientation of the IMS anode fan at the times when the three main ion peaks appear in anode 7 (18:12 UT, 18:45 UT and 19:13 UT) are shown in Figure 3.14. Panel a) shows that at 18:12 UT this population was flowing southward and tailward. By 18:45 UT there was a clear change in direction of the incident flow which now flowed tailward, and slightly northward (panel b) and the same at 19:13 UT (panel c), with a slightly larger northward component. Based on this the deflection of the ion flow seen at 18:12 UT compared with the two populations at 18:45 and 19:13 UT is ~ 84°.

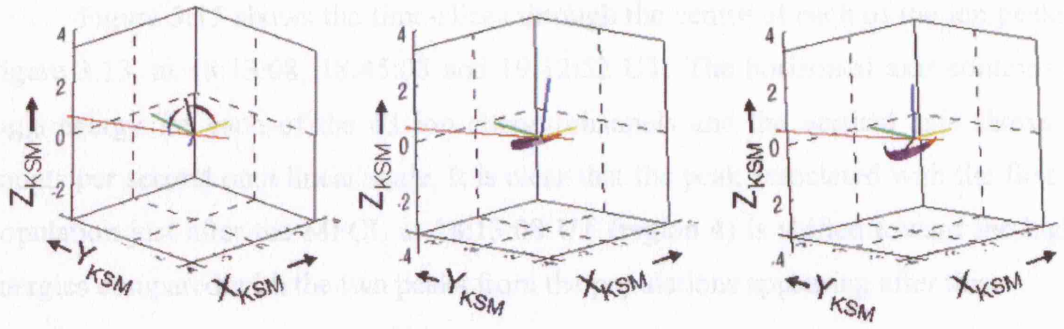

Figure 3.14 The orientation of the IMS anode detector (same as ELS) at the three times of the ion observations at a) 18:12 UT, b) 18:45 UT and c) 19:13 UT. The spacecraft trajectory for the whole day (17April 2005) is marked in red from left to right in KSM coordinates. The planet and Sun directional vectors are in green and yellow respectively and the magnetic field direction is shown in blue. The anode fan is also drawn on with anode 8 coloured in red. The pointing at 18:12 UT shows the flow must have been originating from the Sun- and northward direction, the latter two plots show a noticeable change in direction of the flow, which changes to show a flow now originating from a slightly southward and duskward direction.

From the observations discussed above and shown in Figure 3.5 and Figure 3.11 it is clear that there was electron heating close to this magnetopause crossing. Although not obvious from the spectrograms, this may have also been the case with the ions. To establish this, time slices through the ion spectrograms can be used to analyse the ion populations and compare the energy of the populations observed at different times.

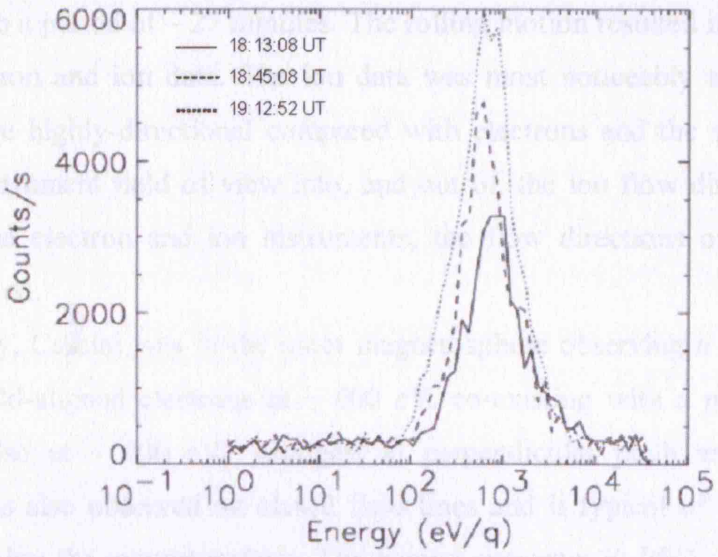

Figure 3.15 Distribution spectra generated by taking timeslices through the ion spectrogram for 17 April 2005. Log_{10} energy is on the horizontal axis and counts per second is on the vertical axis. Ion spectra have been plotted for each of the three peaks at 18:13:08 UT, 18:45:08 UT and 19:12:52 UT. For each population the point of maximum counts has been chosen as this represents the peak flow of the ion beam. It is apparent that the peak at 18:13:08 UT is shifted toward the higher energies ~ 1000 eV, compared with the peak energy for the two later populations at 18:45:08 UT and 19:12:52 UT of ~ 600 eV. In addition the first population is narrower, suggesting that this population may have been more beam-like compared with the other two.

Figure 3.15 shows the time-slices through the centre of each of the ion peaks in Figure 3.13, at 18:13:08, 18:45:08 and 19:12:52 UT. The horizontal axis contains the $\log_{10}$ energy for each of the 63 ion energy channels and the vertical axis shows the counts per second on a linear scale. It is clear that the peak associated with the first ion population just after the MPCL at 18:13:08 UT (region 4) is shifted toward the higher energies compared with the two peaks from the populations appearing after this.

3.4.5 Discussion

A single magnetopause crossing occurred on 17 April 2005, when Cassini was on the dawn flank of Saturn's magnetopause at a Saturn-centric distance of 26 R_S, close to the equatorial plane. This event was analysed utilising both plasma (electrons and ions) and magnetic field data. It was selected as it shows clear evidence of heated electrons in the magnetosheath just after the magnetopause crossing. In addition, the ion population was captured within the instrument field of view during at least part of this crossing, which aids in the interpretation.

Throughout this event, although the actuator was fixed at + 90°, the spacecraft was performing a roll about its Z-axis, effectively providing a slowly spinning spacecraft with a period of ~ 27 minutes. The rolling motion resulted in a modulation of both the electron and ion data. The ion data was most noticeably affected since ion populations are highly-directional compared with electrons and the spacecraft motion rotated the instrument field of view into, and out of, the ion flow direction. From the pointing of the electron and ion instruments, the flow directions of the populations could be inferred.

Initially, Cassini was in the outer magnetosphere observing a population of bi-directional field-aligned electrons at ~ 600 eV, co-existing with a persistent electron population (also at ~ 600 eV) strongest at perpendicular pitch angles. This latter population was also observed on closed field lines and is typical of a trapped plasma population within the magnetosphere. The energy spectrum in PSD of this population shows (in Figure 3.11), as expected, a peak near ~ 500 – 600 eV with very few counts at the lower energies. No ions were detected in the magnetosphere, probably due to the pointing of the instrument not capturing the ion flow.

At ~ 18:12 UT Cassini crossed into a region of higher density, lower energy plasma indicative of the magnetosheath. At the same time there was an abrupt

appearance of ions. These changes in the plasma occurred at the same time that the field underwent a small rotation. This was the first of three significant rotations of interest in the magnetic field at 18:12, 18:32 and 19:16 UT yet only the first of these coincided with the changes in the plasma. In order to facilitate the analysis of this event, we first confirmed which rotation represented the crossing of the magnetopause current layer. First, MVA was applied to each rotation and the magnetopause normals determined. The second rotation at 18:32 UT was very large, starting from a strongly negative B_Z orientation and rotating to a positive B_Z orientation (there was very little change in the other components). However, the lack of coincident changes in the plasma, plus the poorly determined normal (which was predominately in the $+X_{KSM}$ direction) was not convincing. The third field rotation during this interval was at 19:16 UT and was not accompanied by any changes in the plasma. In fact, it appeared much later (~ 45 minutes) than the main change in the plasma at 18:12 UT. Therefore, the first field rotation at ~18:12 UT was identified as the MPCL.

For completeness, if the rotation at 18:32 UT had been the magnetopause, the field prior to this, starting at 18:12 UT would be assumed to be boundary layer since, although very disturbed; it had a magnetospheric orientation and magnitude. The deflection in the ion flow between the boundary layer and magnetosheath is still valid since the rotation still separates the first ion population from the later two. As the first field rotation was approached, the appearance of low-energy electrons was followed minutes later by an abrupt appearance of the ions. The field rotation was observed for ~ 30 s before the magnetosheath-like electron population appeared. This could be an observation of the internal electron then ion separatrix layers. However, this 'alternate' magnetopause at 18:32 UT would now occur between the first and second views of the heated parallel electron population. The observation of parallel-heated electrons both inside and outside the 'magnetopause' is not viable, since the magnetic field is directed toward the reconnection site one side and away from it on the other, thus heated particles streaming from the reconnection site will be directed anti-parallel and parallel respectively. This strongly suggests that the magnetopause cannot be located at 18:32 UT since the magnetic field configuration at this position on the magnetopause indicates that both the heated populations observed must have been outside the magnetopause.

Thus, at the inferred magnetopause (18:12 UT), a small B_N component, ~ 1 nT, was found. However, the criterion applied from Neugebauer et al., [1984] of $B_N/|B| \geq 0.4$ was not met, suggesting that the magnetopause was not locally open. In addition, the sharp change in plasma density also confirmed that this boundary was locally closed. If

it was open, the leakage of plasma into and out of the magnetosphere would result in approximately constant plasma parameters across the boundary [Sonnerup, 1976].

It was also noted that there was very little change in the magnetic field magnitude across the magnetopause, suggesting that the magnetosheath and magnetospheric magnetic pressures balanced. If this is the case, then the plasma and dynamic pressures will also balance across the boundary (Chapter 1). Using values for the density and temperature in the magnetosheath and magnetosphere, together with the inferred velocity of the bulk magnetosheath flow (339 kms^{-1}), we find that: $P_{Dyn_{SW}} + P_{P_{SW}} = 0.0195nPa > P_{P_{MS}} = 0.0029nPa$. Thus, there was clearly an imbalance between the plasma pressures which suggests that Saturn's magnetopause was not in simple pressure balance with the external plasma and magnetic field at this time. Of course we have not considered any pressure effects due to the internal plasma.

Just prior to the magnetopause crossing, an additional lower-energy electron population appeared at ~ 18:08 UT (Figure 3.7). This is the signature of magnetosheath electrons having entered the magnetosphere and was seen equally in all anodes. From the field of view this equates to a pitch angle range of at least ~ 90° to 180°. Since we infer the magnetopause to be locally closed, it is assumed to have been on field lines that are open elsewhere and adjacent to the magnetopause. The source of these particles can be inferred by calculating the energy increase expected due to the reconnection process if they are on open field lines. Cowley and Owen [1989], considered the theoretical motion of a newly reconnected flux tube across the surface of the magnetopause based on the interplay between the tension in the newly reconnected field line and the magnetosheath flow. They calculated the de Hoffmann-Teller frame for a given flux tube to calculate the resultant velocity of the accelerated boundary layer plasma. Although this analysis is pertinent to ions, the electrons also receive a 'kick' from the field line by the same physical means. Therefore, from the inferred velocities and the known field orientations Equation 3.1 (equation 8b in Cowley and Owen [1989]) can be applied to the data to estimate the velocity of boundary layer particles passing through a reconnection site:

$$\underline{v}_{BL} = \underline{v}_{SH} \pm v_A \left(\hat{\underline{b}}_{BL} - \hat{\underline{b}}_{SH} \right)$$

Equation 3.1

where $\hat{\underline{b}}_{BL}$ and $\hat{\underline{b}}_{SH}$ are the unit vectors of the fields in the boundary layer and magnetosheath respectively. For this region of the magnetosheath, the Alfvén speed was

239 kms^{-1}. If the un-energised magnetosheath electrons had a thermal velocity of ~ 5000 kms^{-1} then, based on the relative field orientations, the expected energy increase is ~ 8 eV. It is clear that such as energy increase would hardly be noticeable in the electrons and thus it is difficult to say for certain that they are heated. They do, however, appear to be a low density equivalent of the local magnetosheath electrons seen after ~ 18:12 UT (in the anti-parallel electron population). Hence, this plasma may have gained entry to the magnetosphere through reconnection at some distant location. Alternatively, the layer could have been generated by some other means, such as inward diffusion through the magnetopause. An ion population was also observed in this layer, but the counts were very low, presumably as the peak of the flow was not in the instrument field of view at this time. There was no change in the field in this layer at ~ 18:11 UT, other than appearing noisier as is indicative of boundary layer [Behannon et al., 1983; Arridge et al., 2006a].

The next change in the plasma at 18:12:40 UT appeared at the start of the magnetopause field rotation, when an abrupt increase in the energised ion counts was detected. These particles were most likely on reconnected field lines outside the magnetopause. The sharp onset of the ions at this time suggests Cassini crossed into a different plasma region. If their appearance was due to the spacecraft motion, it would have been a more gradual appearance as the population came into view, much like the two later ion peaks at ~18:45 and ~19:12 UT. This indicates that there was an ion layer just outside of the magnetopause which, from the instrument pointing, was flowing in a tailward and southward direction. The electrons also showed a density increase, ~ 30 seconds later, toward the end of the field rotation.

In order to explain this observation, we consider a simple particle model of the magnetopause (Figure 1.9) [i.e. Kivelson and Russell, 1995] which suggests that, as the magnetopause is crossed outbound, the magnetosheath ions would be observed first due to their larger gyroradius, enabling them to penetrate further into the current layer. Cassini's orbital velocity across the magnetopause at this time was ~ 4.3 kms^{-1} (the magnetopause speed is unknown); therefore, making the simple assumption that the magnetopause is stationary, we calculate the magnetopause width to be ~ 130 km. This is smaller than the gyroradius of an ion at this location (R_g ~ 760 km). However, the boundary was likely to have been moving relative to the spacecraft resulting in an underestimate of the true width. Another magnetopause model used to infer observations of particle behaviour at a reconnecting magnetopause, as we assume is the case here, is that of Gosling et al., [1990]. Thus, these observations could also be

consistent with the spacecraft encountering an ion layer outside the magnetopause and then, some time later, the electron layer. However, we would still expect to see magnetosheath electrons in the ion layer since they were originally frozen to the magnetosheath field line which has undergone reconnection, which invalidates this explanation. The fact that the main magnetosheath population is not seen until the rotation in the field is complete, may suggest that the electrons have been retarded by the ion population.

Shortly after the MPCL at 18:12 UT, the first population of heated electrons was encountered, starting at ~ 18:16 UT. This population had a maximum energy of ~ 500 eV. The heating initially appeared in the low-energy, dense population and occurred while the rarer, hotter population was still visible. The hotter population is assumed to have leaked out of the magnetosphere at some distant location and therefore was on field lines with one end still connected to the planet and the other in the solar wind. Similar heated electron signatures appeared again starting at ~18:34 UT and ~19:03 UT. The heated populations appeared whenever the spacecraft roll brought parallel pitch angles into the instrument field of view. The fact that the electrons were heated, coupled with their strong field-aligned nature, suggests they originated from a reconnection site and had formed a layer outside the magnetopause on reconnected field lines [Fuselier et al., 1995; Onsager et al, 2001]. The other clue to the nature of the electrons is that no corresponding anti-parallel heated population was observed when the field of view allowed. The observation of this population at three separate times was simply a product of the spacecraft roll bringing the heated, parallel pitch angle population into the instrument field of view.

The second view of this heated electron population visible at ~ 18:34 UT, was very similar in appearance to the first; however the third time this population entered the ELS field of view at 19:03 UT, it was visible only very briefly (~ 2 min compared with the previous ~ 10 minutes). From the pitch angle orientation plots, the instrument was still looking along the field, therefore Cassini may have crossed the last open field line connected to the planet and thus observed a cut-off of the heated population. After this final heated population, the plasma observed was characteristic of unheated magnetosheath at all pitch angles. The magnetosheath distribution at Saturn is found to have the same characteristic 'flat-topped' shape as seen at Earth [Scudder et al., 1973]. The ions were of lower energy than the accelerated beam observed at the magnetopause and they were flowing tailward and northward, consistent with the expected

magnetosheath flow at this location, i.e. above the Sun-Saturn line, on the dawn magnetopause.

Electron population phase-space distributions from different times as the boundary was crossed showed an evolution of the electrons from magnetospheric to magnetosheath via a number of intermediate populations. These layers are suggestive of boundary layer plasma as defined in section 3.2. The density of the boundary layer plasma increased as the magnetopause was approached, in agreement with the expected gradual change of plasma parameters [Eastman and Hones, 1979]. Once outside the magnetopause, the heated population appeared as an enhancement at mid-energies (~ 60 eV to 400 eV), which resulted in the distribution profile lying outside the limits of normal magnetosheath plasma.

In comparing the parallel, perpendicular and anti-parallel flows, the preferential heating in the parallel direction was evident. The perpendicular and anti-parallel populations showed a 'flat-topped' PSD characteristic of undisturbed magnetosheath plasma, thus further suggesting that only the near- parallel population had undergone heating by having passed through a reconnection site, and the perpendicular/anti-parallel pitch angle particles were unheated magnetosheath.

The field-aligned population of heated electrons persisted for ~ one hour and ~ three rolls of the spacecraft. However, during this time the field pointing rotated from [4,4,-3] KSM to [3,4,4] KSM. Thus, there was a change in the field (B_Z) without any noticeable change in the plasma. The observation of heated electrons continued after the field rotation implying that the field line must still have been connected to a reconnection point somewhere on the magnetopause. Therefore, there may have been two distinct sites which were favourable to reconnection in these two field orientations. One way of distinguishing whether there was a change in reconnection site, is to use the ion data to detect any changes in flow directions. However, the only accelerated ion flow observed is at 18:12 UT and was travelling southward and tailward, and is assumed to have originated from the 'first' reconnection site. After this, only the undisturbed magnetosheath ion flow was observed, and no further accelerated beams were detected. Thus we cannot verify a change in the location of reconnection site. The field line geometry may be considered in a qualitative fashion, for the different field orientations:

Southward IMF

From Figure 3.5 the magnetosheath field orientation containing the first accelerated flow at ~ 18:19 UT was southward with $\underline{B}$ = [4,4,-3] nT KSM. The magnetospheric field at this location had an orientation of $\underline{B}$ = [3,3,-4] nT KSM. This is a product of Cassini being below the magnetospheric current sheet or 'magnetodisc' and also due to the known lagging of the magnetospheric field from pure corotation (hence the positive B_X and B_Y components) [Arridge et al., 2006b]. Based on these observed planetary and magnetosheath magnetic fields, as measured by Cassini on the dawn flank at ~ -3° latitude, one region where a near anti-parallel configuration might be encountered is shown in two different views in Figure 3.16.

Figure 3.16 suggests that, based on a small amount of draping round the magnetosphere, together with the sub-corotating (or 'lagging'), southward, magnetospheric field (solid lines), the magnetosheath field (dashed lines) will be roughly anti-parallel to the magnetospheric field in the northern hemisphere on the dawn side, tailward of the cusp. This is tailward and northward of Cassini at this time. We sketch these field orientations in Figure 3.16 and the supposed reconnection site is shown bounded by the box and is further expanded in Figure 3.17.

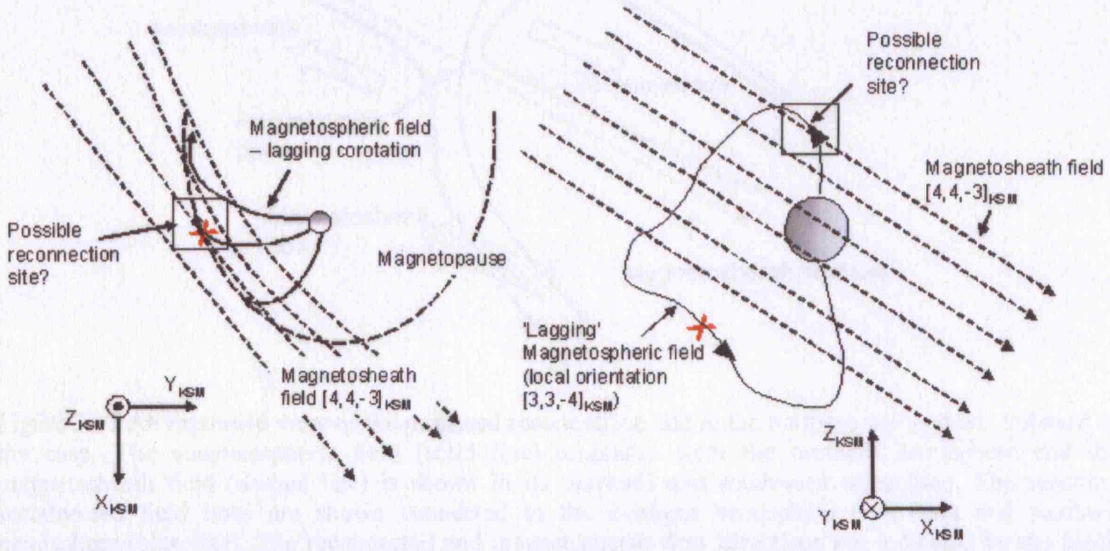

Figure 3.16 Sketch showing field line geometry at the dawn magnetopause based on the orientations of the magnetosheath and magnetospheric fields observed at Cassini. This shows the situation for the interval where the heated population was first observed starting at ~ 18:16 UT after the magnetopause crossing on 17 April 2005. The view on the left is looking down on Saturn's north pole and shows the orientation of the field lines in the northern hemisphere once the sub-corotation (or 'lagging') is taken into account. The magnetopause is marked by the dashed parabola encompassing the magnetospheric field lines and Cassini's position is shown as the red 'X'. The magnetosheath field is in a sunward, duskward and southward orientation. The sketch on the right shows the view looking towards dusk (Y_{KSM}), with the magnetosheath and magnetospheric fields in the orientations shown. The magnetospheric field is modified by the lagging and also the magnetodisc which stresses the field at the equator to result in the tail-like configuration observed. Cassini's position is again marked by the red 'X'. The point at

which reconnection is most likely and is the proposed site of reconnection for this event, is where the magnetosheath field is approximately anti-parallel to the magnetospheric field in the northern hemisphere tailward of the cusp and is bounded by the box. An expanded view of this box is given in Figure 3.17.

The newly reconnected field lines will recoil away from the reconnection site, carrying with them accelerated plasma. A new pair of open magnetic field lines will be created and will now be subject to forcing from both the magnetic tension in the kinked field lines, and from the magnetosheath flow. The conditions on the dawn flank are such that the Alfvén Mach number is ~ 5. The magnetosheath flow is therefore super-Alfvénic and will thus impart substantial forcing tailward to the reconnected field lines. The reconnected field line attached to the southern hemisphere will try to straighten itself by moving tailward, in the same direction as the magnetosheath flow. However, the tension in the newly reconnected field line connected to the planet in the northern hemisphere will act in the opposite direction to the magnetosheath flow, i.e. Sunward (see Figure 3.17). Thus, for this case, the significant tailwards magnetosheath flow will dominate the motion of the field line and will sweep the field line tailward.

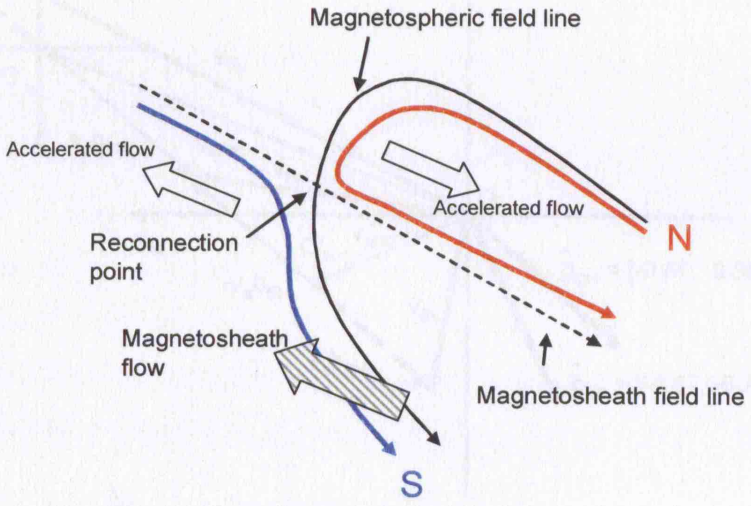

Figure 3.17 An expanded view of the proposed reconnection site in the northern hemisphere, tailward of the cusp. The magnetospheric field (solid line) originates from the northern hemisphere and the magnetosheath field (dashed line) is shown in its Sunward and southward orientation. The resulting reconnected field lines are shown connected to the northern hemisphere (red line) and southern hemisphere (blue line). The reconnected and magnetosheath flow directions are indicated by the block arrows (not to scale).

We can now apply the method from Cowley and Owen [1989] to better understand the motion of the reconnected field lines and plasma flows and then compare the latter with the observed values. We first derive a boundary normal coordinate frame [Russell and Elphic, 1978] using the normal component derived from the MVA of the magnetopause crossing at 18:12 UT. This allows us to transform the field and plasma

flow directions into the magnetopause surface frame. The resultant vectors have been transformed into velocity space and are shown in Figure 3.18.

Consider the observed field orientations, the south and Sunwards magnetospheric ($\hat{\underline{b}}_{SP}$) and magnetosheath ($\hat{\underline{b}}_{SH}$) fields (heavy black arrows) and the magnetosheath flow $\underline{v}_{SH}$ (red arrow) which is flowing northwards and tailwards. We first transform to the rest frame of the field lines connected to the northern (O'_N) and southern hemispheres (O'_S) which is the de Hoffman Teller velocity, $\underline{v}_{dHT}$ (blue arrow). In this frame, the magnetosheath velocity will be seen travelling at the Alfvén velocity in the field aligned direction, i.e. $v_A \underline{b}_{SH}$ due to the field line geometry of the reconnection site (see Figure 3.17). We can then draw the boundary layer flow vector $\underline{v}_{BL}$ (green arrow) since in the de Hoffman-Teller frame its velocity (at the Alfvén speed) is directed along the magnetosheath field (since it is an external layer).

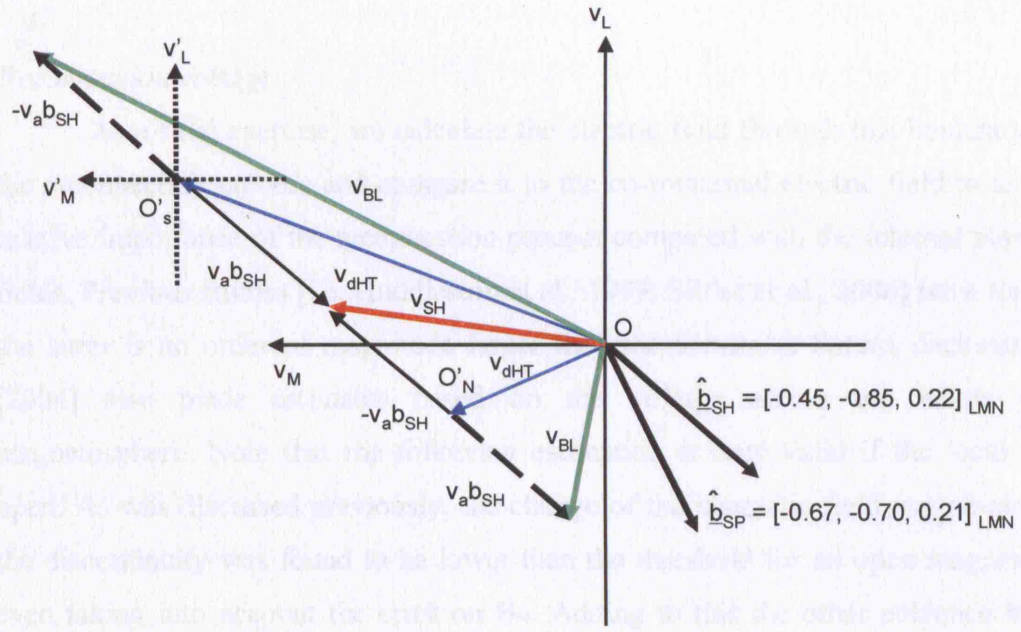

Figure 3.18 Schematic of the observed normalised magnetic field and velocity flow vectorsin a plane tangential to the magnetopause. The magnetic field orientations (heavy black arrows) in the magnetosphere ($\hat{\underline{b}}_{SP}$) and the magnetosheath ($\hat{\underline{b}}_{SH}$) are shown. In Saturn's rest frame (O) the de Hoffman Teller frame (O') for the field lines connected to either hemisphere, is obtained by knowing that the magnetosheath velocity $\underline{v}_{SH}$ must be equal to the Alfvén speed v_A. Once the field line rest frame is derived, we know the electric field is zero, thus there is no acceleration of the plasma, and thus it must flow out of the reconnection site, also at the Alfvén velocity $\pm v_A \underline{b}_{SH}$ (heavy dashed lines). The resultant boundary layer velocity $\hat{\underline{v}}_{BL}$ in the frame of the observer (at Saturn) is then equal to the field line velocity plus the outflowing magnetosheath plasma at the Alfvén speed, $\underline{v}_{BL} = \underline{v}_{dHT} \pm v_A \underline{b}_{SH}$. The field line rest frame connected to the northern and southern hemispheres are denoted by $O'_{S \text{ or } N}$. We can see that the boundary flow connected to the northern hemisphere is travelling in a southwards and slightly tailwards direction similar to that observed.

From Figure 3.18, we know that the boundary layer velocity will be $v_{BL} = v_{dHT} \pm v_A b_{SH}$ and in fact for the northern hemisphere field line we can show that $v_{BL} = v_{SH} + 2v_A b_{SH}$ which results in the boundary layer flow $\hat{\underline{v}}_{BL}$ travelling in a predominately southwards direction as observed.

Northward IMF

Now we consider the likely site of reconnection for the second field orientation, when the magnetosheath field is northward after ~ 18:32 UT. The fact that Cassini continued to observe heated, field-aligned electrons after this rotation is evidence that the field line was continuing to undergo reconnection at some remote site. A northward IMF is expected to be conducive to reconnection at Saturn; therefore it is not hard to envisage reconnection taking place. However, the location of the reconnection site cannot be verified since no further accelerated ion beams are observed.

Reconnection voltage

As a final exercise, we calculate the electric field through this boundary due to the reconnection process and compare it to the co-rotational electric field to assess the relative importance of the reconnection process compared with the internal plasma and fields. Previous studies [i.e. Huddleston et al., 1997; Sittler et al., 2006] have found that the latter is an order of magnitude larger than the former at Saturn. Jackman et al., [2004] also made estimates based on the voltage across the whole dayside magnetosphere. Note that the following estimation is only valid if the local field is open. As was discussed previously, the change of the magnetic field magnitude across the discontinuity was found to be lower than the threshold for an open magnetopause, even taking into account the error on B_N. Adding to this the other evidence from the plasma data, it is assumed that this field is locally closed, or certainly not clearly open. However, a rough order of magnitude of the values can still be estimated using the derived normal component of $B_N \sim 1.2$ nT.

The direction and magnitude of B_N across the MPCL at 18:12 UT are known from MVA and the accelerated ion flow velocity is ~ 437 kms^{-1}. The angle between the velocity and B-field is ~ 84°. The convection electric field $(\underline{v}_{BL} \times \underline{B}_N)$ is therefore = 0.52 mVm^{-1}. This value is of the same order as that estimated by Huddleston et al., [1997] from Voyager 1 data who found a value of ~ 0.2 mVm^{-1} based on B ~ 1 nT and an ion velocity increase of 200 kms^{-1}. It is also comparable to the value calculated by

Jackman et al., [2004], who found values ranging from 0.0828 mVm^{-1} to 0.663 mVm^{-1} based on a dayside reconnection voltages of ~ 10 kV (for weak IMF) to 400 kV (for strong IMF regions) across L_o ~ 10 R_S, bearing in mind the high dynamic pressure during this event. It is, however, larger than the estimate from Sittler et al., [2006] of 20 μVm^{-1}. We find that the convective electric field value is lower than the corotation electric field at the magnetopause $(\underline{v}_{corot} \times \underline{B}_{MP})$ ~ 1.64 mVm^{-1} (at the average magnetopause distance of 26 R_S with |B| ~ 6 nT and assuming strict corotation) which agrees with the findings of Huddleston et al., [1997] and Sittler et al., [2003, 2006]. Therefore, based on estimates of the reconnection voltage supplied by the IMF at a point local to Cassini, external driving to the magnetospheric dynamics is not insignificant. Additionally, the dynamic pressure of the solar wind at this crossing was inferred from the Arridge et al., [2006a] magnetopause model to be 0.094 nPa, with an associated subsolar magnetopause distance of 16.9 R_S. This is one of the largest dynamic pressures (and smallest subsolar distances) inferred for the crossings observed prior to January 2006, suggesting that compressive upstream conditions are conducive to the reconnection processes.

Internally driven reconnection?

Extensive consideration has been given to the likely reconnection scenarios possible with the magnetospheric and magnetosheath fields during this interval. There is no investigation of the possibility of this plasma acceleration being generated by an internally driven reconnection process. As discussed in Chapter 1, there are significant stresses on the magnetospheric field lines caused by the outward motion of plasma from the inner magnetosphere. In the outer magnetosphere this can result in the release of a plasmoid filled with magnetospheric material, which might ultimately impact and break through the magnetopause [Southwood and Kivelson, 2005], thus triggering reconnection of these fields. This may happen on the dawn side if the mass-laden plasmoid rotating around to the dayside can no longer enforce the rotation due to the dayside solar wind pressure. The magnetospheric plasma observed outside the magnetopause in the magnetosheath is consistent with a heated parallel electron flow, rather than a bi-directional flow expected if a plasmoid with a closed field geometry is released. In addition, when the instrument pointing was favourable, the heated plasma was observed for over 30 minutes. During this time (when the anti-parallel population is viewed) the electron characteristics were purely magnetosheath-like, as were the ion populations. There was also no evidence of plasma with a magnetospheric composition

in these regions as would be expected if plasma originating from the inner magnetosphere was being released. To summarise, this reconnection event was clearly driven by the IMF rather than an internal mechanism.

3.5 21 September 2005

On 21 September 2005 Cassini crossed the magnetopause outbound close to the equator (-0.32° KSM) at a Saturn-centric distance of ~ 23 R_S and a local time of 09:03. A sketch of the spacecraft position is shown in Figure 3.19

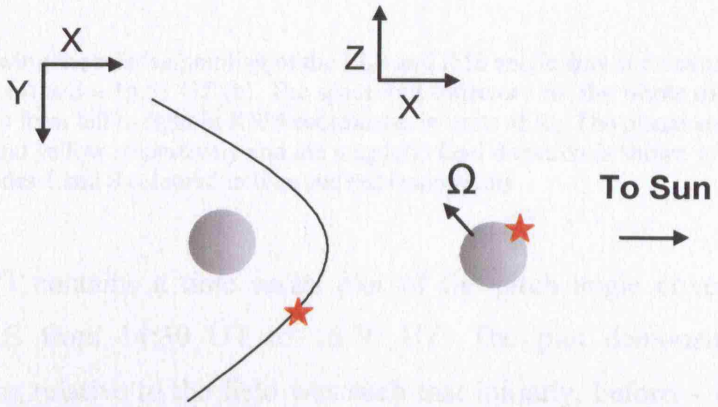

Figure 3.19 Location of Cassini relative to the planet on 21 September 2005. Left: the view in the X-Y_{KSM} plane with the magnetopause indicated by the solid line. Right: the view in the X-Z_{KSM} plane with the rotation, Ω (and magnetic) axis tilted by ~ 21° for this period. In both cases, Cassini's position is indicated by the red star and the Sun is to the right.

3.5.1 Spacecraft motion and instrument pointing

During this interval, the spacecraft attitude was relatively stable and the actuator swept between -60° and + 90° with respect to the spacecraft Y-axis. The platform therefore performed one full sweep in ~ 5 minutes. This resulted in the orientation of CAPS varying between tailward and nearly Sunward-pointing throughout this event. Figure 3.20 shows the pointing of the anode fan at the two extremes of the actuator sweep. Figure 3.20a shows the most tailward orientation, pointing toward a local time of ~ 01:00 and Figure 3.20b shows the most Sunward orientation, toward a local time of ~ 14:00.

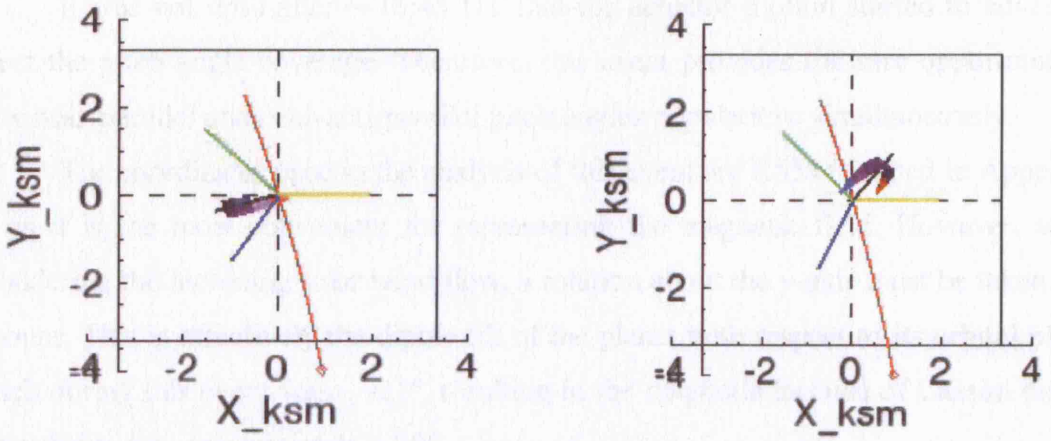

a **b**

Figure 3.20 Plots showing the relative pointing of the ELS and IMS anode fans at extremes of the actuator sweep at ~ 15:48 UT (a) and ~ 15:51 UT (b). The spacecraft trajectory for the whole day (21 September 2005) is marked in red from left to right in KSM coordinates in units of R_S. The planet and sun directional vectors are in green and yellow respectively and the magnetic field direction is shown in blue. The anode fan is drawn with anodes 1 and 8 coloured in blue and red respectively.

Figure 3.21 contains a time series plot of the pitch angle coverage for each anode of the ELS from 14:30 UT to 16:30 UT. The plot demonstrates that the instrument pointing relative to the field was such that initially, before ~ 15:10 UT, the full range of pitch angles was visible with some slight modulation due to the actuator.

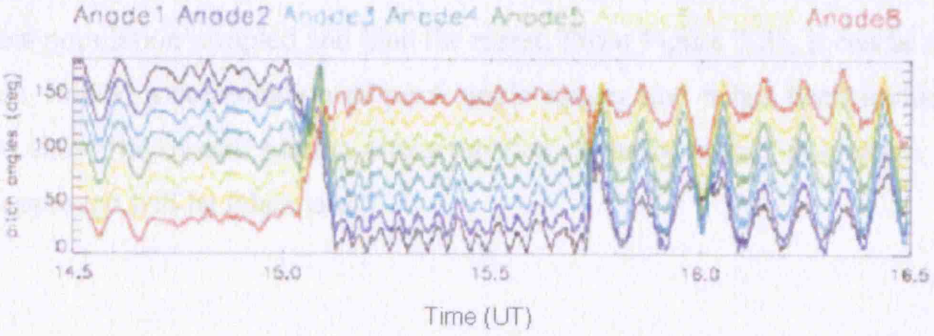

Figure 3.21 The variation over time of pitch angle coverage for each anode. Pitch angle is on the vertical axis and time is along the vertical axis. The coverage for each anode is plotted in a different colour. This shows that during most of this interval there is full pitch angle coverage until ~ 15:45 UT when the field rotation relative to the instrument pointing introduces a more variable coverage. The colours of the anodes are listed along the top of the plot.

Figure 3.21 shows that just after 15:02 UT, there was a significant effect on the pitch angle coverage of most of the anodes individually (since the spacecraft pointing was unchanged, this must have been due to a change in the magnetic field direction), but still resulted in full pitch angle coverage for the instrument. For example, prior to the rotation, anode 1 (black line) was able to view near-anti-parallel pitch angles, but after the rotation this changed to viewing near-parallel pitch angles.

It was not until after ~ 15:45 UT that the actuator motion started to adversely affect the pitch angle coverage. Therefore, this event provides the rare opportunity to view near-parallel and near-anti-parallel pitch angles populations simultaneously.

The coordinates used in the analysis of this event are KSM (defined in Appendix C) as it is the most convenient for representing the magnetic field. However, when considering the incoming solar wind flow, a rotation about the y-axis must be taken into account. This is effectively the dipole tilt of the planet with respect to its orbital plane, which during this event was ~ -21°, resulting in the magnetic latitude of Cassini during this event being approximately + 20°.

3.5.2 Overview of the magnetopause encounter

Now the spacecraft pointing has been established, the data can be introduced. The crossing of interest occurred at ~ 15:02 UT during a series of seven crossings made on the 20 and 21 September 2005. Figure 3.22 shows a two hour data plot providing an overview of the event. Panel a) of Figure 3.22 contains a spectrogram of the electron counts from anode 1 of the ELS, with time on the horizontal axis, energy in $\log_{10}$ eV on the vertical axis and the number of counts indicated by the colour scale, with red being the densest population sampled and blue the rarest. From Figure 3.21, it can be seen that this anode viewed a combination of pitch angle ranges and it has been included here simply to show the overall plasma characteristics as the boundary is crossed. A more detailed approach will be taken later.

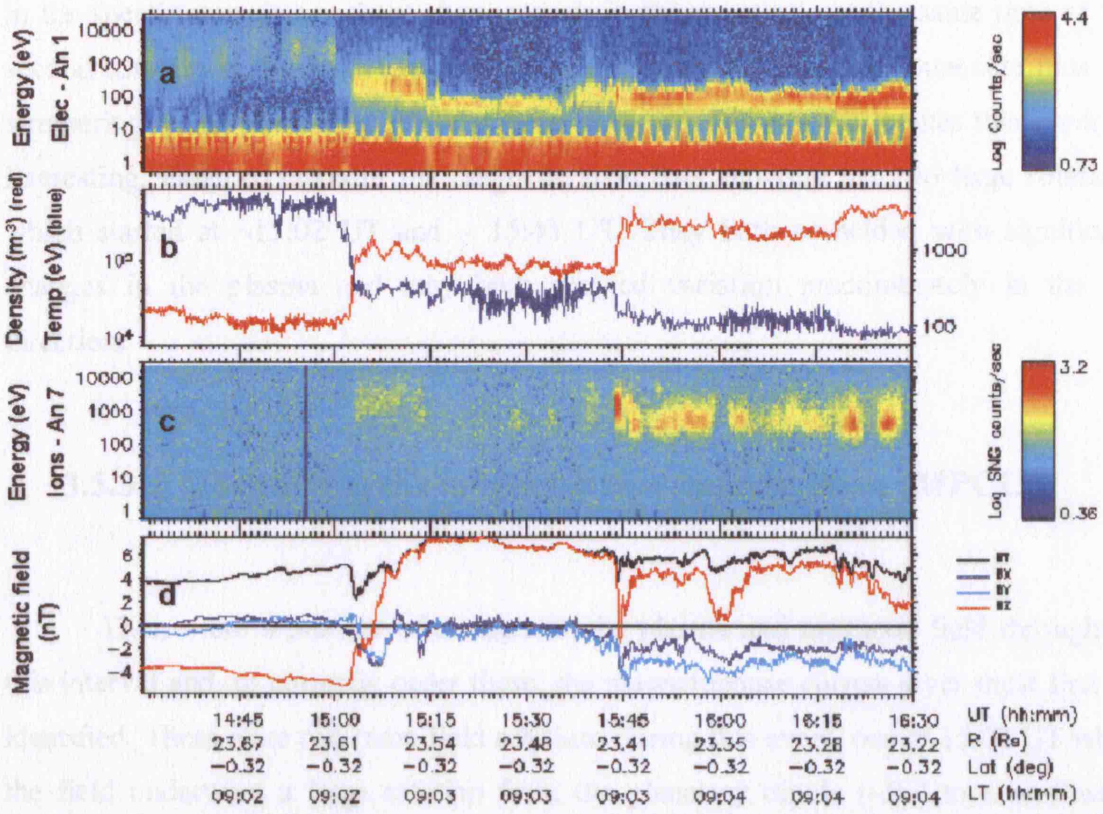

Figure 3.22 Data from 21 September 2005 14:30 UT to 16:30 UT when Cassini was exiting the magnetosphere at the magnetic equator at a local time of ~ 09:02. The CAPS actuator was sweeping between -60° and +80° throughout this period. Panel (a) shows the electron spectrogram for anode 1 of the ELS in the same format as used previously. Initially, Cassini was inside the magnetosphere evidenced by the high energy, rare magnetospheric population. Then there was a clear change in the electron characteristics at ~15:00 UT indicative of a crossing into a magnetosheath-like regime where the electron energy reduced and the density increased, there were further changes in the characteristics of the plasma at 15:15 UT and 15:45 UT until ~16:18 UT when the nature of the plasma appeared to settle. There is also evidence of heated plasma in this external region, which is discussed in more detail in the text. Panel (b) shows the electron density (red) and temperature (blue) confirming the change in electron plasma characteristics at ~ 15:00 UT and again at 15:45 UT and 16:18 UT. Panel (c) contains the ion data from anode 7 of the IMS, the plot is in the same format as that used for the electron data. The ions appeared at ~ 15:02 UT coincident with the time of the first electron transition although only low counts are detected. Later, at ~ 15:45 UT, there is a noticeable increase in the counts and also the population appears accelerated with respect to the rest of the population. Panel (d) contains the three magnetic field vectors, BX_{KSM} (dark blue), BY_{KSM} (light blue) and BZ_{KSM} (red) and the field magnitude, |B| (black). There were two significant magnetic field rotations beginning at ~ 15:02 UT and 15:45 UT.

This interval shows an outbound crossing from rare, hot magnetospheric plasma ($n \sim 2x10^4$ m^{-3}, $T \sim 4000$ eV) into a markedly different plasma regime that is more akin to a magnetosheath population with $n \sim 4x10^5$ m^{-3} and $T \sim 80$ eV. This crossing demonstrates a sharp boundary in the plasma as is obvious from the abrupt increase (decrease) in the density (temperature) in panel (b) and also coincides with a large rotation in the field (panel d). Cassini then appears to enter a magnetosheath-like region, lasting for ~ 15 minutes, before another slight decrease (increase) in the density (temperature) at ~ 15:15 UT. Cassini remains in this region until 15:45 UT when there is another sharp increase (decrease) in the density (temperature). It is here that the ions

in the spectrogram in panel (c) show a peak in the count rate at the same time as the second rotation in the field (panel d). It is this increase in the ion count rate plus the structuring in the plasma regions encountered during this exit that makes this event so interesting. Panel d) contains the magnetic field data showing the two large rotations which started at ~15:02 UT and ~ 15:45 UT. They both coincided with significant changes in the plasma and they both showed variation predominately in the B_Z direction.

3.5.3 Identifying the magnetopause current layer (MPCL)

There were a number of changes in the plasma and magnetic field throughout this interval and, to correctly order these, the magnetopause current layer must first be identified. There were two main field rotations during this event, one at 15:02 UT when the field underwent a large rotation from the planetary dipole ($-B_Z$) to a northward pointing field. The second was at 15:45 UT and was also a rotation predominately in the B_Z direction.

The first rotation lasted ~ 12 minutes during which the field turned from an almost exactly southward pointing field of -5 nT to almost exactly northward with a magnitude of ~ 7 nT. At the start of the rotation at 15:02 UT the field strength initially decreased from ~ 5 nT to ~ 2 nT as the B_Z component started to decrease. Immediately afterward the B_X and B_Y components increased briefly as the field rotation extended into the tailward and dawnward direction and this contributed to the overall field strength. The changes in B_X and B_Y then reached a maximum value before beginning to return to their magnetospheric values of ~ 0 nT. The B_Z component continued to increase before completing the rotation at ~ 15:14 UT. Note that the field was stronger in this region than in the magnetosphere. The MVA was applied to the data from 15:00 UT to 15:15 UT and produced a well determined (λ_2/λ_3 = 13.2) normal $\underline{N}$ = [0.656, -0.752, -0.063] which is reflected in the low angular error ± 0.602°. This result can be seen in Figure 3.23 which shows the line traced out by the end of the field vector in minimum, intermediate and maximum variance-space.

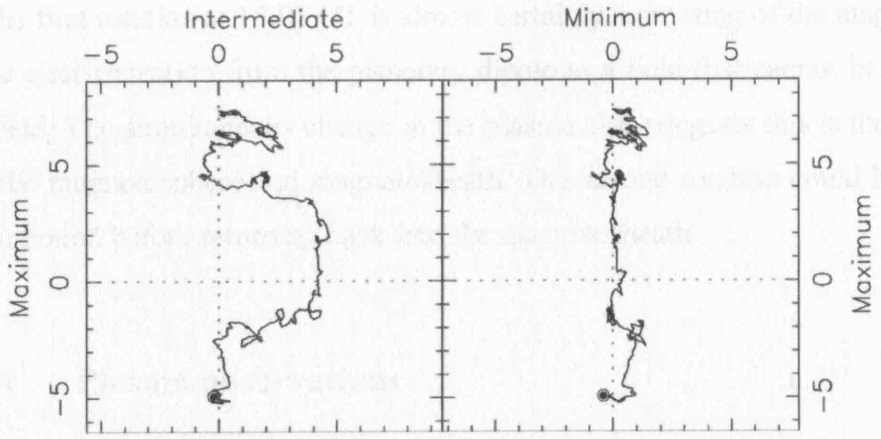

Figure 3.23 Results of the MVA for the magnetic field rotation starting at 15:02 UT. The plots show the trace of the end of the field vector in minimum-, intermediate- and maximum-variance space (nT). It is clear that the minimum component is zero throughout.

It is apparent that the minimum component, identified as the normal component to the magnetopause, is negligible, $B_N \sim 0.0$ nT ± 0.02 nT, throughout the majority of this period. Comparing this to the Arridge et al., [2006a] model normal, $\underline{N}$= [0.864, -0.475, 0.165] indicates that the inferred normal is slightly less sunward and southward pointing than the model normal. The angular difference between these two vectors is 21°.

During the second rotation at 15:45 UT, the B_Z component decreased from 6 nT to 0 nT, became briefly negative, before returning to + 5 nT. At the same time the B_X and B_Y components of the field increased, becoming directed tailward and dawnward. This increase counteracted the large decrease in the B_Z component and the magnitude of the field remained steady. As the B_Z component returned to its northward orientation the B_X and B_Y components reduced slightly, ending in a configuration that pointed northward with B_X and $B_Y \sim 0$ nT. The MVA on this crossing is applied over 15:43 UT to 15:45 UT and provides a reasonably well-determined normal with $\lambda_2/\lambda_3 \sim 15$ and $\underline{N}$ = [0.928, 0.278, -0.248] (with an angular error of 1.47°). Comparing this to the Arridge et al., [2006a] model normal: $\underline{N}$ = [0.865, , 0.473, 0.166] gives a 51° angular disagreement with the minimum variance vector which is more sunward pointing than the model normal. The MVA frame provides a finite B_N component of ~ + 2.0 to 2.8 nT ± 0.05 nT which, from the criteria applied previously, indicates that the field encountered here was locally open and is pointing outwards. The final orientation of the field was northward, slightly tailward and dawnward, which is assumed to be the local orientation of the magnetosheath field. In comparing the magnetospheric and the magnetosheath fields, this crossing outbound was found to be very high shear, ~ 149°.

The first rotation at 15:02 UT is almost certainly a crossing of the magnetopause due to the clear transition from the planetary dipole to a field that cannot be due to the internal field. The simultaneous change in the plasma also suggests this is the boundary between the magnetosphere and magnetosheath. The second rotation could be a partial crossing inbound before returning back into the magnetosheath.

3.5.4 Plasma observations

From the electron and ion data in Figure 3.22, Cassini appeared to encounter several distinct plasma regions as it left the magnetosphere. To aid in the interpretation of this event, the pitch angles of the different electron populations are examined. Figure 3.24 contains three electron spectrograms for anodes 1, 5 and 7 (panels a to c). The different plasma regions have been labelled to aid in the descriptions. Panel (d) contains a time series plot of the anode orientation where the anodes are listed on the vertical axis and the colour scale indicates the pitch angle coverage. Panel (e) contains the magnetic field data. Note the continued coverage of the majority of the pitch angle range from 14:30 UT to 15:45 UT. The choice of the anodes in panels (a) to (c) is made on the basis that from 14:30 UT to ~ 15:02 UT anode 1 provided a view of near anti-parallel populations, anode 5 perpendicular, and anode 7 parallel populations. After the first field rotation at ~ 15:02 UT, this changed to anode 1 viewing near parallel and anode 7 viewing near anti-parallel populations, with anode 5 still observing the perpendicular electrons (apart from a brief period when the instrument could not view the parallel population between 15:05 UT to 15:07 UT). After ~ 15:45 UT the pitch angle coverage varied due to the field orientation relative to the actuator motion, but there was still a good coverage of most of the population.

From Figure 3.24, Cassini is initially in the outer magnetosphere (region 1), where the plasma encountered is rare and hot. From panels (a-c) there appear to be greater counts in the near- anti-parallel direction (anode 1) compared with the other directions. Additionally, when the count rate drops in the near-antiparallel direction i.e. between 14:32 UT – 14:34 UT, there was a slight increase in the count rate in the near-parallel direction. This weak anti-correlation did not continue to the magnetopause.

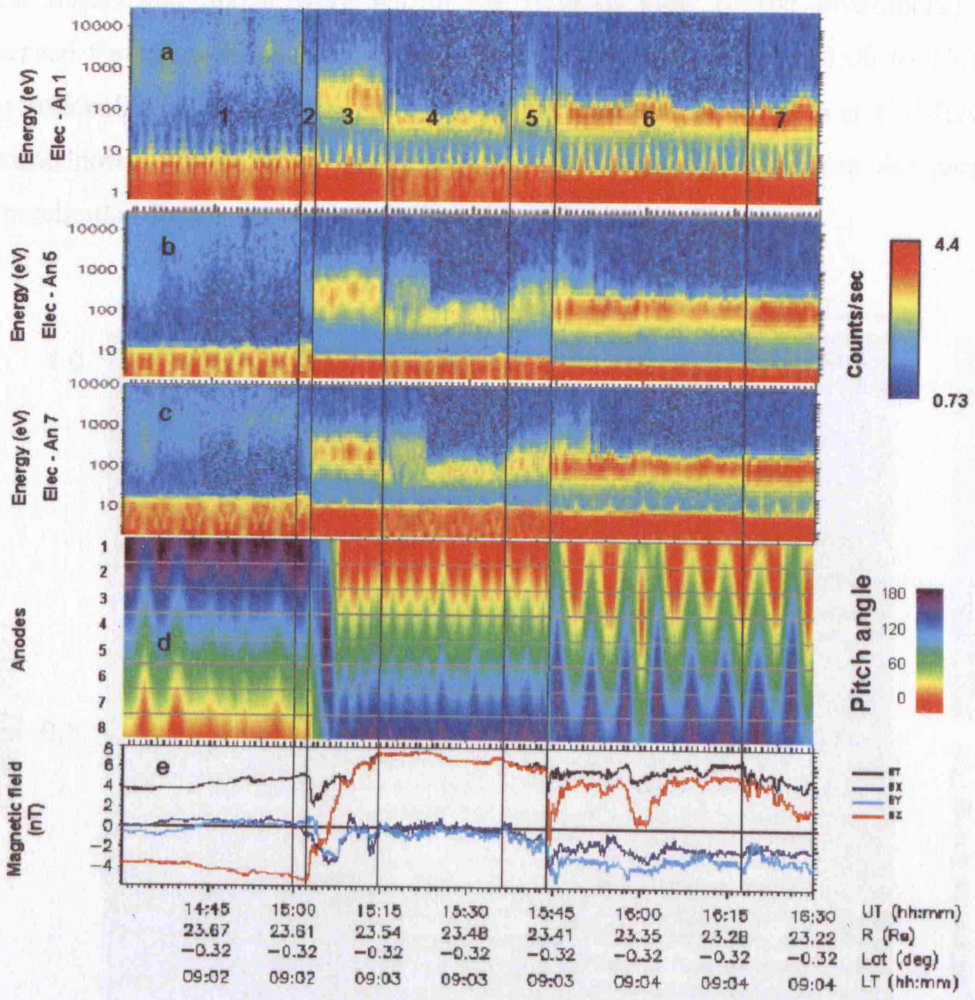

Figure 3.24 Spectrograms viewing populations at different pitch angles . Panels (a–c) contain spectrograms (in the same format as used before) for anodes 1 (~ anti-parallel until 15:02 UT then ~ parallel), 5 (~ perpendicular) and 7 (~ parallel until ~ 15:02 UT then ~ anti-parallel) of the ELS. The structure in the plasma regions is evident and each of the regions labelled from 1 to 7 are described in the text. Panel (d) contains the pitch angle coverage for each anode as a time series in the same format as used before. Panel (e) contains the three magnetic field vectors, BX_{KSM} (dark blue), BY_{KSM} (light blue) and BZ_{KSM} (red) and the field magnitude, |B| (black). Note the continuity in the full pitch angle coverage even after the MPCL at 15:02 UT. This permits the parallel and anti-parallel flows to be compared simultaneously.

A pitch angle plot for this period is shown in Figure 3.25 for electrons of energy 11 eV to 1100 eV (to focus on the main energy range containing the populations of interest). The bi-directional population in the magnetosphere prior to ~ 15:00 UT is noticeable. Just two minutes before the magnetopause crossing at 15:02 UT, this high energy population disappeared and a cooler (~ 300 eV), still rare population was briefly observed (region 2).

The field rotation associated with the MPCL began at 15:02:30 UT, the plasma density increased from ~ 2×10^4 m^{-3} to 3 $\times 10^4$ m^{-3} and the temperature decreased from ~1500 eV to ~ 300 eV (regions 2 and 3) (not shown). This denser plasma appears to be isotropic (apart from the brief interval between ~ 15:04 UT to 15:07 UT when only 90°

pitch angles and above were within the field of view of the instrument) and was observed throughout the field rotation. The isotropy between ~ 15:00 to 15:15 UT is also noticeable in Figure 3.25. Once the field completed the rotation at 15:14:20 UT and became northward-directed, the dense population disappeared from the parallel and perpendicular directions, slightly before the anti-parallel direction.

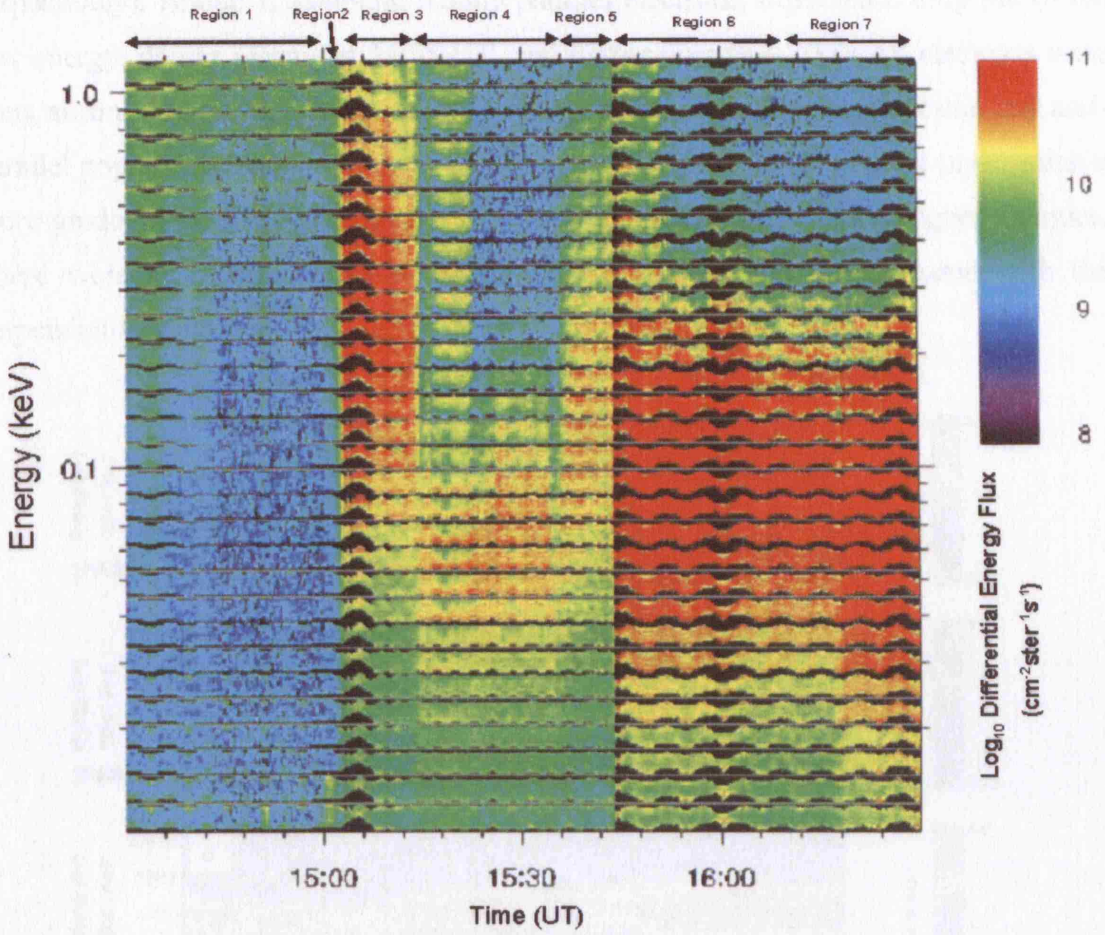

Figure 3.25 Pitch angle plot for 14:30 UT to 16:30 UT on 21 September 2005. Time is along the horizontal axis, energy is on the vertical axis in keV from 11 eV to 1100 eV (to cover the energy range of interest), and the colour scale indicates the differential energy flux. Each of the energy bins is divided into 15 pitch angle bins (with 12° per division) to show the differential energy flux at each pitch angle with 0° at the bottom of the bin and 180° at the top. The regions identified in Figure 3.24 are labelled across the top of the plot.

In region 4, the energy of the population decreased to ~ 80 eV and the width in energy of the population reduced. This denser, ~ 7 x10^4 m^{-3}, plasma, was initially observed in all pitch angle directions. Then, at 15:15:40 UT a brief peak in the energy of the parallel electrons was observed. At 15:16:40 UT this low energy, denser isotropic plasma disappeared and rare, heated plasma (~ 100's eV) was observed until 15:22:30 UT in the perpendicular and anti-parallel directions only. After this time, the heated plasma disappeared and each anode once again observed the low energy, dense isotropic

plasma as seen throughout this period in anode 1 (parallel), with perhaps slightly more counts in the field-aligned directions.

The next significant change occurred at 15:35 UT (just prior to entry into region 5 at 15:36 UT). This region is shown in three spectrograms in Figure 3.26 covering the period from 15:30 UT to 15:50 UT for anodes 1, 5 and 7 (panels a, b and c respectively). Anode 1, sampling mainly parallel electrons, observed a drop out of the low energy, denser plasma at 15:35 UT, and higher energy ~ 100's eV electrons were seen, at times co-existing with the lower energy population. The perpendicular and anti-parallel populations show a more abrupt change at ~ 15:36:10 UT, before undergoing a more gradual transition to a broader distribution extending to slightly higher energies. There were also stronger fluxes in the field-aligned directions compared with the perpendicular direction.

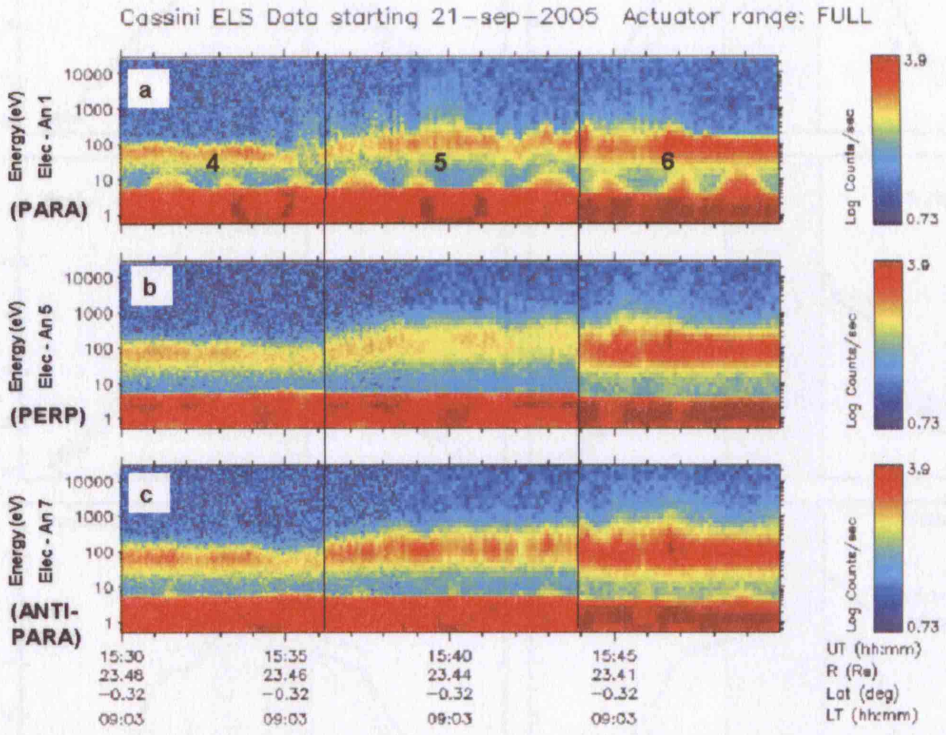

Figure 3.26 A subset of data from Figure 3.24 containing spectrograms from anodes 1, 5 and 7 (panels a, b and c respectively) for the interval from 15:30 UT to 16:00 UT. This plot shows a closer look at three of the numbered plasma regions 4, 5 and 6 and the disturbed nature of the plasma is especially apparent in anode 1 (parallel).

At ~ 15:44 UT there was a transition into region 6 and denser, cooler plasma (see panel (b) in Figure 3.22), although there was once more a rare, heated tail of the plasma population in the anti-parallel direction which is absent in the parallel direction. Finally, at ~ 16:16 UT, there was an increase in the density and a decrease in the temperature of the electrons (labelled region 7). Previously, upon inspection of the

magnetic field, the first rotation at 15:02 UT was thought to almost certainly be a crossing of the magnetopause due to the clear transition from the planetary dipole to a field that cannot be due to the internal field. The simultaneous change in the plasma also suggested that it was the boundary between the magnetosphere and magnetosheath. The observation of isotropic plasma from ~ 15:22 to ~15:44 UT now substantiates this interpretation that Cassini is outside the magnetopause for this period. It indicates that the second rotation could be a partial crossing inbound before returning back into the magnetosheath.

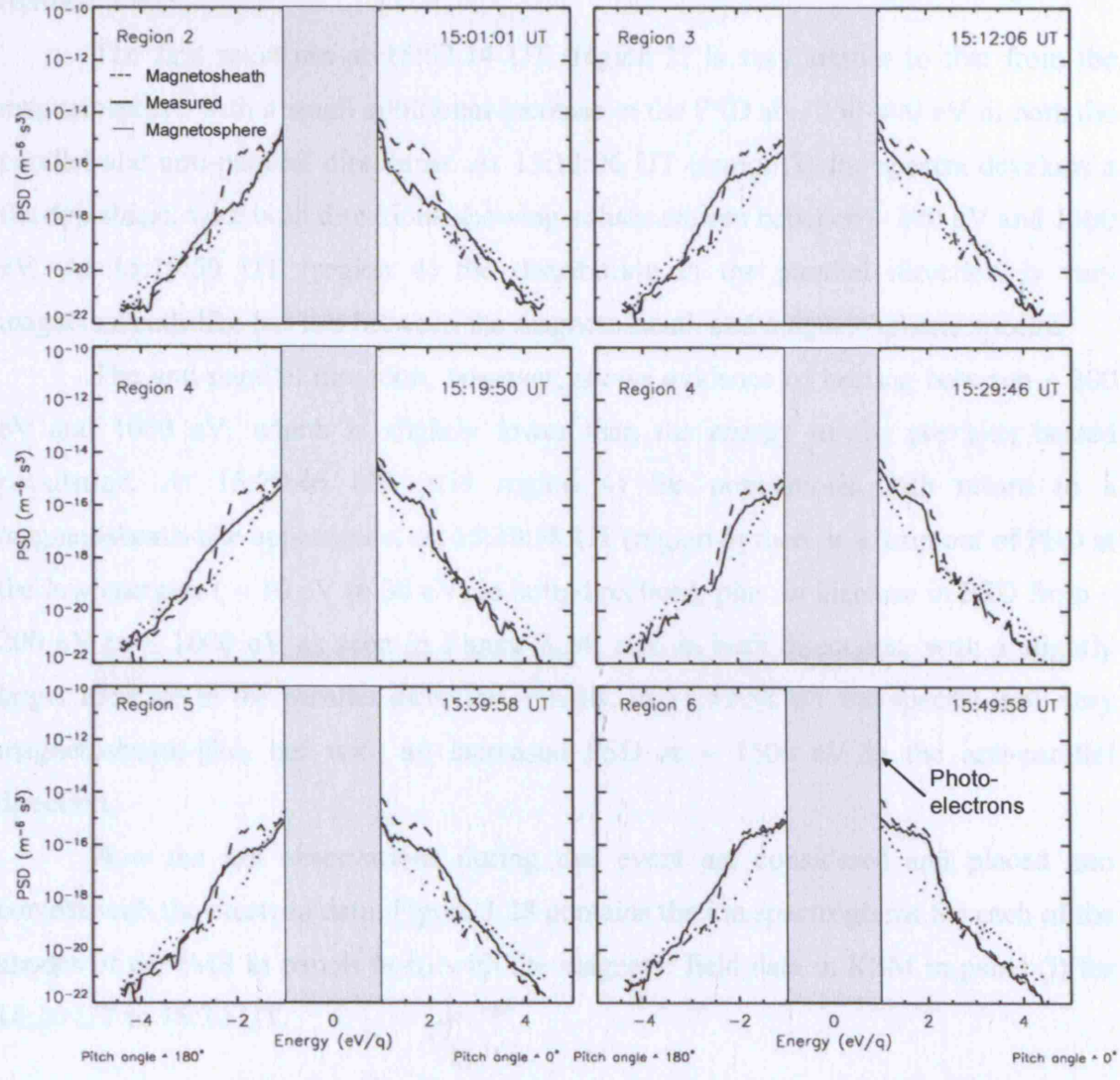

Figure 3.27 PSD distribution spectra from each of the regions marked in Figure 3.24 with PSD on the vertical axis and energy in $\log_{10}$ eV on the horizontal axis. In each plot the spectra of interest from each of the numbered regions has been plotted (dashed line), together with the 'pure' magnetospheric spectra (dotted line) and the spectra in the magnetosheath (solid line). The parallel populations are on the right and the anti-parallel on the left. Descriptions and comparisons of each of the populations are described in the text.

In order to further compare the different electron populations in each region identified in Figure 3.24, the PSD can be plotted for the direction parallel and anti-parallel to the magnetic field. Figure 3.27 contains six plots at different times showing the PSD in the parallel and anti-parallel directions. Energy is on the horizontal axis and PSD is on the vertical axis. These plots allow the parallel and anti-parallel populations to be visualised (right and left hand side respectively). In each case, the typical spectra from the magnetosphere (at 14:56:46 UT –dotted line) and the magnetosheath (at 16:23:02 UT – solid line) have also been plotted along with the spectrum of interest (dashed line).

The first spectrum at 15:02:14 UT (region 2) is very similar to that from the magnetosphere with a small additional increase in the PSD at ~ 250-400 eV in both the parallel and anti-parallel directions. At 15:12:06 UT (region 3) the spectra develops a flat-top shape, with both directions showing enhancements between ~ 200 eV and 1300 eV. At 15:19:50 UT (region 4) the distribution in the parallel direction is very magnetosheath-like but lies between the magnetosheath and magnetospheric spectra.

The anti-parallel direction, however, shows evidence of heating between ~ 300 eV and 1000 eV, which is slightly lower than the energy of the previous heated population. At 15:29:46 UT (still region 4) the populations both return to a magnetosheath-like appearance. At 15:39:58 UT (region 6) there is a drop out of PSD at the low energies (~ 10 eV to 30 eV) in both directions, plus an increase in PSD from ~ 200 eV to ~ 1000 eV as seen in Figure 3.24, also in both directions, with a slightly larger increase in the parallel direction. Finally, at 15:49:58 UT the spectra look very magnetosheath-like, but with an increased PSD at ~ 1500 eV in the anti-parallel direction.

Now the ion observations during this event are considered and placed into context with the electron data. Figure 3.28 contains the ion spectrograms for each of the anodes of the IMS in panels (a-h) with the magnetic field data in KSM in panel (i) for 14:30 UT to 16:30 UT.

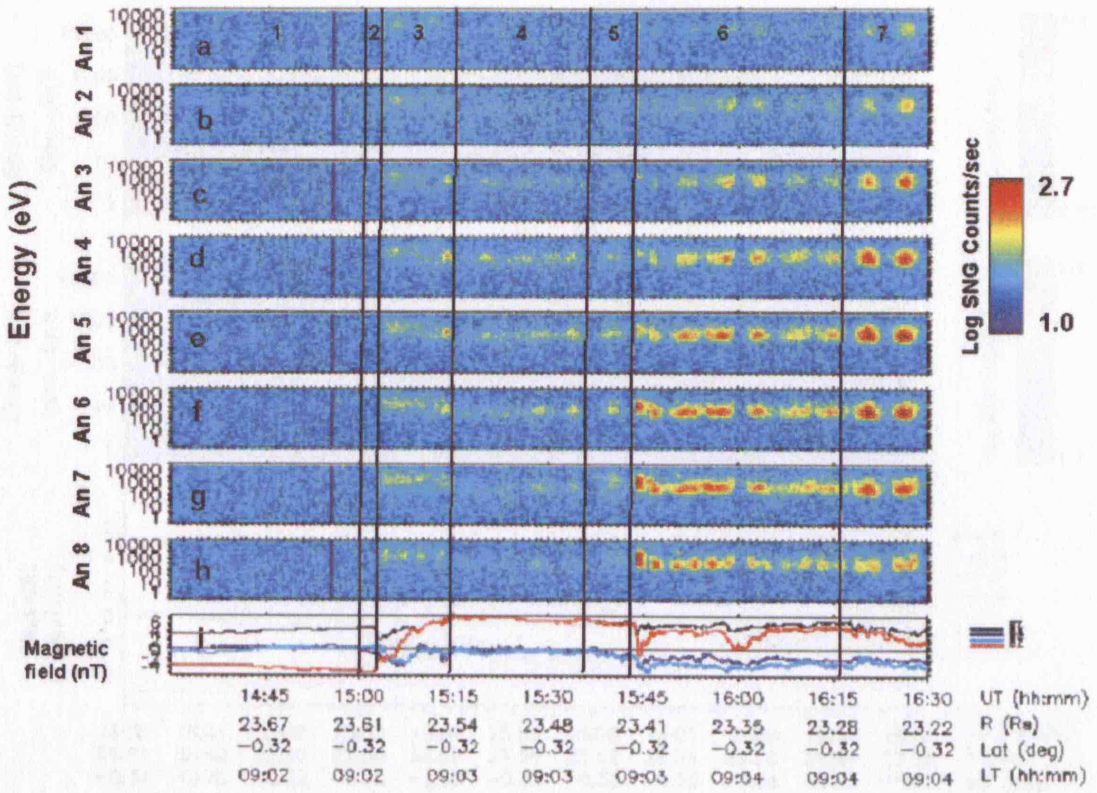

Figure 3.28 Ion spectrograms are plotted for anodes 1- 8 in panels (a-h) in the same format used previously. Panel (i) contains the three magnetic field vectors, B_{XKSM} (dark blue), B_{YKSM} (light blue) and B_{ZKSM} (red) and the field magnitude, |B| (black). The varying structure in the plasma regions is apparent as the magnetopause is crossed. No ions were detected in the magnetosphere, probably due to pointing of the instrument. Upon crossing the MPCL at 15:02 UT heated ions were observed. From 15:15 UT to 15:44 UT there were low energy ions observed until ~15:45 UT when a clear, bright peak was observed in the ions in anodes 6, 7 and 8. The regions identified in Figure 3.24 are indicated.

No ions were seen in the magnetosphere prior to 15:02 UT. This was most likely due to the pointing of the instrument at this time being unable to view the ion flow in any boundary layer or in any corotating magnetospheric population. The MPCL was crossed at 15:02:50 UT when the electron flux increased and the ions appeared a short while later at ~15:03:20 UT. This offset in the appearance of the electrons and ions is shown in Figure 3.29 which contains the spectrograms for the ELS anode 5 (panel a) and the IMS anode 8 (panel b) plus the magnetic field data (panel c). At this point, the population was flowing Sunward, dawnward and northward. From 15:00 UT to 15:15 UT (region 3) heated ions (~ 1000 eV) were detected with the peak flow directed northward, dawnward and either Sunward or tailward (both are observed). From 15:15 UT to 15:23 UT (electron region labelled 4) when energised electrons appeared in the anti-parallel direction, the ion count rate was low, apart from a slight enhancement in anode 4 at 15:19 UT which was observing a Sunward and slightly northward flow.

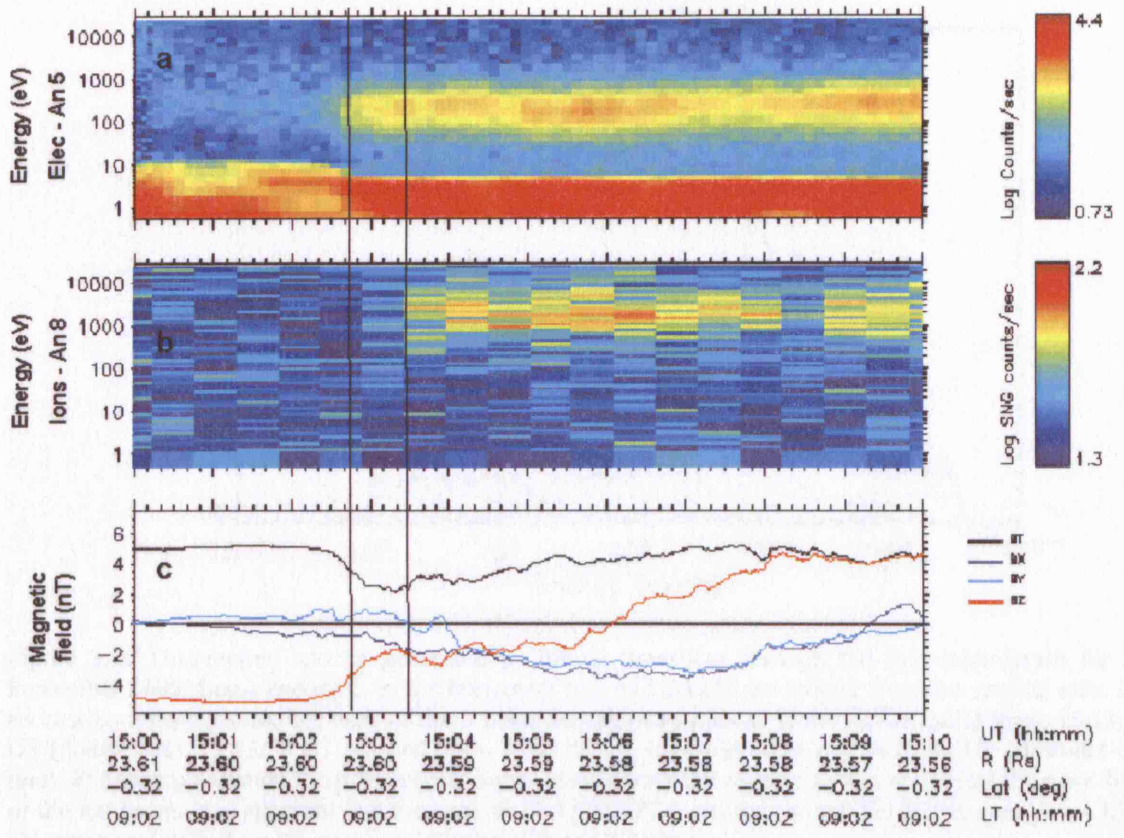

Figure 3.29 Zoom in of the event Spectrograms for the electrons, anode 5 (panel a), ions, anode 8 (panel b) and the magnetic field data (panel c) from 15:00 UT to 15:10 UT (regions 2 and 3). The onset of the denser electrons is apparent at ~ 15:02:50 UT (first line) but the ions do not appear until ~ 30 seconds later at 15:30:20 UT, after the start of the field rotation.

From ~ 15:30 UT to 15:45 UT (electron regions labelled 4 to 6), the ion spectrograms in Figure 3.28 show consecutive peaks and troughs in the ion counts. This is due to the actuator motion moving the field of view of the instrument in and out of the peak flow direction which appears to be predominatly in a tailward direction.

The next interval from 15:45 to ~ 16:30 UT (electron regions labelled 6 and 7) began with a very intense ion count rate and a noticeably accelerated peak at 15:44 UT in anodes 6, 7 and 8. From the anode pointing, these ions were flowing northward, dawnward and Sunward with a velocity vector ~ $[0.3,-0.1, 0.9]_{KSM}$. The following peaks also mainly appeared in anode 8 but they originated Sunward of Cassini. After ~ 16:00 UT there was a change in the nature of the ions observed, with less counts detected in the peaks although the pointing remained the same. At ~16:19 UT there was another increase in the ion count rate, with the peak of the flow appearing in anodes 4, 5 and 6. This indicates a tailward, dawnward and roughly equatorial flow direction.

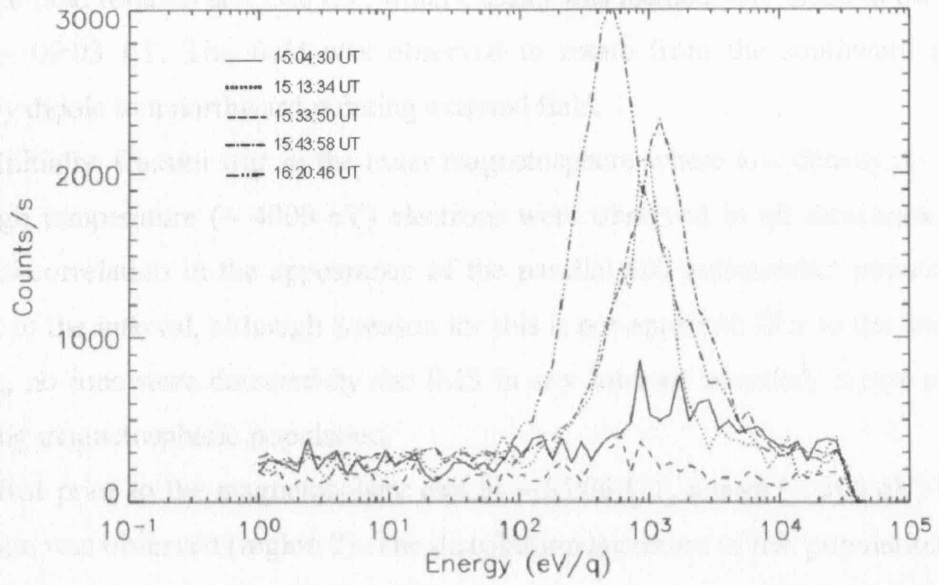

Figure 3.30 Distribution spectra generated by taking timeslices through the ion spectrogram for 21 September 2005. Log_{10} energy is on the horizontal axis and counts per second is on the vertical axis. Ion spectra have been plotted for each of the 5 main ion regions peaks at 15:04:30 UT (solid line), 15.13:34 UT (dotted line), 15:33:50 UT (dashed line), 15:43:58 UT (dash-dot line) and 16:20:46 UT (dash-dot-dot line). For each population the point of maximum counts has been chosen as this represents the peak flow of the ion beam. It is apparent that the peak at 15:43:58 UT is shifted toward the higher energies ~ 1500 eV, compared with the peak energy of the rest of the populations.

To compare these ion populations directly, Figure 3.30 contains time slices through the energy spectrograms at the centre of each of the ion peaks from Figure 3.28 at 15:04:30 UT, 15.13:34 UT, 15:33:50 UT, 15:43:58 UT and 16:20:46 UT. It is clear that the peak at ~ 15:44 UT is shifted toward the higher energies compared with the other peaks, with an energy of ~ 1500 eV. The populations in the interval from 15:02 to 15:15 UT have peak energies of ~ 1000 eV, from 15:30 to 15:45 UT the energy is about ~ 600 eV and finally, the last population to be sampled at ~ 16:20 UT has energy of ~ 500 eV. Note that the peak energies for the populations observed at 15:02 and 15:34 UT are not as obvious as for the other populations due to the low count rates.

3.5.5 Discussion

A magnetopause crossing on 21 September 2005 has been analysed utilising both plasma (electrons and ions) and magnetic field data. This event was selected since it showed a series of structured plasma regions during the exit from the magnetosphere with clear evidence of acceleration in the ion data. It also provided simultaneous sampling of the full range of pitch angle populations. The MPCL was identified as the

first large field rotation at 15:02 UT, when Cassini was located very close to the equator and at ~ 09:03 LT. The field was observed to rotate from the southward pointing planetary dipole to a northward pointing external field.

Initially, Cassini was in the outer magnetosphere where low density, (~ 2 x 10^4 m^{-3}), high temperature (~ 4000 eV) electrons were observed in all directions, with a brief anti-correlation in the appearance of the parallel and anti-parallel populations at the start of the interval, although a reason for this is not apparent. Due to the instrument pointing, no ions were detected by the IMS in any internal boundary layers or in the corotating magnetospheric population.

Just prior to the magnetosphere exit at ~ 15:00 UT, a cool (~ 300 eV) electron population was observed (region 2). The distribution spectrum of this population is very similar to that of the magnetosphere with the addition of a reduced PSD at energies > ~ 1000 eV and an increase at energies ~ 250 eV to 400 eV suggestive of the observation of cool magnetosheath electrons inside the magnetopause. From the spectra this appeared to be rare boundary layer plasma since the density was ~ 3 x 10^4 m^{-3} which is low compared with typical boundary layer at Earth, whose density is usually closer to that of the magnetosheath [Haerendel et al., 1978].

At 15:02 UT (the start of region 3), the magnetic field began its ~12 minute rotation from southward to northward, representative of crossing a very high shear MPCL. The count rate of ~ 300 eV electrons increased at ~ 15:02:40 UT, followed by an increase in the intensity of heated ions (~ 1000 eV), ~ 30 seconds later. Upon inspection of the instrument pointing for this period, it was found to initially point tailward. The ions came into view when the anode fan moved only very slightly to point in a more dawnward direction. If this population had been present previously it would have been seen throughout this period, since the angular range covered by the populations observed were generally wider than this change in pointing. This suggested that the population was initially absent rather than the instrument not being able to detect the ions. This delay in the ions is typical of dispersion or the 'velocity filter effect' at a reconnecting magnetopause [Gosling et al., 1990].

The energised plasma encountered in region 3 (within the MPCL itself, 15:02 UT to 15:14 UT) was more magnetosheath-like, with a density that is consistent with boundary layer plasma. Increases in the PSD were observed equally in all directions, suggesting that these electrons had passed through a reconnection site, mirrored in the low-altitude magnetosphere and were returning to the spacecraft in the parallel direction. From 15:00 UT to 15:15 UT heated ions (~ 1000 eV) were detected with the

peak flow directed northward, dawnward and either Sunward or tailward (both are observed), although there was a slightly higher count rate when the flow was tailward. The observed magnetosheath flow directions were found to agree with the expected flow at this local time and latitude, i.e. tangential to the magnetopause. Thus, the expected flow would be northward and tailward. The amount of the flow in the dawn-dusk direction would depend on the local orientation of the magnetopause. A bright peak in the ion count rate was seen in anodes 4 and 5 at ~ 15:14 UT, implying a Sunward, duskward and northward flow.

MVA applied to this rotation found that it was a tangential discontinuity, i.e. B_N ~ 0 nT, suggestive of a locally closed magnetopause. Thus, the internal electron boundary layer observed could be originating from a distant reconnection site southward of the spacecraft (based on the flow directions observed above). In looking for a site which is conducive to reconnection, the magnetic field would appear to offer an ideal configuration, with almost exactly anti-parallel magnetosphere and magnetosheath fields. The fact that reconnection was not occurring locally, may be because the fields had reconnected elsewhere, probably southward of Cassini's location, which changed the conditions along the magnetopause and kept the reconnection point localised. The MVA produced a normal that pointed more dawnward than the model predicted, suggesting a less flared magnetopause. In addition the MVA unit normal had a Z-component of -0.248 KSM whereas the model indicated that this should be ~ 0.0 KSM. This displacement could have arisen from wave motion or other surface disturbance.

At 15:14 UT the field rotation ended and the bi-directional, energised population disappeared. This marked the start of region 4. Initially, for a brief interval only, magnetosheath-like electrons were detected in both field-aligned directions until ~ 15:16 UT, when an energised population appeared in the anti-parallel direction only. The observation of accelerated electrons in one direction together with colder, magnetosheath-like electrons in the opposite direction is an unambiguous signature that the spacecraft was outside the magnetosphere [Lavraud et al., 2005] and located on a reconnected field line. Here the magnetosheath field was northward, thus an energised population of electrons in the anti-parallel direction indicated that Cassini was southward of the reconnection site. During this period, the ion flow was generally very weak. The highest count rate is seen in anode 4, corresponding to ions originating below Cassini.

At 15:23 UT (still in region 4) the energetic population in the anti-parallel direction disappeared as Cassini most likely lost connection with the reconnected field line. Cold, rare, magnetosheath-like plasma was then observed in both directions for the next ~ 12 minutes. The energy of the ions seen in this layer reduced to ~ 600 eV, (similar to the magnetosheath) which indicates that these ions had not been accelerated downstream of a reconnection site.

During the period 15:15 UT – 15:45 UT (region 4 and 5) the magnetic field adopted a smoother configuration (relative to the magnetosheath field observed after ~ 15:45 UT) with a larger field strength than that observed in the magnetosphere (7 nT compared with 5 nT). This could have been the result of magnetic field pile-up (with an increase of ~ 40%) occurring on the dayside magnetosphere akin to a plasma depletion layer (PDL) [Zwan and Wolf, 1976]. The low density is consistent with plasma being pushed away from the site of high field strength (~ 16% reduction). Since we believe that reconnection was occurring at some nearby location on the magnetopause, this PDL may be formed in a manner similar to that reported by Maynard et al., [2004], where flux pile-up occurs as the reconnection process cannot erode the incoming solar wind flux fast enough (see chapter 4).

The next change in the plasma occurs at ~ 15:36 UT (region 5) resulted in Cassini observing a more disturbed magnetosheath-like plasma in both directions, with a reduction in the PSD at lower energies (~ 20 eV). Additionally, the populations appeared to widen in energy compared with the previous boundary layer distributions. There appeared to be no change in the ions in this interval. There was also an increase in PSD at energies of ~ 200 to ~ 1000 eV which could have been due to heated magnetosheath or escaping magnetospheric electrons and this was slightly larger in the parallel direction which suggests that Cassini was now above the reconnection site.

At ~ 15:45 UT the field then underwent a second rotation. This was suggestive of a partial re-entry into the magnetosphere since the B_Z component reduced from strongly northward to slightly southward (akin to the planetary field) then returned to northward pointing with a more tailward and dawnward direction. The MVA on this crossing produced a normal which was deflected 56° from the model normal and 65° from the normal derived for the MPCL at 15:02 UT. The field was found to be locally open with $B_N \sim +2$ nT ± 0.05 nT, thus, the deflected normal could have arisen from the change in magnetic topology due to reconnection. It is possible that this rotation was simply a RD in the solar wind, although the corresponding change in the plasma characteristics would suggest that this was a rotation associated with the magnetopause.

As Cassini traversed the second field rotation (into region 6) there was a noticeable entry into denser (3 x 10^5 m^{-3}), more magnetosheath-like plasma. However, with an open boundary one would expect to see a more gradual transition of the plasma across the regions. The presence of rarer, hotter plasma, suggestive of escaping magnetospheric plasma agrees with the locally open nature of the field. Note that this was slightly enhanced in both field-aligned directions, which could indicate a reconnection site either above or below Cassini. The positive sign of B_N indicated that Cassini was still above the reconnection site. At this field rotation, accelerated ions (~ 1500 eV) were observed flowing northward past the spacecraft in a northward direction ~ $[0.4, -0.1, 0.9]_{KSM}$, at the point of the partial entry into the magnetopause, which is expected if Cassini was northward of the reconnection site.

In region 6, magnetosheath-like plasma was seen in both field-aligned directions but with an additional component at ~ 1-1.5 keV in the anti-parallel direction. This now indicates that the reconnection site was above Cassini. Although the ion flow was still originating south of the spacecraft, it was no longer energised and E ~ 400 eV. There was a final transition in the density and temperature at ~16:20 UT before Cassini entered the magnetosheath-proper (labelled region 7) as is clear from the PSD spectral shape with the characteristic flat-top. The inferred flow direction gave a velocity unit vector of ~ $[-0.7,-0.7, 0.1]_{KSM}$. The field line geometry in the frame tangential to the magnetopause is now considered to try and better understand the processes occurring.

Northward IMF

The interchange between observing heated parallel and anti-parallel electron populations, together with the flow directions of heated ions and the sign of the normal component at the reconnecting magnetopause, indicates that not only was reconnection occurring during this magnetopause crossing, but that the reconnection site must be sporadic both in time and location. This is most likely driven by short timescale fluctuations of the IMF north-south component which has been shown to occur on the timescale of minutes at Saturn [Jackman et al., 2004]. This is one apparent explanation of the intervals of energised plasma observed in both the field-aligned flow directions. In addition, due to the high-shear nature of this magnetopause, reconnection could be favourable over a large area of the magnetopause.

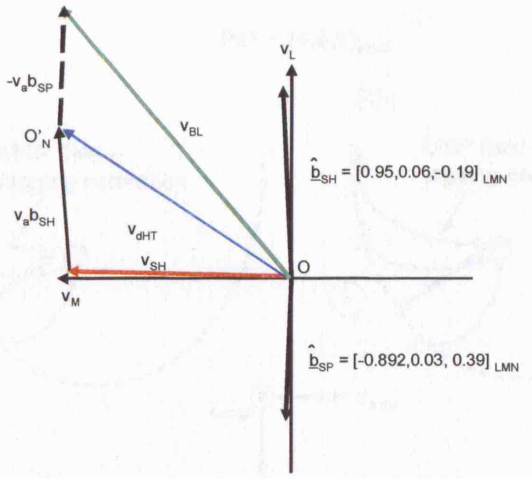

Figure 3.31 Schematic of the observed normalised magnetic field and velocity flow vectors in a plane tangential to the magnetopause from Cowley and Owen [1989]. The magnetic field orientations (heavy black arrows) in the magnetosphere ($\hat{\underline{b}}_{SP}$) and the magnetosheath ($\hat{\underline{b}}_{SH}$) are ~ anti-parallel. In Saturn's rest frame (O) the de Hoffman Teller frame (O'_N) for the field lines connected to the northern hemisphere, is obtained by knowing that the magnetosheath velocity $\underline{v}_{SH}$ must be equal to the Alfvén speed v_A. Once the field line rest frame is derived, we know the electric field is zero, thus there is no acceleration of the plasma, and thus it must flow out of the reconnection site, also at the Alfvén velocity $-v_A \underline{b}_{SP}$ (heavy dashed line). The resultant boundary layer velocity $\hat{\underline{v}}_{BL}$ in the frame of the observer (at Saturn) is then equal to the field line velocity plus the outflowing magnetosheath plasma at the Alfvén speed, $\underline{v}_{BL} = \underline{v}_{dHT} - v_A \underline{b}_{SP}$. The field line rest frames connected to the northern hemisphere is denoted by O'_N. We can see that the boundary layer flow is travelling in a northwards and tailwards direction as observed.

Based on the known ion speeds plus the inferred directions, and the field directions, we can apply the method used in Cowley and Owen, [1989] to predict the boundary layer flow direction and compare it to the observed flow. As with the first reconnection event on 17 April 2005, we construct the geometry of the fields and flows in velocity space tangential to the magnetopause (Figure 3.31). We first draw the known field orientations (heavy black arrows) in the magnetosheath and magnetosphere (or boundary layer) and the magnetosheath flow direction (red arrow). The field line rest frame can be obtained since we know that in this frame the magnetosheath flow must be equal to the field aligned Alfvén velocity $v_A \underline{b}_{SH}$. The boundary layer flow is then simply the magnetospheric field-aligned flow also at the Alfvén speed (since the particles do not get accelerated in the field line rest frame) $\underline{v}_{BL} = \underline{v}_{dHT} + v_A \underline{b}_{SP}$ which is the same as Equation 3.1. This results in a boundary layer flow that is predominately northward, agreeing with our findings that the accelerated flow is found to be deflected by ~ 94° compared with the nominal magnetosheath flow.

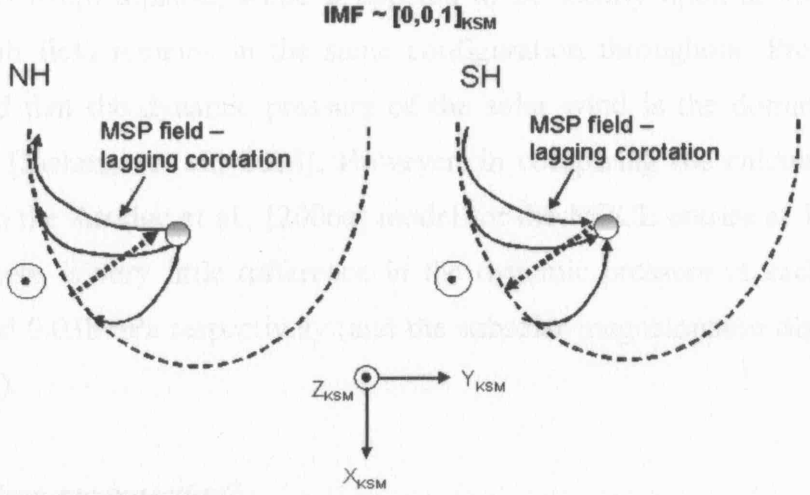

Figure 3.32 Sketch showing the field line geometry of the magnetosheath and magnetospheric fields for this event. Both views are looking down on Saturn's north pole, the left-hand side is for the northern hemisphere (NH) and the right-hand side is for the southern hemisphere (SH), looking down 'through' the planet. The Sun is toward the bottom of the figure and the northward magnetosheath field is marked approaching from the left. The magnetopause is marked by the dashed parabola encompassing the magnetospheric field lines. In the magnetosphere sub-corotation of the field has been assumed. It is apparent that due to the northward field, reconnection is favourable along the entire field line.

From the orientation of the fields, reconnection is favourable along the whole magnetospheric field line from both the northern and southern cusps as is apparent in Figure 3.32. The figure shows a sketch looking down from above the north pole onto each hemisphere with a northward pointing magnetosheath field, approaching from the sunward direction and draping over the magnetosphere. The dotted arrow represents the draped magnetosheath field. A lagging magnetospheric field in the dawnside magnetosphere has been assumed, although this does not affect the result significantly.

Reconnection Voltage

As a final task, the convection electric field has been estimated for this event. This is an acceptable exercise since the field has been shown to be locally open at 15:44 UT and a finite normal component identified. The accelerated ions have a velocity of 536 kms^{-1}, the B_N component ~ +2 nT ± 0.05 nT and the angle between them is 86°. These values produce a value of E_{CONV} ~ 1.07 mVm^{-1}. This is larger than our previous value derived for 17 April 2005 and values found by Huddleston et al., [1997], Sittler et al., [2006] and predicted by Jackman et al., [2004]. It is, however, more comparable to the corotational electric field at the magnetopause ~ 1.64 mVm^{-1}.

This event shows an ideal case of almost exactly anti-parallel fields at the magnetopause crossing at 15:02 UT, and yet the plasma data and the MVA on the field (with a very high confidence) show that the first rotation observed at 15:02 UT is a

locally closed magnetopause, while it appears to be locally open at 15:44 UT. The magnetosheath field remains in the same configuration throughout. Previous studies have reported that the dynamic pressure of the solar wind is the dominant factor of reconnection [Jackman et al., 2004]. However, in comparing the calculated dynamic pressure from the Arridge et al., [2006a] model for the MPCL entries at 15:02 UT and 15:44 UT, there is very little difference in the dynamic pressure at each crossing, ~ 0.037 nPa and 0.038 nPa respectively (and the subsolar magnetopause distances which are ~ 20.8 R_S).

Internally driven reconnection?

The previous crossing event was suggestive of a reconnection signature driven by the shear between the magnetosheath and magnetospheric fields. However, it is unclear at this crossing whether reconnection could have arisen from an internally driven process. However, there is strong evidence to suggest that the interaction of the magnetospheric field with the magnetosheath field is the driving mechanism for the energisation observed.

3.6 Conclusions

Two separate magnetopause crossings on Saturn's dawn flank have been analysed using the electron, ion and magnetic field data. In both cases the spacecraft was close to the equatorial plane at local times of 06:00 and 09:00. For both intervals the instrument look directions were such that the ion population was in the field of view, allowing a detailed look at both the ion and electron data.

Internal and external boundary layers were identified and characterised in both magnetopause crossing events. For electron boundary layer plasma it is not always possible to determine whether it has undergone energisation due to the low Alfvén speed compared with the electron thermal speed. Alternative mechanisms for entry, such as diffusion through the magnetopause, have not been ruled out.

Other plasma regions adjacent to the magnetopause have a clear structured nature, an observed dispersion in the appearance of the plasma species, and this, in conjunction with signs of heating and acceleration of the plasma, is clear evidence of reconnection processes occurring at Saturn's magnetopause.

On 17 April 2005 the magnetosheath field had two orientations, $[+X, +Y, -Z]_{KSM}$ and $[+X, +Y, +Z]_{KSM}$. Signatures of reconnection were observed outside the

magnetopause during both of these orientations. The reconnection site for the first case was inferred to be tailward of the dawn/dusk meridian and in the northern hemisphere. The energised electron population was observed for nearly one hour, with a corresponding acceleration observed briefly in the ions. The reconnection voltage was estimated to be 0.52 mVm^{-1}, lower than the corotational voltage at the magnetopause. A high solar wind dynamic pressure value of 0.094 nPa was inferred from the Arridge et al., [2006a] model. This may indicate that there was a CIR impacting Saturn's magnetopause, resulting in a high dynamic pressure and perhaps triggering steady-state reconnection.

On 21 September the magnetosheath field was strongly northward pointing. Signatures of reconnection were observed in both the electrons and the ions over a period of ~ one hour. The magnetopause crossing appeared to be locally closed, however a partial entry ~ 30 minutes later had a finite B_N component suggestive of a reconnection site in the southern hemisphere, below Cassini. The reconnection voltage was estimated to be 1.07 mVm^{-1}. This is larger than the previous value calculated, due to the larger acceleration and B_N component used, but still lower than the corotational voltage at Saturn's magnetopause. The solar wind dynamic pressure had a value of 0.038 nPa which is lower than the previous value. Thus we may infer that steady reconnection is possible at Saturn under medium-to-high dynamic pressures, which the magnetosphere is compressed and the magnetic fields are anti-parallel. None of the findings suggest internally driven reconnection.

4 Low energy electrons and magnetic field at Saturn's magnetopause and in the boundary layer

4.1 Introduction

In Chapter 3, two magnetopause crossings were studied in detail using the electron and ion plasma data and the magnetic field measurements. In order to gain an appreciation of the general electron plasma properties at Saturn's magnetopause, a further 203 crossings between Saturn orbit insertion in June 2004 and January 2006 have been identified in the data, and their characteristics studied. This is the first survey of the electron data from a large number of Saturnian magnetopause crossings and provides new information about the general characteristics of the magnetopause as observed by Cassini. This then provides a baseline against which future magnetopause observations can be compared.

As described in Chapter 1, the magnetopause is an important boundary for magnetospheric dynamics, since processes on this surface are of importance in determining the interaction of the magnetosphere with the solar wind particles and fields [Cowley, 1984]. The magnetopause is complex in structure, and undergoes continual motion due to the constantly shifting pressure balance between the variable solar wind and the internal plasma and fields. By analysing a significant number of measurements of its properties, assumed to be under many different solar wind and internally generated conditions, a better understanding of how this boundary behaves can be gained. Some general properties of the magnetic field topology of the magnetopause have been analysed in separate studies such as Arridge et al., [2006a], in their model of the magnetopause, and Achilleos et al., [2005], who looked at six orbits worth of data to characterise the boundary dynamics. However, a thorough inspection of the magnetic field characteristics at every crossing identified here has yet to be carried out and is not the focus of this study.

One important feature often observed at Earth's magnetopause is an internal boundary layer. As described in Chapter 1, observations of this boundary layer yield important information about the mixing of magnetospheric and magnetosheath plasma and thus the coupling of these two systems. Different types of boundary layer, which may have different methods of formation [i.e. Eastman and Hones, 1979; Haerendel et

al., 1978], are expected at different locations on the magnetopause. However, due to orbital considerations, which restrict sampling to the near-equatorial region, we shall mainly be considering the Saturnian equivalent of Earth's Low Latitude Boundary Layer (LLBL) [Eastman et al., 1976; Eastman and Hones, 1979; Haerendel et al., 1978; Sckopke et al., 1981; Mitchell et al., 1987; Song and Russell, 1992]. Using data from the Cassini electron spectrometer (ELS) and magnetometer, we explore the internal region adjacent to Saturn's magnetopause for evidence of such a layer. If one is present, we can establish typical characteristics of the plasma and magnetic field during the transition from the magnetosheath to the magnetosphere-proper. Observations of the boundary layer can be correlated with other parameters such as the upstream dynamic pressure, to test for conditions under which it is formed, and subsequently the processes behind its generation. The general changes in density and the magnetic field will also be investigated to understand how these parameters change as the boundary is approached and in the boundary layer itself. The number of crossings is too large to permit as detailed an analysis on each as that carried out in Chapter 3. Nevertheless some of the plasma and field characteristics can be obtained and studied from a statistical point of view. In addition, a survey has the benefit of looking at the wider trends observed at the magnetopause, rather than focusing on specific crossings and events which may not be representative of the "normal" magnetopause or may be the result of extreme solar wind conditions.

4.2 Data

The magnetopause crossings observed in the first 18 months of Cassini's tour of Saturn, from June 2004 to January 2006 have been catalogued. Figure 4.1 shows the location of these crossings in the X-Y, X-Z and Y-Z planes in KSM coordinates. Over-plotted on the X-Y plane is an average model magnetopause surface as calculated using the Arridge et al., [2006a] model. The model describes a functional form for the magnetopause, which is upstream pressure-dependent. Since there is no upstream monitor at Saturn, this can be used to infer the upstream solar wind pressure. The model assumes that the boundary is static and that the pressure impacting the magnetosphere is balanced by an internal vacuum dipole magnetic field. Thus, the magnetic pressure just inside the magnetopause is used to infer the external dynamic pressure at each crossing location.

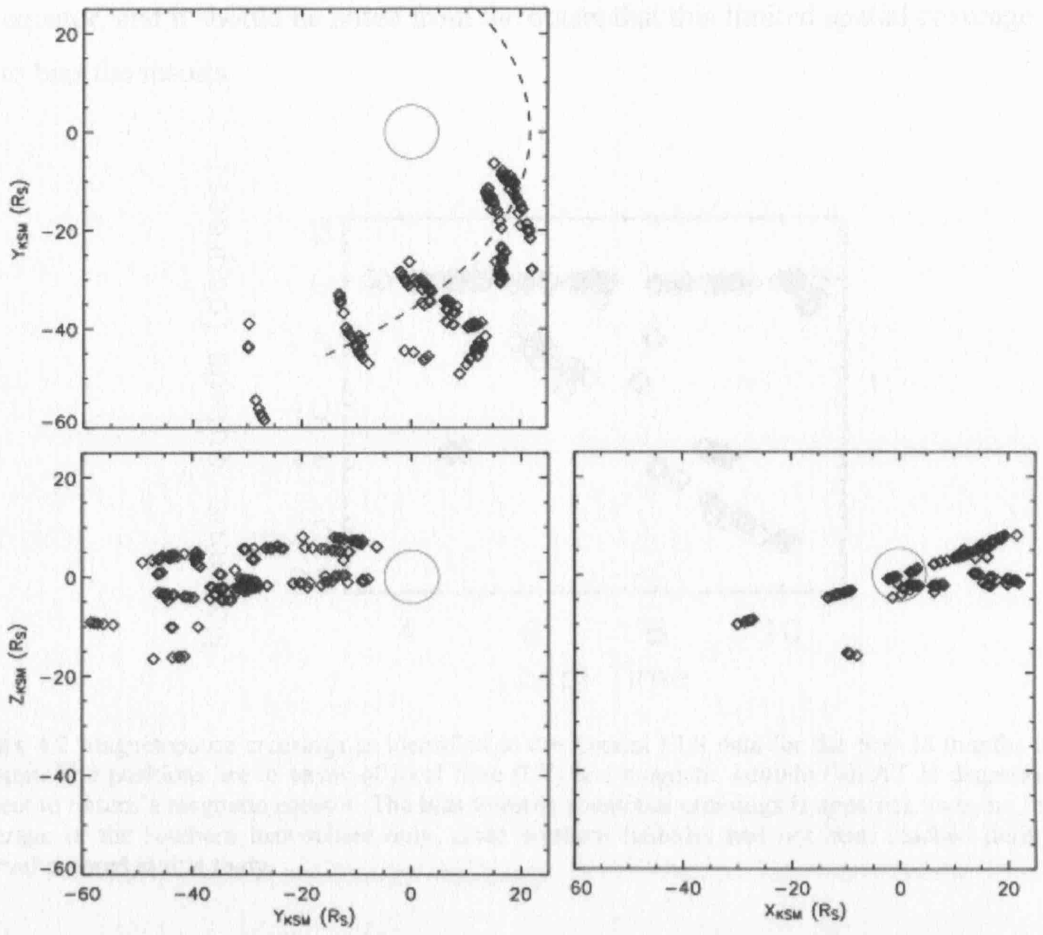

Figure 4.1 Magnetopause crossings (diamonds) as identified in the Cassini ELS data for the first 18 months of the mission at Saturn. The positions are projected onto the X-Y, X-Z and Y-Z planes in the Kronocentric Solar Magnetic (KSM) frame (as described in Appendix C). The Arridge et al., [2006a] magnetopause model surface and Saturn's position (circle centred at X_{KSM}=0, Y_{KSM}=0, Z_{KSM}=0) are indicated. The magnetopause surface in the X-Y plane has been produced using the model for the average solar wind pressure encountered during the period covered in this survey of 0.032 nPa (dashed line). Note the limited LT and latitudinal coverage. Scales are in Saturn radii (1 R_S = 60,268 km).

Of course, this is a crude approximation, since the magnetopause is not a static boundary. This is apparent from the numerous crossings generally observed on each inbound or outbound orbital pass. In addition, the model does not take into account internal pressure effects, which at Saturn could be significant [e.g. Clarke et al., 2006]. Nevertheless, this is the only current method of deriving the upstream pressure and so is used with caution throughout this work.

The model surface plotted in Figure 4.1 has been generated for a solar wind pressure of 0.032 nPa, which is the average of the fitted values for all the crossings in the database. It can be seen to broadly lie in the middle of the crossing positions. As a consequence of the nature of the initial stage of the tour, all encounters with the magnetopause between June 2004 and January 2006 are in the morning sector, close to

the equator, and it should be noted from the outset that this limited spatial coverage may act to bias the results.

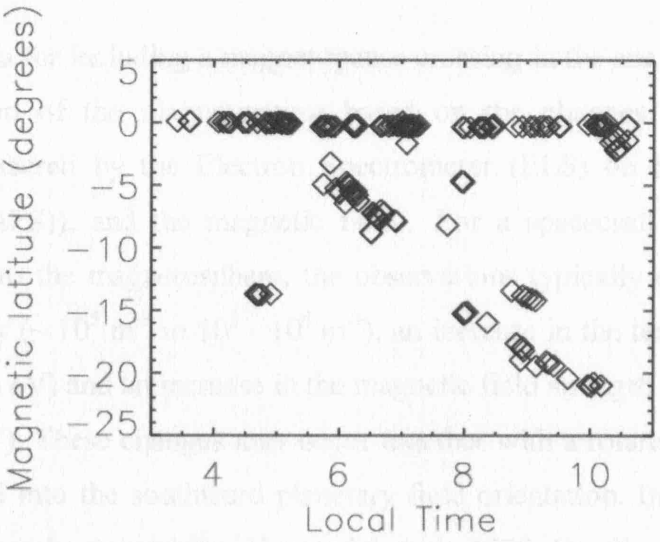

Figure 4.2 Magnetopause crossings as identified in the Cassini ELS data for the first 18 months of the mission. The positions are in terms of local time (LT) and magnetic latitude (MLAT in degrees) with respect to Saturn's magnetic equator. The bias towards equatorial crossings is apparent, as is the limited coverage of the southern hemisphere only, since northern latitudes had not been reached during the interval covered in this study.

The locations of the crossings are also displayed as a function of local time and magnetic latitude in Figure 4.2, as this is a convenient way of visualising the coverage. It is clear that for this period, Cassini's orbital plane was principally aligned with Saturn's equatorial plane resulting in the preponderance of near equatorial crossings. The crossings at high negative magnetic latitudes occurred during the Saturn insertion orbit and orbits containing Titan encounters, when the flyby was used to change Cassini's orbital inclination. Note that the differences between the distribution of magnetic latitudes and the plots in Figure 4.1 are due to Saturn's magnetic axis being tilted relative to Z_{KSM}. Thus a distribution of crossings at varying values of $\pm X_{KSM}$ and $\pm Z_{KSM}$ may lie exactly on Saturn's magnetic equator. This is demonstrated by considering a tilt of the X-Z plot in Figure 4.1 approximately 26° (the tilt of Saturn's dipole axis during this period) about the Y-axis.

To summarise, the events included in this study are all on Saturn's dawn flank magnetopause, between 3 and 11 LT, with magnetic latitudes of – 21° to 0.1° and Saturn-centric distances to 65 R_S.

4.3 Event selection

The criteria for including a magnetopause crossing in the analysis first requires a clear identification of the magnetopause based on the changes in the low-energy electrons (as measured by the Electron Spectrometer (ELS) on the Cassini Plasma Spectrometer (CAPS)), and the magnetic field. For a spacecraft crossing from the magnetosheath into the magnetosphere, the observations typically show a decrease in the plasma density (~ 10^5 m^{-3} to 10^3 - 10^4 m^{-3}), an increase in the temperature (~ 50 eV to 100's to 1000's eV) and an increase in the magnetic field strength (typical values ~ 2-8 nT to ~ 5-12 nT). These changes may occur together with a rotation (if necessary) of the magnetic field into the southward planetary field orientation. Internal and external boundary layers may be present [i.e. Haerendel et al., 1978; Fuselier et al., 1995] and/or magnetic pile-up may be occurring [Zwan and Wolf, 1976; Violante et al., 1995]. These are all complex processes which may hinder our ability to see the plasma transition clearly. Additionally, a strong southward magnetosheath field may result in a low magnetic shear magnetopause, which can also make the identification of the magnetopause in the magnetic field data difficult [Phan et al., 1997]. There may also be significant variations in the plasma and magnetic field properties over time, especially in the dynamic magnetosheath region [Sibeck, 1994], which may also hinder the identification of the magnetopause.

The criteria applied to each crossing event to determine whether it is included in this survey are as follows:

- Continuous electron data must be available;
- Continuous magnetic field data must be available;
- The transition from magnetosheath plasma (as defined in Chapter 3: high density, low temperature plasma with a plateau in the phase space density (PSD) distribution in the mid-energy range known as a 'flat-top' and a variable magnetic field) to magnetospheric plasma (planetary field orientation, low density, high temperature plasma), including any boundary layer, must be identifiable.

Once events are identified in the data, further analysis of the crossing also requires:

- The ability to derive the transition parameter of the crossing (since this is an important diagnostic of the boundary layer)

As the Cassini data set used in this study is limited to 205 crossings (including the two studied in detail in Chapter 3), every identifiable crossing has been included without grouping based on proximity to other crossings in space or time. Although this maximises the number of events included in the analysis, it may introduce bias simply because groups of crossings may have similar positions and conditions, i.e. upstream magnetic field orientation or magnitude. However, we cannot assume *a priori* that crossings occurring within a few hours of each other (as is generally the case) have similar upstream parameters, since the IMF is observed to have significant variation in substructure over tens of minutes to hours, as discussed in Jackman et al., [2004]. Based on the selection criteria outlined above, 191 crossings have been included for analysis.

For each crossing, the date and time of the magnetopause encounter, the sense of the crossing, i.e. was Cassini crossing inbound or outbound to the magnetosphere, Saturn-centric distance (R_S), R_X, R_Y, R_Z, magnetic latitude and local time (LT) were noted. The following parameters were also determined for each crossing:

- the orientation of the 'upstream' field with respect to the downstream field in the plane of the magnetopause, the magnetic shear;
- the boundary layer *temporal* width, determined from the time spent in a region where the plasma has characteristics intermediate between typical magnetospheric and magnetosheath plasma;
- The average density and temperature in the boundary layer (where finite boundary layer widths were identified)
- The magnetopause stand-off distance (R_0) as calculated using the Arridge et al., [2006a] magnetopause model and the inferred solar wind dynamic pressure (D_P) assuming a static magnetopause.
- Whether or not energised electrons are evident at the magnetopause.

The derived parameters and summary data for each of the 191 events are listed in Appendix D.

4.4 Analysis methods

4.4.1 Introduction

The Cassini mission is sophisticated, but the single point measurements introduce limitations into the analysis, since it is not possible to accurately untangle spatial and temporal variations in the data. A key aim of this study is to attach some significance to the presence and the characteristics of any boundary layers adjacent to the magnetopause. The density of the boundary layer at Earth is generally intermediate between that of the magnetosheath and outer magnetosphere [Haerendel et al., 1978, Sckopke et al., 1981]. This value is found to be up to ~ 25% of the magnetosheath density, but can also be lower than this [Haerendel et al., 1978]. Due to motions of the boundary, and thus the spacecraft with respect to the boundary, an accurate spatial 'width' cannot be determined. Nevertheless, meaningful conclusions can still be established by measuring the maximum time that Cassini remains within a boundary layer during a pass. This method was used in the survey by Mitchell et al., [1987] who used a temporal width to give a rough measurement of LLBL thickness and establish trends in the data.

The determination of this width, plus the density in the boundary layer, may then be used to highlight any consistencies or trends in the data. Re-ordering of the data by the transition parameter , τ, [Bryant and Riggs, 1989; Hapgood and Bryant 1990; 1992] which provides a numerical means of segregating different populations across a magnetopause boundary crossing, forms the basis of much of the analysis, and allows us to probe the structure in any layers identified. This will be described further below. We have also investigated the conditions in the magnetosheath upstream of the magnetopause to establish if plasma depletion layers are present at Saturn. In addition, we have visually inspected the data to establish whether any acceleration or energisation of the plasma is observed. This is likely to have been the result of a reconnection process at the magnetopause. The results of this study will be useful in shaping future magnetopause studies and identifies conditions under which reconnection is likely.

4.4.2 Transition Parameter

4.4.2.1 Introduction

In order to identify boundary layer from magnetosheath and magnetospheric plasma, the transition parameter is applied to the data. This is a method used in magnetopause boundary layer studies at Earth in order to remove variations due to the magnetopause motion and thus can be used to quantify the relative distance travelled into the boundary layer or the relative transition from 'pure' magnetosheath or magnetospheric plasma. It also provides a way of effectively removing temporal variations in the data, which may arise due to the highly variable position of the magnetopause over time. It does this by assuming that the boundary layer and magnetopause have fixed characteristics throughout the crossing and any changes are due to the back and forth motion of the magnetopause moving the spacecraft into a different region of the boundary. There is an assumed monotonical change in the plasma characteristics across the boundary [Bryant and Riggs, 1989] with a decrease in the density and an increase in the temperature. The transition parameter exploits this anti-correlation of electron density and temperature.

4.4.2.2 Calculation of the Transition Parameter

To calculate τ, the density and temperature across the period must first be obtained. The electron density values are derived from the raw ELS counts via the method described in Appendix B. A period of continuous data measured during a crossing or multiple crossings is needed, containing data from both magnetospheric, magnetosheath and any boundary layer populations. The density and temperature at each measurement point in time during a complete transition (or multiple transitions) is plotted on a $\log_{10} - \log_{10}$ scatter plot (an example is shown in Figure 4.3). A polynomial curve is then fit to the resulting distribution of points. Once this line of best fit has been calculated, each data point is projected onto the nearest point on the curve. Where these intersect gives the distance 'd' along the curve. The values of 'd' are then normalized from 0 to 100, giving a dimensionless τ value for each point. The lowest values on the

plot are assumed to represent a density:temperature ratio of the 'purest' magnetosheath, and the highest values the 'purest' magnetosphere observed.

4.4.2.3 Uses of the Transition Parameter

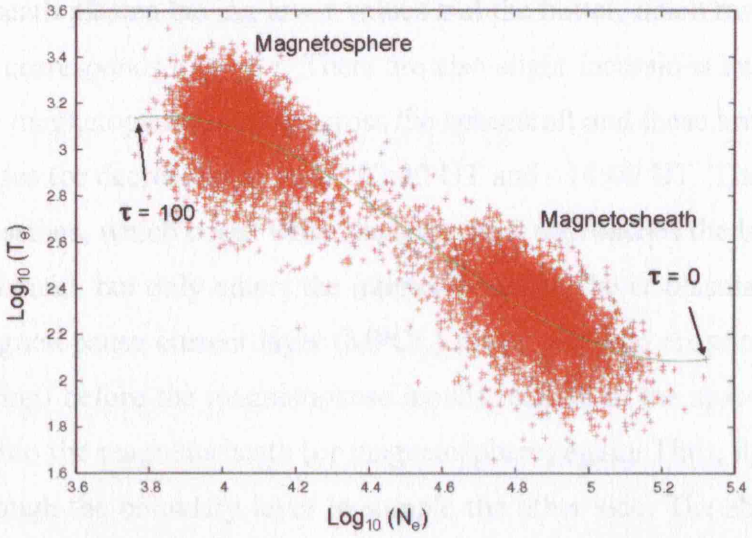

Figure 4.3 Scatter-plot showing how the transition parameter (τ) for a time series of plasma measurements is generated. This example is taken from 31 January 2006, 00:00-17:00 UT which contains three crossings (in-out-in) of the magnetopause. The $\log_{10}$ density is plotted on the horizontal axis and the $\log_{10}$ electron temperature on the vertical axis. The resultant distribution of points can be seen to cluster at the bottom-right (high density, low temperature) characteristic of the magnetosheath and the top-left (low density, high temperature) characteristic of the magnetosphere. A third-order polynomial is then fit to the distribution of points (green line). A line from each data point is projected down (or up) onto the best-fit line. The distance along this line is then normalised with 0 being the furthest bottom right point on the line and 100 being the furthest top left point. The value assigned to each point is τ, where the lowest value of τ is the purest magnetosheath plasma in the interval used and the highest value of τ is the purest magnetospheric plasma in the interval. The gradual change from magnetosheath to magnetospheric plasma is evident, with the points between the two main populations constituting intermediate values between these populations.

Although it is generally apparent in the data when the electrons are intermediate in energy and density compared with either the magnetospheric or magnetosheath electron populations, it is useful to have a quantitative method to assign populations to the boundary layer. In order to do this, the transition parameter was derived for each cluster of crossings or individual crossing.

Figure 4.3 shows the determination of τ for a period on 31 January 2006, between 00:00 and 17:00 UT, containing three crossings (in-out-in) while Cassini was inbound to the magnetosphere. The plot clearly contains a cluster of points in the bottom-right (high density, low temperature), characteristic of the magnetosheath, and assigned low values of τ and also in the top-left (low density, high temperature), characteristic of the magnetosphere and given high values of τ. The points in between

and joining the two populations indicate the presence of mixed, boundary layer plasma. The data can then be plotted against the transition parameter (rather than time) and the different boundary layer regions that the spacecraft encounters can be more readily distinguished. The τ vs. time plot, together with the spectrogram for the period is shown in Figure 4.4. The τ values clearly represent the changes in the plasma, with the dense, cool magnetosheath plasma having low τ values and the hotter, much rare plasma of the magnetosphere corresponds to high τ. There are also slight incursions into the boundary layer due to the magnetopause motion across the spacecraft and these are evident by the transient increases (or decreases) in τ at ~ 02:30 UT and ~14:00 UT. These are referred to as partial crossings, which occur when the spacecraft approaches the boundary, either inbound or outbound, but only enters the interior boundary layer plasma (either having crossed the magnetopause current layer (MPCL) for an inbound crossing or not for an outbound crossing) before the magnetopause moves relative to the spacecraft such that it moves back into the magnetosheath (or magnetosphere) again. Thus, it never makes it all the way through the boundary layer to sample the other side. The sharp, significant changes in τ are either due to a lack of any boundary layer (and thus Cassini travels directly from approximately pure magnetosheath to pure magnetosphere or visa-versa) or the rapid motion of the spacecraft across the magnetopause preventing the ELS from sampling the boundary layer plasma population.

For the example in Figure 4.3 boundary layer plasma appears to populate values $\sim 40 < \tau < 60$. If we consider the density values, this range of τ corresponds to a density range that is ~ 25% to ~ 60% of the average density in the magnetosheath. This inferred value is thus larger than the typical density ratio observed in the boundary layer at Earth [Haerendel et al., 1978]. From the spectrogram in Figure 4.4 for the same interval, only ~ one hour is spent in the boundary layer compared with the rest of the five hour period which samples magnetosheath or magnetospheric plasma, hence these populations appear to dominate. As a result we must take care when interpreting these plots as they cannot tell us the *quantity* of boundary layer plasma there is in the layer, just the amount that is sampled in a particular interval relative to the magnetosheath or magnetospheric populations.

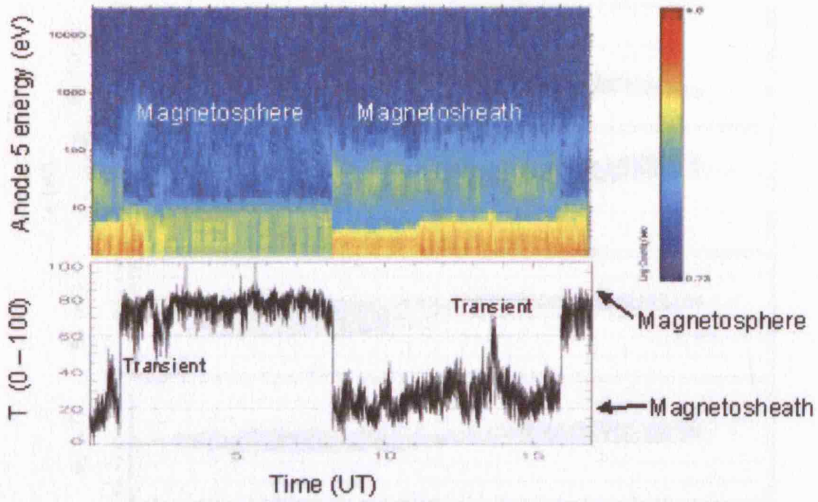

Figure 4.4 Data from 31 January 2006, 00:00-17:00 UT The top panel contains data from anode 5 of the ELS in electron spectrogram format. Electron energy in eV is on the vertical axis and the colour scale indicates counts. The dense, lower energy population is where Cassini is sampling magnetosheath plasma and the rare, hotter plasma is typical of magnetospheric plasma. The time series of τ is plotted in the bottom panel and shows how τ traces the position of the spacecraft relative to the magnetosphere and magnetosheath.

For each crossing (or cluster of crossings) a plot of τ is generated and the limiting values for the boundary layer are chosen.

Once derived, τ may also be used to re-order other parameters that change with the boundary crossing, such as magnetic field magnitudes [Bryant and Riggs, 1989] allowing a clearer understanding of how these parameters change across the magnetopause and any boundary layers. This re-ordering is applied to the plasma density, temperature, the three magnetic field components and the magnitude from 31 January 2006 and shown in Figure 4.5. The monotonical decrease and increase in the density and temperature respectively is apparent. The field components, however, show more variation, particularly in B_X and B_Z in the magnetosheath ($\tau < \sim 40$). Such a spread in the field orientation may be due to temporal changes in the region being sampled or that the orientation is changing between different periods, and on 31 January 2006 there are two magnetosheath entries. Data between $40 < \tau < 60$ represents intermediate plasma consistent with the boundary layer, and this appears to be a fairly stable region, before a slight change in the field characteristics after $\tau \sim 60$. We will use this method of analysis to better understand the boundary layer configuration for events studied later in this chapter.

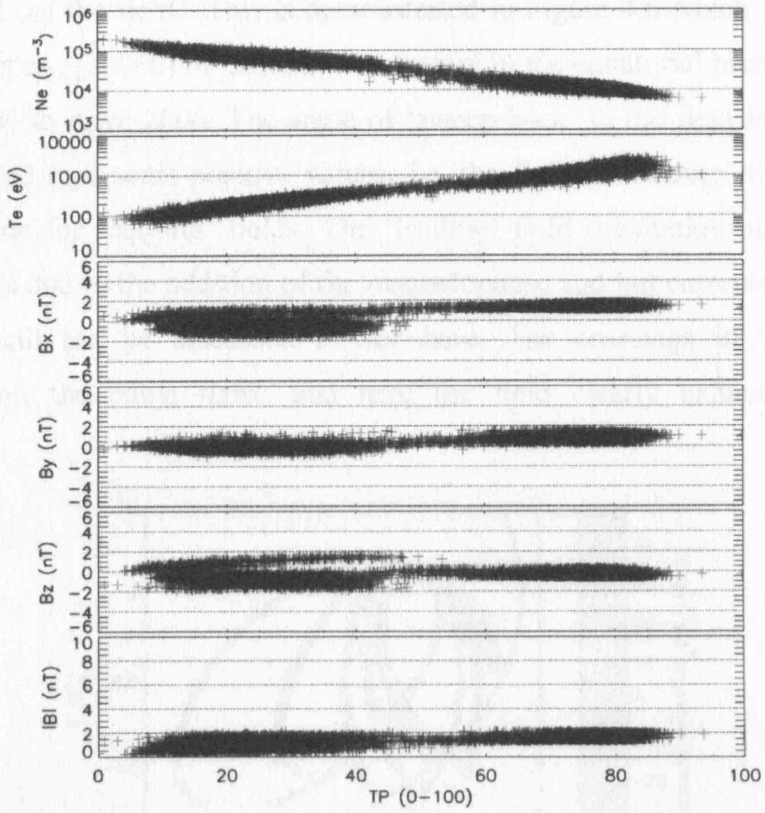

Figure 4.5 Plasma and magnetic field parameters re-ordered by transition parameter for an interval from 00:00 UT to 17:00 UT on 31 January 2006. The gradual transition in the plasma density and temperature is apparent. The variability in the field is apparent in the magnetosheath.

4.4.3 Magnetic field considerations

4.4.3.1 Saturn's magnetospheric configuration at the dawn magnetopause

Saturn's planetary field does not have the form of a simple dipole in the outer magnetosphere. The fast rotation of the planet, together with the large quantities of plasma in the magnetosphere, results in the plasma moving radially outwards and being confined to the equatorial plane, which stretches the field. This creates a plasma sheet and associated current layer known as the magnetodisc [Arridge et al., 2006c, *submitted*]. Thus, in the outer magnetosphere the field adopts a strong radial component. In addition, as this mass moves outward, and due to the conservation of angular momentum, it slows. Since the magnetic field is frozen to the plasma, it must also slow, resulting in a lagging planetary field [Kivelson, 2002; Bunce et al., 2003]. This also introduces a significant azimuthal component to the field [Arridge et al., 2006b] due to

the 'bend back' of the field. This is demonstrated in Figure 4.6 which contains a plot from Arridge et al., [2006b] of Cassini's' trajectory in the equatorial plane of the planet from June 2004 to April 2006. The angle of 'sweep back' in the field is shown by the colour scale, red represents positive values, i.e. the field is 'leading' the corotational plasma and blue for 'lagging' fields. The 'leading' field orientation observed on the dusk side arises due to the addition of the magnetopause and tail currents [Bunce et al., 2003], and shall not be discussed further here. The crossings in this study are concentrated on the dawn flank, and here the field clearly exhibits a 'lagging' behaviour.

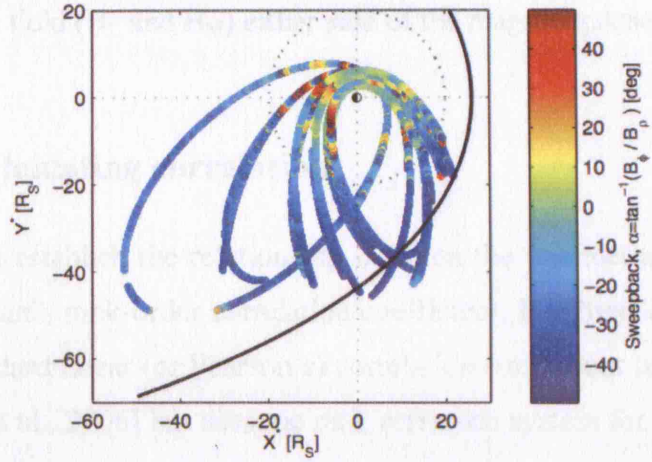

Figure 4.6 A trajectory plot of Cassini's orbit taken from Arridge et al., [2006b] in the equatorial plane of the planet. The departure of the magnetic field from a solely radial orientation, i.e. α, is positive or negative depending on whether the field is leading or lagging the corotational plasma.

One of the key questions to be addressed at Saturn is how important the interplanetary magnetic field (IMF) or magnetosheath field orientation relative to the planetary field is in the coupling process between these two magnetic fields. For obvious reasons, data from a single spacecraft places limitations on the determination of the upstream conditions when the spacecraft is inside the magnetosphere. Thus, for the purposes of this study, the upstream field orientation observed by Cassini immediately before (after) the magnetopause crossing inbound (outbound) has been used to represent the orientation of the magnetosheath field when Cassini is inside the magnetopause. Of course, this may introduce errors due to the inherent time variability of the magnetosheath magnetic field orientation and strength. Another point to note is that the local shear may not be representative of the global shear. For example, a high shear measurement may suggest that local or patchy reconnection is likely. Extrapolation to infer a more global interaction in which large areas are undergoing reconnection or that

very long X-lines exist or that reconnection occurs at many different sites across the magnetopause [Phan and Paschmann 1996] cannot be made with certainty.

4.4.3.2 Magnetic shear

We calculate the magnetic shear by considering the field components in the plane tangential to the magnetopause. We first derive the magnetopause normal from the Arridge et al., [2006a] model. Using this normal, the boundary normal coordinate frame can be derived as described in Appendix C. We then rotate the field vectors from either side of the magnetopause into this frame and find the angle between the tangential components of the field (B_L and B_M) either side of the magnetopause.

4.4.4 Calculating correlation

In order to establish the relationship between the parameters in this survey we have used Spearman's rank-order correlation coefficient, R, [Press et al., 1988]. This is similar to the standard linear (or Pearson's) correlation coefficient used by many studies [e.g. Bogdanova et al., 2006] but uses the rank reference system for each variable rather than its value. This eliminates the need for the data to have a normal distribution. The concept is, that if we replace all the values of x_i in a distribution with their associated ranks amongst all the other values of x, i.e. r_i, then the resulting list of numbers will be drawn from a perfectly known distribution function. It is also more robust than the Pearson's method since it is more resistant to spurious values in the datasets [Press et al., 1988], thus only the order of the data is important, not the level. The equation for R is:

$$R = \frac{\sum_i \left(r_i - \bar{r}\right)\left(t_i - \bar{t}\right)}{\sqrt{\sum_i \left(r_i - \bar{r}\right)^2}\sqrt{\sum_i \left(t_i - \bar{t}\right)^2}}$$

Equation 4.1

where r_i is the rank of x_i among the dataset of x's and t_i the rank of y_i among the y's. Note that when $R = 0$ it is not due to a lack of correlation, simply that the correlation is not linear. Associated with this is a measure of the statistical significance, S, of the result which is the two-sided significance of the deviation of R from zero, or

the probability that $|R|$ should be larger than its observed value in the null hypothesis. The null hypothesis being that the two datasets are completely uncorrelated. The value of S is a number between 0 and 1 where a *small value* indicates a significant correlation and is calculated using:

$$S = erfc\left(\frac{|R|\sqrt{N}}{\sqrt{2}}\right)$$

Equation 4.2

where *erfc* is the complementary error function [Press et al., 1988] and N is the number of samples. A line of best fit is also included for each plot by applying a simple linear model $y = A + Bx$ to aid the eye.

4.4.5 Superposed Epoch Analysis (SEA)

As we are interested in studying the average behaviour of the data at the magnetopause over a number of crossing intervals, we have also chosen to employ superposed epoch analysis (SEA). We apply this method to study plasma depletion layers (PDLs), and we wish to compare our results directly with those obtained at Earth. We therefore follow the technique used in Paschmann et al., [1993] and later in Phan et al., [1994]. Several stages are involved in the SEA:

1. We first determine a key time to use as the reference point for all the data intervals. This is chosen to be the magnetopause since we are most interested in the changes as this boundary is approached;
2. If the crossing is outbound, the data is reversed so that the upstream side is always on the left of the key time in the resultant plots;
3. The interval is chosen to include both upstream (in the magnetosheath) and downstream (in the magnetosphere) data either side of a single magnetopause crossing;
4. Since the absolute magnitude of these parameters may vary considerably and as we are most interested to see how the parameters vary with respect to their average values, we normalise all data with respect to the average of each interval. Thus, for each set of crossing data the average value is taken and all data points are then divided through by this average;

5. We then logarithmically sum the data across all crossings and divide through by the number of intervals used. This method of averaging the entire data set together eliminates those crossings with large dynamic ranges dominating the result.

4.5 Plasma and field changes across the magnetopause

4.5.1 Using the transition parameter to re-order data

We now present three crossing periods as examples of the type of variation seen in the plasma and field parameters across Saturn's magnetopause. The three examples are taken from inbound crossing intervals containing varying number of magnetopause crossings. The first had only three encounters with the magnetopause while during the second and third, the magnetopause was undergoing significant motion in the vicinity of the spacecraft, resulting in nine partial and full crossings.

4.5.2 Re-ordered data across three magnetopause encounters

Figure 4.7 contains a time series plot of τ and Figure 4.8 shows a series of panel plots containing the electron density, temperature and the magnetic field components and strength as a function of the corresponding transition parameter for the same interval.

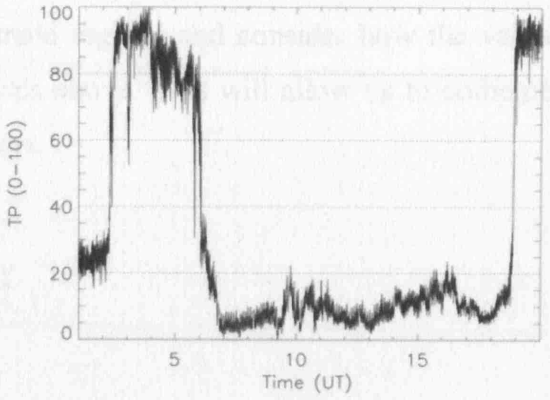

Figure 4.7 Time series of τ values for the 2 December 2005 from 00:00 UT to 20:00 UT. The three magnetopause crossings are evidenced by the jump in low to high (or visa-versa) τ values at 02:20 UT, 06:00 UT and 18:53 UT.

The values of density, temperature, magnetic field orientation and magnitude are determined for each point in time, and assigned a value of τ as seen in Figure 4.7.

The plots are derived using data from 2 December 2005 00:00 UT to 20:00 UT as Cassini was inbound to the magnetosphere. We further divide the data into three time intervals covering the three different magnetopause crossings (as shown in Figure 4.7):

- Interval 1 is from 00:00 to 04:00 UT and the data from this interval is indicated by the black crosses;
- The data from interval 2 is from 04:00 to 08:00 UT (blue crosses);
- The data from interval 3 is sampled between 17:00 and 20:00 UT (green crosses).

Figure 4.8 shows the transition from the high density, low temperature, disturbed field region of the magnetosheath (left hand side, $\tau \rightarrow 0$) to the low density, high temperature, slightly more ordered magnetosphere (right hand side, $\tau \rightarrow 100$. There are fewer points between these two regions than within them, suggesting that little boundary plasma was recorded during this interval used to calculate τ relative to the magnetosheath and magnetospheric populations sampled or that the spacecraft-magnetopause relative velocity is high, preventing Cassini from resolving many data points in the layer, or both. This is also apparent from the sharp increase and decreases of τ corresponding to the boundary crossings in the time series plot.

Note that there is little change in the plasma characteristics (top two panels of Figure 4.8) within the magnetosheath, the magnetospheric or the boundary layer regions between each of the crossings. This is evidenced by the populations all lying on the same slope, which are spaced up to ~16 hours apart (for intervals 1 and 3). The magnetic field does, however, change between these intervals. We thus divide the data by τ-value into three main regions and consider how the values vary in and between each of the time intervals above. This will allow us to compare the three independent magnetopause encounters.

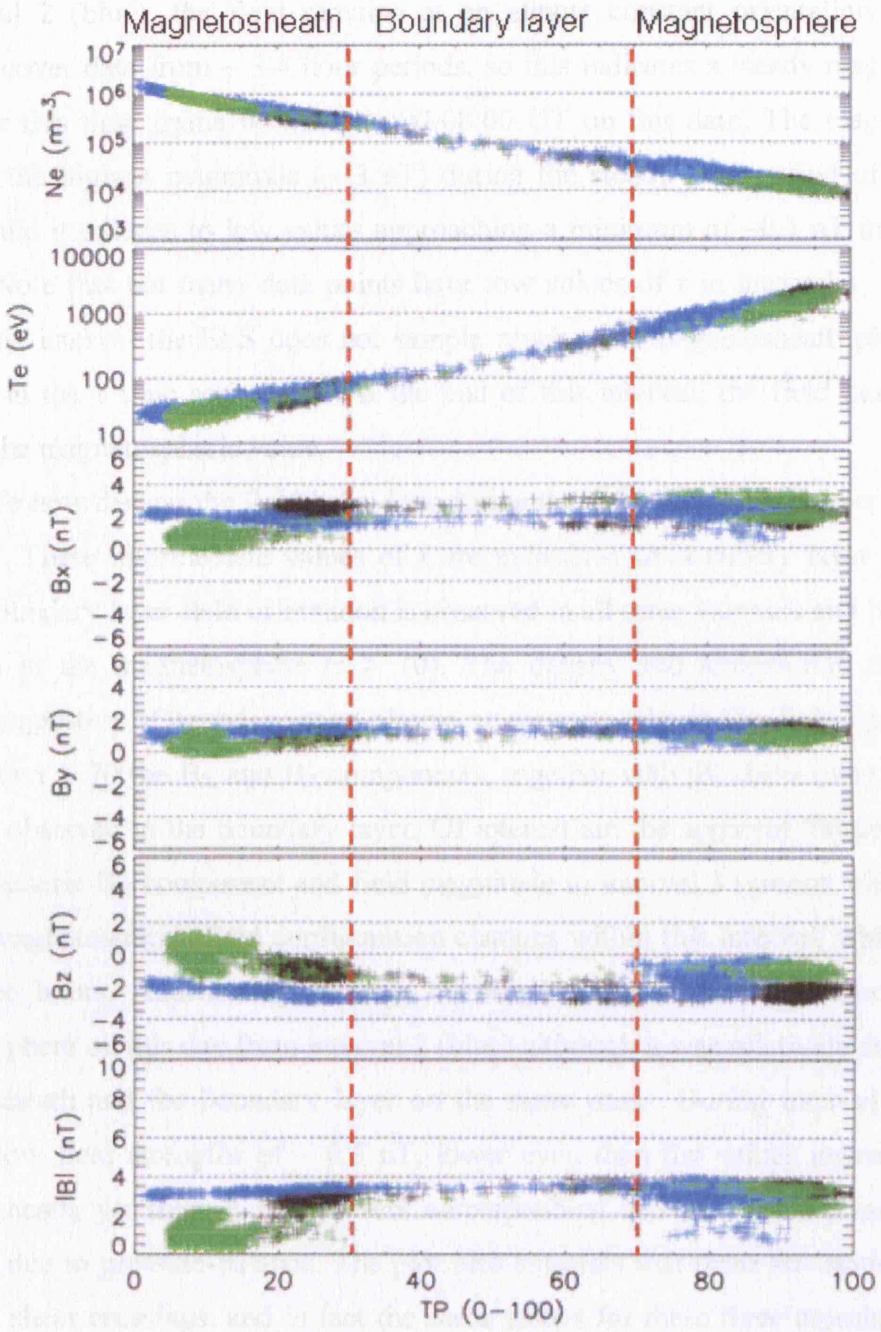

Figure 4.8 Data from three magnetopause crossings observed on 2 December 2005. Plots of N_e, T_e, B_X, B_Y, B_Z and |B| have been re-ordered by τ (0-100 on the horizontal axis). The different regions of τ have been marked out by the vertical lines. The transition from the high density, low temperature, disturbed field region of the magnetosheath (left hand side, $\tau \rightarrow 0$) to the low density, high temperature, ordered magnetosphere (right hand side, $\tau \rightarrow 100$) is obvious. The data is divided into three different time intervals to coincide with the three crossings from 00:00 to 04:00 UT (black crosses), 04:00 to 08:00 UT (blue) and 17:00 to 20:00 UT (green).

We first assess the behaviour of the field for each of the intervals at low values of τ ($0 < \tau < 30$). Generally, this will correspond to measurements from the magnetosheath. On this day, the field magnitude varies between ~ 0 – 3 nT. There is a spread of field orientations, most noticeable in interval 1 (black), followed by interval 3 (green), indicating a disordered field as is typical of the magnetosheath [Sibeck, 1994].

In interval 2 (blue), the field remains at an almost constant orientation. All three intervals cover data from ~ 3-4 hour periods, so this indicates a steady magnetosheath field over this time frame between 04:00-08:00 UT on this date. The magnetosheath field has the highest magnitude (~ 3 nT) during the steady field period of interval 2 (blue) while it reduces to low values approaching a minimum of ~0.1 nT in interval 3 (green). Note that not many data points have low values of τ in interval 1, suggesting that in this interval the ELS does not sample much pure magnetosheath plasma, also apparent in the τ time series plot. At the end of this interval, the field has generally adopted the magnetospheric value.

We now discuss the field behaviour during the different crossing intervals for $30 < \tau < 70$. These intermediate values of τ are indicative of boundary layer plasma. A similar boundary layer field orientation is observed in all three intervals and is similar to that seen in the magnetosphere ($\tau > 70$). The density and temperature continue to change, suggestive of boundary layer plasma on magnetospheric-like field lines.

For $\tau > 70$ the B_X and B_Z components, together with |B| show more variability than that observed in the boundary layer. Of interest are the apparent 'branches' in the magnetospheric B_X component and field magnitude in interval 3 (green). This suggests that the magnetospheric field configuration changes within this interval, which extends over three hours. Additionally, a more disturbed magnetic field is observed in the magnetosphere on this day from interval 2 (blue) although it was relatively steady in the magnetosheath and the boundary layer on the same pass. During interval 2 we also observe low field strengths of ~ 0.5 nT, lower even than the values measured in the magnetosheath, yet there is no apparent corresponding increase in the plasma density expected due to pressure-balance. The plot also suggests that these are moderately low magnetic shear crossings, and in fact the shear values for these three crossing are all < 18°.

4.5.3 Re-ordered data across a set of nine magnetopause encounters

The second example of plasma and magnetic field changes during a magnetopause transit is from 15 October 2005 between 05:00 UT and 21:00 UT. The time series plot of the τ parameter is in Figure 4.9 and the re-ordered data is in Figure 4.10.

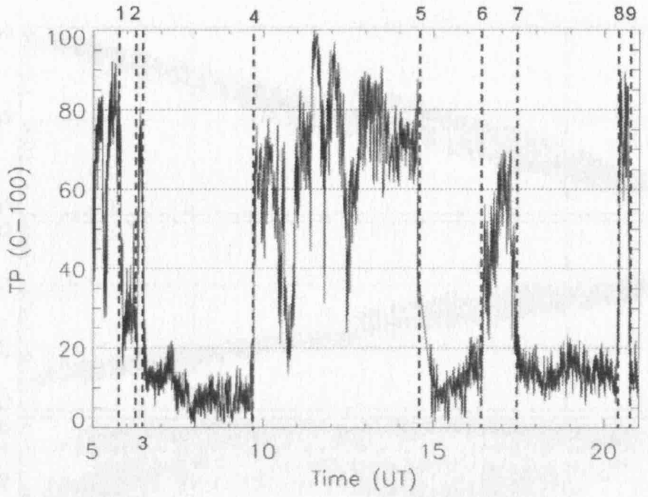

Figure 4.9 Time series of τ values for the 15 October 2005 from 05:00 UT to 21:00 UT. The nine magnetopause crossings (full and partial) are evidenced by the jump in low to high (or visa-versa) τ values at 05:50, 06:20, 06:25, 09:45, 41:45, 16:40, 17:15, 20:25 and 20:45 UT.

There are nine full and partial crossings during this interval, over a period of ~ 15 hours as seen in Figure 4.9. Once again, there is a general transition from the high density, low temperature region of the magnetosheath (left hand side, $\tau \rightarrow 0$) to the low density, high temperature region (right hand side, $\tau \rightarrow 100$). However, this time the graduation of the plasma from one region to the other is not straightforward and there is a clear departure of some points from a simple monotonical transition.

The magnetic field is also clearly disturbed throughout the interval. Again, we have separated the data into intervals corresponding to the different magnetopause crossings observed within this period. As two of the crossings are spaced only five minutes apart, we have grouped those data into a single interval. We have tried to keep a similar amount of data in each interval by dividing the data into ~ one hour periods and these, together with the associated colours used in Figure 4.10 are:

- Interval 1: 05:00 to 06:00 UT (black crosses);
- Interval 2: 06:00 to 07:00 UT (blue crosses);
- Interval 3: 09:30 to 10:30 UT (green crosses);
- Interval 4: 14:15 to 15:15 UT (red crosses);
- Interval 5: 16:20 to 17:00 UT (yellow crosses);
- Interval 6: 17:05 to 17:30 UT (cyan crosses);
- Interval 7: 20:00 to 21:00 UT (purple crosses).

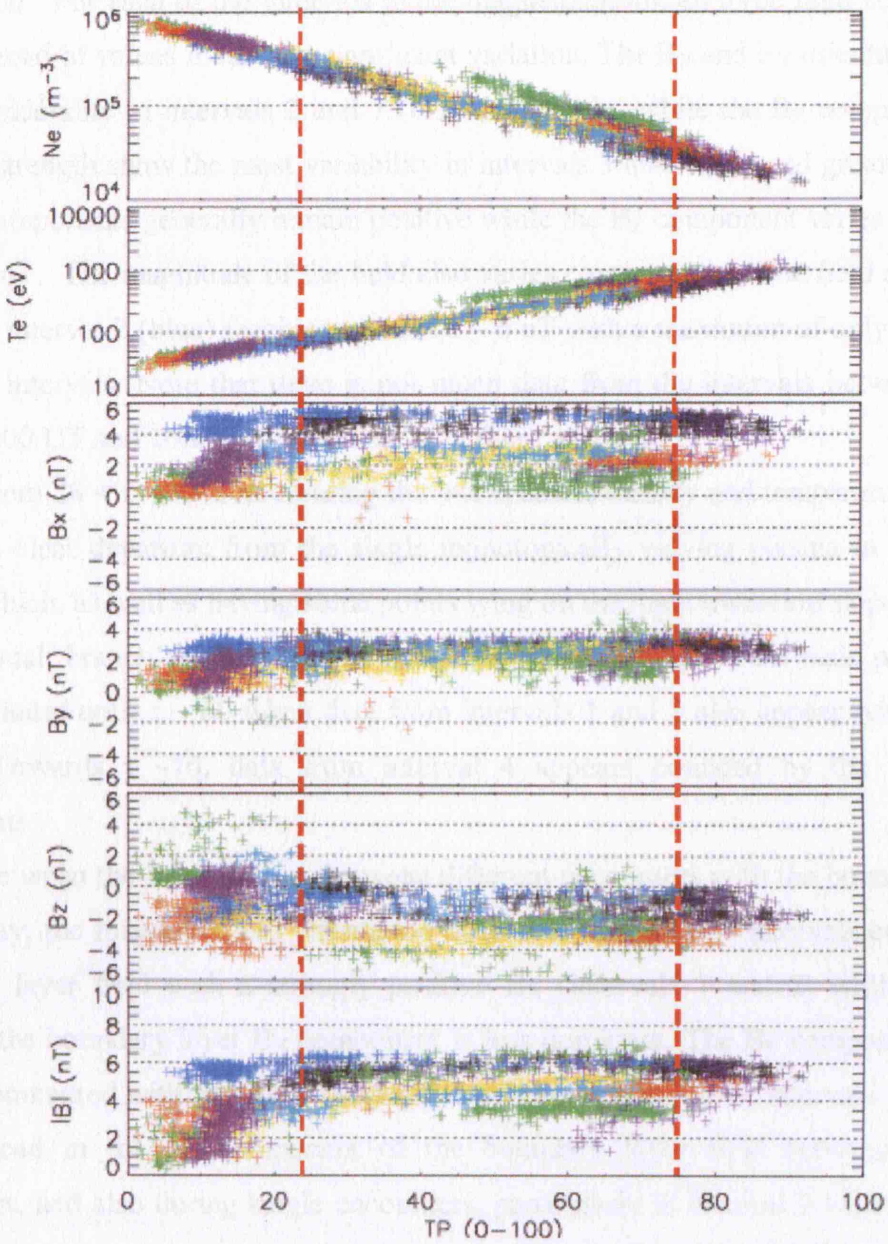

Figure 4.10 Data from nine magnetopause crossings (including four partial entries) observed on 15 October 2005. The plot takes the same format as that used previously in Figure 4.8. The data clearly varies within and between intervals as demonstrated by the spread of data points in each interval (single colour) and between intervals. There is a large spread of values in all three field components and the magnitude throughout the whole period and this is discussed further in the text. The data is divided into seven different time intervals to coincide with the nine crossings from 05:00 to 06:00 UT (black crosses), 06:00 to 07:00 UT (blue crosses), 09:30 to 10:30 UT (green crosses), 14:15 to 15:15 UT (red crosses), 16:20 to 17:00 UT (yellow crosses), 17:05 to 17:30 UT (cyan crosses) and 20:00 to 21:00 UT (purple crosses).

We first consider those low values of τ corresponding to the magnetosheath ($0 < \tau < 28$) since this appears to be a natural boundary in the plasma regions, and discuss the behaviour of the plasma and magnetic field during the individual magnetopause crossings (intervals 1 to 7). The density and temperature show evidence of a single population in all intervals, which varies monotonically as the magnetopause is

approached. For each of the intervals in the magnetosheath, all three field components have a spread of values indicating significant variation. The B_X and B_Y orientations vary most considerably in intervals 2 and 7 (blue and purple) while the B_Z component and the field strength show the most variability in intervals 3 and 4 (red and green). The B_X and B_Y components generally remain positive while the B_Z component varies from ~ -5 nT to +5 nT. The magnitude of the field also varies considerably. The field strength is largest in interval 2 (blue) reaching values of ~ 6 nT with a maximum of only ~ 4 nT in the other intervals. Note that there is not much data from the intervals between 05:00 UT to 06:00 UT and 16:20 UT to 17:00 UT at these τ values.

From $28 < \tau < 75$, representing the intermediate density and temperature values, there is a clear departure from the single monotonically varying plasma in interval 3 (green) which, as well as having some points lying on the main transition slope, also has an additional 'branch' in the plot with an almost identical slope to the main population. This continues until $\tau \sim 60$ when data from intervals 1 and 7 also appear lying on this branch. Towards τ ~70, data from interval 4 appears bounded by the two main populations.

Between the intervals, i.e. between different encounters with the boundary layer on this day, the magnetic field orientation is seen to vary. Some intervals encounter a boundary layer field with a strongly positive B_X (intervals 1 and 2) while in other intervals the boundary layer B_X component is less dominant. The B_Y component is less variable compared with B_X in the boundary layer throughout all the intervals. There is a large spread in the B_Z component of the boundary layer field between different encounters, and also during single encounters, particularly in interval 3 when values of B_Z range from ~ -6 nT to +2 nT. This interval covers only an hour of observations and indicates how changeable the field orientation is in this region. There is a slight departure from this at the start of the τ range, when intervals 1 and 6 do not assume a southward orientation until τ values of 30-35. Also, at high values of τ (~ 65-70) which are close to the magnetosphere in τ-parameter space, a few measurements of the boundary layer in interval 3 have values of $B_Z \sim +1$ nT. Note that there is not much data in this τ range from intervals 4 and 7 (red and purple) suggestive of fast crossings, and in fact, in the time series plot (Figure 4.9) these crossings do appear to be abrupt transitions in τ.

Finally, between $\sim 70 < \tau < 95$, the data represents that sampled in the magnetosphere proper. The plasma appears to return to a simple monotonical transition, yet the field remains fairly disturbed. The orientation of the field is positive in both the

B_X and B_Y components with more variation seen in B_X, and negative in the B_Z component. The field magnitude remains high (~ 4-6 nT) in most intervals in the magnetosphere.

4.5.4 Re-ordered data across a set of eight magnetopause encounter

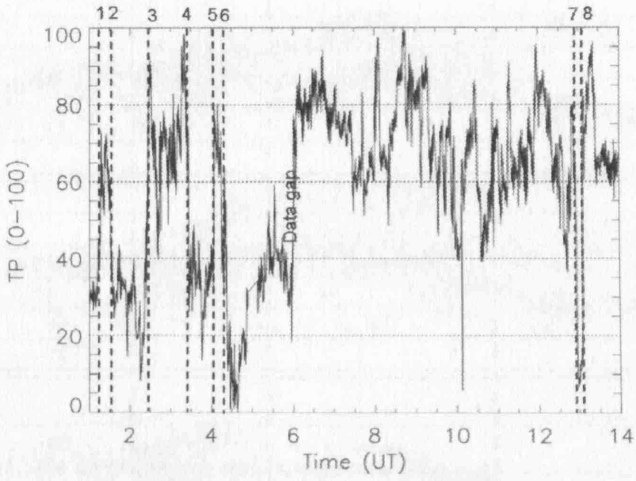

Figure 4.11 Time series of τ values for 28 March 2005 from 01:00 UT to 14:00 UT. The eight magnetopause crossings (full and partial) are evidenced by the jump in low to high (or visa-versa) τ values at 01:24, 01:35,02:30, 03:20, 04:04, 04:23, 12:55 and 13:06 UT.

The last example of τ- re-ordered data is from 28 March 2005 between 01:00 UT to 14:00 UT. The original time series plot for τ values is in Figure 4.11 and the associated re-ordered data in Figure 4.12. This is clearly a region with much variation in the magnetopause position relative to Cassini, resulting in a number of partial crossings in addition to full crossings. Note that there is a data gap over one crossing resulting in an even number of encounters. Again, we have separated the data into intervals corresponding to the different magnetopause crossings observed within this period. As several of the crossings are closely spaced we have grouped some data into a single interval. The colours used in the plot are:

- Interval 1: 01:00 to 02:00 UT (black crosses);
- Interval 2: 02:00 to 03:00 UT (blue crosses);
- Interval 3: 03:00 to 03:45 UT (green crosses);
- Interval 4: 03:45 to 04:30 UT (red crosses);
- Interval 5: 12:30 to 13:30 UT (yellow crosses).

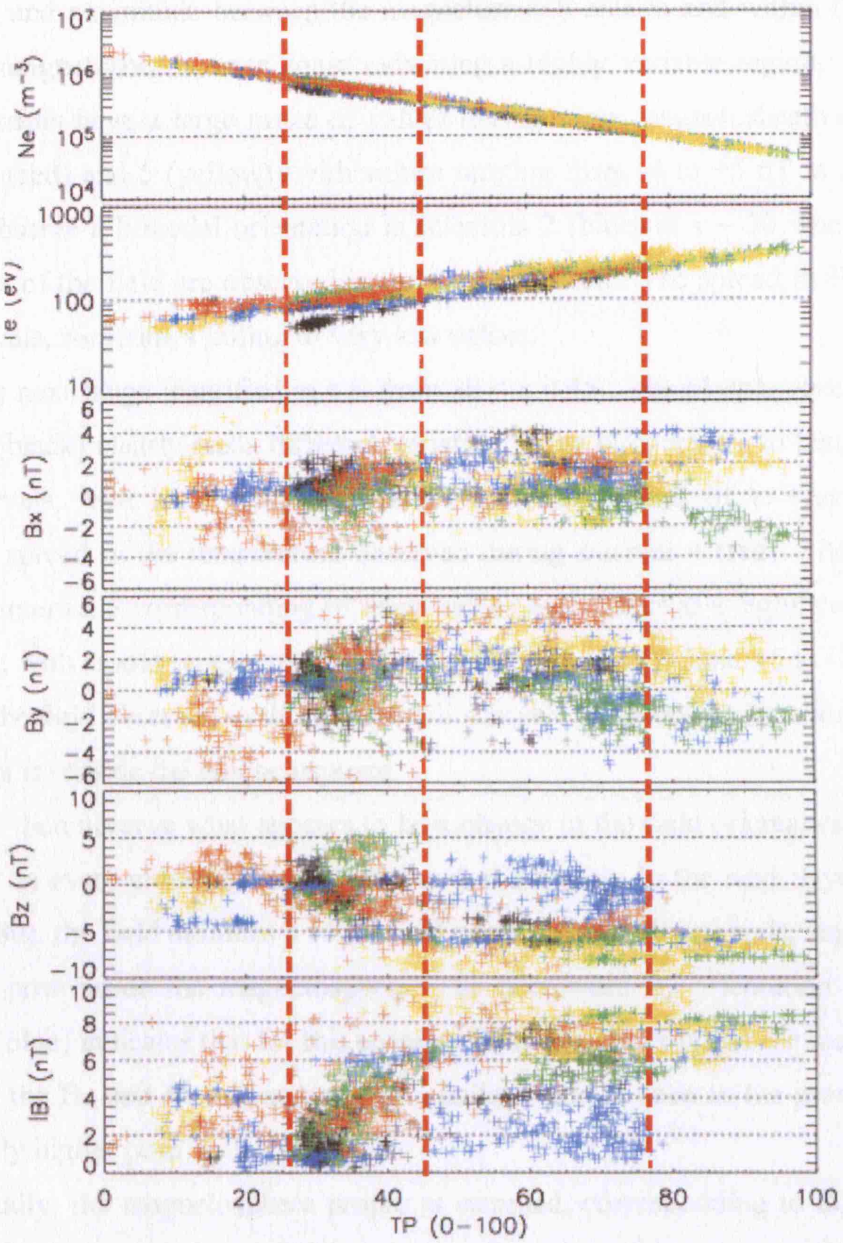

Figure 4.12 Data from eight magnetopause crossings (including four partial entries) observed on 28 March 2005. The plot takes the same format as before. The magnetic field is highly disturbed throughout the transition. The data is divided into five different time intervals to coincide with the eight crossings from 01:00 to 02:00 UT (black crosses), 02:00 to 03:00 UT (blue crosses), 03:00 to 03:45 UT (green crosses), 03:45 to 04:30 UT (red crosses) and 12:30 to 13:30 UT (yellow crosses). The different regions of τ have been marked out by the vertical lines.

The period has been divided into several regions which have similar characteristics in τ parameter-space. The first is $0 < \tau < 30$, when Cassini is in the magnetosheath. There are slight differences in the values for the plasma temperature in this region for different intervals (note the spread in values between intervals 2 (blue), 4 (red) and 5 (yellow)). Note there is little data from intervals 1 and 3 with these τ values indicating that not much magnetosheath plasma was included in these intervals, also seen in the time series plot in Figure 4.11. There is a large distribution of the field

orientation and magnitude between the magnetosheath entries and within the intervals inside the magnetosheath, once again indicating a highly variable region. The B_X and B_Y components have a large range of values during some magnetosheath entries (e.g. intervals 4 (red) and 5 (yellow)) with values ranging from -4 to +5 nT in some cases. We also observe a bimodal orientation in intervals 2 (blue) at $\tau \sim 20$ when two main orientations of the field are observed in the magnetosheath. The spread in $|B|$ is evident in all intervals, sometimes falling to very low values.

The next range identified in τ is from $30 < \tau < 45$. The plasma observed during interval 1 (black) clearly has a different variation in the temperature to that seen in the other intervals, with lower temperatures for the same values of τ. There is also a noticeable spread in the temperature observed during interval 4 (red). There are little data from interval 5 corresponding to these values of τ. There is a significant variation in the field, with values ranging from $\pm$ 4 nT in B_X, $\pm$ 6 nT in B_Y and +5 to -10 nT in B_Z. Note that the field observed in this region still shows a northward orientation, indicating that Cassini is outside the magnetosphere.

We then observe what appears to be a change in the field orientation at constant values of τ in every crossing, marking the end of a region. In the next 'layer' observed ($45 < \tau < 80$), the field assumes a southward orientation in all intervals, suggesting that Cassini is now inside the magnetosphere. The northward B_Z orientation observed in interval 2 (blue) indicates that for this crossing Cassini is still outside the magnetopause. Generally, the B_X and B_Y orientations are similar to those seen in the previous 'layer' with slightly higher positive B_Y values.

Finally, the magnetosphere proper is sampled, corresponding to $80 < \tau < 100$. Only data from intervals 2, 3 and 5 are present since intervals 1 and 4 (as apparent from the time series plot in Figure 4.11), are only partial entries into the magnetosphere. As expected from a simple picture of the magnetosphere, the field strength is high and steady and the B_Z component is strongly southward. However, there is still a large variation in the orientation of B_X and B_Y between and within intervals 2, 3 and 5 indicative of a magnetically variable interior. The variations in the local magnetosphere are seen over timescales ranging from ~ one hour to ten hours. Note that in interval 3 the B_X component actually points anti-sunward suggesting that Cassini is below the magnetodisc whereas only ~ one hour prior to this observation in interval 2, it is above the magnetodisc.

Overall, the large variability within the intervals suggests that these field changes occur on timescales less than one hour. Additionally, the field variations seen

in the boundary layer exceed those seen in either the magnetosheath or the magnetosphere suggesting that it is not changes in these regions driving the boundary layer variation but instead there are processes in the boundary layer itself causing the disturbance.

4.6 Survey of Magnetopause crossings

4.6.1 IMF conditions

Initially, we consider the sense of the magnetosheath B_Z component recorded just outside the magnetopause. From the 191 crossings used in this study, there are 142 instances where the magnetosheath field is southward and 49 where it has a northward orientation. This immediately suggests that there is a bias towards low shear crossings in the dataset, assuming that the magnetospheric field is predominately southwards. However, as already discussed in section 4.4.3 this may not be the case. Thus, a more representative measure of the difference between the upstream and downstream field orientations has been calculated using the method detailed in section 4.4.3.2.

Figure 4.13 shows a plot of the magnetic shear calculated for all crossings. The clear bias towards low shear (~ < 30°) crossings along the flank magnetopause is maintained. Values greater than this indicate a slightly bi-modal shape to the distribution centred on shear values of ~ 80° and ~ 110° with minima near 50°, ~ 90° and ~180°. The average shear is 63°. We classify crossings as high shear > 60° to agree with Phan et al., [1994] and low shear as < 60°.

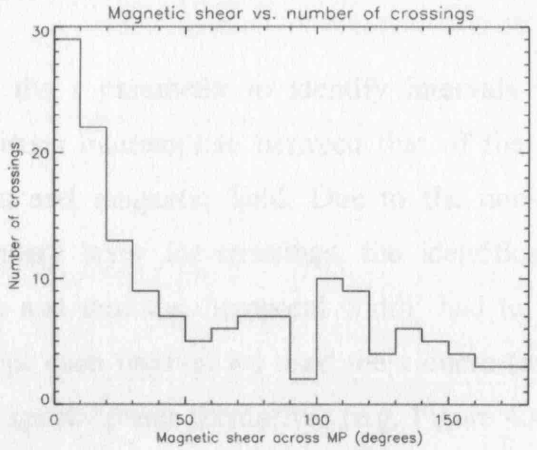

Figure 4.13 Histogram of magnetic shear for all crossings. There is a clear tendency for lower shears.

The low and high shear cases were plotted as function of position in local time and magnetic latitude on the magnetopause. However, there is no clear pattern, with all magnetic shears being observed at all locations, and hence these data are not shown here.

4.6.2 Variability in the magnetopause position

Many of the 191 crossings were observed to occur in groups as the magnetosphere expanded and contracted continuously over the spacecraft location. Multiple crossings are seen to occur over the full range of subsolar stand-off distances inferred from this Cassini dataset, whether the magnetosphere is in a compressed state at 19 R_S (e.g. 28 March 2005, where there are eight crossings in 13 hours) or in an expanded state (e.g. 20 November 2005 with Cassini at 32 R_S where there are five crossings in 19 hours). There does not appear to be a tendency for a more variable magnetosphere when compressed or expanded. Most crossings occurred with magnetopause stand-off distances < 30 R_S, with the exception of a few multiple crossings near $R_0 \sim$ 32-33 R_S. The average subsolar stand-off distance is 24 R_S, slightly lower than that quoted by Arridge et al., [2006a] of 25 $R_S \pm$ 1.238 R_S, but within the error. This study includes a larger range of crossings than used to generate the Arridge model.

4.6.3 Identification and properties of the magnetopause boundary layer

We have used the τ parameter to identify intervals when Cassini observes plasma with characteristics intermediate between that of the magnetosheath and the magnetospheric plasma and magnetic field. Due to the non-uniformity in τ values representative of boundary layer for crossings, the identification of the regions of boundary layer plasma and thus the 'temporal width' had to be considered for each interval individually. For each interval we used the τ curve (as in Figure 4.3), a time series plot of τ and the spectrograms themselves (e.g. Figure 4.4) to determine 'by eye' the range of τ bounding boundary layer electrons. Of course, this makes the analysis subjective, but it allows the extent of the boundary layer to be carefully chosen for every case.

Two methods of sorting the boundary layer have been applied; the first determines the 'temporal width' of the boundary layer and the second, the density in the boundary layer.

4.6.3.1 Boundary layer type based on 'temporal width'

We quantify the duration that Cassini spends in a region characterised by boundary layer plasma, i.e. how long it took Cassini to traverse from pure magnetosheath plasma into pure magnetospheric plasma, assuming the spacecraft was moving approximately normal to the boundary which seems adequate for the this period of the mission. This provides a temporal 'width' of the layer rather than a spatial width.

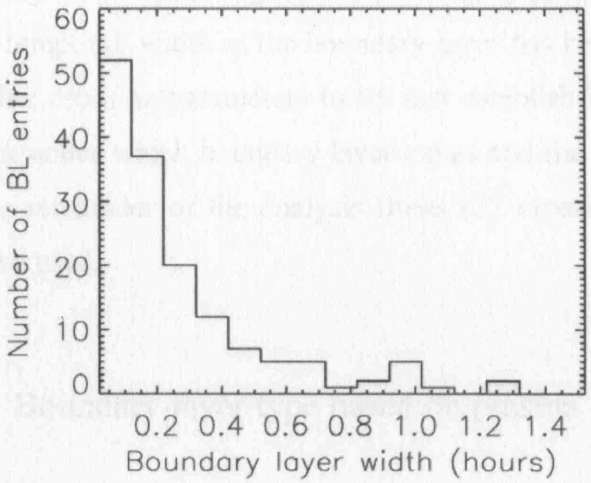

Figure 4.14 Histogram of boundary layer temporal widths for all 152 magnetopause crossings (those crossings with no boundary layer have been omitted from the plot). The plot shows those widths up to one hour 30 minutes in duration. Overall, there is a tendency for a short boundary layer crossing duration, with the majority of the crossings encountering boundary layer plasma for $< \sim 25$ minutes.

Of the 191 crossings used in the boundary layer analysis, the ELS detected a region of intermediate boundary layer plasma between the magnetosheath and the magnetosphere for 79% of crossings (152) while 21% (40) showed no evidence of a transitional plasma layer. The frequency of the boundary layer temporal widths is shown in histogram format in Figure 4.14. The occurrence rate of boundary layer plasma is similar to that for Earth as discussed by Eastman et al., [1996] who found that crossings without boundary layer ('pristine' crossings) only occurred for 10% of crossings. Of course, those cases without boundary layer could arise from very rapid magnetopause motion relative to the spacecraft, resulting in the ELS being unable to resolve the layer.

Of the 152 crossings with a boundary layer, there are six with durations lasting over one hour, the maximum being one hour and 57 minutes, but note that the histogram in Figure 4.14 only shows those boundary layer durations under one hour 30 minutes for clarity. The average temporal width is 17 minutes.

The high temporal resolution of the plasma instrument (2s) allows the time within a layer to be well sampled. No consideration is given to the width of the magnetopause, i.e. the width of the current layer, where the field rotates between magnetosheath and the planetary field, since we are focussing on the plasma properties of the boundary layer. However, the magnetopause current layer is expected to be thin compared with the boundary layer width [e.g. Berchem and Russell, 1982]. Thus, the 'width' derived here is the time interval between crossings of the outer edge of the MPCL and the inner edge of the boundary layer [Phan and Paschmann, 1996].

Now that the 'temporal' width of the boundary layer has been extracted, this can be correlated with other crossing parameters to try and establish if there are particular conditions or locations under which boundary layer exists and the nature of the layer in these regions. For the remainder of the analysis these 152 crossings with measurable boundary layers will be used.

4.6.3.2 Boundary layer type based on plasma density

Another boundary layer property of interest is the density of the plasma compared with that in the local magnetosheath and magnetosphere. Previous studies at Earth have suggested that the boundary layer can be further subdivided into different layers with different properties, e.g. the lower density, higher temperature (boundary layer halo) and the lower temperature, higher density (boundary layer proper) regions of intermediate plasma as reported in Sckopke et al., [1981]. However, we will treat the layer as a single population and establish the average density in the layer as a whole.

We expect the plasma in the boundary layer to be formed by the entry of magnetosheath plasma into the magnetosphere. Thus, for each boundary layer an average density within that layer as a fraction of the magnetosheath density has been calculated. In order to gauge the amount of magnetosheath plasma gaining entry to the magnetosphere, we first remove the magnetospheric density from that observed in the boundary layer before taking the ratio.

$$N_{ratio} = \left(\frac{n_{bl} - n_{sp}}{n_{sh}} \right)$$

Equation 4.3

The average magnetosheath (magnetospheric) density was calculated by taking a five minute long interval five to ten minutes upstream (downstream) of the crossing. The magnetospheric values were taken outside of any boundary layers.

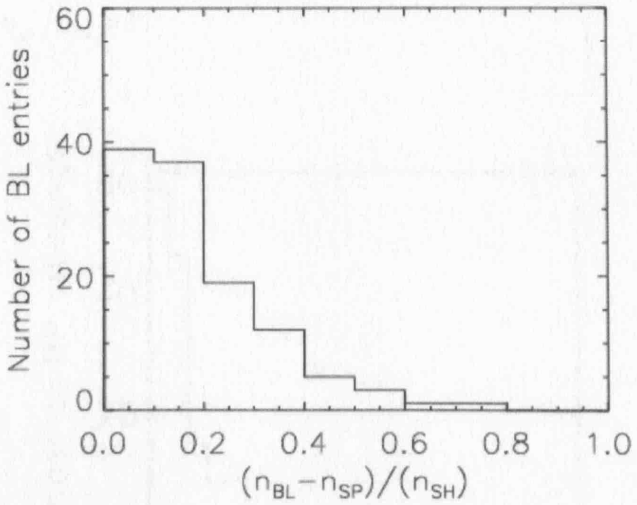

Figure 4.15 Histogram of the electron density ratio against the number of crossings. We subtract the average magnetospheric density from that in the boundary layer (n_{BL}), before dividing by the magnetosheath density (n_{SH}), to take into account variations in the local conditions inside the magnetopause. We have not included 30 cases where the ratio < 0.

In 30 of the cases (~ 20%), the density in the magnetosphere was found to be larger than that in the boundary layer, giving a negative ratio. This may result if Cassini crosses directly into the plasmasheet in the outer magnetosphere. Here the density is expected to be larger than that typically found in the outer magnetosphere. These cases are found to occur for crossings on the same inbound/outbound passes. These negative values are omitted from the resultant histogram, which is shown in Figure 4.15 for the remaining 122 cases, and shows the frequency of the boundary layer density ratios.

The mean of the remaining density values is 0.19, thus the boundary layer has an average density which is 19% that of the magnetosheath value. From this analysis we conclude that 78 of the 122 boundary layers (with positive ratios) have a density that is at least 10% of the magnetosheath density and 22 have a density greater than 30% of the magnetosheath density.

We also consider the typical ratio of the magnetospheric density to the magnetosheath density for all crossings with a boundary layer (so we now include the

cases where the density in the magnetosphere is higher than the local boundary layer density, i.e. all 152 cases). The results of this are again shown in histogram format in Figure 4.16. We would expect this ratio to be < 1 in all cases since the outer magnetospheric plasma is typically rare (see chapter 3). However, we have also demonstrated that the magnetospheric density is greater than the density in the boundary layer in ~ 20% of cases. Therefore we cannot assume this is the case. In fact we find that only 8 of the intervals studied have a larger magnetospheric density than that in the magnetosheath, i.e. $n_{sp}/n_{sh} > 1$.

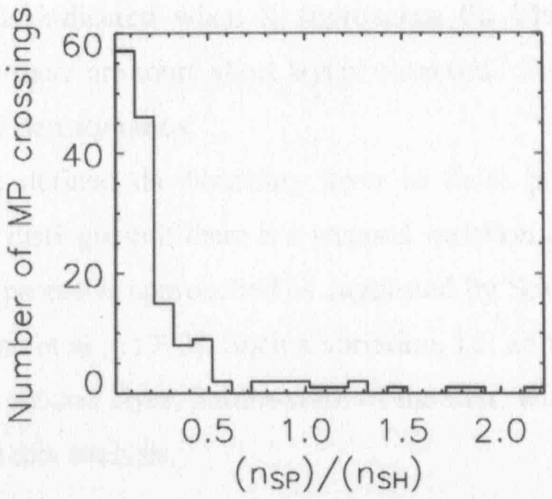

Figure 4.16 Histogram of the electron density ratio either side of the magnetopause (outside any boundary layers) against the number of crossings (152) This gives an indication as to the typical density ratio between the magnetosheath and magnetosphere. The low values indicate the low density of the magnetosphere compared with the magnetosheath.

The average ratio of $n_{sp}/n_{sh} > 1$ is ~ 0.27, which is considerably larger than the value found for the average ratio of the boundary layer density to magnetosheath density. However, that number is found if we include those 8 values with $n_{sp}/n_{sh} > 1$ which may be biasing the mean. If we calculate the average ratio for values where $n_{sp}/n_{sh} < 1$ we get a value of 0.20 which still suggests that, on average, the local magnetospheric density is comparable to that in the boundary layer. This is puzzling if we consider that the boundary layer is most likely formed from the entry of dense magnetosheath plasma into the rarer (usually) outer magnetosphere.

For those cases where the magnetospheric plasma density is unexpectedly high, Cassini could be crossing directly into Saturn's plasmasheet, which might be expected to have a much higher density than nominal outer magnetospheric, lobe-type plasma [e.g. Arridge et al., 2006b]. These results indicate that this must occur often enough to

affect our results and suggests that knowledge of the local magnetospheric density is crucial to understanding the boundary layer characteristics.

4.6.3.3 Plasma density in boundary layers of different widths

Here we examine if there is a relation between the density and the width of the boundary layer. Figure 4.17 shows a scatter plot of boundary layer temporal width and the boundary layer density ratio, N_{ratio} and, based on the low correlation coefficient, R = 0.04 there is no clear linear correlation between the temporal width and density of the boundary layer. The high value of S indicates that this value of R has little significance (a high significance is indicated when S approaches 0). This may be due to the parameter space, since there are more short layers observed. From the plot, the thicker layers tend to have low density ratios.

Since we have defined the boundary layer as those points with intermediate values of τ, we cannot distinguish if there is a stepped variation in the plasma behaviour as the magnetosphere proper is approached as suggested by Sckopke et al., [1981] and indicated by Paschmann et al., [1993]. Such a variation, i.e. an initial layer with higher density, followed by a second layer, Saturn-ward of the first, with lower density, would not be distinguished in this analysis.

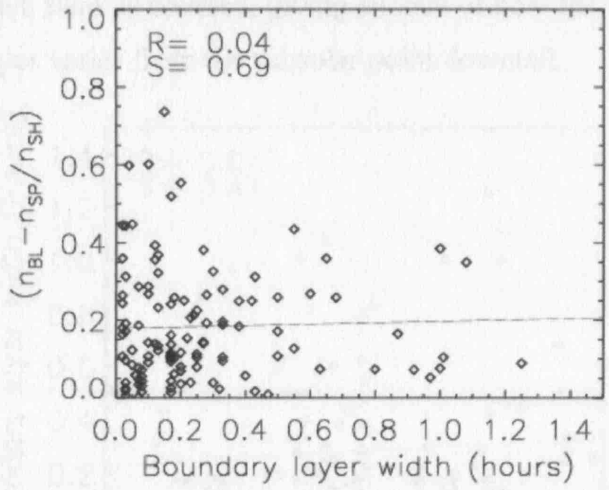

Figure 4.17 Boundary layer width against the density in the boundary layer as a function of the magnetosheath density (defined in Equation 4.3). There is no correlation found between these two boundary layer parameters indicated by the low value of R.

4.6.4 Boundary layer at different locations on the magnetopause

Here we examine if there is any local time or latitudinal dependency of the boundary layer at the magnetopause.

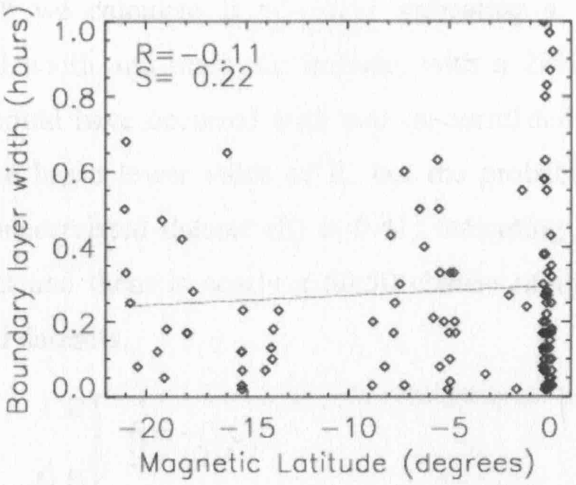

Figure 4.18 Boundary layer width (hours) plotted against magnetic latitudes from -22° to 1°. This range is a product of Cassini's orbit in the first 18 months of the mission. A line of best fit is also included. The bias of the measurements to crossings at the equator is apparent by the clustering of points at ~ 0°. The negative value of the rank correlation (see section 4.4.4) R suggests an inverse relationship between these two parameters, the low associated value of significance S indicates that there is a 22% probability of this correlation being achieved with two unrelated sets of data.

The boundary width is plotted in Figure 4.18 and Figure 4.19 against magnetic latitude and the local time of each crossing. As is shown in Figure 4.1, there is a limited range of LTs and latitudes sampled for use in this study due to Cassini's trajectory in the first part of its mission. So this is not a full assessment of the dependence of the boundary layer characteristics on the position on the magnetopause. Nevertheless, almost the whole dawn flank is covered, giving an idea of how the near-equatorial width and density of the layer varies from the subsolar point downtail.

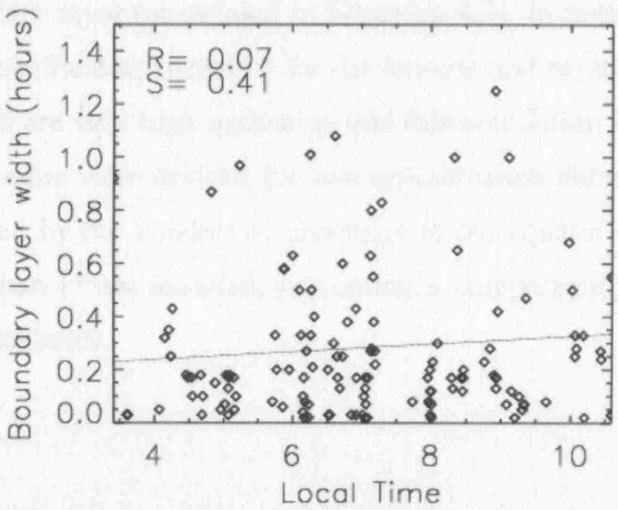

Figure 4.19 Boundary layer width (hours) plotted against local time from 3 to 11. This range is a result of Cassini's orbit in the first 18 months of the mission. A line of best fit is also included to aid the eye as is the value of the rank correlation (see section 4.4.4) R, and the associated significance S. These two values suggest that there is a very weak linear relationship between these two datasets, with the same relationship being achieved with an uncorrelated dataset 41% of the time.

In Figure 4.18 we calculate R = - 0.11 indicating a weak anti-correlation between the temporal width and magnetic latitude, with a 22% probability that this value of correlation could have occurred with two un-correlated datasets. The second plot against local time has a lower value of R, but the probability of achieving this correlation with an uncorrelated dataset (S) is 0.41, indicating that this value is not statistically significant and there is nearly a 50:50 chance of finding this correlation between two unrelated datasets.

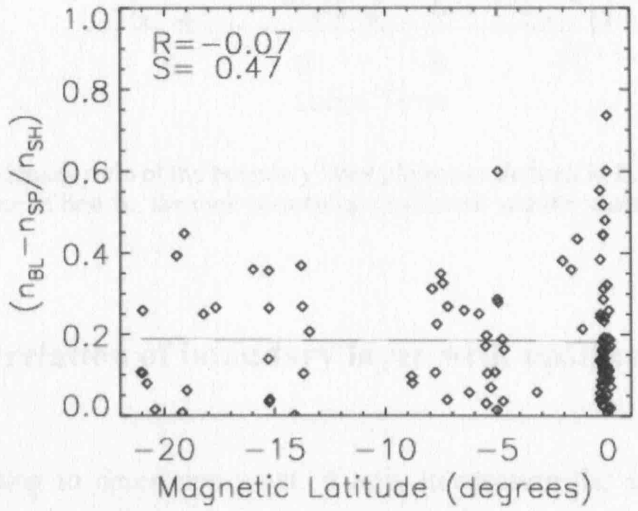

Figure 4.20 Plot of the density ratio of the boundary layer plasma as defined in Equation 4.3 against magnetic latitude from -22° to 1°. A line of best fit is also included for each data set. The bias of the measurements to crossings at the equator is apparent by the clustering of points at ~ 0°.

In Figure 4.20 and Figure 4.21 we carry out the same analysis using the density ratio of the boundary layer (as defined in Equation 4.3). In both cases there are very weak correlation coefficients (negative for the latitude and positive for the local time) but the values of S are very high indicating that this correlation is no more significant than if the same value were derived for two un-correlated datasets. Of course, these data may be biased by the number of crossings at the equator, (points near 0°). No latitudes greater than 1° are sampled, preventing a comparison between the northern and southern hemispheres.

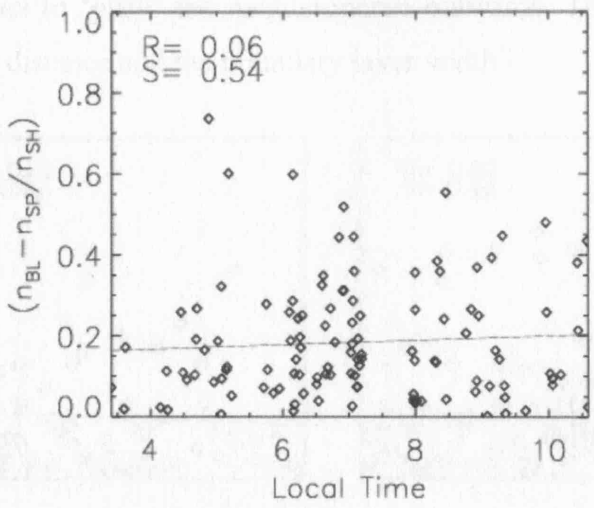

Figure 4.21 Plot of the density ratio of the boundary layer plasma as defined in Equation 4.3 against local time from 3 to 11. A line of best fit, the rank correlation coefficient and the statistical significance of the value is also included

4.6.5 Correlation of boundary layer with upstream parameters

We are hoping to determine what, if any, interaction the solar wind magnetic field and pressure have on the magnetopause and magnetosphere. We now explore the correlation of these parameters with boundary layer width and density.

4.6.5.1 The variation in boundary layer with solar wind dynamic pressure

Figure 4.22 contains four plots of the boundary layer temporal width and density ratio against the inferred dynamic pressure and magnetopause stand-off distance from the Arridge et al., [2006a] magnetopause model as described in section 4.2. Thus, we can test whether the strength of the solar wind pressure controls the width of, and density in, the boundary layer. The very weak negative correlation between the width and dynamic pressure has an associated significance value that suggests a lack of any relationship. There is a very low value of S (0.05) associated with the negative correlation between the density ratio and the dynamic pressure. This is a significant result and indicates that the dynamic pressure may play a role in the formation and population of the boundary layer. There is a weak correlation of subsolar distance to increase with the density in the layer, suggesting that the density inside the

magnetopause may act to 'push' the magnetopause outwards. There is no correlation between the subsolar distance and the boundary layer width.

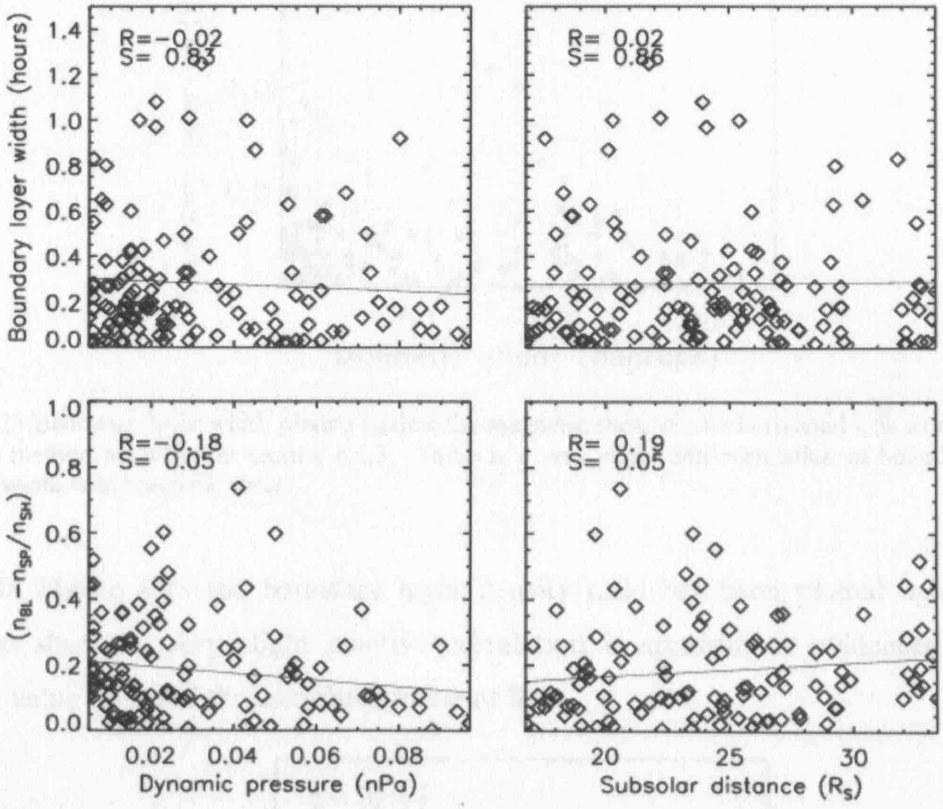

Figure 4.22 Correlation plots of boundary layer temporal width and density ratio, against the inferred upstream solar wind dynamic pressure in nPa and the resultant subsolar stand-off distance of the magnetopause as calculated from the Arridge et al. [2006a] magnetopause model. Top left: there is no significant correlation. Bottom left: The best fit line and negative correlation coefficient (which, from the low value of S is significant) indicates a decrease of density in the layer as a function of the magnetosheath density with increasing dynamic pressure.

4.6.5.2 The variation in boundary layer with magnetic shear

As well as the solar wind pressure, the orientation of the magnetosheath field can have a significant impact on the topology of the magnetopause. The shear was calculated as described in section 4.4.3.2 and in Figure 4.23 is a scatter-plot of shear against boundary layer width. The correlation indicates a very slightly negative trend with shorter boundary layers at higher magnetic shear. This correlation has only a 13% chance of being achieved with two unrelated datasets.

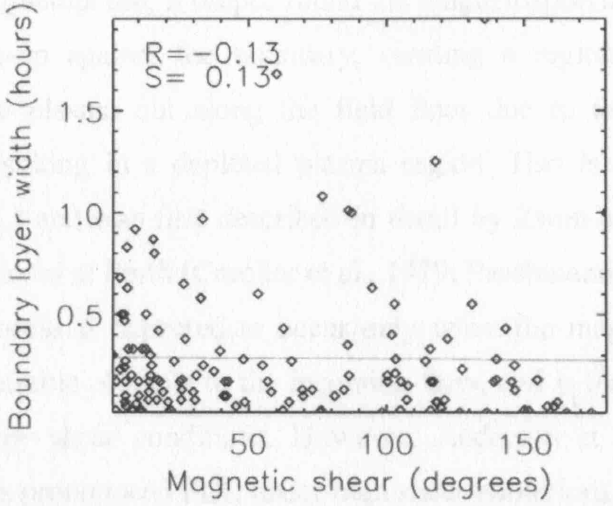

Figure 4.23 Boundary layer width plotted against the magnetic shear on the horizontal axis as calculated using the method described in section 4.4.3. There is a very slight anti-correlation of boundary layer temporal width with magnetic shear.

In Figure 4.24 the boundary layer density ratio has been plotted against the magnetic shear. A very slight positive correlation is apparent as evidenced by the positive value of R and the associated value of S.

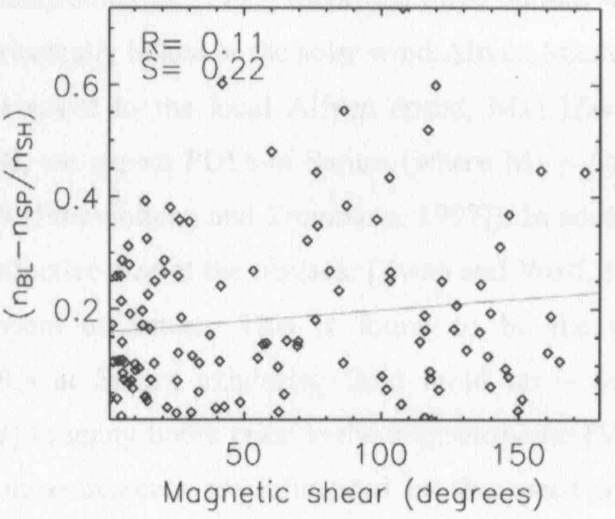

Figure 4.24 Boundary layer density ratio plotted against the magnetic shear on the horizontal axis as calculated using the method described in section 4.4.3. A weak positive correlation is apparent.

4.7 Plasma Depletion Layers (PDL's)

4.7.1 Introduction to PDLs

In this section we investigate the plasma and magnetic field variations on the magnetosheath side of the magnetopause. As the solar wind flow carries the magnetic

field towards the magnetopause, it drapes round the magnetospheric obstacle. Magnetic flux tubes will pile-up against the boundary, creating a region of increased field strength, forcing the plasma out along the field lines due to the need to maintain pressure balance, resulting in a depleted plasma region. This is known as a plasma depletion layer (PDL) and was first described in detail by Zwan and Wolf [1976] and have often been observed at Earth [Crooker et al., 1979; Paschmann et al., 1993; Phan et al., 1994]. This process is expected to occur only when the magnetopause is acting largely as an impenetrable obstacle to the incoming flow, and is therefore magnetically closed, i.e. under low shear conditions. However, Anderson et al., [1997] reported observations of a less pronounced PDL under high shear conditions, indicating that pile-up was occurring despite the presence of reconnection. They suggested that the difference in the prevalence of PDLs for high and low shear cases may be related to the reconnection efficiency.

Maynard et al., [2004] also reported PDLs under presence of high magnetic shear conditions, although the merging site was remote from the observed region. Observations of PDLs at Earth show typical temporal widths of ~ 10 minutes [Phan et al., 1994], while Paschmann et al. [1993] identified three minute wide PDLs. Since the PDL thickness is intrinsically linked to the solar wind Alfvén Mach number (the ratio of the local solar wind speed to the local Alfven speed, M_A) [Zwan and Wolf, 1976; Farrugia et al., 1998], we expect PDLs at Saturn (where $M_A \sim 5$) to be wider than at Earth (where $M_A \sim 8$ [Baumjohann and Treumann, 1997]). In addition, the depletion is proportional to the effective size of the obstacle [Zwan and Wolf, 1976] which will also result in thicker layers at Saturn. This is found to be the case, with previous observations of PDLs at Saturn exhibiting field build up ~ one hour [Bavassano Cattaneo et al., 1998] to many hours prior to the magnetopause [Violante et al., 1995]. Additionally, these measurements are influenced by the speed of the magnetopause; however, we do not know typical values for this at Saturn preventing us from comparing with typical values at Earth.

Evidence for a PDL has also been reported at Saturn in Voyager 2 data [Violante et al., 1995] upstream of a low shear magnetopause. A gradual increase in the magnetic field strength was accompanied by a corresponding decrease in the total proton density representative of a PDL. The observation of PDLs at Saturn has so far been limited to this one crossing. With the wealth of magnetopause crossings in the Cassini data, we are able to study the overall properties of the upstream region. This will allow us to establish both the presence and also the frequency of such a phenomenon at Saturn.

4.7.2 Survey of PDLs

4.7.2.1 Data Selection

In order to establish the presence of PDLs and under what conditions they occur at Saturn, we use superposed epoch analysis (SEA) as applied in Paschmann et al., [1993] and Phan et al., [1994] to illustrate the average properties of the magnetosheath upstream of the magnetopause. This will allow us to compare the results directly with those obtained at Earth, aiding in comparative magnetosphere studies. We performed this analysis over five minutes in the magnetosphere and a range of timescales upstream (~five minutes to two hours upstream) of the magnetopause, to try to establish over what time frame any variations in the magnetic field or plasma occurred.

We have only included data for crossings that are well spaced so that there is at least two hours of upstream data. This ensures we are sampling undisturbed magnetosheath plasma (e.g. not too close to another crossing) and allows us to estimate any field build-up over a significant time frame. We have also removed any encounters with data gaps in the upstream magnetosheath. We have chosen a two hour timescale since the previous observation at Saturn suggests the field build up may occur over at least one hour prior to the magnetopause. This has left us with 127 crossings. Unlike some previous studies e.g. Paschmann et al., [1993], we have not made any *a priori* assumptions about the magnetic shear required for a plasma depletion layer to form, since there have been observations of PDLs at a high shear magnetopause e.g. Anderson et al., [1997]. We later separate the results according to shear, where we define high shear as shear angles > 60° and low shear < 60° as in section 4.6.1. Of our 127 crossings, 69 are considered low shear and 58 are high shear.

4.7.2.2 Observations

We have applied superposed epoch analysis (SEA) to the electron density and pressure and the magnetic field strength and pressure as the magnetopause is approached. We have chosen these parameters and applied this analysis to be able to directly compare with the results of Paschmann et al., [1993] and Phan et al., [1994] who applied this technique to study the variability in the magnetosheath at Earth in a

systematic way. Anderson et al., [1997] used the ratio of the plasma and magnetic pressures, i.e. the plasma beta to investigate the differences upstream of low and high shear crossings, but for the purposes of this study we shall consider these two parameters separately.

We calculate the electron pressure using: $P_e = n_e T_e e$, where n_e is the electron density is in units of m^{-3}, T_e is in eV and the pressure is in nPa. The magnetic pressure is calculated using $P_B = \frac{B^2}{2\mu_0}$, where B is the field strength. During this analysis we neglect the pressure contribution from the ions, which is expected to be ~ three times the electron pressure [Thomsen, 2006, *private communication*].

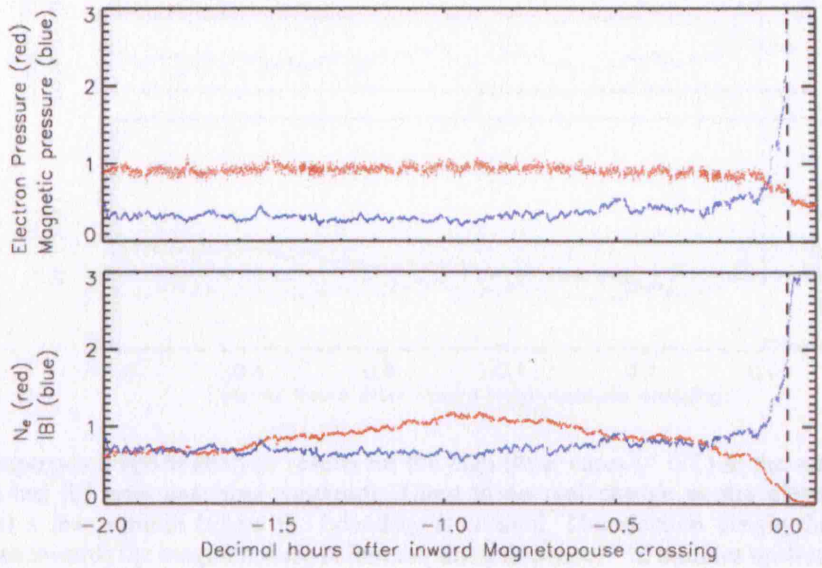

Figure 4.25 Superposed epoch analysis for all crossings showing the variation in electron and magnetic pressure (in nPa) and electron density (m^{-3}) and magnetic field strength (nT) two hours before the magnetopause is crossed. Time is in decimal hours, negative prior to the crossing and positive after the crossing. The magnetopause is indicated by the dashed line at 0.0. The electron data is plotted in red and slightly decreases as the boundary is approached while the magnetic data is in blue increases as the magnetopause is approached.

Ideally, we would like to be able to study the spatial profiles of these parameters as the magnetopause is approached. However, as described earlier in this chapter, we are not able to determine spatial thicknesses so rely on the temporal thickness to provide us with a proxy for the width of any PDLs.

The results from the SEA analysis using an upstream time of two hours is shown in Figure 4.25. The magnetosheath is on the right and the magnetopause is shown by the vertical dashed line. The electron pressure (red) starts to gradually decrease ~ 45 minutes before the boundary before dropping significantly ~ six minutes upstream of the magnetopause. The magnetic pressure (blue) more obviously starts to slowly

increase ~ one hour before the boundary and again increases sharply ~ six minutes prior to the magnetopause crossing. Once inside the magnetosphere, the electron pressure starts to drop off rapidly while the magnetic pressure increases almost immediately. The magnetic field strength also shows an increase towards the magnetopause. The density actually increases (with no corresponding increase in the plasma pressure) ~ one hour 30 minutes to one hour upstream of the magnetopause before eventually reducing just prior to the boundary.

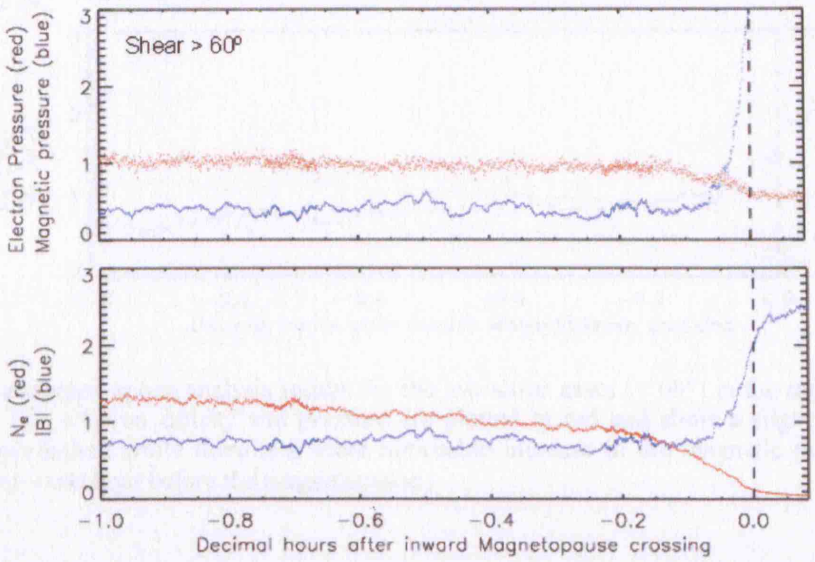

Figure 4.26 Superposed epoch analysis results for the high shear cases (> 60°) in the same format as the previous plot but for only one hour upstream. There is no real change in the electron or magnetic pressures until a few minutes before the boundary is crossed. The electron density however shows a steady decrease towards the magnetopause before the sharp decrease ~ 12 minutes upstream.

Since the theory behind PDL formation indicates they are more prevalent, or at least the depletion is greater, upstream of low shear boundaries, we have divided the data into low and high shear cases as defined in section 4.4.3.2 and re-run the SEA. The results from the low shear (< 60°) cases are shown in Figure 4.26 and the high shear (>60°) crossings are plotted in Figure 4.27. The difference in the field build-up between the cases is apparent and suggests that the changes observed in Figure 4.25 were being dominated by the low shear cases.

We observe a gradual build-up in the magnetic field strength and pressure in the low shear cases, starting ~ one hour prior to the magnetopause with a final sharp increase seen in the last ~ six minutes. The high shear case shows no such long-term increase, but there is a sharp increase ~ six minutes prior to the boundary. The change in the electron density and pressure is less straightforward; with a noticeable decrease

immediately upstream of the magnetopause but little evidence of a clear steady decrease further upstream when the magnetic pressure starts to increase.

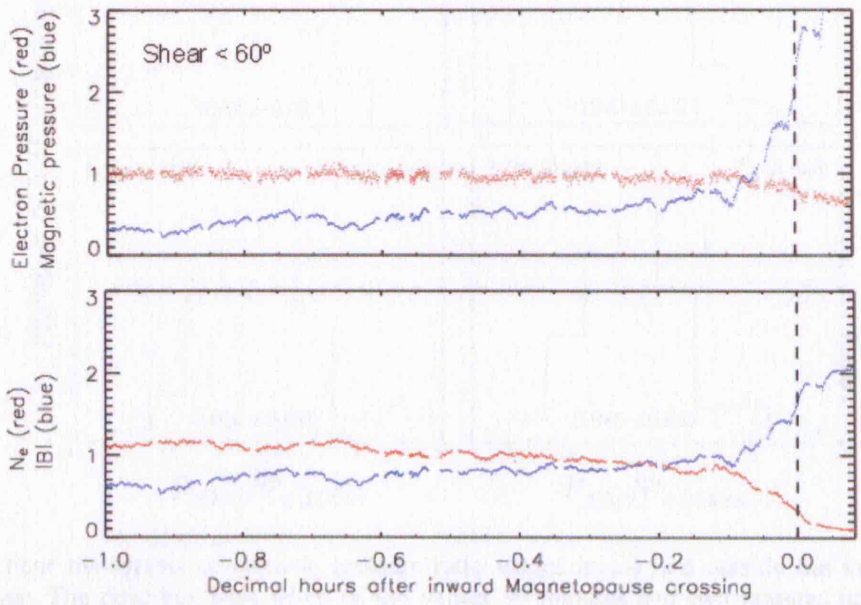

Figure 4.27 Superposed epoch analysis results for the low shear cases (< 60°) in the same format as the previous plot. The electron density and pressure are plotted in red and show a slight decrease as the boundary is approached while there is a more noticeable increase in the magnetic pressure and field strength starting ~ one hour before the magnetopause.

Now we have an estimate for the temporal extent of the field build-up and associated density decrease, we are able to compare values in the estimated pile-up region to those outside it. From the above analysis we chose three points relative to the magnetopause: a) one hour and 30 minutes prior to the magnetopause, which according to the findings from Figure 4.25 is outside the PDL, b) 30 minutes prior to the crossing inside a region where the field has started to build-up and c) two minutes upstream of the crossing where the magnetic (electron) pressure has begun a sharp increase (decrease) in all cases. We have also further divided the data into high and low shear crossings.

- Figure 4.28 contains histograms of ratios of the electron pressure values 30 minutes to one hour 30 minutes and two minutes to one hour 30 minutes upstream of the magnetopause for the high and low shear cases. The means are indicated on each plot. We have chosen to take the ratio of these values since if a PDL were present, starting at ~ one hour upstream as the above analysis indicates, we would expect $P_{e_{1h30m}} > P_{e_{30m}} > P_{e_{2m}}$. Note that for clarity we have omitted values greater than two from the plots. Several observations can be inferred from these results:

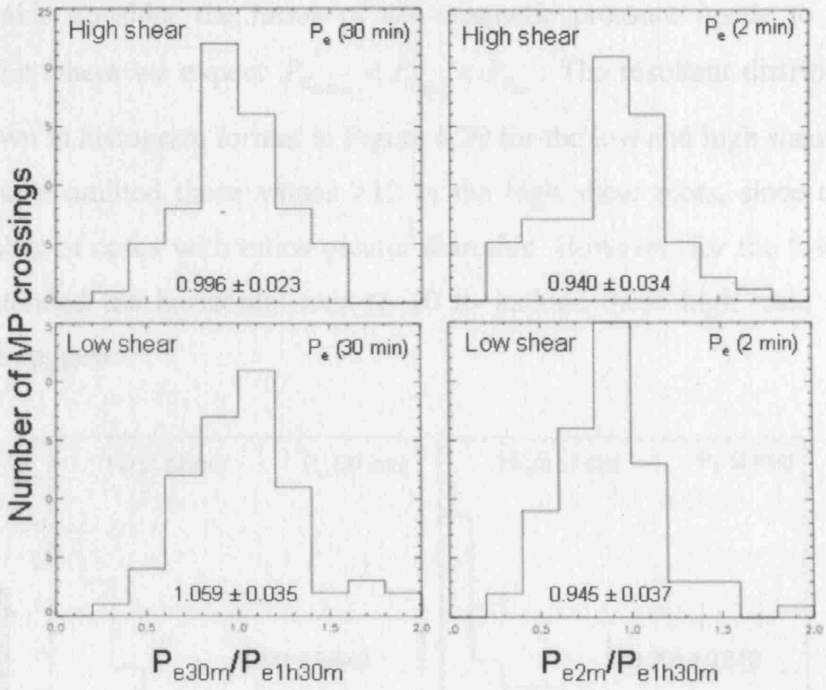

Figure 4.28 Four histograms of electron pressure ratio values inside and outside the inferred plasma depletion layer. The ratio has been taken of the values 30 minutes and two minutes upstream of the magnetopause to the value one hour and 30 minutes upstream (outside any PDL) for the low and high shear events. The means, together with the standard error on the mean ($\sigma_M = \sigma/\sqrt{N}$, where σ is the standard deviation and N the number of samples) are included on each plot.

- The most striking thing is the similarity of the distribution of the ratios for high and low shear cases;
- There is a noticeable decrease in the electron pressure as the boundary is approached in both the low and high shear cases as evidenced by an overall decrease in the ratios and the means;
- A greater density depletion is observed 30 minutes upstream of the boundary in the high shear case. Two minutes upstream of the boundary the increased depletion is seen at the low shear magnetopause;
- The electron pressure ratio of values sampled two minutes before the magnetopause to outside the PDL is smaller for the low shear case;
- There is a larger depletion of density between 30 minutes to two minutes inside the PDL for the low shear case as suggested by the plots and the marginally larger decrease in the mean value (1.059 to 0.945) compared with that for the high shear case (0.996 to 0.940);

We have also considered the number of events where the ratios are > 1.0. In the high shear case there are 30 examples with $P_{e_{30m}} : P_{e_{1h30m}} > 1$ and 26 with $P_{e_{2m}} : P_{e_{1h30m}} > 1$ and for low shear conditions these values are 40 and 22 respectively.

We also consider the ratios of the magnetic pressure inside to outside the inferred PDLs where we expect $P_{B_{1h30m}} < P_{B_{30m}} < P_{B_{2m}}$. The resultant distribution of the ratios is shown in histogram format in Figure 4.29 for the low and high shear cases. For clarity we have omitted those values >12 in the high shear plots, since there only a limited number of cases with ratios greater than this. However, for the low shear case we have extended the horizontal axis to 30 to include these high ratio events. The observations suggest:

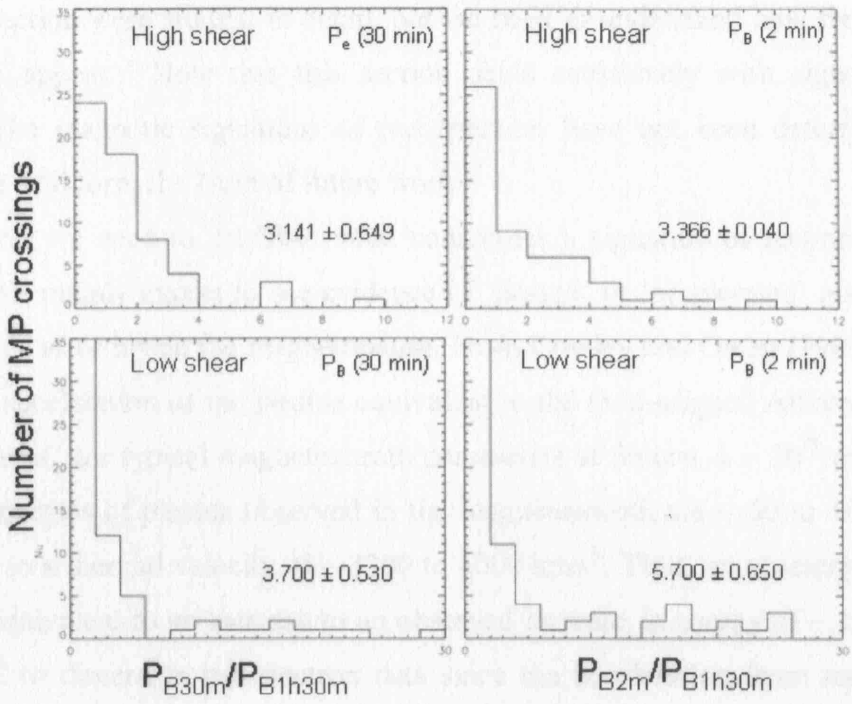

Figure 4.29 Four histograms of magnetic pressure ratio values inside and outside the inferred plasma depletion layer. The ratio has been taken of the values 30 minutes and two minutes upstream of the magnetopause to the value one hour and 30 minutes upstream (outside any PDL) for the low and high shear events. The mean and the error on the mean are included on each plot. Note that for the low shear cases the range of the horizontal axis has been extended to 30 to show the cases with high ratios. Since there are only a few examples with ratios > 12 in the high shear plots we have limited the plot range.

- The magnetic pressure shows evidence of an increase as the boundary is approached in both high and low shear cases as evidenced by the plots and the increasing average value of the ratio;
- The increase in the magnetic pressure is clearly larger at the low shear magnetopause both 30 minutes and two minutes prior to the magnetopause being crossed;
- The number of cases where the ratios are > 12 are, under high shear conditions, $P_{B_{30m}} : P_{B_{1h30m}} > 10$ for three cases and $P_{B_{2m}} : P_{B_{1h30m}} > 10$ for six events and for low shear conditions these values are 12 and 19 respectively (shown on the plots). This clearly

suggests an increase in larger values of the ratio, and thus increased field build-up under low shear conditions.

4.8 Signatures of plasma energisation

One of the aims of this thesis is to establish whether reconnection is occurring at Saturn's magnetopause and whether it is a dominant process for driving Saturn's magnetospheric dynamics. In Chapter 3, two magnetopause encounters with signatures of reconnection were studied in detail, but we need to understand how frequently such signatures appear. Note that this section deals exclusively with signatures in the plasma. The magnetic signatures of reconnection have not been determined in this survey but will form the basis of future work.

First we need to establish what constitutes a signature of reconnection in the plasma. We mainly expect to see evidence of 'heated' or 'accelerated' magnetosheath-type plasma at or inside the magnetopause. From Cowley and Owen [1989], we expect to see an acceleration of the plasma equivalent to the field-aligned Alfvén speed. This is ~ 400 kms^{-1} for typical magnetosheath parameters at Saturn, n ~ 10^{-5} m^{-3}, B ~ 6 nT. Typical energies of plasma observed in the magnetosheath are ~ 30 to 100 eV, which translates to a thermal velocity of ~ 3300 to 6000 kms^{-1}. Thus, an acceleration of ~ 400 kms^{-1} is equivalent to an increase to an observed increase in energy of ~ 10 eV. This is not trivial to discern in the electron data since the acceleration from reconnection is minor compared to the already considerable thermal velocity of the electrons. However, we might expect to see a high energy tail to such a distribution which might more easily be identified.

Typical plasma energies observed by the ELS in the outer magnetosphere are ~ 1 keV to many keV. It is also much rarer than the plasma seen in the magnetosheath (n ~ 10^3-10^4 m^{-3} compared with 10^5-10^6 m^{-3}), thus, it is possible to easily distinguish these populations from heated magnetosheath plasma, which has a larger density than the magnetospheric plasma. An example of energisation of magnetosheath plasma seen inside the magnetopause is shown in Figure 4.30. The ELS spectrogram contains data from 26 October 2004 and shows a partial entry and exit of the magnetosphere. The magnetopause crossings are denoted by the red vertical lines at ~ 06:58 UT and 07:13 UT. Here a rarer, higher energy magnetospheric plasma appears (~ 100's eV) and the appearance of denser magnetosheath plasma becomes more sporadic. These populations

are slightly higher in energy than the magnetosheath plasma seen outside the magnetopause. The energy increase appears to be ~ 20 eV.

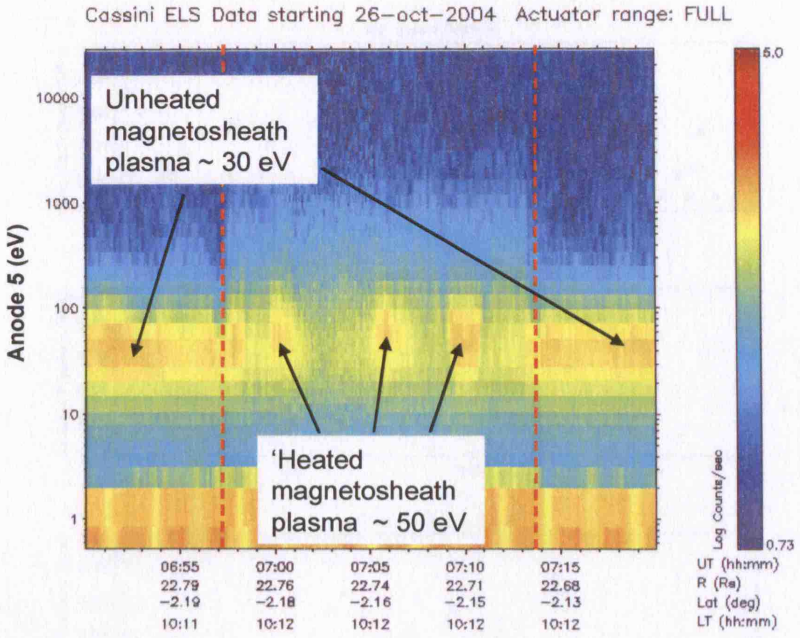

Figure 4.30 Spectrogram containing ELS data, with time along the horizontal exist, energy on the vertical axis and count rate is indicated by the colour scale. It is clear that inside the magnetopause (red vertical lines) there is a population which looks similar to the magnetosheath population but with a slight increase in the energy. This appears to be an example of heated magnetosheath plasma inside the magnetopause.

Despite these challenges, each crossing was visually inspected for signs of such energisation in the electrons in the interior boundary layer and designated as not showing signs of energisation, definitely showing energisation or where it is not clear either way. Of the 191 events analysed, 40 (21%) showed clear energisation in the electron signatures suggestive of reconnection. In addition, 59 (31%) are possible candidates for a reconnecting magnetopause. The remaining ~ 50% of the crossings showed no energisation.

These events were split into the three categories of energisation as outlined above and plotted against magnetic shear and dynamic pressure (from the Arridge et al., [2006] model) in Figure 4.31. It is expected that under high shear in particular, reconnection is favourable and the electrons should show evidence of acceleration. In addition, it has been proposed by Jackman et al., [2004] that the solar wind dynamic pressure is important in controlling the reconnecting magnetopause. In the top panel, the cases where no energisation is apparent are spread across all shears, but are generally seen when D_P is low. In the middle panel, signs of reconnection are seen and these occur at all shears < 170° and for all D_P's. The final panel contains the data when

energisation might be present and again appear at all shears < 170° and for the highest D_P values. There is a slight inclination for these events to occur at high D_P's at lower shears.

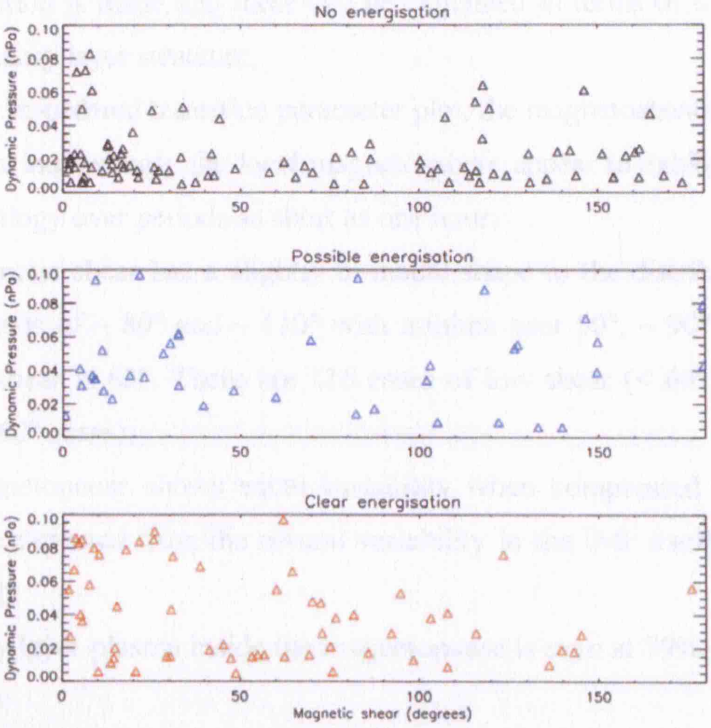

Figure 4.31 Correlation of magnetic shear (horizontal axis) and dynamic pressure, (Dp, vertical axis) for three states of energisation observed in the electrons. The top panel contains magnetopause encounters which show no signs of electron energisation (black triangles), the middle panel for cases where there might be energised electrons present (blue triangles) and the final panel for clear signs of energisation (red triangles).

4.9 Summary of observations

A survey was carried out of all magnetopause crossings observed during the first 18 months of Cassini's tour of Saturn. The crossings were limited to the dawn flank, between 3 and 11 LT, with magnetic latitudes of – 21° to 0.1° and Saturn-centric distances of 17 R_S to 65 R_S. 191 crossings were selected for inclusion in the study due to the availability of both the electron and magnetic field data and being able to derive the transition parameter. The results were then described and correlated with location on the magnetopause and inferred upstream parameters to establish the existence of any dependencies. Based on the analysis carried out, a series of inferences can be made about the magnetopause and the boundary layer at Saturn:

1. Re-ordering data by the transition parameter is a useful tool for evaluating and comparing the state of the magnetopause and boundary layers at Saturn;
2. Different plasma and magnetic field regions can be identified in τ-ordered data as the transition is made and these can be explained in terms of the magnetopause and boundary layer structure;
3. From the re-ordered transition parameter plot, the magnetosheath, boundary layer and, most interestingly the local magnetosphere appear to exhibit changes in the field topology over periods as short as one hour;
4. The magnetic shear has a slightly bi-modal shape to the distribution centred on shear values of ~ 80° and ~ 110° with minima near 50°, ~ 90° and ~180°. The average shear is 63°. There are 116 cases of low shear (< 60°) and 75 of high shear (> 60° cases);
5. The magnetopause shows equal variability when compressed or expanded, as would be expected from the natural variability in the IMF itself [i.e. Jackman et al., 2004].;
6. Boundary layer plasma inside the magnetopause is seen at 79% of magnetopause crossings;
7. The range of times spent in the boundary layer by Cassini was highly variable from one minute (the minimum width we could determine) to one hour 57 minutes;
8. The average boundary layer temporal thickness is ~17 minutes;
9. It was found that in 20% of cases with boundary layer, the density in the local magnetosphere is greater than that in the boundary layer, resulting in a negative density ratio (note that these values were omitted from further boundary layer analysis);
10. The average density in the boundary layer is 19% and the maximum is 74% of the magnetosheath density;
11. From this analysis we conclude that 78 of the 122 boundary layers (which have a density ratio > 0) have a density that is at least 10% of the magnetosheath density and 22 with a density greater than 30% of the magnetosheath density;
12. The average magnetospheric density is 27% of the magnetosheath density, however, this includes some cases where the density in the magnetosphere is larger than that in the magnetosheath. If these are discounted from the results we find this ratio to be 20%, suggesting interesting characteristics of the outer magnetospheric plasma in some cases;

13. There is no correlation of the boundary layer temporal width with density in the layer;
14. There is a very weak anti-correlation of the temporal width with magnetic latitude and no correlation with local time;
15. There are no correlations between the density ratio in the boundary layer with magnetic latitude or local time;
16. There is no correlation between the width of the boundary layer and the inferred upstream dynamic pressure; however there is a slight anti-correlation with the density ratio in the layer and the dynamic pressure. This latter correlation also has the highest significance of any of the results;
17. There is no correlation between the width of the boundary layer and the subsolar stand-off distance, but there is a significant correlation between the density ratio in the layer and the stand-off distance;
18. There is a weak anti-correlation of temporal width of the boundary layer, and a slight positive correlation of the ratio, with magnetic shear;
19. Plasma depletion layers are present at Saturn (although we do not determine the frequency) and are observed to form ~ one hour upstream of the low shear magnetopause;
20. In the PDL a gradual increase in the magnetic field strength and pressure and a slight decrease in the electron density and pressure are initially observed. As the boundary is approached these changes become more evident with a final sharp increase in the magnetic |B| pressure and a decrease in the electron density and pressure within ~ six minutes of the magnetopause;
21. There is evidence of a reduction in the plasma pressure 30 minutes upstream of the high shear magnetopause, and this is observed to be greater than the depletion seen at the same point prior to a low shear magnetopause. This level of depletion reverses as the magnetopause is approached with a larger depletion seen adjacent to the low shear magnetopause;
22. Signatures of electron energisation occurred across all shears and dynamic pressures, but those cases without apparent energisation are generally seen when D_P is low;
23. 21% of crossings contained energised electron signatures consistent with reconnection, 31% are possible candidates and 48% showed no energisation.

4.10 Discussion

The Transition Parameter at Saturn

It is clear that τ is a useful tool for analysing electron and magnetic field data across Saturn's magnetopause. Three different time intervals were selected containing different numbers of magnetopause crossings. We use data from an entire inbound pass to the magnetosphere to derive τ and then compare the results for each subset of data covering a particular crossing, rather than deriving τ individually for each crossing period. This allows us to compare directly the transits, how the magnetosheath and magnetospheric data compare and what changes occur in these regions over time frames of ~ one to three hours (typical duration of the intervals). These data were used to establish some typical characteristics of the boundary layer and the local magnetosheath and magnetospheric conditions.

In the magnetosheath: The only departure from the main slope which adequately represents the plasma characteristics of all populations tends to be a small spread in the temperature values. This change in temperature between regions is probably due to minor changes in the upstream conditions. Most of the intervals exhibited significant variation in the magnetic field strength and orientation in the magnetosheath. This is to be expected since this is a turbulent region with considerable variation in the field [Sibeck, 1994]. In general, the highest field strength occurred in intervals exhibiting minimal variability.

We can also infer the magnetic shear from the re-ordered magnetic field data, and, in general, we find a more disturbed magnetosheath region when the shear is high. This may be due to time varying reconnection disturbing the field upstream of the magnetopause [Phan et al., 1994]. The most variation is seen in the magnetosheath B_Z component, both between intervals (of variable spacing) and within intervals (generally ~ one to three hour duration) indicating frequent changes in the solar wind B_Z field and agreeing with Jackman et al., [2004]. However, due to the non-dipolar configuration observed in the outer magnetosphere [Arridge et al., 2006b] B_Z is not necessarily the most important component when establishing the likelihood of reconnection at the magnetopause. We do not consider the effect of the IMF B_Y component, which might vary over longer timescales due to large scale variations in the IMF.

The boundary layer (external): The intermediate values of density and temperatures indicate a region of mixing suggestive of boundary layer and we observe both internal and external layers in the examples. Plasma with intermediate properties

on northward magnetic field lines reveals the external nature of the layer. This may take the form of the magnetosheath boundary layer as seen at Earth [Fuselier et al., 1995; Onsager et al, 2001], or possibly a plasma depletion layer [Zwan and Wolf, 1976] upstream of the magnetopause. We also note that for some intervals the field strength is higher in this region compared with the nominal magnetosheath, supporting the latter suggestion. The transition parameter can therefore be used to identify external boundary layers which may otherwise be difficult to discern from internal boundary layers, especially at a low shear magnetopause.

The boundary layer (internal): In the internal boundary layer (identified by a negative B_Z component), a smooth variation was seen in the density and temperature with increasing τ as the magnetopause was traversed as expected from the assumptions behind the transition parameter. However, there were instances where the density and temperature within and between intervals varied differently with τ. This indicates that plasma characteristics are not static in the boundary layer. We observed hotter and sometimes denser populations, intermingled with the 'nominal lower temperature population on southward pointing field lines. Such a departure of the plasma behaviour from a monotonical distribution assumed in the derivation of τ based on a simple-mixing model [Bryant and Riggs, 1989; Hapgood and Bryant, 1992], is indicative of heating of the plasma on closed field lines in the boundary layer, which may be due to active processes such as reconnection.

In this region the magnetic field continues to be variable within timescales of ~ one hour and in some cases this region showed more variability than seen in the magnetosheath or magnetosphere (28 March 2005). This is also indicative of active processes in the boundary layer itself, which is not necessarily linked to the variation in the regions either side. This may be explained by reconnection and/or wave activity. At times very low field strengths are observed in the boundary layer with no corresponding increase in the plasma density as would be expected if this region were in pressure balance. Overall, the use of the transition parameter has provided insight into the structure in the boundary layer.

The magnetosphere: At times, the magnetosphere-proper contains significant variations in the magnetic field including clear bimodal distributions in B_X and the field strength (2 December 2005). This demonstrates that two different magnetospheric configurations are being sampled within a short time frame (~ three hours in this case). In fact, for this interval the magnetic latitude actually changes from positive (above the magnetic equator) to negative, without a corresponding change in the sign of B_X as if

Cassini had crossed below the magnetodisc. In addition, Cassini is at 5 local time, and, if we take into account the lagging field in this region, we would expect B_X to be negative while the spacecraft is above the magnetodisc. The northward shift in the magnetodisc as described by Arridge et al., [2006c, *submitted*] would explain why when Cassini is crossing the magnetic equator (based on the assumption of a simple, unperturbed dipole field) it does not observe a change in the sign of B_X. In general there is little change in the configuration of the magnetosphere between crossings over ~ 16 hours suggesting that, at times, the magnetosphere remains fairly stable. We can therefore use the re-ordered data to probe the field behaviour in this region.

This is the first close look at the boundary layer plasma at Saturn and the application of the transition parameter has allowed us a better understanding of how the plasma and magnetic field may change in this region.

Multiple crossings

A general look at the magnetopause position shows it is a highly variable boundary, often observed in multiple crossings on a single pass. This indicates a very dynamic magnetopause, which makes the assumption used in this work that the magnetopause is a time stationary boundary in its own frame for the derivation of τ, questionable. This variation does not appear to be affected by the size of the magnetosphere, i.e. whether it is in a compressed or expanded state and could be due to either large-scale motions of the boundary or more localised wave effects. Studies are currently being carried out to calculate the magnetopause normals and establish the nature of the magnetopause motion.

Boundary layer width

Each crossing was categorised depending on the presence, or lack thereof, of boundary layer plasma, the duration spent inside the boundary layer by Cassini and the average density in the layer. We found a dominance of layers with a temporal extent < 20 minutes, with an average boundary layer duration of 17 minutes. The boundary layer was also observed for longer periods, with six cases where intermediate plasma was observed for over an hour once inside the magnetopause, up to a maximum of one hour and 57 minutes. However, as has been stressed during this analysis, a temporal quantification of the width of the boundary cannot truly establish any spatial scales due to the unknown magnetopause motion. The fact that most layers are found to be short could simply indicate that the magnetopause moves swiftly over the spacecraft.

It is clear that the presence of the boundary layer plasma at Saturn is frequent, appearing in 79% of cases which agrees closely with the results of Eastman et al., [1996] at Earth, where only 10% of crossings showed no evidence of magnetosheath-like plasma close to the subsolar magnetopause. However, Paschmann et al., [2005] report that 42% of their crossings studied showed no evidence of boundary layer plasma, a much higher value than that quoted by Eastman et al., [1996], although they were sampling earlier local times (~ 3-5 LT) which may suggest a variation in the boundary layer width with local time at Earth. Furthermore, Mitchell et al., [1987] reported an increase in the thickness of the boundary layer with distance from the subsolar point. The variation in the findings at Earth's magnetopause highlights the highly variable nature of the boundary layer and the importance of obtaining as wide a local time and latitudinal coverage as possible in order to truly characterise its presence at the magnetopause.

Density in the boundary layer

Once we had identified when Cassini was observing boundary layer plasma, we calculated the density in that layer as a fraction of the local magnetosheath density. There were 30 cases where the local magnetospheric density was larger than the density observed in the boundary layer, resulting in a negative ratio. These were discounted from further analysis since, for this study, we are most interested in the boundary layer, rather than the local magnetospheric characteristics. Of the remaining cases the density in the boundary layer was found to be lower than in the magnetosheath agreeing with findings at Earth [Haerendel et al., 1978; Sckopke et al., 1981].

The boundary layer density was found to be, on average, 19% of the magnetosheath density, with a maximum of 74%. We also identified ~ 20 % of cases where the magnetospheric density was larger than that in the boundary layer, and, more surprisingly, ~ 5% of cases where the density in the magnetosphere was greater than that in the local magnetosheath. We attribute these cases to particularly low densities in the magnetosheath (possibly due to PDLs) combined with unusually high densities in the local magnetosphere, outside of any boundary layer. This could arise if Cassini is crossing the magnetopause directly into the plasmasheet rather than the tenuous, outer magnetosphere where the density in the former is expected to be higher [Arridge et al., 2006c, *submitted*].

The higher values of the density in the magnetosphere make it uncertain that the magnetosheath plasma is necessarily the dominant source of the boundary layer, which

is the case at Earth. The typical value for the boundary layer density as a function of the magnetosheath density is 25% at Earth [Haerendel et al., 1978; Sckopke et al., 1981].

We were unable to find any correlation between the density and the temporal width of the layer, but again, this may arise due to the inaccuracies inherent in attempting to sample a boundary under motion. Previous studies at Earth have indicated that the density reduces in the layer as the magnetosphere-proper is approached, irrespective of the layer thickness [Haerendel et al., 1978; Paschmann et al., 1993; Paschmann et al., 2005]. If this is true at Saturn we might not expect any correlation of density with temporal width of the boundary layer.

Width and density of the boundary layer at different locations on the magnetopause

Our results showed very low coefficients of correlation and low significance (represented by high values of S). For most cases this lack of any significant relationship of boundary layer width with position suggests once more that the width is a strong function of the boundary speed. However, we would expect our values of density in the layer to be representative, and the lack of any strong correlation suggests that either the magnetosheath plasma gains entry to the magnetosphere fairly evenly across the whole magnetopause sampled, or that the internal plasma plays a more important role in populating the boundary layer, at some location.

At Earth, Eastman and Hones [1979] and Mitchell et al., [1987] saw an increase in boundary layer thickness anti-sunward as would expect to be the case if the boundary layer was populated via diffusive processes only. However, Eastman and Hones [1979] also found the boundary layer width to be highly variable with distance tailward along the flank. Haerendel et al., [1978] also showed a latitudinal dependence on the thickness and density in the boundary layer due to the different entry mechanisms of the boundary layer plasma, i.e. at the cusp or the low latitude magnetopause, but our limited data coverage prevented us from carrying out the same comparison. This suggests that the determination of the boundary layer size is a difficult task.

Correlation of boundary layer with upstream parameters

Since we have no upstream monitor at Saturn, our upstream conditions have been inferred using the Arridge et al., [2006a] magnetopause model. We were able to extract both an inferred upstream dynamic pressure and, via derivation of the magnetopause normal, the magnetic shear in a plane tangential to the magnetopause.

Since the model is pressure dependent, the dynamic pressure is inversely proportional to the magnetopause stand-off distance.

We find no correlation of the boundary layer width with dynamic pressure or stand-off distance, and only a very slight decrease in width with magnetic shear. Conversely, Mitchell et al., [1987] found a thicker LLBL at Earth when the IMF was northward, which at Earth is not conducive to reconnection. They explained this by considering the erosion of boundary layer flux on the dayside during reconnection.

We also find a very weak increase in the density of the layer as a function of magnetic shear, which may be indicative of a reconnection process triggering the entry of more magnetosheath plasma into the magnetosphere to form a layer. However, with low significance we cannot state this for certain. We find a significant anti-correlation ($R = -0.18$, $S = 0.05$) of the density ratio with the dynamic pressure, suggesting that this is a controlling factor in allowing entry of magnetosheath plasma into the magnetosphere. This would agree with the findings of Jackman et al., [2004] who propose that the role of the upstream dynamic pressure in reconnection is significant at Saturn. There is thus a positive correlation with the position of the subsolar magnetopause relative to the planet and the density in the layer, suggesting that the amount of plasma in the layer can influence the magnetopause position, 'pushing' it outwards when the internal pressure increases. It is clear that Saturn is a complicated system, and we note clearly that internal processes cannot be ignored when trying to understand the magnetopause and boundary layer.

Plasma Depletion Layers

We applied superposed epoch analysis to the electron and magnetic field data from each crossing interval to allow us to see the trends in the data in the magnetosheath region upstream of the magnetopause. We applied the analysis over a two hour period upstream and from this were able to identify a slow field build-up starting ~ one hour prior to the magnetopause. There is a noticeable increase in the field strength and pressure in the low shear cases, with both the low and high shear exhibiting a sharp increase of the order of minutes prior to the magnetopause crossing. The associated long-term depletion of density and the associated reduction in the electron pressure was not so apparent, but again once very close to the magnetopause a sharp decrease was seen in all cases. The depletion observed upstream of the high shear magnetopause case could be due to a change the solar wind, however, we have no additional measurements from this upstream region to either confirm or deny this.

There was a clear field build up in the low shear case, evident ~ one hour upstream of the boundary while both cases showed an increase two minutes upstream. The depletion in the density was not so clear. Initially, the depletion appeared more significant in the high shear case, but as the boundary was approached, depletion in the low shear case became more significant.

We find an average magnetic pressure increase 30 minutes upstream of the low shear case to be ~ six times that seen in the undisturbed magnetosheath, and 16 times the value two minutes upstream of the magnetopause, indicating a significant increase. The maximum depletion reduces the electron pressure down to only ~ 93% of the undisturbed magnetosheath two minutes upstream of the crossing. This shows that hardly any depletion is occurring despite the field build-up.

There is clearly a pile-up region and associated depletion at all shears, suggesting that if reconnection is occurring under high shear, it does not preclude formation of an upstream PDL. This indicates that any reconnection occurring is slow compared to the incoming flow speed, permitting field build-up despite the removal of flux. The observed field build-up over ~ one hour agrees with previous findings at Saturn [Violante et al., 1995; Bavassano Cattaneo et al., 1998]. This also tentatively agrees with predictions by Zwan and Wolf [1976] and Farrugia et al. [1998] who expect a wider PDL at Saturn compared with typical widths upstream of Earth's magnetopause. However, until we can resolve spatial and temporal variations we are not able to confirm this.

Signatures of reconnection

One of the key signatures that reconnection is occurring is the energisation of the plasma. 50% of the crossings showed signs of possibly or definitely having energised electrons. This suggests that for many of the observations on the dawn flank, reconnection was occurring somewhere on the magnetopause. There was no strong correlation with the upstream conditions, although it is clear that those crossings where no energisation is seen occur predominately under low dynamic pressure conditions.

4.11 Conclusions

From the above analysis we are able to summarise some overall findings about the boundary layers at Saturn's magnetopause. There is clearly a mechanism allowing

magnetosheath plasma entry into the magnetosphere. The resulting boundary layer is present inside 79% of magnetopause crossings indicating that either the reconnection process or diffusive entry is a frequent occurrence. Evidence of such an interaction between the solar wind and magnetospheric plasma regions was not expected to be a dominant process due to the rapidly rotating, mass-laden magnetosphere and the high mach numbers of the solar wind at 9 AU.

Boundary layer plasma is present inside the magnetopause along the entire dawn flank and it appears to thin with increasing magnetic latitude suggesting a preferential entry of plasma at the equatorial regions. The boundary layer temporal width reduces with magnetic shear but does not appear to be influences by the dynamic pressure. If reconnection was the dominant entry process we might expect larger magnetic shears, which are conducive to reconnection to facilitate plasma entry, but there is clearly other factors influencing this process. The amount of plasma in the layer does, however, increase with the magnetic shear, thus we can infer that an increased amount of plasma can gain entry to the magnetosphere when the shear is high. Yet the plasma density decreases with increasing dynamic pressure. Since we might expect both these factors to influence the presence of reconnection it is puzzling that their individual effects are anti-correlated. Signatures of energisation in the electrons do not tend to occur when the dynamic pressure is low, but occur across all shears, indicating that the dynamic pressure is a dominant factor for magnetopause reconnection.

The plasma inside the magnetopause is variable, with densities occasionally approaching those observed in the boundary layer or even in the magnetosheath. This could be explained by Cassini encountering the plasmasheet where the density is increased compared with the surrounding outer magnetospheric regions. When the plasmasheet is adjacent to the magnetopause it may influence the characteristics and formation of the boundary layer and this should be explored.

The presence of PDLs is indicative of a closed magnetopause, or a relatively slow reconnection rate. The field build-up occurs ~ 30 minutes to one hour upstream of the magnetopause which places upper limits on the rate, although this is not established here.

5 Saturn's Icy Satellites: results from the CAPS Electron Spectrometer

5.1 This chapter

The analysis in this chapter will concentrate on the absorption cavities carved out in the high energy electron (~ MeV) fluxes by the moons Tethys, Enceladus and Mimas. We first review the background of this subject, starting with an overview of previous results obtained at Jupiter and Saturn. We then review the findings from Cassini reported by the high-energy electron instrument. The expected behaviour of electrons at these energies will be reviewed, particularly with respect to their motions in the vicinity of the moons and the implications this has on the absorption cavities. We then outline the sensitivity of the ELS to electrons of these energies and how this can be exploited in the analysis of these cavities using ELS data. The expected fluxes of electron energies of interest will also be reviewed. The different depletion signatures observed at each of the moons is then described before a survey of the cavities is carried out. Finally we review our findings and discuss the implications.

5.2 Introduction

Cassini first encountered the Saturnian moon system just prior to Saturn orbit insertion (SOI) with the close flyby of Phoebe on June 11 2004 while remaining outside the magnetosphere. However, of most interest in this study are the twenty moons which orbit inside the magnetosphere. We concentrate here on moons in the inner magnetosphere which orbit within the radiation belts. In this region the flux of high energy particles is significant [Young et al., 2005] and therefore the absorption wakes are prominent.

The moons which we shall focus on in this work, for which clear absorption signatures exist in the ELS data, are Tethys, Enceladus and Mimas. We list their radius, L-shell and orbital velocity in Table 5-1. The 'L-shell' of a moon is the equatorial distance in planetary radii ($1R_S$ = 60,268 km) at which a field line crosses the equator.

Table 5-1 Data on three of Saturn's satellites. The equatorial radius, L-shell and orbital velocity of Tethys, Enceladus and Mimas [from the IAU] ($1R_S$ = 60268 km).

	Radius (km)	L (R_S)	Orbital velocity (kms^{-1})	Orbital velocity ($rads^{-1}$)
Tethys	535.6	4.89	11.36	3.86×10^{-5}
Enceladus	256.3	3.95	12.64	5.30×10^{-5}
Mimas	209	3.08	14.32	7.70×10^{-5}

All three of the moons under study orbit almost exactly in the equatorial plane with the orbital inclinations of Mimas and Tethys being 1.51° and 1.12° respectively. These are very low inclinations and, together with the highly axisymmetric nature of the magnetic field of Saturn, any effect on the interaction with the plasma is probably insignificant. Additionally, the eccentricities are very low for Tethys and Enceladus while Mimas has an orbital eccentricity of ~ 0.02 which may prove to be significant.

The aim of this chapter will be to study the characteristics of the depleted cavities carved out by these moons in the energetic electron population. These data will give us an insight into electron behaviour in the inner magnetosphere and also at these higher energies, which the ELS is not specifically designed for. We will show, nevertheless that the ELS is a valuable additional tool to complement and enhance the measurements made by the MIMI-LEMMS instrument [Krimigis et al., 2004] which is designed to make measurements in these energy regimes. We will use these data to derive diffusion coefficients for the inner magnetosphere at a variety of local times around the planet adding to the information currently available. Since this work concentrates on the electron wakes, we will review only previous electron measurements.

5.3 Previous observations of high-energy satellite wakes

5.3.1 Observations at Jupiter

The concept of satellite absorption signatures was first considered at Mars, when Singer [1962] theorised the sweeping effect of Mars' moon Phobos on a hypothesized magnetospheric system of particles. This later proved to be irrelevant due to the lack of Martian radiation belts. Later work analysed the effect of Earth's own Moon creating a particle wake when crossing Earth's magnetotail and in the solar wind [Van Allen, 1982; Ogilvie et al., 1996]. However, the large magnetospheric systems of Jupiter and

Saturn, both containing numerous satellites provide a rich and varied environment with remarkable particle shadows in which to study the properties of satellite sweeping.

The first detailed theory behind satellite sweeping of particles was applied to the Jupiter system by Mead and Hess [1973] using remotely sensed data, prior to the arrival of Pioneer 10 and 11. The assumption they made, and which in general has been adopted was that any trapped radiation belt particles impacting the moon, would be absorbed. They assumed that the moons were inert bodies without an atmosphere. Thus they act as insulators and there is no deflection of electric or magnetic fields.

For most cases, the absorption is either total, i.e. all of the particles whose guiding centre comes into contact with the moon are absorbed, or the absorption is effectively 'random' and the absorption probability < 100%. There are a number of processes that can result in a particle avoiding absorption. Firstly, if the gyroradius of the particle is comparable to, or greater than, the moon radius, then as a field line threads a moon the particles trapped on that field line may circumvent the moon and "survive" the encounter. The second process that can occur is known as 'leapfrogging'. Here, the longitudinal distance covered by a particle during its bounce motion (assuming it's a non-equatorial mirroring particle) is greater than the sum of the distance travelled by the moon plus its diameter in the same time. Finally, we consider the corkscrew effect which is a product of a particles gyroradius and the phase of gyration. This occurs when the distance travelled by a particle along the field line during a gyration is greater than the moon radius and therefore the particles 'misses' impacting the moon [Thomsen et al., 1977; Rairden, 1980; Paonessa and Cheng, 1985; Paranicas and Cheng, 1997].

Upon the arrival of Pioneer 10 and 11 at Jupiter, scientists were able to further the theoretical work of Mead and Hess [1973] with empirical data [Simpson et al., 1974; Mogro-Campero, 1976; Thomsen et al., 1977]. The results focused mainly on the sweeping effect of Io, Jupiter's third largest moon.

5.3.2 Observations at Saturn: Pioneer 11 and Voyager

Analysis of the moon interactions at Jupiter naturally led to the same effect being considered at Saturn where the close alignment of the dipole and rotation axes provide a symmetric system in which to study absorption profiles. A number of moon wakes were detected by Pioneer 11 and later Voyagers 1 and 2, facilitating a detailed analysis of this phenomenon.

Saturn has, under current knowledge, a total of 35 moons in its system, not including the countless, ~ tens of metres-sized moons that make up the main ring system. The orbits range from 2.28 R_S for Pan [Morrison et al., 1984], which sits within the rings of Saturn, through to the outermost moon, Phoebe, which orbits far beyond the magnetosphere at 215 R_S.

Pioneer 11 electron instruments detected an absorption signature at the L shell of Mimas during both its inbound and outbound flyby of the magnetosphere [Van Allen et al., 1980a, 1980b; Simpson et al., 1980a, 1980b]. The depletion was seen in energy channels sampling 7-17 MeV electrons [Simpson et al., 1980a] and ~ 0.040 to 21 MeV electrons [Van Allen et al., 1980a] but the latter attribute the cavity to electrons of ~ 1.6 MeV since a monoenergetic electron population exists at the orbit of Mimas. The narrow energy range of this population is discussed further later in this chapter.

Instruments on Pioneer 11 were not able to properly distinguish the electron absorption signatures of Tethys and Enceladus, despite crossing the L shells of these moons. This was either due to a lack of any cavities or because they could not be resolved [Simpson et al., 1980a; Van Allen et al., 1980a].

A signature observed close to the L shell of Mimas ~ 3.065 R_S was interpreted by Simpson et al. [1980a, 1980b] as the passing through of the depleted flux tube of unknown matter at a Lagrangian point in Mimas' orbit, rather than an effect directly caused by Mimas, due to its distance from the moon. However, Van Allen et al., [1980b] realised that absorption effects could also be seen some distance from the moon if the newly created 'hole' in the population survived and 'drifted' around Saturn with the same orbital velocity that the absorbed particles would have done. This signature does not require the spacecraft to pass through the depleted flux tube attached to a satellite; instead the spacecraft could sample the past effect of the sweep-up mechanism. The sharp boundary is then caused by the presence of particles on adjacent flux tubes, which did not intersect the moon and are thus undisturbed.

Based on these limited observations, Van Allen et al., [1980b] defined two distinct wake effects. The longitudinally and time-averaged effect known as a 'macrosignature', typical of absorption effects caused by ring material since there is a constant process of absorption occurring. This also appears in high energy protons that encounter the moon frequently and therefore suffer continual losses and over a larger region of space due to their large gyroradii. The second effect which we shall focus on in this chapter is the instantaneous effect of a satellite in longitude: a 'microsignature' (also described in Selesnick, [1993]). This is observed as a dip in particle counts, whose

depth depends upon the 'age' of the signature, i.e. how far from the generating moon it is observed. Once this vacant region of space is created, it will undergo gradual refilling by processes such as diffusion and dispersion. Thus, as the hole extends longitudinally away from the moon, the absorption profile reduces and broadens. Therefore, we are able to infer properties about the surrounding plasma based on the survival time of this cavity.

Particle diffusion comes about through fluctuations in magnetic and electric fields [Walt, 1994], which occur on timescales shorter than the characteristic motion of a particle. Since the gyration and bounce periods associated with the first and second adiabatic invariants are short, these are generally conserved. The drift period however, is longer and thus the third adiabatic invariant can be violated resulting in cross-field diffusion. Hood [1983] carried out an initial look into the possible driving mechanisms of radial diffusion at Saturn and attempted to establish which might be dominant at Saturn. The three main processes considered were:

- Magnetic impulses
- Electrostatic impulses
- Centrifugal interchange

Van Allen et al., [1980b] applied a 1-d diffusion equation to derive a value for the diffusion coefficient (D_{LL}) for a particular energy and radial distance. Van Allen [1984] indicated that for an ideal treatment of the filling in rates, we would need a series of signatures at different longitudes, radial distances and energy.

From this treatment, Van Allen et al., [1980b] found that the width of the signature seen at the orbit of Mimas was inconsistent with its development under the influence of the above-described diffusion effects only. They suggested that these microsignatures are a superposition of different energy and pitch angle components of the particle populations. If this is the case, the width of the observed cavity is a function of the energy dispersion of the cavities which in turn, places an upper limit on the width of the signature. Van Allen et al., [1980b] further postulated that the population of electrons at the orbit of Mimas were effectively limited to a small energy range about a mean energy. The maximum and minimum energies would suffer depletions that would then drift and disperse, forming the extremes of the 'hole'. Thus, an alternate hypothesis for the changing depth and width of the moon cavities with longitude was attributed to energy dispersion effects.

The next visitors to Saturn were the Voyager spacecraft, and the instruments on board were able to detect particle absorptions due to nearly all the moons, Mimas,

Enceladus, Tethys, Dione and Rhea [Vogt et al., 1982; Krimigis et al, 1982; Van Allen, 1984; Carbary et al., 1983]. Chenette and Stone [1983] used Voyager 2 data to analyse an absorption signature near the orbit of Mimas. An energy-dependent absorption signature was seen in the electrons which varied both in depth and shape. They proposed that the absorption was due to a cloud of material at the L shell of Mimas. We note that previous studies of particle absorption at or close to the orbit of Mimas have reached varying conclusions for the process behind the depletion of electrons. Van Allen et al., [1980b] attributed it to the microsignature of the moon, others concluded that the spacecraft had passed through a flux tube connected to a cloud of material or other body orbiting at the same L shell [Simpson et al., 1980a, 1980b; Chenette and Stone 1983]. Such disagreements in interpretation can arise due to the difficulty in accurately determining the species and energy of particles which dominate the response of the detectors.

Other microsignature observations of interest were described by Carbary et al., [1983] who observed an absorption profile due to Enceladus which was much larger than the 'effective diameter' of the moon. Based on this they suggested that the cavity might be caused by clumps of material in the E-ring itself.

5.3.3 Findings from Cassini

The arrival of Cassini has provided a much larger dataset of microsignatures. This is a product of its dedicated orbit around Saturn routinely crossing the L-shells of the moons in the inner magnetosphere. Several studies have reported on the findings from the LEMMS instrument on the MIMI suite (see Chapter 1 for details of the instrument) [Roussos et al., 2005; Paranicas et al., 2005; Jones et al., 2006]. A brief introduction to these findings is given here and a more detailed comparison is given when we discuss the cavities observed at the different moon L shells.

Roussos et al., [2005] and Paranicas et al., [2005] reported on the observations of signatures made during multiple crossings of the L shell of Tethys in the LEMMS 'low' energy electrons. Here 'low' energy refers to electrons with ~ 30 keV < E < 100 keV. They did not see depletions in any of the 'high' energy electrons (> 100 keV). They noted that the position and shape of the low energy absorption have appreciable energy dependence. They also observed radial displacements of the microsignatures from the expected L-shell, suggesting that this could be due to the convective electric

field from the solar wind and the ring current. This displacement is also found to have a local time dependence.

They also report several cases of double signatures. These are interpreted as being due to geometrical effects of the relative positions of the moon and spacecraft orbits, where the drift shell of the signature is undergoing minor fluctuations back and forth across the spacecraft trajectory. Alternatively, it could be due to the radial drift of the signatures resulting in different signatures on different L shells. They also conclude that these depletions can last over one orbit of the planet, such that signatures of different 'ages' can be observed in the vicinity of the L shell of the moon.

The varying signatures due to Enceladus in both the electrons and the protons were analysed in Paranicas et al., [2005] and Jones et al., [2006]. The latter discussed the cavities seen in both the high and low energy channels of LEMMS. The high energy signatures appear upstream of the moon with respect to corotation and these showed sharp depletions of the order of the size of the moon. The signatures in the low energy electrons appeared downstream of the moon with respect to corotation and contained significant variation. This was suggested to be due to the effect of magnetic draping around the moon, the outgassing of neutrals and dust from the moon itself [Dougherty et al., 2006] and/or wave activity in the vicinity of the moon.

Note that no findings on the micro- or macrosignature of Mimas have so far been documented from data collected by Cassini instruments.

5.3.4 Previously calculated diffusion coefficients

The analysis of signatures seen in both Pioneer and Voyager data and, more recently, the Cassini (LEMMS) data, have yielded a number of values for the radial diffusion coefficients for energetic particles in Saturn's magnetosphere at different L-shells and energies. Those values derived for electrons and L-shells of relevance to this study have been listed, together with their source, in Table 5-2.

There is clearly a wide spread in the values previously derived, including some with large uncertainties, highlighting the need to further refine estimates of diffusion in the magnetosphere. The uncertainties can come from various sources, either the inherent error in the measurements themselves or the lack of certainty in the particle energy being detected, especially in the presence of high background counts, which can penetrate through the outer casing of instruments and appear as noise in the data. Of

course, an additional error is introduced in some of the assumptions used to derive these values. Overall, we see from this table that there is a general trend towards larger diffusion coefficients at higher energies and at larger L, which agrees with Walt [1994].

Table 5-2 Values of diffusion coefficients derived at several moon orbits and radial distances at Saturn. They are listed, together with the energy of electrons and the reference.

Moon	D_{LL} ($R_S^2 s^{-1}$)	Electron energy (MeV)	Reference
L=2.5	1.5×10^{-10}	1.5	Van Allen, 1982
L=3	3.7×10^{-11} to 8.3×10^{-12}	1	Van Allen et al., 1980b
Mimas	4×10^{-8}	10	Simpson et al., 1980b
Mimas	$< 3.9 \times 10^{-10}$	1-2	Simpson et al., 1980b
L=3.1	$> 1.5 \times 10^{-8}$	> 2.5	Chenette and Stone, 1983
Enceladus	$2.0 \pm 0.5 \times 10^{-9}$	0.98 – 3.28	Jones et al., 2006
L=4	1×10^{-10}	1	Van Allen et al., 1980b
Tethys	$0.5\text{-}1.0 \times 10^{-9}$	$2 - 100 \times 10^{-4}$	Paranicas et al., 2005

These values have all been calculated using instruments that nominally measure 'high' energy electrons (i.e. > ~ 1 MeV). As we will expand upon in the next section, the ELS is also able to contribute to the knowledge of the diffusion occurring at these energies. This provides a valuable additional resource for determining accurate values through inter-instrument comparison. The data from the ELS potentially doubles the number of measurements of the moon depletions observed by the high energy electron experiment (MIMI-LEMMS) since for each encounter, both instruments can, potentially, detect any absorption.

5.4 Energetic particles in the inner magnetosphere

5.4.1 High-energy electron behaviour

To decipher the signatures created by the absorption of particles by the moons in the magnetosphere, we must first have a clear understanding of the undisturbed particle environment and behaviour in the regions of interest. Electrons exhibit several different types of motion in the magnetosphere due to the influences of the electric and magnetic fields (for a description of some of these motions see Chapter 1). Here we consider their drift around the planet, their orbital motion about the field line and their motion along a field line and the subsequent mirroring when the field strength reaches a certain value.

The electrons will drift around the planet at an angular velocity which is a combination of the magnetic gradient and curvature drifts, ω_D. We apply the equations detailed in Thomsen and Van Allen [1980], describing the relativistic motions for particles of these energies. The total azimuthal velocity of the particles ω_I which is of interest when considering their motion with respect to the orbiting moons, is governed by the sum of these drift motions. This is particularly relevant for electrons, since their magnetic drift velocity acts in the opposite sense to the corotational drift, Ω :

$$\omega_I = \Omega \pm \omega_D$$

Equation 5.1

where the positive sign is used for protons and the negative sign for electrons. It is apparent that at some 'transitional' energy, E_T, the electron drift will equal and oppose the corotational motion (i.e. ω_I =0). Hence, when $\omega_D \geq \Omega$, the electrons move in the opposite sense round the planet, i.e. westwards against corotation. The transitional energy therefore delineates electrons travelling eastwards or westwards around the planet. These values of E_T for electrons (i.e. $\omega_D = \Omega$) at the orbit of Tethys, Enceladus and Mimas are given in Table 5-3 for a range of pitch angles.

Table 5-3 Transitional energy, E_T, values for electrons of different pitch angles at Tethys, Enceladus, and Mimas.

E_T of the Moon	α_{eq} = 10° (MeV)	α_{eq} = 60° (MeV)	α_{eq} = 90° (MeV)
Tethys	1.73	1.30	1.23
Enceladus	2.20	1.67	1.58
Mimas	2.93	2.22	2.10

A further definition of the electron motion with respect to the moon is now considered. We consider a frame in which the moon is at rest. From Equation 5.1 we now include the Keplerian angular velocity of the moon, ω_k :

$$\Omega + \omega_D - \omega_k = 0$$

Equation 5.2

when this equation is satisfied, the electron and the moon are travelling round the planet at exactly the same rate. An electron with this velocity is known as 'resonant' and has a resonant energy, E_R. Values for E_R have been plotted in Figure 5.1 for a range of L-shells and pitch angles. The plot takes this form as it is defined by the drift velocity of a particle and the orbital velocity of the moon. As L increases, the orbital velocity of the

moon decreases, and thus the drift velocity does not need to be as large to balance it and the associated energy of the electron reduces. The reason for the steep increase within ~ 4 R_S is because there is not much difference between the drift velocities required to counteract the velocity of these moons at relatively closely spaced values of L.

The concept of resonant particles leads to the idea that if an electron is travelling round the planet at the same rate as the moon, then it will never actually impact the moon, and it may escape absorption. Thus, the time between encounters with the moon (T_e), approaches infinity.

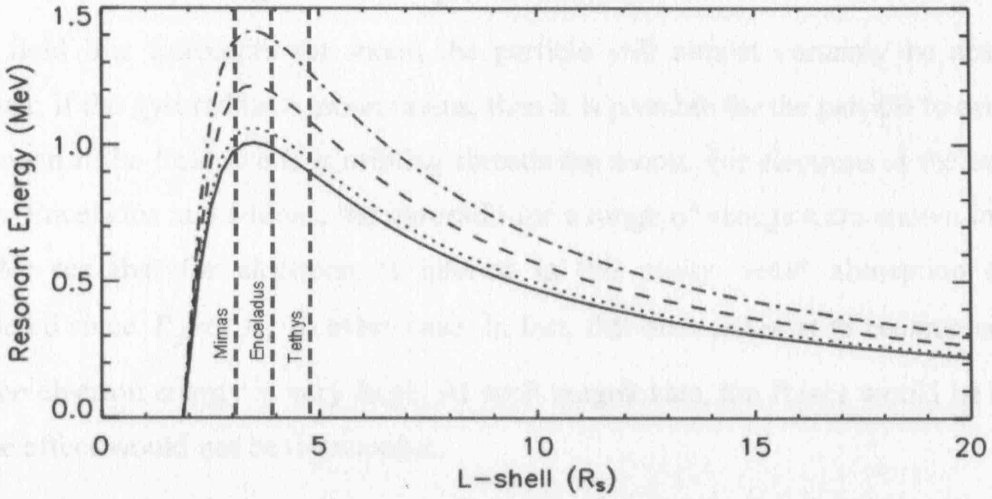

Figure 5.1 Plot of resonant energies for a range of L-shells for electrons with pitch angles of 90° (solid), 60° (dotted), 30° (dashed) and 10° (dash-dot). It is clear that there is a peak of these resonant energies near ~ 3.5 L, close to the orbit of Enceladus. We have not included the eccentricity of Mimas to this plot and expect the effect to be minor since the orbital velocity of the moon will increase at points closest to Saturn (perikron) and decrease at the furthest point in the orbit (apokron). The L shells of the moons of interest have been indicated.

The resonant energies corresponding to an infinite time between encounters at different pitch angles for these three moons are given in Table 5-4. Differences between these values and Thomsen and Van Allen, [1980] are due to the updated value for Saturn's rotation used here. The similarity of the values for Enceladus and Mimas are simply a product of the difference between the orbital velocity of these two moons (see Table 5-1) and the difference in the drift velocities between the two L shells. From Equation 5.2, Ω is constant in both cases, $\Delta\omega_k = 2.4 \times 10^{-4}$ rads^{-1} and for each of the three pitch angle values $\Delta\omega_D \sim 2.4 \times 10^{-4}$ rads^{-1} thus the value of the resonant energies are equal since $\Delta\omega_D \approx \Delta\omega_k$. Electrons of these energies will escape absorption and should not show depletion.

Table 5-4 Values for resonant energy in MeV for particles of 30°, 60° and 90° pitch angles at the orbit of Tethys, Enceladus and Mimas.

E_R of the Moon	α_{eq} = 10° (MeV)	α_{eq} = 60° (MeV)	α_{eq} = 90° (MeV)
Tethys	1.25	0.94	0.89
Enceladus	1.39	1.04	0.98
Mimas	1.39	1.04	0.98

As described in Chapter 1, a particle will gyrate about a field line with a particular radius depending on the field strength, charge and particle mass. We can see that for a particle with a gyroradius (R_g), that is less than the radius of the moon (R_m), if the field line intercepts the moon the particle will almost certainly be absorbed. However, if the gyroradius > moon radius, then it is possible for the particle to avoid the moon even if the field line it is orbiting threads the moon. For electrons at the orbits of Tethys, Enceladus and Mimas, the gyroradii for a range of energies are shown in Table 5-5. We see that for electrons of interest in this study 'total' absorption can be considered since $R_g << R_m$ in every case. In fact, this does not start to become an issue until the electron energy is very large. At such magnitudes, the fluxes would be so low that the effect would not be discernable.

Table 5-5 Gyroradii of 0.8, 1.5 and 3 MeV electrons at the orbits of Tethys, Enceladus and Mimas compared with the moon radii. The moon is larger than the electron gyroradii for all cases given here.

Moon and radius (R_m)	0.8 MeV	1.5 MeV	3 MeV
Tethys (536 km)	17 km	24 km	33 km
Enceladus (256 km)	9 km	13 km	18 km
Mimas (209 km)	4 km	6 km	8 km

The motion along a field line is also of interest. If, during half a bounce period ($L_{B/2}$), a particle drifts a longitudinal distance that is greater than the moon travels in an equivalent time, it may escape impacting the moon altogether. This is the 'leapfrogging' effect [Mead and Hess, 1973; Thomsen et al., 1977; Rairden, 1980]. To establish at what energies this may become significant, we calculate the longitudinal distance covered by a particle in half a bounce period for several energies (Table 5-6). We then compare these with the sum of the distance the moon travels in the same time plus the size of the moon.

From the moon diameters (Tethys ~ 1060 km, Enceladus ~ 500 km and Mimas ~ 400 km) we see that in the time it takes most of these electrons to complete half a bounce period, the moon will have only moved a small distance and since $D_m >> L_{B/2}$ the electrons will be completely absorbed. We note that this effect only becomes

significant at very large energies which indicate that this escape mechanism is not observed in the electrons.

Table 5-6 Distances travelled in half a bounce period by 0.8, 1.5 and 3 MeV electrons at the orbits of Tethys, Enceladus and Mimas. Since the values for the relative velocity of the moon and drifting particle for the energies considered here are either side of the transitional energy (Table 5-3), some of these distances travelled are eastwards, and some are westwards (indicated by a negative sign), hence the lack of a monotonical relationship with energy. Since these distances are considerably smaller than the moon diameter and the longitudinal distance travelled by the moon in the same time, leapfrogging does not become an issue for electrons at these energies.

Moon and distance it travels in half a bounce period (D_m)	0.8 MeV	1.5 MeV	3 MeV
Tethys (~ 18 km)	13 km	- 6 km	- 26 km
Enceladus (~ 16km)	30 km	2 km	- 27 km
Mimas (~ 26 km)	30 km	10 km	- 10 km

5.4.2 Particle motion with respect to the moon

The idea of resonant energy also leads to the idea of a 'transitional' energy at each moon. Here we describe the implications for the motion of energetic electrons (and therefore cavities in these populations) relative to the moons themselves and define the notion of 'upstream' and 'downstream' with respect to the moons and corotation.

There are several 'rules' of electron motion which we can outline to aid in the interpretation of the depleted plasma cavities carved out by the moons (see Figure 5.2):

a) the moon has a leading and a trailing edge associated with its orbital motion around the planet. The leading edge faces its direction of motion, which is in the same direction as the corotational flow (eastwards around the planet);

b) below the transitional energy, the net drift of an electron is in the eastwards direction, (i.e. in the same direction as the moon), since corotation dominates the drift motion and therefore any absorption cavities will also travel in this direction;

c) below the resonant energy of the moon (and still below the transitional energy), i.e. when $(\omega_I - \omega_k) > 0$ electrons will drift faster than the moon (in the prograde direction) and thus any depletion signature will travel faster than the moon and the cavity will be observed downstream with respect to corotation;

d) when the electron energy is above the resonant energy (and still below the transitional energy), $(\omega_I - \omega_k) < 0$ and the moon will be moving faster than the electron is drifting. Thus, although the electron is travelling in the same direction as the moon, any depletion signature will appear on the upstream side of the moon with respect to corotation [e.g. Paranicas and Cheng, 1997];

e) when the electron energy is higher than the transitional energy, the population, plus any depletions present, will be upstream of the moon with respect to corotation and will travel westwards away from the moon.

Note that for electrons of a particular pitch angle $E_T > E_R$ always at the orbits of Tethys, Enceladus and Mimas. We can further illustrate these points using a simple sketch (Figure 5.2).

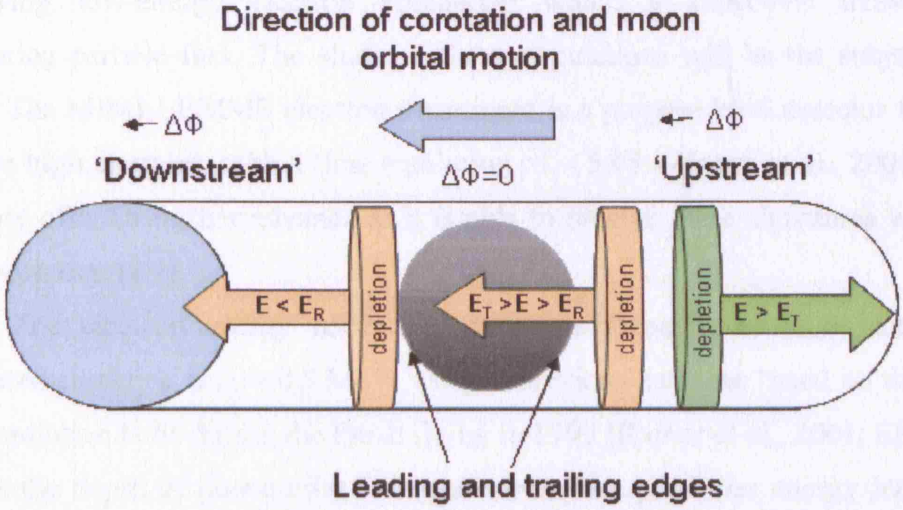

Figure 5.2 Sketch demonstrating the motion of depleted wakes relative to the moon and corotation depending on the energy range undergoing absorption. We have not indicated the relative speeds of these travelling signatures with respect to the moon, since the speeds are dependent on the energy of the particle and the orbital speed of the moon. The upstream and downstream edges of the moon (with respect to corotation) have been indicated as has the direction in which longitudinal separation of the moon and the particle population occurs ($\Delta\phi$).

5.4.3 Electron energy of interest

For the purposes of this study, a high energy electron is defined as one with an energy which is greater than the ELS is designed to measure (> 26 keV), and which can penetrate through the instrument casing and impact the detector plates. The ELS is not capable of analysing electrons at such energies, since they do not pass between the hemispherical surfaces and thus energy, direction and pitch angle can not be determined. Nevertheless, they are still detected by the multi-channel plates. Therefore, we are also able to detect the absorption of these penetrating particles as a drop in the count rates. We do not consider any additional shielding effects from the spacecraft body itself, depending on Cassini's orientation, which might change the energy of electrons being detected at ELS since a comparative analysis of fluxes versus

orientation is beyond the scope of this thesis. We also do not observe any significant differences in fluxes between anodes.

We are therefore able to apply the ELS to the challenge of investigating the moon absorption wakes by means of a hitherto unused by-product of our data, providing an additional dataset to contrast and compare with results from other instruments on Cassini. An additional benefit is that during the absorption we are able to see the underlying low-energy electron population which is otherwise masked by the penetrating particle flux. The study of these populations will be the subject of future work. The MIMI-LEMMS electron instrument is a purpose built detector for electrons of these high energies, with a time resolution of ~ 5.65 s [Jones et al., 2006]. The ELS therefore offers a further advance as it is able to resolve these signatures with a higher time resolution (2 s).

The electron energy needed to penetrate through the ELS instrument and associated shielding is > ~ 0.8 MeV, using a previous estimate based on data collected in the radiation belts during the Earth fly-by in 1999 [Rymer et al., 2001; ESA, 1993]. It tells us the depth of penetration for an electron of a particular energy into 1.6mm of Aluminium shielding before it loses all its energy. We can therefore consider in which energy the ELS will observe absorption wakes based on the minimum energy that can be detected. Based on the values for transitional and resonant energies in Table 5-3 and Table 5-4, we can see that the ELS is able to observe energies both above and below the resonant energy at each of the three moons. Thus, the ELS is sensitive to both upstream and downstream wakes (with respect to corotation) of the moon. In fact, the location of absorption wakes may aid in determining the maximum energy being observed by the ELS.

5.4.4 High-energy electrons in the inner magnetosphere

From observations made with the Pioneer and Voyager spacecraft, the energetic electron environment at the L shells of interest, i.e. within the orbits of Tethys (4.89 R_S) to Mimas (3.08 R_S) has been characterised [Krimigis et al., 1982, 1983; Chenette and Stone, 1983; Van Allen, 1984] and we review these here.

Krimigis et al., [1983] discussed the functional dependence of the electrons, showing plots of hourly averaged electron spectra. In general, the spectrum hardens with decreasing L. They also report on a decrease in 'low-energy' electrons (< 30 keV)

inside the orbit of Rhea (~8.7 R_S), although this will not effect our analysis since here we are measuring electrons which have an energy > 0.8 MeV. Electrons of energies ~ 0.5 to ~ 1 MeV are depleted inside the orbit of Tethys. There also appeared to be a large asymmetry between orbits and sometimes during the same orbit for the inbound and outbound passes which we have also seen in the Cassini data [André et al., 2006]. This effect occurs due to the variation in the external forcing of the solar wind, CIRs for example.

At the orbit of Tethys, the spectrum follows the shape of a power law with the spectral index, γ = 1.95 below ~ 150 keV. At energies above this a secondary component is present, but the flux reduces sharply above ~ 1.5 MeV. This is also seen at Enceladus and Mimas. This lack of data on the relative fluxes between electrons of energies of ~ 1 MeV to several MeV is unfortunate, since it is in these energies that we are observing absorption signatures.

Van Allen et al., [1980], Van Allen [1984], Krimigis et al., [1983] and Chenette and Stone, [1983] also described a process whereby, due to a resonance of electrons of certain energies at the various moon L shells, a 'filtering' effect occurs. This preferentially allows electrons of 'resonant' energy (see Table 5-4) to pass radially inwards, across the L shell of a moon, without suffering absorption. Combined with the conservation of the first and second adiabatic invariants, this explained the reason for the peak in the electron spectrum at ~ 1.6 MeV at the orbit of Mimas. From Figure 5.3, we see that there is also a peak at ~ 1.6 MeV at the orbits of Tethys and Enceladus also, although this is not explained and may not be due to the same process.

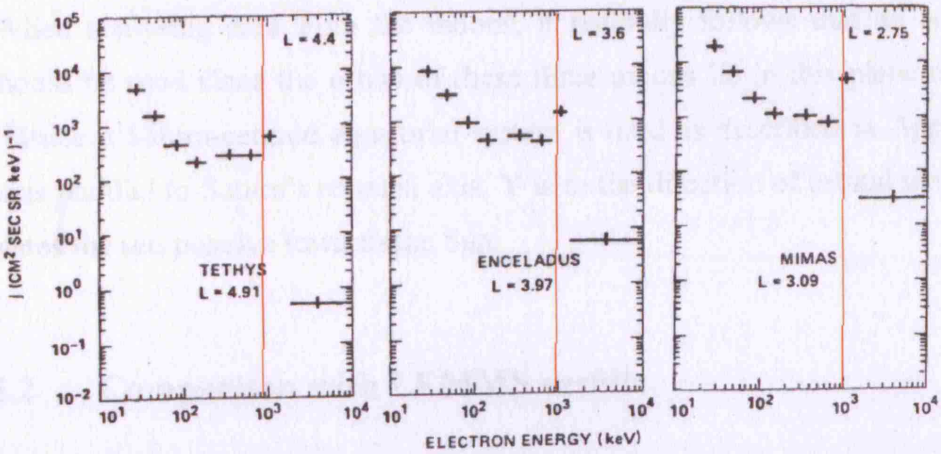

Figure 5.3 Electron energy spectrum at the L shells of Tethys, Enceladus and Mimas (reproduced from [Van Allen et al., 1984]). We have indicated the resonant energy for 90° pitch angle particles with the red line. Note the lack of data above 1 MeV. At Tethys, the first population below 150 keV has a power law with γ=1.95.

5.5 Observations

5.5.1 Introduction

The sensitivity of the ELS to penetrating particles results in a constant count rate across all energies. The immunity of these high energy electrons to the voltage sweep of the analyser and the geometry means that energy partitions and pitch angle information are not obtainable for these counts. The ELS simply registers a count, thus all intensities referred to in this chapter are un-calibrated counts. This results in the ELS having a broad energy response from ~ 0.8 MeV up to some unknown maximum energy.

Satellite wakes (either upstream or downstream), will disperse with time resulting in a longitudinal variation of wakes of particles of different energy due to the energy dependence of the drift velocity [Chenette and Stone, 1983]. Thus, the broad energy response of the ELS will simply result in an observation of a superposition of these different signatures, which will appear to broaden and decay with time as 'older' wakes become more spread out in both longitude and radial distance.

We inspected the data for absorption effects for those periods when Cassini crossed the L-shells of three of Saturn's medium-sized icy moons, Tethys, Enceladus and Mimas. From this we have identified several clear, and a few less clear, examples of moon absorption signatures from a period covering Saturn Orbit Insertion (SOI) in June 2004 through to July 2005. While in these inner magnetospheric regions, the effect of the penetrating electrons on the ELS observations was obvious.

When analysing data from the moons, it naturally follows that an equatorial frame should be used since the orbits of these three moons lie in this plane to within 0.168°. Hence a Saturn-centred equatorial system is used as described in Appendix C with Z axis parallel to Saturn's rotation axis, Y is in the direction of orbital motion and X completes the set, positive towards the Sun.

5.5.2 Comparison with LEMMS results

The moon depletion signatures observed in the ELS data which are also seen in the LEMMS data provide an opportunity to compare datasets. There are eight events which are detected by both the ELS and LEMMS. Where the published LEMMS results contain enough details of the observation, we shall compare them to the ELS findings

with the aim of establishing the physical origin of any differences. The events in which signatures are seen in both instruments are:

- Tethys: 9 March 2005 at 06:51 UT and 16:28 UT [Roussos et al., 2005] and 06:15 UT [Paranicas et al., 2005]. On 30 March 2005 Roussos et al., [2005] report a strong signature at 04:25 UT when no depletion is detected in the ELS data. These signatures are all seen in the LEMMS 'low energy' electron channels: ~ 28 - 100 keV;
- Enceladus: 16 February 2005 at 22:45 UT and 17 February, 03:27 UT [Paranicas et al., 2005]. On 9 March at 09:07 UT, 21 May at 03:52 UT and 14 July 2005 at 19:55 UT [Jones et al., 2006];
- Note that there are currently no reported results at the L shell of Mimas from the LEMMS data.

5.5.3 Observations at the L shell of Tethys (L=4.89 R_S)

5.5.3.1 Tethys, 06:51:06 UT, 9 March 2005

Figure 5.4 contains the energy-time spectrogram and the intensity plot for a depletion signature observed at the L shell of Tethys on 9 March 2005, 06:51 UT. Time is along the horizontal axis from 06:46 UT to 06:55 UT, the vertical axis shows the energy in eV and the colour scale indicates the count rate. The constant counts before 06:49 UT at all energies due to the penetrating electrons are obvious as the predominately yellow band from ~ 20 eV upwards. Below this, the photoelectrons are evident as the red band at low energies, as they have a higher count rate than the penetrating particles in this region (~ 4.89 R_S). The absorption signature is also obvious centred on 06:51 UT. In the intensity plot (bottom panel), the vertical axis shows counts per second summed over all anodes and over energies > 100 eV upwards. We sum over energies > 100 eV so that the true depth of the signature is not affected by the photoelectron counts (apparent below ~ 20 eV, although this varies between signatures) and any low energy population masked by the penetrators.

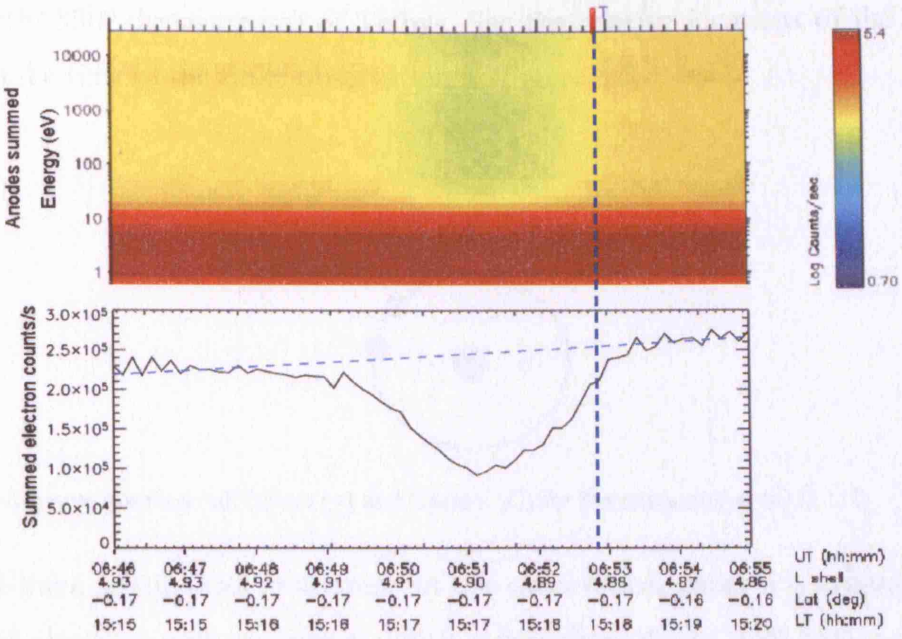

Figure 5.4 Energy-time spectrogram for the absorption signature for Tethys from 9 March 2005 (top) between 06:46 UT to 06:55 UT. Time is along the horizontal axis, the vertical axis shows the energy in eV and the colour scale indicates the count rate summed across all anodes. The constant counts at all energies due to the penetrating electrons are obvious as the yellow colour above ~ 20 eV. Below this are the photoelectrons, evident as the red band at low energies. (Bottom) The intensity plot shows counts per second on the vertical axis. The normalised background count rate profile is indicated by the dashed blue line. The L-shell of Tethys is indicated by the dark blue dashed line at ~ 4.89 R_S.

Also plotted is a fit to the undisturbed background count rate profile (blue dashed straight line), assumed to be representative of the background counts as if the cavity was not there. In general, Cassini travels predominately radially towards (or away from) the planet, thus the profile of counts tends to show an increase (or decrease) as the fluxes become more intense with decreasing (increasing) L-shell. We fit a line to the intensity by extrapolating the values from one side of the dip to the other, to establish what form the data would take in the absence of the absorption profile. We define the start and end of the dip as the point at which the counts begin to fall off or return to the background levels. We find the depth of the absorption by taking the ratio of the counts at the deepest point in the profile to what the surrounding counts would have been at the same point in time.

$$Signature\ \ depth = \frac{C_{\min}}{C_{surr}}$$

Equation 5.3

For this example, the depth = 0.37. So the cavity is depleted of 73% of the electrons in the observed range. At the time of this measurement, Cassini is 30° upstream (or

equivalently 330° downstream) of Tethys. See the relative locations of the moon and Cassini at the time of the wake observation in Figure 5.5.

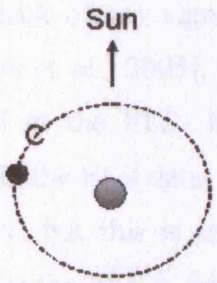

Figure 5.5 Relative positions of Tethys (•) and Cassini (C) for the encounter at 06:51 UT.

There are three possibilities to account for this observation, either it is caused by:

a) electrons with an energy which is less than E_R (< 0.89 MeV to 1.25 MeV depending on the pitch angle) which have travelled downstream of Tethys, in which case this cavity has extended round the planet for ~ 330°;

b) electrons which have $E_R > E > E_T$, i.e. 0.89 MeV < E < 1.23 - 1.73 MeV (depending on the pitch angle). There is an overlap in the energy range due to the difference between the highest resonant energy for α=10° (1.25 MeV) and the lowest transitional energy for α =90° (1.23 MeV) but since we cannot measure any pitch angles of the penetrators we shall consider only energies of 90° pitch angle electrons for simplicity. Absorption of electrons of these energies would result in a wake upstream of Tethys (with respect to corotation) but which is still travelling eastwards. Thus, due to their smaller relative speed compared with the moon, the depleted region is simply lagging the moon by 30° and is a relatively 'young' cavity;

c) a cavity in electrons with sufficient energy to counteract corotation, i.e. E $> E_T$, and which have travelled only 30° upstream of the moon.

Of course we also note that for any of these cases the cavity may have lasted for more than one orbit of the planet. So the longitudinal separation from the moon itself may be $360° n$ + observed separation as noted in Paranicas et al., [2005]. Since the ELS is sensitive to all of these energy ranges, it makes the accurate determination of the nature of the signature a difficult, if not impossible task without further information.

The depletion in the electrons as detected by the ELS is observed at 06:51 UT. In comparing with the observations by LEMMS, they report a 'strong' depletion at the *expected* L shell crossing [Roussos et al., 2005]; although it is not clear whether this corresponds to the exact time they see the absorption. They suggest, based on this

evidence, and with knowledge of the particle energy, which is in their 'low-energy' range, i.e. < ~ 100 keV that the depletion at this L shell encounter has in fact lasted nearly a full rotation and is therefore a downstream signature agreeing with case a) above. In addition, they report a lack of any signature in electrons of 94 keV to 4.4 MeV in the LEMMS data [Roussos et al., 2005]. Since this covers the likely energy range of electrons being observed at the ELS, it is a puzzle to understand which electrons are causing the signature in the ELS data. The ELS may be detecting a flux of penetrators of the order ~ 100 keV, but this is unlikely since the amount of energy required to penetrate the shielding on the ELS is fairly well known [Rymer et al., 2001; ESA, 1993]. Alternatively, the ELS is detecting a signature in electrons of energy > 4.4 MeV, which would fall into category c) above, and have travelled upstream away from the moon. In fact, Roussos et al., [2005] suggest that the lack of any signatures in these channels has most likely arisen due to the low signal-to-noise ratio of their detectors at these energies or the low fluxes at these energies (see Figure 5.3) which would indicate that the ELS is detecting a signature which is below the detection threshold of LEMMS.

We also note that the LEMMS data report the signature as displaced from the moon L shell outwards by 0.2 R_S. We note a slight displacement outwards of ~ 0.01 R_S as apparent in Figure 5.4. This encounter was observed at a local time of ~ 17:16 on the dusk flank. This variation in the radial drift may be a result of a deviation in the drift shells for particles of different energies.

We also observe a slight asymmetry to the cavity, most noticeable in the count rate profile (lower panel of Figure 5.4), with steeper absorption seen as the signature is entered at ~ 06:50 UT. This leads us to consider the process by which these signatures are refilled. If it is due to diffusion from surrounding electrons, is there a preferential direction of diffusion, i.e. radially inwards or outwards? Does the radial motion of the cavity itself modify the profile?

5.5.3.2 Tethys, 16:15 UT and 16:28 UT, 9 March 2005

The next example of a Tethys L-shell crossing occurred on 9 March 2005. The spectrogram and associated count rate plot are shown in Figure 5.7. This time we see moderate depletion in the counts at two distinct points centred on 16:15 UT and 16:28 UT. There is clearly more refilling in these cavities compared with the previous example at 06:51 UT and from Equation 5.3 we find $C_{\min}/C_{surr} = 0.89$ for both cases, indicating that there is only 11% depletion. This suggests that these signatures are of the

same age (and older than that observed at 06:51 UT), although this is not supported by the difference in their positions in L-shell and the difference in width of the cavities.

In contrast to the previous example, Cassini is 29° downstream (or 331° upstream) of Tethys (Figure 5.6).

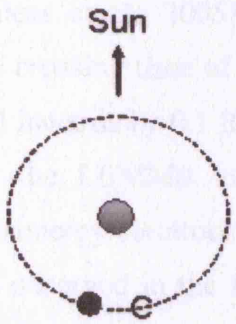

Figure 5.6 Relative positions of Tethys and Cassini for the encounter at 16:15 UT

We again consider the energies needed to create these profiles at this distance from the moon.

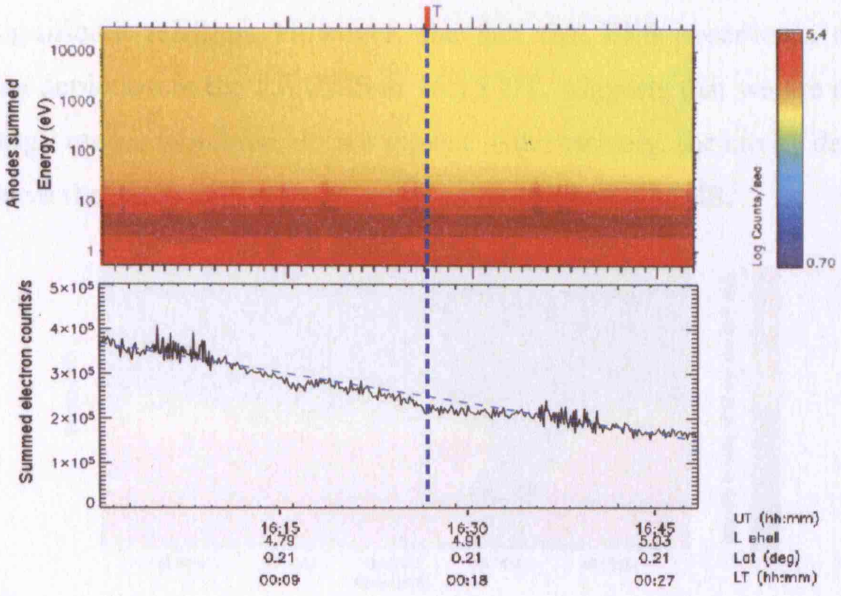

Figure 5.7 Spectrogram and count rate profile plots showing depletions at 16:15 UT and 16:28:30 UT in the same format as for the previous plot. Note the two dips, one slightly displaced inwards.

As for the previous example, there are several situations that could have resulted in the observation of a cavity at this distance from the moon. Either this is a downstream propagating cavity (case a), with E < E_R that has drifted 29° ahead of the moon (with respect to corotation), or it is an upstream signature but travelling eastwards in the same direction as the moon, lagging it by 331°, with E > E_R (case b) or case c, it is an upstream travelling signature (i.e. with $E > E_T$) and has travelled 331° upstream. We

are not able to say for certain which of these energy ranges is being detected by ELS and thus whether this is an up- or downstream travelling signature.

Comparing our observations to those reported by LEMMS [Roussos et al., 2005; Paranicas et al., 2005] we find that they observe only a single cavity at 16:15 UT (reproduced in Figure 5.8) [Paranicas et al., 2005]. In fact, this is the cavity which corresponds to the *expected* L shell crossing time of 16:28 UT mentioned in Roussos et al., [2005]. This cavity is displaced inwards by 0.1 R_S [Roussos et al., 2005].

Again the depletion is in the LEMMS low energies < 100 keV, with no corresponding signature in the high energy electrons (100 keV < E < 4.4 MeV). This is clearly more depleted than the dip observed in the ELS counts, suggesting that we are responding to a different energy population which would explain the difference in count rate profiles. Since we do not expect to be able to see the signature in these low energies, we once more assume that we are detecting the high energy electrons not observable by LEMMS. This possibly explains the signature at 16:28 UT, which is most likely an upstream signature which has survived nearly a full orbit of Saturn (~ 331°), hence the significant refilling. However, the fact that ELS observes a depletion co-located with a depletion in the LEMMS at 16:15 UT, suggests that we are responding to a similar energy range, which we do not expect. Alternatively, the cavity detected by the ELS could have the same drift history as the cavity in the LEMMS.

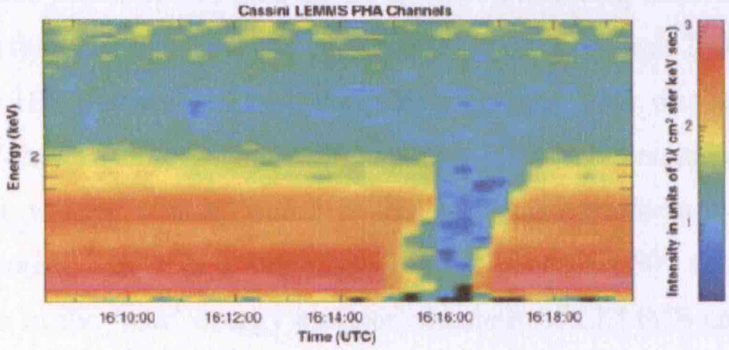

Figure 5.8 Electron intensity spectrogram for 20 – 400 keV electrons for 9 March 2005 reproduced from Paranicas et al., [2005]. The dip in their low energy electrons is evident at ~ 16:15 UT extending to ~ 100 keV.

We are unable to say whether the depletions at 16:15 UT and 16:28 UT are exhibiting the asymmetric behaviour of the previous cases because the level of absorption is so slight.

5.5.3.3 Tethys, 04:25:00 UT, 30 March 2005

On 30 March 2005 Cassini crossed the L-shell of Tethys without any apparent reduction in the ELS counts. At this time Cassini was 280° upstream of the moon (or 80° downstream).

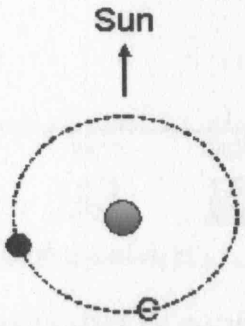

Figure 5.9 Relative positions of Tethys and Cassini for the encounter at 04:25 UT

Hence Cassini was closer to the moon upstream compared with the depletion on 9 March at 16:28 UT but closer to the moon downstream with respect to the depletion at 06:51 UT on 9 March 2005. In either case, no depletion is observed, either because the wake has refilled to background levels due to the age of the signature, or that the local conditions of the magnetosphere have changed relative to those encountered on 9 March resulting in a faster elimination of the cavity by the surrounding plasma.

We note that LEMMS saw a clear absorption on 30 March 2005 [Roussos et al., 2005] (Figure 5.10), that was, in fact, a double signature. This was attributed to either the geometry of the L shell crossing or the activity in the magnetosphere as Tethys was 'shedding' these wakes. This appeared in the 'low' energy electron population (20 – 102 keV), indicating that it is a signature that has extended 80° downstream. Again, such a depletion in the 'low' energy electron channels of LEMMS are not expected to be detected by the ELS. A corresponding depletion in the high energy may not be detected due to its distance from the moon and the increased diffusion rate at higher energies, resulting in a faster refilling occurring over 280°.

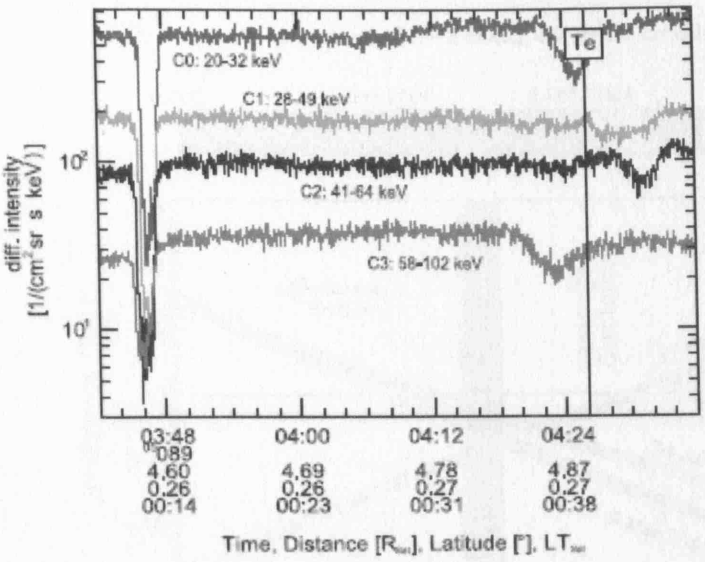

Figure 5.10 Differential intensity flux from LEMMS for the 30 March 2005 when Cassini crossed the L shell of Tethys. The double signature at ~ 03:46 UT and 04:24 UT is apparent in the 20 – 102 keV electrons (reproduced from Roussos et al., [2005])

5.5.4 Observations at the L shell of Enceladus (L=3.95 R_S)

We now review the signatures seen at the L-shell of Enceladus. There are six examples which we have used in this analysis, all at varying degrees of separation from the moon itself, and therefore providing a range of signature 'ages'. There are three signatures which occurred very close to the moon, within 1° upstream (with respect to corotation). The positions of these relative to Enceladus, together with the intensity of the ELS absorption, have been plotted in Figure 5.11.

In each case, the intensity has been over-plotted onto the spacecraft trajectory with respect to the moon orbital position in Saturn equatorial coordinates in the X-Y and X-Z planes. Cassini crossed below the orbital plane for two of the flybys (9 March 2005 and 14 July 2005) within ~ 1.5 R_{EN} and 0.7 R_{EN} respectively and above for the flyby on 17 February 2005 (within ~ 4.5 R_{EN}). These encounters have produced new absorption profiles which are very deep, since there has not been time for the refilling to occur. We now consider each of these in more detail.

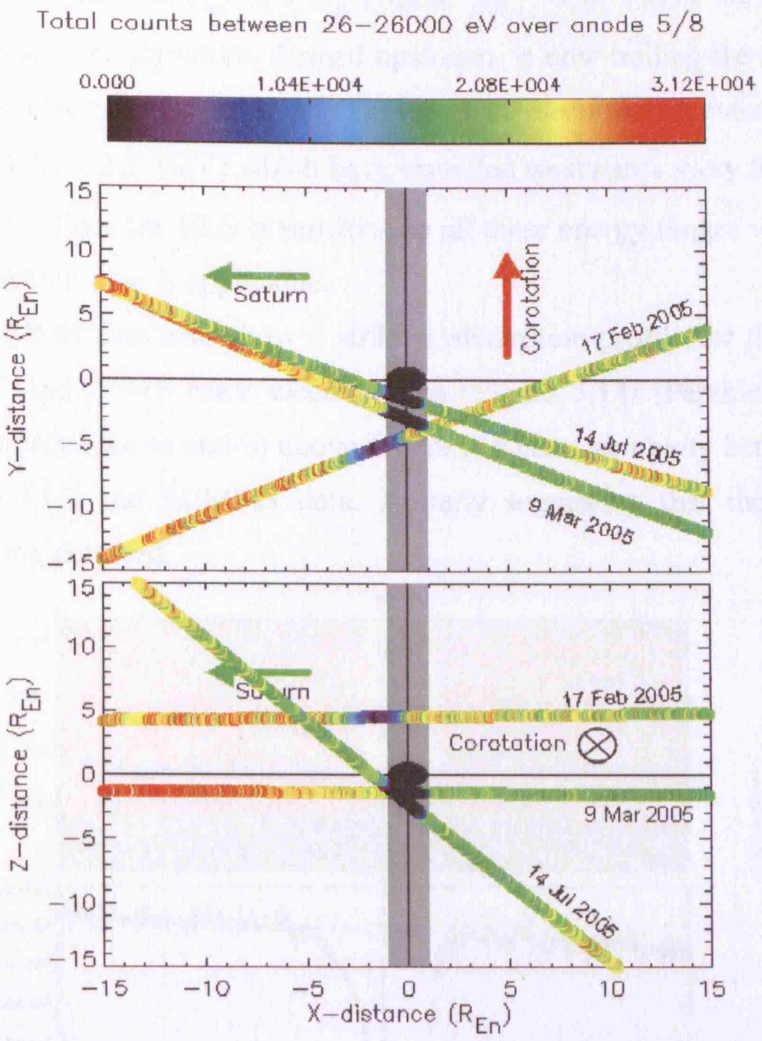

Figure 5.11 Trajectory plots in the X-Y and X-Z planes in an Enceladus-centred equatorial frame of the three closest Enceladus flybys on 17 February 2005 (outbound), 9 March 2005 (inbound) and 14 July 2005 (inbound) [after Jones et al., 2006]. ELS electron intensities (counts per second) are shown by the colour scale, with black the lowest, showing the counts summed over all anodes and over energies > 100 eV. This energy is chosen to omit the photoelectrons and any low energy population previously masked by the penetrating radiation. The three absorption signatures are apparent close to the nominal moon radial distance. The directions of Saturn and the corotation flow are indicated. For our purposes we assume the magnetic field to be a simple, southwards-oriented dipole. However, results published by Dougherty et al., [2006] suggest this may not be the case and this is discussed further in the text.

5.5.4.1 Enceladus, 03:27 UT, 17 February 2005

On 17 February 2005 Cassini made the closest ever flyby to Enceladus at distance (from the centre of the body) of 1512 km. Figure 5.12 contains the spectrogram and intensity plot from the interval containing a very striking absorption signature at ~ 03:27 UT. The nature of the flyby, plus the almost total absorption, $C_{\min}/C_{surr} = 0.12$ is highly suggestive that this is an upstream signature in the 'high' energy electrons. Thus we consider the depletion in electrons in case a) where the energy of the electrons is

greater than the resonant energy $E > E_R$ (where E_R = 0.98 – 1.39 MeV depending on the pitch angle) and the signature, formed upstream, is now trailing the moon by 0.39°, or case b), the electron depletion has occurred in electrons of even higher energy $E > E_T$ (i.e. > 1.58 – 2.2 MeV) which have travelled westwards away from the moon a distance of 0.39°. Since the ELS is sensitive to all these energy ranges we are unable to say for certain which case is applicable.

The LEMMS data also show a striking absorption profile for this encounter in the 0.9-3 MeV and 2.7-18 MeV electron data (Figure 5.13) [Paranicas et al., 2005] which would satisfy case a) and b) above. There is a clear similarity between the cavity profiles in the ELS and LEMMS data, strongly suggesting that the same electron energies are being detected.

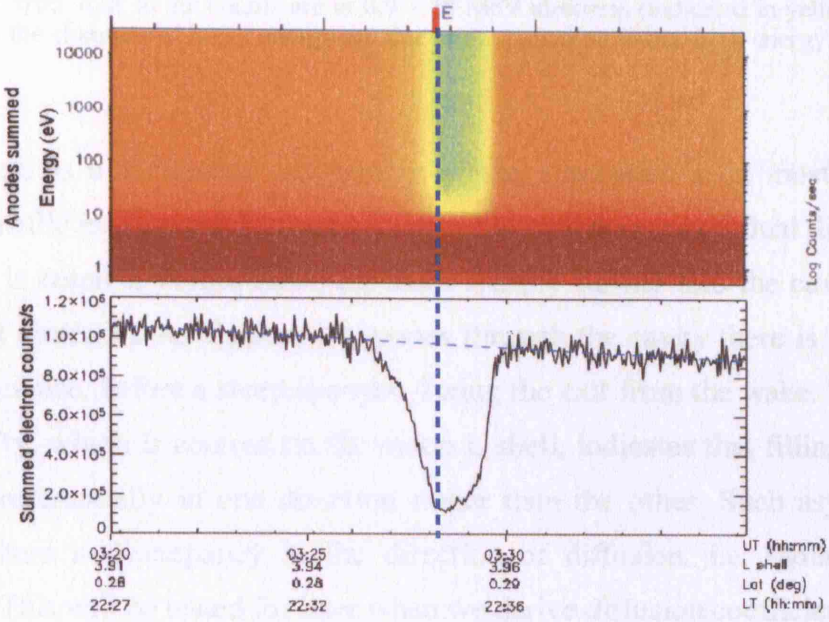

Figure 5.12 The absorption signature of Enceladus detected on 17 February 2005 at 03:27 UT in the same format as previously used. The absorption signature at 03:27 UT is striking and is closely aligned with the L-shell of Enceladus.

In addition, we estimate the depth of absorption in these two energy channels to be $C_{\min}/C_{surr}$ ~0.006 and 0.008 respectively. This is a stronger depletion than we observe however; there is an error on these values since they are inferred from Figure 5.13. Alternatively, since the ELS has a broad energy response (with an unknown upper energy) we may be detecting additional background counts which decreases our depth of depletion.

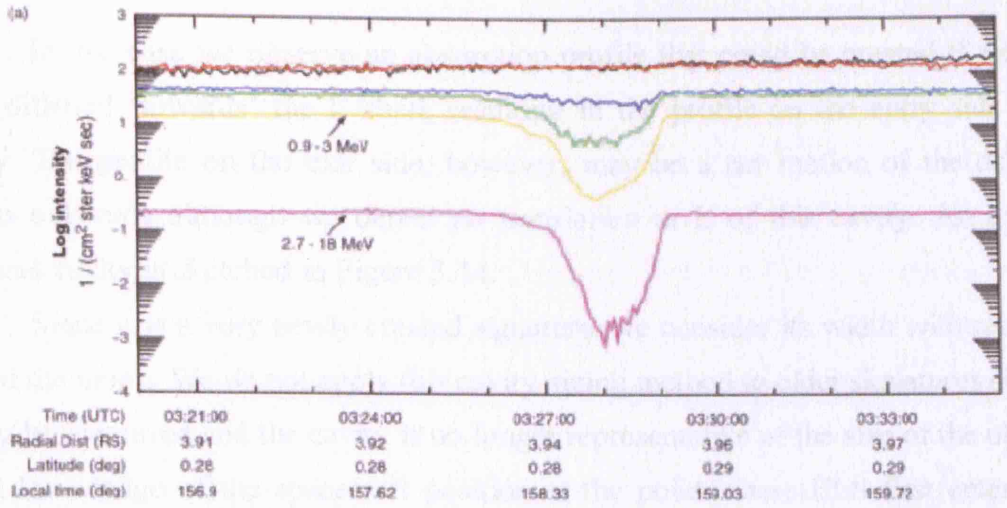

Figure 5.13 Intensity of high energy electrons as detected by LEMMS (reproduced from Paranicas et al., [2005]). The 'true' dips in the counts are in 0.9 – 18 MeV electrons (indicated in yellow and pink). The depletions in the channels of lower energy are due to the reduction in the high energy penetrators due to the moon.

There is a noticeable asymmetry of the absorption seen most clearly in the intensity profile in Figure 5.12 (and Figure 5.13), with a more gradual drop in counts as the cavity is entered, before reducing more sharply further into the cavity in the anti-planetward direction. As Cassini progresses through the cavity there is initially a more gradual decrease, before a steep increase during the exit from the wake. The asymmetry of the cavity, which is centred on the moon L shell, indicates that filling in has begun, possibly preferentially in one direction rather than the other. Such asymmetries may occur if there a discrepancy in the direction of diffusion, i.e. radially inwards or outwards. This will be tested for later when we derive diffusion coefficients.

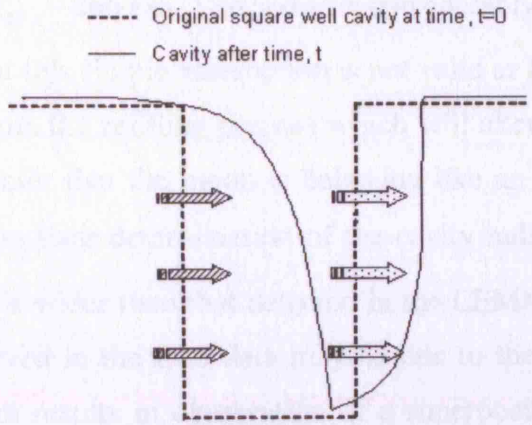

Figure 5.14 Sketch demonstrating how a cavity may evolve in time and the resulting profile. The initial square well carved out in the electrons is subject to diffusion from the surrounding plasma. This fills in one side of the cavity, while the depleted region becomes displaced in L on the other side. The similarity to the actual profile in Figure 5.12 is apparent.

In this case we observe an absorption profile that could be created if electrons have diffused 'towards' the L shell, resulting in the profile on the entry side of the cavity. The profile on the exit side, however, may be a net motion of the depletion region outwards although we detect no translation in L of this cavity. An example resultant cavity is sketched in Figure 5.14.

Since it is a very newly created signature, we consider its width with respect to that of the moon. We do not apply this cavity-sizing method to older signatures since re-filling has occurred and the cavity is no longer representative of the size of the obstacle. From knowledge of the spacecraft position at the point where ELS first entered and exited the depletion, we can estimate the radial width of the signature. The depletion is observed between ~ 03:26:30 UT to 03:30 UT, which, using the radial velocity of the spacecraft, gives a total cavity radius of ~ 700 km (~ 2.7 R_{EN}). Previous estimates of the effective absorbing width of an inert body [Van Allen et al., 1980] have used a simple expression which is the sum of the gyroradius of the absorbed particle and the moon radius. This can be easily explained by assuming that the moon can absorb particles whose guiding centres pass within one gyroradius of the moon. Thus;

$$R_{eff} = R_m + R_g$$

Equation 5.4

where R_m and R_g are the radius of the absorbing moon and the gyroradius of the particle being absorbed. We apply this equation to calculate the minimum effective radius of the cavity. Since R_g ~ 10 km for electrons of ~ 1 MeV at the orbit of Enceladus, we find R_{eff} ~ 266 km. This value is considerably smaller than the observed cavity, suggesting that this simple assumption is not valid at Enceladus. In addition, this wake has already begun the refilling process which will alter the original wake profile. Jones et al., [2006] infer that the moon is behaving like an insulator and atmosphere-free which is based on their determination of the cavity radius ~ R_{eff}. Thus, the cavity detected by the ELS is wider than that detected in the LEMMS electrons. The reason a wider cavity is observed in the ELS data may be due to the broad energy response of our instrument, which results in observation of a superposition of cavities, each with different widths. If, for example, we are sensitive to very high energy electrons, R_{eff} will increase, resulting in a larger cavity. However, the discrepancy between the ELS

and LEMMS widths is inferred to be ~ 400 km which cannot be accounted for by depletion of electrons with an increased gyroradii unless we start considering unrealistic particle energies.

At the orbit of Enceladus, a simple southward dipole is valid and thus the unperturbed magnetic field is pointing southwards (-Z in Figure 5.11). However, findings by Dougherty et al., [2006], demonstrated that Enceladus has an atmosphere, which results in a significant interaction with the magnetic field in the vicinity of the moon. There are thus significant perturbations of the magnetic field due to the slowing and deflection of the corotating plasma flow [Tokar et al., 2006] and the field was observed to tilt in both the X (in the direction of the corotating flow) and Y (towards Saturn) components, with a compression in the southward component [Dougherty et al., 2006]. However, we expect the ELS to be responding to the same energies as LEMMS, which should respond to any field perturbations in the same manner.

5.5.4.2 Enceladus, 09:07 UT, 9 March 2005

On 9 March Cassini executed another dedicated and even closer flyby of Enceladus (closest approach ~ 748 km). At the time the absorption cavity was detected, the spacecraft-moon separation was ~ 0.24° upstream and is due to absorption of high energy electrons above the resonant energy or even the transitional energy. The depth of the signature $C_{\min}/C_{surr}$ ~ 0.002 indicates almost total absorption, suggesting that this is an almost instantaneous snapshot of the depleted flux tube threading Enceladus. However, it is also apparent that at the lower energies the absorption is not total, since we observe counts below ~ 50 eV. At the very lowest energies the spacecraft photoelectrons are now able to be detected. Above this > ~ 8 eV there is a low energy population underlying the penetrating counts. This was not apparent during the flyby on 17 February 2005 since re-filling had begun. This population is most probably the low energy population associated with production from Enceladus, and was also observed during the flyby on 14 July 2005 [Tokar et al., 2006] when the moon once again carved out a cavity in the high energy electrons and which is discussed in the next section.

Based on the duration of the depletion and the spacecraft velocity, we estimate the cavity radius to be ~ 316 km (~1.25 R_{EN}) which is much closer to the estimate for R_{eff} than the previous example on 17 February 2005. We might expect this since this cavity is 'younger' and has undergone less re-filling. There is a very slight asymmetry

to the signature inbound and outbound as seen by the more gradual increase in counts on the outbound traverse in the spectrogram.

We also note a displacement in L, with the signature appearing ~ 0.015 R_S outwards of the moon L shell (~ 3.5 R_{EN}). At this time Cassini's orbit has a very low inclination, as it does for all three close flybys, so this offset is not expected to be due to a latitudinal effect. This displacement is also observed in the cavity in the LEMMS data. The normalised counts in the LEMMS (0.98 – 3.28 MeV) electrons are shown in Figure 5.16 from Jones et al., [2006] and appear very similar to those seen at ELS, with almost total absorption.

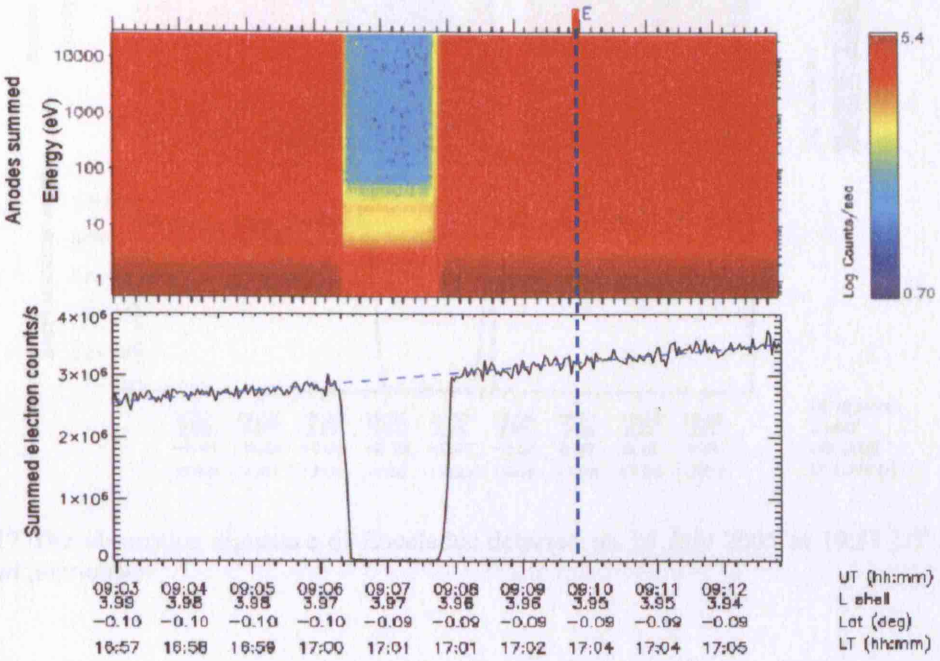

Figure 5.15 The absorption signature of Enceladus detected on 9 March 2005 at 09:07 UT plotted in the same format used before. Note the displacement in L.

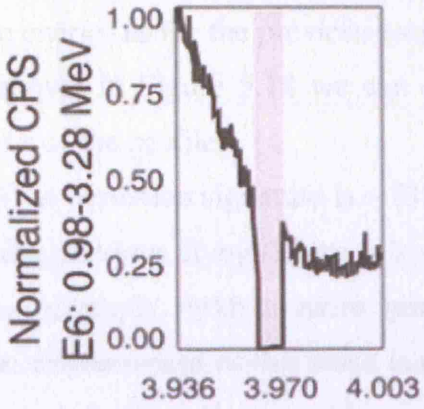

Figure 5.16 Normalised 0.98-3.28 MeV electron counts from the LEMMS data (reproduced from Jones et al., [2006]) shown for L shells of 3.936 to 4.003. Note the displacement in L.

5.5.4.3 Enceladus, 19:53 UT, 14 July 2005

The final close encounter (420 km) with Enceladus produced an absorption cavity in the data as shown in the spectrogram and associated summed intensity plot in Figure 5.17. It was observed on 14 July 2005 at 19:53 UT while Cassini was 0.11° upstream (with respect to corotation) of the moon.

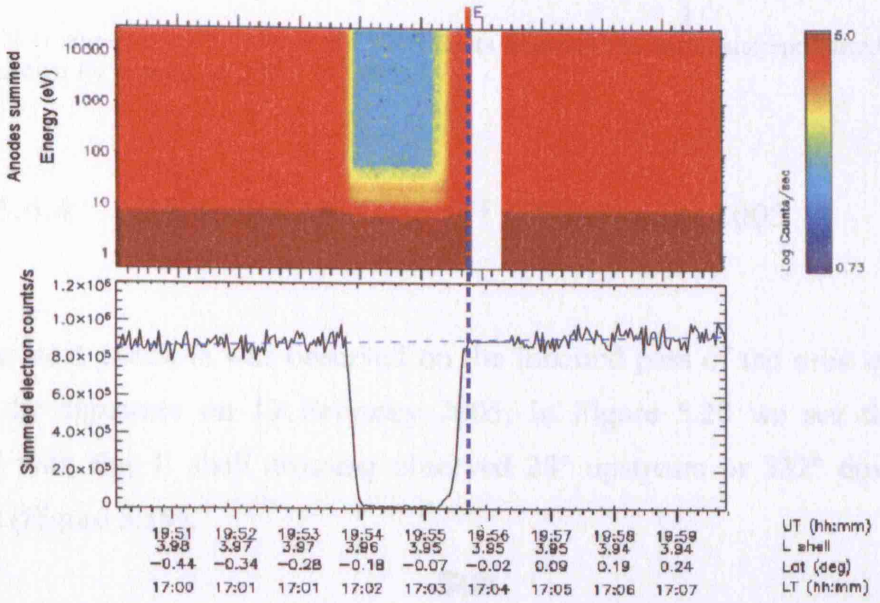

Figure 5.17 The absorption signature of Enceladus detected on 14 July 2005 at 19:53 UT in the same format used previously.

The signature is very similar to the previous example from 9 March 2005, and is approximately the same depth ($C_{\min}/C_{surr}$ ~0.003), as might be expected given their similar distance from the moon. This electron wake is expected to be created by electrons of the same energy as for the previous example, and from comparison with the LEMMS signature shown in Figure 5.18 we can see that this is most likely the case based on the similarity of the profiles.

The radius of the depletion signature is ~ 316 km (~ 1.25 R_{EN}) which is the same as that observed in the previous flyby. There is a slight asymmetry to the signature as seen in the previous example, with a more gradual change in the counts on the planetward edge. The displacement of this wake is minor, with the dip centred on ~ 3.94 R_S, which is a displacement of 1.4 R_{EN} inwards.

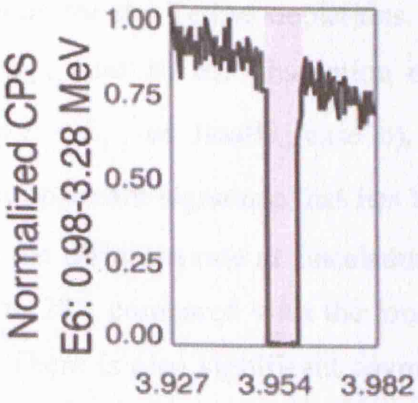

Figure 5.18 Normalised 0.98-3.28 MeV electron counts from the LEMMS data(reproduced from Jones et al., [2006]) shown for L shells of 3.927 to 3.982.

5.5.4.4 Enceladus, 22:45 UT, 16 February 2005

The next example was observed on the inbound pass of the orbit on which we observed the signature on 17 February 2005. In Figure 5.20 we see the depletion associated with this L shell crossing observed 28° upstream or 332° downstream of Enceladus (Figure 5.19).

Figure 5.19 Relative positions of Enceladus and Cassini for the encounter at 22:45 UT

There is a marked difference in depth compared with the previous examples and this is most likely due to the increased 'age' of the cavity and therefore there has been a longer time for the refilling process to act. We find $C_{\min}/C_{surr} \sim 0.57$ and the signature is clearly very broad (~ 26 R_{EN}) suggesting that the cavity has widened as well as reduced in depth.

The ELS is sensitive to high energy electrons > 0.8 MeV, therefore, from Table 5-4 we see that we are sensitive to depletions in electrons with energy less than the resonant energy (0.98 MeV). Thus, this cavity may have travelled either upstream or downstream from the moon and we apply the same process to the calculation of the

diffusion coefficients as for the Tethys depletions. Either this is a depletion of case a) electrons with $E < E_R$, case b) the absorption occurred upstream of the moon in electrons with $E_R < E < E_T$, or finally, case c), the depletion is in electrons with $E > E_T$. If this is an upstream signature that has travelled only 28° from the moon it clearly suggests that the diffusion rate at Enceladus is high since the cavity has almost completely re-filled in 28°, compared with the long-lasting depletions seen up to 331° away from Tethys. There is also significant asymmetry, with a more gradual drop in counts as Cassini enters the cavity on the anti-planetward edge.

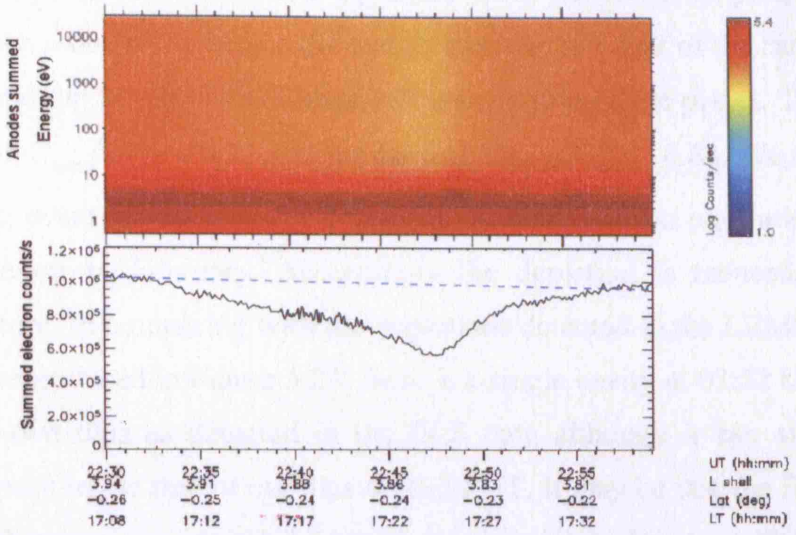

Figure 5.20 The absorption signature of Enceladus detected on 16 February 2005 at 22:45 UT in the same format used previously.

This cavity is also observed in the LEMMS data for electrons between 2.7 to 18 MeV [Paranicas et al., 2005]. We do not include their data here since they plot it together with the proton absorption data and the dip in the electrons is negligible on the scale used. Note that we see this signature 21 R_{EN} further in towards Saturn than the L shell of Enceladus so the position of Enceladus is beyond the range of the plot in Figure 5.20.

5.5.4.5 Enceladus, 03:50 UT and 03:54 UT, 21 May 2005

The final Enceladus wake was observed 36° upstream or 314° downstream (see Figure 5.21) and is shown in Figure 5.22.

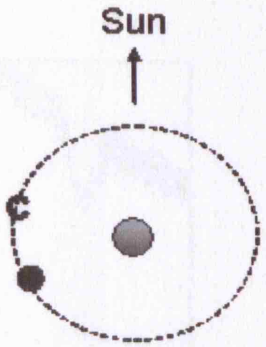

Figure 5.21 Relative positions of Enceladus and Cassini for the encounter at 03:50 UT

This appears to be a double signature from the intensity plot, with a deeper absorption seen ~ 03:50 UT before the counts increase to ~ half of the background level, before a second dip at ~ 03:54 UT slightly closer in toward the planet. The first dip has a depletion of $C_{\min}/C_{surr} \sim 0.71$ and the second $C_{\min}/C_{surr} \sim 0.88$. We note that this L shell crossing occurred for a larger upstream spacecraft-moon separation than for the previous case on 16 February. Accordingly the depletion is reduced, indicating an 'older' signature. In comparing with the depletions detected in the LEMMS data [Jones et al., 2006] reproduced in Figure 5.23, there is a single cavity at 03:52 UT. This lies in-between the two dips as detected in the ELS data although it has almost the same depletion as seen in the first of our dips at 03:50 UT. It may be that the ELS is detecting a slightly different energy to the LEMMS, resulting in a signature which is displaced (an effect also observed at the L shell of Tethys [Roussos et al., 2005]).

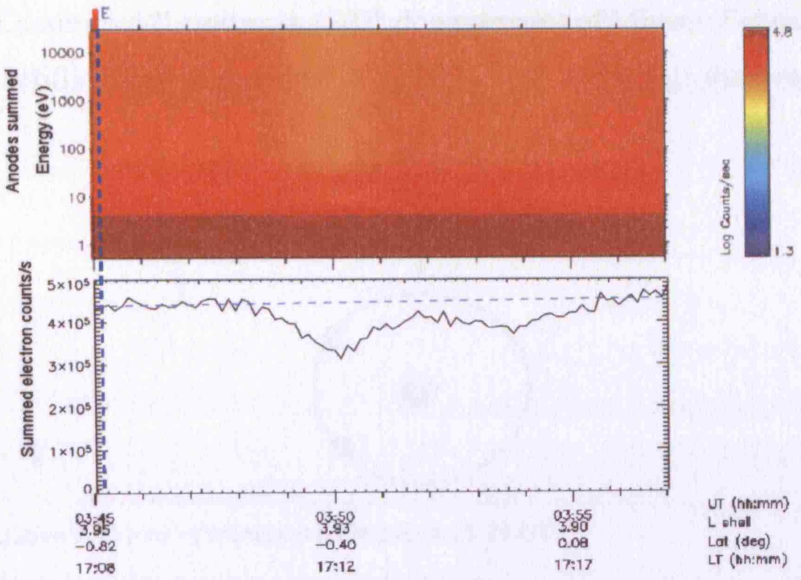

Figure 5.22 The absorption signature of Enceladus detected on 21 May 2005 at 03:52 UTin the same format used previously.

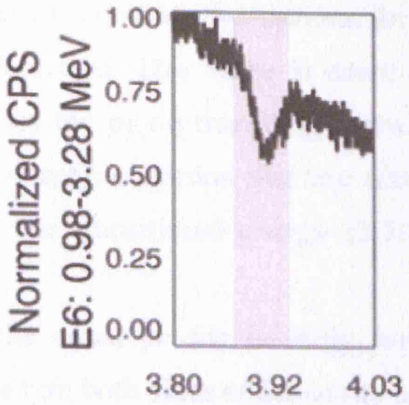

Figure 5.23 Normalised 0.98-3.28 MeV electron counts from the LEMMS data (reproduced from Jones et al., [2006]) shown for L shells of 3.80 to 4.03.

The signature centred on 03:50 UT is observed 0.02 R_S (4.7 R_{EN}) further in towards the planet than the L shell of Enceladus, while the second depletion is displaced even further by 0.04 R_S. These two signatures are clearly of different ages and have undergone different displacements.

5.5.5 Observations at the L shell of Mimas (L=3.08 RS)

5.5.5.1 Mimas, 21:29 UT, 14 April 2005

Figure 5.25 shows a signature observed close to the L shell of Mimas on 14 April 2005. Cassini is 57° upstream (303° downstream) of Mimas (Figure 5.24) and it is evident that refilling has begun with $C_{\min}/C_{surr}$ ~0.3 and a signature radius of ~ 3.25 R_{MS}.

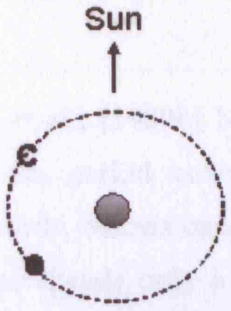

Figure 5.24 Relative positions of Mimas and Cassini at 21:29 UT.

The range of energies where electrons exhibit resonant behaviour is from 0.98 – 1.39 MeV and we again consider the options for the different energies in which we could be seeing a depletion. This wake is either downstream of the moon travelling eastwards, upstream of the moon travelling eastwards but lagging the moon or it is a wake in the higher energy electrons that are travelling westwards and thus have an energy greater than the transitional energy (2.10 to 2.93 MeV depending on pitch angle).

The dip in the count profile is fairly symmetric, suggesting that refilling is occurring at the same rate both sides of the cavity and therefore radial diffusion rates are equal inwards and outwards at the orbit of Mimas. We note finally, that this signature shows a large displacement (~17.3 R_{MS}) from its expected location of L ~ 3.08 R_S, being observed at 3.02 R_S. This indicates that there has been a large translation of this cavity since its creation. However, we do not necessarily expect the case at Mimas to be that straightforward due to the eccentricity of the orbit.

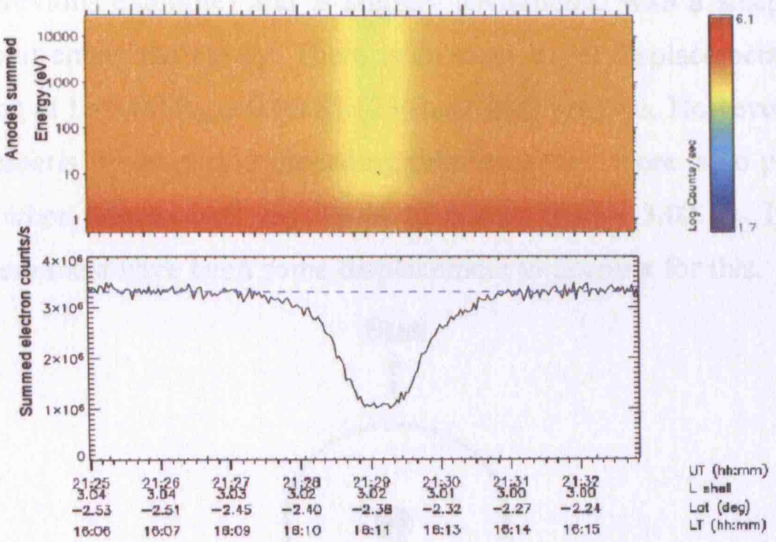

Figure 5.25 The absorption signature of Mimas detected on 14 April 2005 at 21:28 UT in the same format as used before.

As described in Van Allen et al., [1980b] Mimas traverses a wide range of L shells throughout its orbit. For the period covering several hours prior to this observation to several hours afterwards, Mimas encounters L shells between ~ 3.02 to 3.2 R_S (52 R_{MS}). Therefore, Mimas spends only a short time at each L shell, which could account for the broad depletions. The depletion at a particular L shell will have been created only when Mimas was last at that exact radial distance. From the position of Mimas for the period prior to this encounter, the last time that Mimas was at L = 3.02 was at 20:30 UT. This would mean that the Mimas signature was created, not when the

electrons (together with their cavity) were last in contact with the moon on this L shell, but when they were last in contact with the moon on L = 3.02, which is ~74° from the point of observation, greater than the 57° separation initially assumed. Of course, this assumes that the displacement is due entirely to the eccentricity of Mimas, when in fact the signature could well have drifted radially as well. We cannot therefore, state for certain the age of this signature without exact knowledge of the energy of the depleted electrons.

5.5.5.2 Mimas, 00:59 UT, 15 April 2005

The final depleted moon wake to be described was observed on 15 April 2005 at 00:59 UT. Cassini was close to the L shell of Mimas (3.023 R_S) 26° upstream (334° downstream) of the moon (Figure 5.26). The depletion is 6.5 R_{MS} in width (double the width of the previous example) and is slightly asymmetric with a steeper drop off in counts as Cassini enters the cavity. There is an even larger displacement in L with the cavity appearing at L=3.00 R_S, a 0.08 R_S (23 R_{MS}) shift inwards. However, if we look at the moon ephemeris in the period preceding this encounter, there is no point within the last two days when Mimas was any closer to Saturn than ~ 3.02 R_S. In this case we assume that there must have been some displacement to account for this.

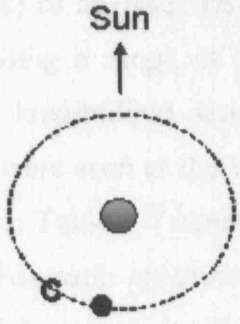

Figure 5.26 Relative positions of Mimas and Cassini at 00:59 UT.

The resultant depletion gives $C_{\min}/C_{surr} \sim 0.4$ hence this cavity exhibits less depletion than the previous example, despite apparently being closer upstream to the moon. However, as we have seen, this signature is shifted in towards Saturn, and therefore may be subject to a different diffusion rate, although we would expect the diffusion rate to slow closer to the planet [Walt, 1994].

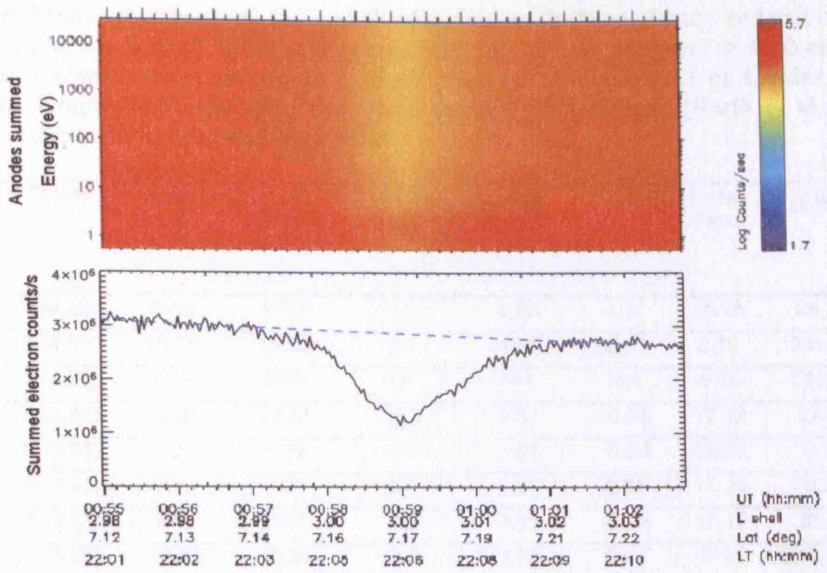

Figure 5.27 The absorption signature of Mimas detected on 15 April 2005 at 00:59 UT in the same format as used before.

We point out again the lack of any reported absorption in the LEMMS instrument at this time preventing a comparison.

5.6 Survey of moon wakes at Saturn

Of the many moon L-shell crossings observed between June 2004 and July 2005 we selected a total of ten absorption signatures (including two apparent 'double' signatures at Tethys and Enceladus) to analyse. These ranged from very deep, to very shallow absorption profiles, providing a range of characteristics. The signatures also provided reasonable coverage of longitudinal separation of the relevant moon and Cassini. Of these, two signatures were seen at the L-shell of Mimas, five at Enceladus and three near the L-shell of Tethys. Table 5-7 contains summary data for each of these signatures used in this analysis. For each encounter some key parameters are listed, including the relative positions of the moons to Cassini and the signature depth. Not every passage across a moon's L-shell had a detectable signature, for example on 30 March 2005 close to Tethys L-shell, the ELS data showed no evidence of absorption, but we consider it in this analysis for purposes of comparison.

Overall, we had a reduced number of Mimas encounters compared to those for the other moons, but this is simply a product of Cassini's orbit about Saturn, which rarely had a periapsis within the orbit of Mimas (L ~ 3.08 R_S) during this stage of the tour.

Table 5-7 Data for each of the electron absorption signatures observed in the ELS data. The columns contain the date (all cavities were observed in 2005) , the object name referring to either T: Tethys, E:

Enceladus or M: Mimas together with the L shell of the moon, the time of entry and exit of the cavity, the width in moon radii, the L-shell at the mid-point of the dip, the displacement in L observed (a negative value indicates a displacement inward in L shell), the Local Time (LT) of Cassini at the time of observation, the longitudinal separation calculated using SKR longitude [Kurth et al., 2006] and the signature depth relative to the surrounding counts.

	Date	Object	Enter Cavity (UT)	Exit cavity (UT)	Width (R_M)	L-shell at mid-point	ΔL	Local Time	$\Delta\phi$	$\frac{C_{min}}{C_{surr}}$
1	09-Mar	T (4.89)	6:49	6:53	1.6	4.90	0.01	15:16	29.77	0.373
2	09-Mar	T (4.89)	16:25	16:32	3.1	4.88	-0.01	0:16	331.24	0.892
3	30-Mar	T (4.89)	4:27	0:00	0.0	N/A	N/A	0:16	279.95	1.000
4	16-Feb	E (3.95)	22:34	22:54	25.5	3.87	-0.08	17:12	27.88	0.573
5	17-Feb	E (3.95)	3:27	3:29	5.5	3.95	-0.00	22:34	0.39	0.012
6	09-Mar	E (3.95)	9:06	9:07	2.5	3.97	0.02	17:00	0.24	0.002
7	21-May	E (3.95)	3:48	3:51	4.3	3.93	-0.02	17:12	35.91	0.713
8	14-Jul	E (3.95)	19:53	19:55	2.5	3.96	0.01	17:02	0.13	0.003
9	14-Apr	M (3.08)	21:28	21:30	6.5	3.02	-0.06	16:10	57.28	0.303
10	15-Apr	M (3.08)	0:58	1:00	7.6	3.00	-0.08	22:05	25.88	0.401

The relative positions of Cassini (at the location of the observed signature) and the moon associated with that L-shell are shown in a sketch of Saturn's equatorial plane in a moon-centred frame in Figure 5.28. The moon locations are on the vertical axis and the associated wakes are distributed in longitude and labelled to correspond with the numbers in Table 5-7. Where the depletions are almost co-located with the moon, as with very close flybys, the number sits almost exactly on the vertical axis. We also note that most of the observations were made on the dusk side of the planet; this is due to the preferential sampling of this region by Cassini's trajectory in the early stages of the tour.

There are a range of longitudinal separations (calculated clockwise from the moon) in the dataset, from less than 1° for three of the closest, dedicated flybys (signatures 5, 6 and 8), through to 331° for signature 2 at the L-shell of Tethys. Of course as previously discussed we do not know for certain whether the signature has travelled upstream (clockwise) or downstream (anti-clockwise) from the moon. Thus a separation of 331° upstream may in fact be a 29° separation downstream. In addition to the longitudinal separation, we have also seen evidence for radial displacement of the signatures, although this is only over a small scale and is not well represented on this figure. It shall be discussed in more detail later in this chapter.

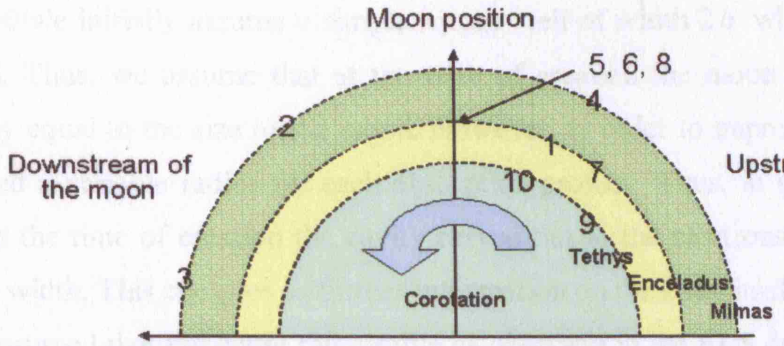

Figure 5.28 Sketch showing the relative position of Cassini and the moon at the time each cavity is observed. It shows a cut through Saturn's equatorial plane in the frame of the moon, which lies on the central axis. In general the signatures lie upstream with respect to corotation, although this does not necessarily indicate a signature that has travelled upstream. Each of the three moon L-shells have been included where Mimas = 3.08 R_S, Enceladus =3.95 R_S and Tethys = 4.89 R_S.

5.6.1 Calculation of diffusion coefficients

When a cavity is created, the surrounding plasma will act to regain equilibrium through radial diffusion into the vacant volume. The observation of asymmetric cavities suggests that there are unequal diffusion rates inward and outward through the magnetosphere in these regions, resulting in different re-filling rates into each side of the cavity. In this chapter we apply a standard method [Van Allen et al., 1980b] to the absorption signatures observed, to derive a value for the diffusion coefficient at each L-shell. Furthermore, we assess the inward and outward diffusion rates separately as described below. We now describe this method and the assumptions behind it. We apply the standard treatment of diffusion using 1-d diffusion equation to describe the time evolution of the distribution function:

$$\frac{\partial^2 n}{\partial x^2} = \frac{1}{D_{LL}} \frac{\partial n}{\partial t}$$

Equation 5.5

Where $n(x,t)$ is the normalised particle number density, x is the radial distance from Saturn, t is the time and D_{LL} is the diffusion coefficient for radial transport. There are a number of assumptions used in this method:

- We assume there are no sources or sinks of energetic particles within dx;
- We assume that D_{LL} is independent of x so that the diffusion rate is the same across the extent of the cavity. Change in the value of D_{LL} or if $D_{LL_{in}} \neq D_{LL_{out}}$ then the absorption profile may become asymmetric as the refilling occurs;

- At t=0 we initially assume a simple square-well of width $2b$ where b is the moon radius. Thus, we assume that at the time of creation the moon sweeps out a hole exactly equal to the size of the moon. However, in order to improve the fits we have allowed a variable radius for each absorption profile. Thus, in some cases we find that at the time of creation the cavity carved out in the electrons is greater than the moon width. This can give us further information on the body itself;
- It is assumed that the count rate profile as observed in the ELS data is representative of the depletion that would be observed in a single energy channel. Of course, since the ELS has such a broad energy response to these penetrating electrons, then the absorption profile will be a superposition of cavities created in several energy channels. Despite this, our comparisons with the absorption profiles for narrower energy channels in the LEMMS data show similar profiles, particularly for some of the Enceladus signatures, (which would also occur if $D_{LL} \neq f(E)$). Therefore, we do not expect this to introduce a large error into the derivation of D_{LL};
- Dispersion is neglected, which would also act to eliminate the cavity. Including it will reduce the estimated value of D_{LL} for a particular absorption profile;
- We assume that since the three moons considered here are all within 5 R_S a simple, axisymmetric dipole magnetic field is valid [Arridge et al., 2006b]. Van Allen et al., [1980b] report that slight departures from this model have a negligible effect on the results. However, Carbary et al., [1983] found better agreement for modelling microsignatures at Dione and Tethys using a complete planetary field model, e.g. the Z3 model [Acuna et al., 1983]. However, worse agreement was found when signatures attributed to Mimas and Enceladus were modelled.
- The model assumes the moons are in orbits of zero-eccentricity and therefore remain at the same L-shell throughout the orbit. If this is not the case, i.e. in the case of Mimas, then we have a situation where the moon absorbs particles across a range of radial distances throughout its orbit. Therefore a signature may have been created further in the past when Mimas was last at that particular L-shell. This may need to be taken into account when calculating the age of a cavity, particularly those observed near the L-shell of Mimas.

The solution of Equation 5.5 is then given by:

$$n = 1 - 0.5\left[ERF\left(\frac{1-x/b}{\sqrt{\tau}}\right) + ERF\left(\frac{1+x/b}{\sqrt{\tau}}\right)\right]$$

Equation 5.6

where ERF is the error function and τ is a dimensionless parameter which is then used to calculate D_{LL} using:

$$\tau = \frac{4D_{LL}}{b^2}$$

Equation 5.7

This functional form describes a series of curves, each with an associated value of τ. Some example curves have been plotted in Figure 5.29, ranging from the initial square-well (of radius b) to relatively broad and shallow density depletions for higher values of τ. We create an array of τ values with a resolution of 0.05 to allow close fits to be obtained. To quantitatively compare the signature in the data with the theoretical profile, we normalise the actual count rate to the undisturbed background counts. The normalised values were obtained by taking the ratios of the observed counts to these extrapolated background counts as described in section 5.5.3.1. Once we have a normalised curve, which has the same profile as before, but counts are now a fraction of the background counts, we can then iteratively compare the data to the family of curves in Figure 5.29. The best fit is that with the minimum value of the χ^2 error statistic and this curve provides the associated τ value. Using Equation 5.7 we can then derive a value for D_{LL}.

The age of the signature, t, is derived using the angular separation of the moon and the relative velocity of the moon and drift velocity of the electrons that have suffered absorption, taking care of the relative directions of the drift of the moon and the electrons. However, since we do not know the exact energy of these electrons we have estimated the energies that might have caused the signature as described in each of the moon sections. It is difficult to attribute an error to this energy since the estimate could be accurate, or the energy range of electrons being absorbed could be several 10's MeV higher than the estimates. Hence for each event, we may surmise that the signature has, for example, in case a), travelled downstream of the moon. In which case the energy of the electrons will be $< E_R$ and for Tethys we have used a value of 0.85 MeV and at Enceladus and Mimas the assumed value is 0.9 MeV. In case b) the electron energy is $E_R < E < E_T$ where, for Tethys we have taken a mid-energy value of 1.1 MeV, and for Enceladus and Mimas the value applied is 1.2 MeV. Finally, for those cases where the energy of the absorbed electrons is assumed to be $E > E_T$, the values are 2 MeV for Tethys, 1.9 MeV for Enceladus and 2.5 MeV for Mimas.

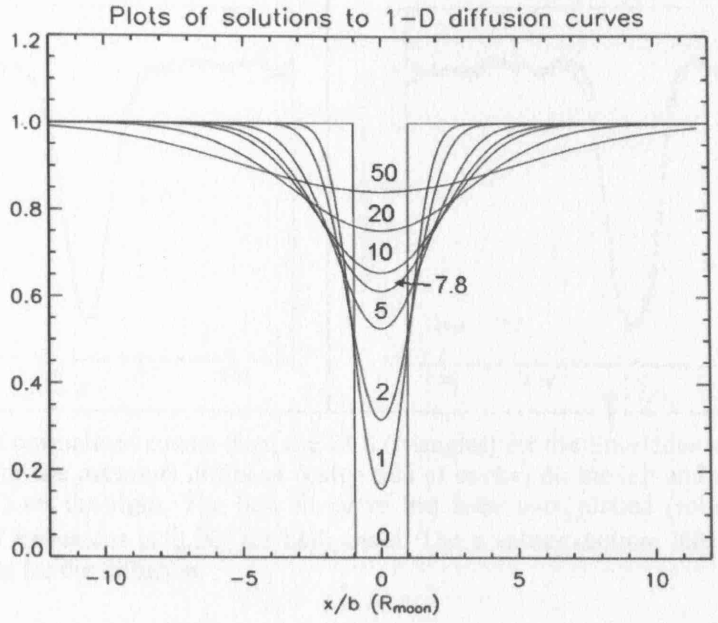

Figure 5.29 A series of example curves each provided by a solution to the 1-d diffusion equation. The functional form is in Equation 5.6 and each curve is labelled by the appropriate value of τ in the solution. The vertical axis contains the solution for density and the horizontal axis is in units of moon radii [reproduced from Van Allen et al., 1980b]

We now apply this fitting to the count rate intensity profiles for each of the nine L shell crossings where depletion is apparent. To assess the directional dependence of diffusion, we fit the curves to each side of the signature independently. This is done by selecting the middle of the absorption profile. We then 'mirror' the data about this point, creating two profiles. Both are now symmetric, representing the outwards or inwards diffusion depending on the direction of the spacecraft across the cavity. For each case we can also vary the initial assumption about the size of the absorbing body by varying b in Equation 5.6 and Equation 5.7.

Two example fits are shown in Figure 5.30 for the Enceladus signature seen on 17 February 2005 at 03:27 UT. The left plot shows the 'recreated' cavity generated by mirroring the entry-side of the original cavity. This is used to calculate the outward diffusion coefficient. The right plot shows the reconstructed cavity using the exit-side of the original cavity and is used to calculate the coefficient for inwards radial diffusion.

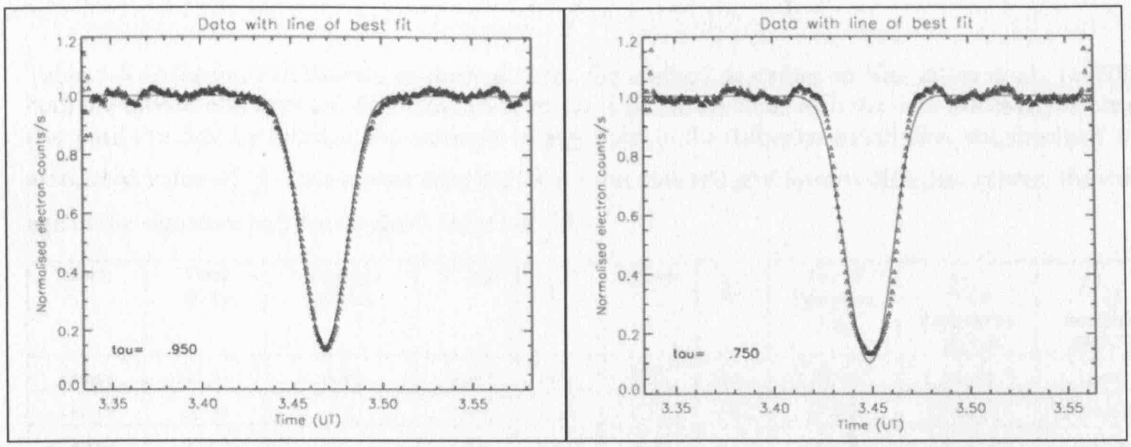

Figure 5.30 Plots of normalised counts from the ELS (triangles) for the Enceladus signature observed on 17 February 2005 for the outwards diffusion (entry-side of cavity) on the left and the inwards diffusion (exit-side of cavity) on the right. The best fit curve has been over plotted (solid line) assuming the absorbing radius of Enceladus is $1.3b$ for both cases. The τ values (bottom left) are similar but give different coefficients for the diffusion.

The outwards curve is a better fit as apparent from the plot and the low χ^2 values in Table 5-8, providing an accurate τ value to use in the equation. For this example, an initial absorbing radius of 1.3 times the radius of Enceladus provided the best fits to these profiles, suggesting that Enceladus is absorbing electrons over a larger radius than for a simple inert body (cf. with the value for $R_{eff.}$).

The resultant values of D_{LL} for inward and outward radial diffusion are listed in Table 5-8 grouped by moon. Note that some fits were less successful and these are indicated by the high value of χ^2.

The values for the diffusion coefficient appear to be the largest at Enceladus, followed by Tethys, then Mimas. Since D_{LL} is proportional to L, we would expect to see an increase with radial distance, suggesting that, in the vicinity of Enceladus, the diffusion rates are faster than predicted. The spread in the values for each moon arises due to the different inferred ages of the cavities due to the uncertainty in the energy of the electrons undergoing the absorption. If we compare the values for D_{LL} between encounters for the same energy (assuming the signature is an upstream signature travelling in the prograde or retrograde direction), they are very similar. Without assuming the result, we can see that some outlying values, such as the low values ~ 10^{-10} $R_S^2 s^{-1}$ at Tethys for the encounter at 06:51 UT (9 March 2005) are for cavities in 0.85 MeV electrons assuming a downstream travelling signature. However, the large discrepancy between this value and the rest of those results derived at the L shell of Tethys for cavities observed upstream of the moon, suggest that this signature is not due to absorption of these low energy electrons.

Table 5-8 Diffusion coefficients as derived using the method described in Van Allen et al., [1980b] for both the inward and outward diffusion. Each moon is listed, together with the time the cavity is observed (we omit the date for clarity), the assumed energy used in the diffusion calculation, the resultant τ and associated value of χ^2 associated with the fit for the outward and inward diffusion curves, the inferred age of the signature and the resultant values of D_{LL}.

Moon	Time (UT)	Energy (MeV)	τ out	χ^2	τ in	χ^2	Age of signature (s)	D_{LL} Outwards ($R_S^2 s^{-1}$)	D_{LL} Inwards ($R_S^2 s^{-1}$)
Tethys	06:51	0.85	4.65	0.30	5.20	0.13	1397155	1.29×10^{-10}	1.24×10^{-10}
Tethys	06:51	1.1	4.65	0.30	5.20	0.13	21484	8.36×10^{-9}	8.06×10^{-9}
Tethys	06:51	2	4.65	0.30	5.20	0.13	4293	4.18×10^{-8}	4.03×10^{-8}
Tethys	16:28	0.85	77.75	0.57	68.35	3.70	121692	1.26×10^{-8}	1.11×10^{-8}
Tethys	16:28	1.1	77.75	0.57	68.35	3.70	237035	6.46×10^{-9}	5.68×10^{-9}
Tethys	16:28	2	77.75	0.57	68.35	3.70	47367	3.23×10^{-8}	2.84×10^{-8}
Enceladus	03:27	1.2	0.95	0.25	0.95	3.09	349	2.08×10^{-8}	1.64×10^{-8}
Enceladus	03:27	1.9	0.95	0.25	0.95	3.09	84	8.59×10^{-8}	6.78×10^{-8}
Enceladus	09:07	1.2	0.35	0.43	0.15	1.70	215	7.36×10^{-9}	9.11×10^{-9}
Enceladus	09:07	1.9	0.35	0.43	0.15	1.70	52	3.04×10^{-8}	3.77×10^{-8}
Enceladus	19:53	1.2	0.30	0.55	0.20	6.35	116	1.16×10^{-8}	7.76×10^{-9}
Enceladus	19:53	1.9	0.30	0.55	0.20	6.35	28	4.82×10^{-8}	3.21×10^{-8}
Enceladus	22:45	0.9	10.80	0.44	26.20	1.41	740490	2.63×10^{-10}	1.60×10^{-10}
Enceladus	22:45	1.2	10.80	0.44	26.20	1.41	24921	7.82×10^{-9}	4.74×10^{-9}
Enceladus	22:45	1.9	10.80	0.44	26.20	1.41	6025	3.23×10^{-8}	1.96×10^{-8}
Mimas	21:28	0.9	2.15	0.41	2.15	0.16	962220	7.41×10^{-12}	7.41×10^{-12}
Mimas	21:28	1.2	2.15	0.41	2.15	0.16	65476	9.87×10^{-11}	9.87×10^{-11}
Mimas	21:28	2.5	2.15	0.41	2.15	0.16	9715	6.65×10^{-10}	6.65×10^{-10}
Mimas	00:58	0.9	4.10	0.30	3.65	0.15	871787	1.28×10^{-11}	1.14×10^{-11}
Mimas	00:58	1.2	4.10	0.30	3.65	0.15	29579	4.17×10^{-10}	3.71×10^{-10}
Mimas	00:58	2.5	4.10	0.30	3.65	0.15	4389	2.81×10^{-9}	2.50×10^{-9}

The values derived at each L shell are similar for the same energies, while there is up to an order of magnitude difference between the values of D_{LL} if different energies are assumed, since this affects the assumed age of the cavity. In Figure 5.31 we have plotted these values against L, including the previously derived coefficients from Table 5-2. The values derived from the ELS data are divided into inward diffusion rates (blue diamonds) and outward diffusion rates (black diamonds). In general, outward diffusion is higher than inward diffusion but there are some examples at the L shell of Enceladus where the opposite is true, suggesting the changeable nature of the magnetosphere in the vicinity of this moon. Values derived from previous studies are indicated by the red squares, although note that some of these are not directly applicable since they are for different energy ranges. We see some agreement between the values at Mimas and those previously derived for 1-2 MeV electrons by Simpson et al., [1980b]. We find a lower value for D_{LL} compared with that calculated by Chennette and Stone [1983] for 2.5 MeV electrons, suggesting that the electrons we detect are of lower energy than this.

Our values are higher than previous estimates at Enceladus both from Pioneer 11 and Cassini-LEMMS data, despite the similarity in the energies used in the calculation. There is one case where our derived D_{LL} is lower than previous estimates. This is derived using data from 16 February 2005 when we considered an eastwards travelling cavity. Since this value is lower than all other estimates, it suggests that the signature has instead drifted upstream of the moon. We also calculate a higher value than published for the diffusion at the orbit of Tethys in all cases bar one. However, the Paranicas et al., [2005] estimate is for lower energies (< 100 keV) and we would expect this to be the case since the diffusion rate is faster for electrons of higher energy. The difference between the values at each of the moon orbits and between the values at each orbit is apparent.

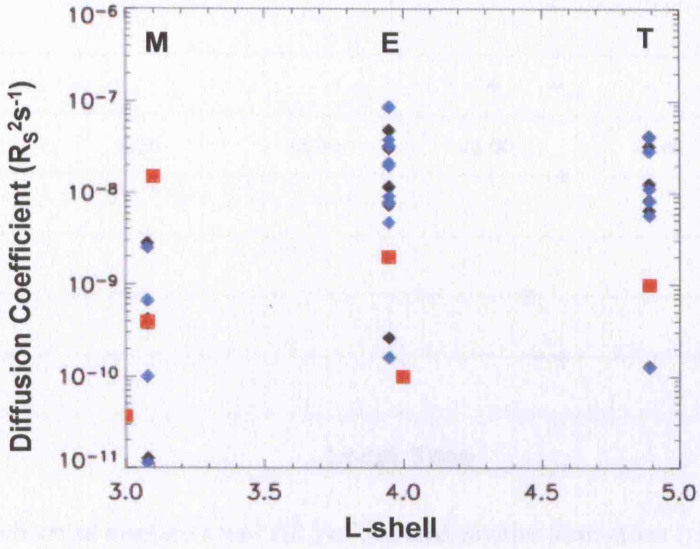

Figure 5.31 Values of diffusion coefficients derived from the moon signatures seen in the ELS data and the previously derived values as listed in Table 5-2. The former are indicated by blue diamonds (inward diffusion coefficients) and black diamonds (outward diffusion coefficients), the latter by red squares. The spread in values is due to the different source data from different crossings and the spread in diffusion coefficients between energy ranges.

5.6.2 Drifting signatures

Throughout the analysis it is clear that the signatures are not always aligned exactly with the L-shell of the moons generating them. This was also observed in the Voyager data for moon cavities due to Enceladus and Tethys [Krimigis et al., 1982] and at Tethys in Cassini data [Roussos et al., 2005]. In Table 5-7 we list the L shell at the centre of the observed cavity together with ΔL, the measured displacement of the signature from the expected location of the moon L shell.

We see both inwards and outwards displaced signatures and it has been suggested [Roussos, 2006, *private communication*] that they have a local time dependency. If we test the displacements in L of our signatures against local time (Figure 5.32) we see both positive ΔL and negative ΔL between midnight and 01:00 and both signs again between 15:00 and 17:30 LT and positive ΔL at 22:00 LT. There is also no apparent correlation of displacement with the age of the signature. Of course, the cavity age is estimated based on an assumption of the energies of the depleted electrons. For those close flybys of Enceladus on 17 February and 9 March 2005, for example, we find the 'younger' of these two signatures on 9 March is actually displaced by -0.02 R_S while the former case is observed precisely on the L shell of Enceladus.

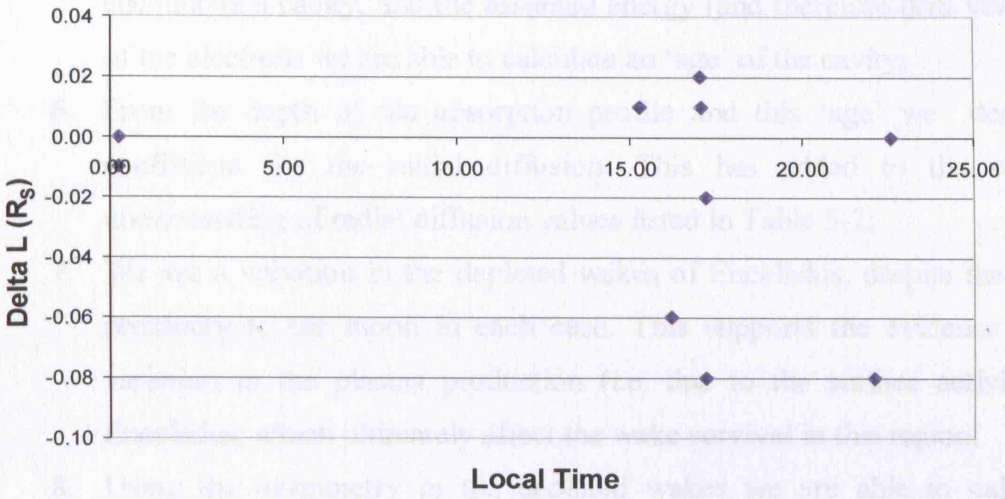

Figure 5.32 Plot of observed displacement (ΔL) of depleted cavities from moon L shells as a function of local time as listed in Table 5-7.

5.7 Review of findings

Based on the data analysis carried out in this chapter we are able to make a number of conclusions about moon wakes at Saturn:

1. We are able to utilize ELS observations of the penetrating electrons into the instrument to resolve high energy electron signatures at the L shells of Tethys, Enceladus and Mimas;
2. The 'high' energy electrons assumed to be detected at the ELS have small gyroradii, and small longitudinal bounce distances compared with the

moon radii, such that escape processes such as leapfrogging and corkscrewing are not an issue;

3. In certain regions and at certain energies, the ELS has an increased sensitivity compared with the LEMMS, allowing it to detect depletions not observed in the purpose-built high energy electron instrument. This validates the importance of also being able to use the ELS data for such detections;
4. Knowledge of the resonant energies at each moon, together with the estimation of a minimum energy for the penetrating electrons allows us to make a further estimation of the energy of the electrons being absorbed;
5. From the separation of the moon and the spacecraft at the time Cassini encounters a cavity, and the assumed energy (and therefore drift velocity) of the electrons we are able to calculate an 'age' of the cavity;
6. From the depth of the absorption profile and this 'age' we derive a coefficient for the radial diffusion. This has added to the current understanding of radial diffusion values listed in Table 5-2;
7. We see a variation in the depleted wakes of Enceladus, despite the close proximity to the moon in each case. This supports the evidence for a variation in the plasma production (i.e. due to the surface activity) at Enceladus, which ultimately affect the wake survival in this region;
8. Using the asymmetry in the depleted wakes we are able to calculate separate values for inward and outward radial diffusion rates in the magnetosphere;
9. We are also able to infer the width of the absorbing body, based on the absorption profile observed;
10. There is an observed displacement of the wakes in L shell but with no strong correlation with position or time since creation.

5.8 Discussion

We selected ten L-shell crossings corresponding to three of Saturn's moons, Tethys, Enceladus and Mimas. Not every passage across these L-shells left a prominent absorption cavity, suggesting that filling-in of the vacant region by the surrounding particles had already occurred. Due to the penetration of high energy particles (> 0.8 MeV) into the instrument, the ELS is able to detect the absorption signatures present in

the MeV electron energy range. We have been able to use this unwanted "noise" in the ELS data to derive valuable science results. At energies of this order and above, electrons have an angular drift velocity that is comparable to the longitudinal velocity of the moons themselves. Thus, we find a 'resonant' energy where electrons travel around the planet at the same rate as, and therefore never encounter, the moon and escape absorption. If the electrons have energy less than this resonant energy they are absorbed and the resulting depleted cavity travels eastwards round the planet. If they have a greater energy, then they can also be absorbed, continue to travel eastwards round the planet but now lag the moon. Thus any depletion will appear upstream (with respect to corotation) of the moon. In addition, at greater energies still they are able to counteract the enforced corotational motion and travel westwards round the planet. This occurs for particles above the transitional energy [Thomsen and Van Allen, 1980] which is 1.3 MeV at Tethys, ~ 1.7 MeV at Enceladus and 2.2 MeV at Mimas (for electrons with α_{eq}=90°, these values will be higher for electrons with lower pitch angles).

We use this information from electrons penetrating into the ELS to determine which electrons are being absorbed by the moons. Where we have calculated diffusion coefficients we have included an error estimate based on a sum of the Poisson error on the counts and the resolution of the fit.

Tethys

We observed two partially filled signatures at the L shell of Tethys and one crossing with no apparent reduction in counts, suggesting that this latter cavity had refilled completely. The event on 9 March 2005 at 06:51 UT showed evidence of significant filling in, with a normalised absorption depth of 0.37, ~ 30° upstream of Tethys. From our knowledge of the drifts of energetic electrons with respect to Tethys, we can make several hypotheses for the energies of the electrons causing this depletion. It is either due to 'low' energy electrons, which are below the resonant energy of Tethys and have drifted eastwards with respect to the moon and we are crossing this cavity 330° downstream of the moon (case a). Alternatively, the cavity is due to electrons with $E_R < E < E_T$ and it has been created upstream of the moon, travelling eastwards (i.e. in the same direction as the moon) and is lagging it by 30° (case b). Or it is created by the absorption of 'high' energy electrons which have drifted upstream away from the moon (case c).

We therefore choose an example energy from each 'case' and use it to calculate the diffusion coefficient. Case a: If we consider that the ELS can only detect a part of

the electron spectrum with energies below E_R, i.e. those with E > 0.8 MeV, then we can define a range between 0.8-0.89 MeV (assuming α=90°) which have travelled 330° downstream with respect to the moon. Based on these energies and the assumption that this cavity was created at the last passage of Tethys, we calculate the outward diffusion coefficient to be 1.29±0.08 x10^{-10} $R_S^2 s^{-1}$ and the inwards value to be 1.24±0.08 x10^{-10} $R_S^2 s^{-1}$ (for E ~ 0.85 MeV). These are very close, suggesting that the rates for inwards and outwards diffusion are comparable at ~ 5 R_S. These are lower than values quoted by Van Allen et al., [1980b] at L=4 (see Table 5-2) for 1 MeV electrons. Although we would expect a slight decrease since the energy is lower, although L is larger (4.89 R_S at Tethys). For case b: $E_R < E < E_T$, we estimate that the depletion could be in electrons of ~ 1.1 MeV. In this case, we find the diffusion coefficients to be (inwards) 8.06±0.06 x10^{-9} $R_S^2 s^{-1}$ and (outwards) 8.36±0.06 x10^{-9} $R_S^2 s^{-1}$. These values are clearly larger than the previous estimate assuming 'low' energy electron depletion, and the estimate by Van Allen et al., [1980b] at L=4. However, we would expect it to be since it is now assuming a much 'younger' signature that has only travelled 30° and thus the re-filling has occurred to the same level but over a shorter time. For case c) we assume the energy $> E_T$ and we choose an example energy of E ~ 2.0 MeV with which to 'test' the assumed formation of the signature. With a 30° degree separation this outputs a value for the inwards D_{LL} = 4.03±0.03 x10^{-8} $R_S^2 s^{-1}$ and outwards D_{LL} =4.18±0.03 x10^{-8} $R_S^2 s^{-1}$ which are higher still. These values are considerably different to the estimates, assuming the absorption is in the lower energies. This discrepancy highlights the problems due to the difficulties in accurately determining the energy of these penetrating particles. Note that, for simplicity, we neglect the values of E_R for lower pitch angles in Table 5-4, although the same treatment can be applied. If we compare these values to that derived from the LEMMS data (1.0 x10^{-9} $R_S^2 s^{-1}$ based on E ~28.1-49 keV electrons [Paranicas et al., 2005]), we see that in some cases the values for D_{LL} are larger and in some cases they are smaller. In fact, we would expect all our estimates in this study to be higher since we are considering electrons with higher energy.

The LEMMS results show a shift in L shell for this signature (outwards by 0.2 R_S), in addition, there is some uncertainty in the time the cavity is observed. Based on this, and from their suggestion that they are not able to detect the depletion in 'high' energy electrons (~ 100 keV to 4.4 MeV), we surmise that we are in fact detecting a 'young' signature agreeing with case b) or c) which is upstream of the moon in electrons with $E > E_T$ and which is not detected by LEMMS.

We suspect the difference in the L shell displacement also arises since we are viewing different signatures, thus the low energy signature observed in the LEMMS data (i.e. ~ 10s keV) has travelled 330° and has drifted outwards in L by 0.2 R_S, whereas our high energy (> MeV) signature has only travelled 30° and in this time has moved only 0.01 R_S outwards. In addition, these two cavities may have travelled through different regions of the magnetosphere which may have an effect if there is a local time dependency on the translation in L as suggested in Roussos et al., [2005]. We also note that the magnetic field starts to depart from the simple L shell assumption at the orbit of Tethys ~ 5 R_S [Arridge, 2006, private *communication*] which will introduce errors into our L shell mapping.

The next signature observed close to the L-shell of Tethys (9 March at 16:28 UT) was even shallower and was detected 331° upstream of the moon. We applied the same analysis, once again assuming the pitch angles were 90° and the signatures had lasted only once around the planet. The output of the Van Allen et al., [1980b] model gives values for electrons of ~ 0.85 MeV (case a), D_{LL} = 1.26 ±0.01 x10^{-8} $R_S^2 s^{-1}$ (outwards) and 1.11 ±0.01 x10^{-8} $R_S^2 s^{-1}$ (inwards), for case b): D_{LL} = 6.46 ±0.07 x10^{-9} $R_S^2 s^{-1}$ (outwards) and 5.68 ±0.07 x10^{-9} $R_S^2 s^{-1}$ (inwards) for E ~ 1.1 MeV and for 2.0 MeV electrons (case c), D_{LL} = 3.23±0.04 x10^{-8} $R_S^2 s^{-1}$ (outwards) 2.84±0.04 x10^{-8} $R_S^2 s^{-1}$ (inwards). There is only a slight difference between values for inwards and outwards radial diffusion, with larger values for outwards diffusion in all cases. Judging on the depth of these signatures, it would make sense that at 06:51 UT the signature is younger than that observed at 16:28 UT. Thus, we might conclude that it is an upstream signature having travelled 331°. These values are again higher than that calculated by Van Allen et al., [1980b] for L=4, but this may be explained by the difference in L shell.

For both of these absorption profiles, we find a better fit if the absorbing radius used in Equation 5.6 to calculate the model curves is increased to $1.3b$. This might suggest that Tethys is presenting a larger obstacle to the flow than a simple, inert body.

At the time this depletion was observed, we noticed another cavity of the same depth at 16:15 UT but displaced in L-shell. If we consider the spacecraft trajectory with respect to the moons L-shell (not shown) we see no evidence that Cassini crosses it twice. Of course, we are considering a steady-state magnetosphere which is unlikely considering the highly dynamic nature of Saturn's magnetosphere [Young et al., 2005]. It is therefore possible that the L shell of Tethys, with its associated depletions, are being moved back and forth across Cassini's trajectory, or that there was some

variability in the magnetosphere when these depletions were created, resulting in their different L shell positions [Roussos et al., 2005].

Enceladus

The clearest, most striking signatures are those seen within 1° upstream of Enceladus. These were observed when Cassini undertook dedicated flybys of Enceladus, with very low-altitude trajectories. The signatures observed on 17 February, 9 March and 17 July 2005 all coincided with, and showed very similar absorption profiles to, those seen in the 0.98 to 3.28 MeV channels in the LEMMS instrument [Jones et al., 2006]. This leaves us in little doubt that these are depletions either of electrons above the resonant energy (> 0.98 MeV for α=90°) which have remained lagging the moon (with respect to corotation), or those above the transitional energy (> 1.39 MeV for α=90°) which are travelling westwards round the planet. Using these assumptions we are able to derive the diffusion coefficients for each of the close flybys.

On 17 February 2005 at 03:27 UT we find for case a) electrons, assuming E ~ 1.2 MeV that D_{LL} = 2.08 ±0.06 x10^{-8} $R_S^2 s^{-1}$ for outwards radial diffusion and D_{LL} = 1.64 ±0.06 x10^{-8} $R_S^2 s^{-1}$ for inwards diffusion. If E ~ 1.9 MeV for case b), D_{LL} = 8.59 ±0.27 x10^{-8} $R_S^2 s^{-1}$ (outwards) and D_{LL} = 6.78 ±0.27 x10^{-8} $R_S^2 s^{-1}$ (inwards). Thus rates are faster for outwards diffusion. We find that to achieve a closer fit between the model and the data, the assumed radius of the absorbing body needs to be ~ 1.3b.

On 9 March 2005 at 09:07 UT: a) D_{LL} = 7.36 ±0.06 x10^{-9} $R_S^2 s^{-1}$ (outwards) and 9.11 ±0.06 x10^{-9} $R_S^2 s^{-1}$ (inwards) and for case b) D_{LL} = 3.04±0.05 x10^{-8} $R_S^2 s^{-1}$ (outwards) and 3.77 ±0.05 x10^{-8} $R_S^2 s^{-1}$ (inwards). Again, a better fit was achieved if the absorbing body had a radius of ~ 1.7b for the inwards case, but for the outwards case, we find the best fit assuming the model curves are based on an absorbing radius of b. On 14 July 2005 at 19:53 UT we apply the same analysis as above as find for case a) D_{LL}=1.16 ±0.06 x10^{-8} $R_S^2 s^{-1}$ (outwards) and 7.76 ±0.06 x10^{-9} $R_S^2 s^{-1}$ (inwards) and case b) D_{LL}=4.82 ±0.06 x10^{-8} $R_S^2 s^{-1}$ (outwards) and D_{LL}=3.21 ±0.06 x10^{-8} $R_S^2 s^{-1}$ (inwards). The best fit is achieved using the radius of the body itself for both the inwards and outwards cases, although from our estimations of the widths of these depletions, there is clearly a larger obstacle being presented to the flow. This indicates that there is some additional complication to this simple comparison with the model. Note that for the cavities observed on 17 February and 14 July 2005 the rate of diffusion outwards is larger than that inwards. Yet for the cavity observed on 9 March, this is reversed,

suggesting that there is some change in the magnetospheric environment during the time that this wake was created.

There is an additional shallow depletion observed on 16 February 2005 at 22:55 UT. We again make an assumption of the energy of the electrons being depleted, in order to calculate the diffusion rates. Using the energies assumed for the previous three cases we find for case a), D_{LL}=2.63 ±0.05 x10^{-10} $R_S^2 s^{-1}$ (outwards) and 1.60 ±0.05 x10^{-10} $R_S^2 s^{-1}$ (inwards) and for case b) D_{LL}=7.82 ±0.05 x10^{-9} $R_S^2 s^{-1}$ (outwards) and 4.74 ±0.05 x 10^{-9} $R_S^2 s^{-1}$ (inwards). For case c) the values are D_{LL}=3.23 ±0.05 x10^{-8} $R_S^2 s^{-1}$ (outwards) and 1.96 ±0.05 x 10^{-8} $R_S^2 s^{-1}$ (inwards). There is a significant difference between the values derived for different energies.

We find that if we assume that the absorbing body is twice the size of Enceladus, we get the best fits with the data, but only for the side of the cavity used to infer outwards diffusion. For the inwards diffusion rate estimates, the body radius is sufficient to provide good model fits. Once again, this raises questions about the generation and subsequent fill in of these cavities. Since the absorbing body is the same for each case, no matter which direction the radial diffusion is acting, we would expect the inferred absorbing radius to be the same in both cases. The fact that we see a difference in the model parameters to achieve better fits for each side of the cavities, may indicate that the absorbing body is asymmetric. This may be the case if we consider the Enceladus plume [Dougherty et al., 2006], which is known to emit dust and gas from the south pole of the planet only. However, Dougherty et al., [2006] suggest that the perturbation observed in the magnetic field indicates a similar interaction for the encounters on 9 March and 14 July 2005. However we find a difference in fits for the inward and outward edges on the 9 March, but not the 14 July 2005, suggesting that there may be additional complicating factors between the production and losses due to this moon, possibly due to a smaller atmosphere.

The values for D_{LL} derived from the ELS data, assuming the cavity is in energies above the resonant energy, are higher than the upper limit given by Jones et al., [2006] of 2.0 ± 0.5 x10^{-9} $R_S^2 s^{-1}$ for 0.98-3.28 MeV electrons. The discrepancy may be due to the slight differences in the fit involved in the derivation of D_{LL}. Of course, the maximum energy of the ELS response is unknown, and it maybe that the ELS measures electrons over a much broader range than the LEMMS electron channels. Therefore, the absorption feature observed by the ELS may have different, energy dependent characteristics from that seen in the LEMMS data. The combined effect over a range of

electron energies, which will drift at a range of different velocities, may create a different profile. The higher value for D_{LL} derived suggests that the ELS signature is shallower than that in the LEMMS data, which would support this hypothesis.

There is an additional depletion observed at the L shell of Enceladus on 21 May 2005 for which we have not been able to successfully derive a diffusion coefficient due to the poor fit with the solutions of Equation 5.6. This was observed 36° upstream of the moon compared with the previous signature on 16 February which was observed 28° upstream of the moon. The fact that the refilling has decreased the cavity depth by ~ 20% in this time is indicative of the fast diffusion times at Enceladus. This was a double signature, with the two depletions having different depths. Both were observed shifted inwards from the nominal L shell of the moon. For the deeper cavity, $\Delta L \sim 0.02$ R_S and for the shallower one $\Delta L \sim 0.04$ R_S. This suggests that over time these signatures have drifted inwards although it is not immediately clear how the second, less depleted cavity could exist. One possibility is that it has survived more than one orbit around Saturn, but as we have seen the fast re-filling would wash out such a depletion. Once way to establish if a signature has lasted more than one orbit, is to establish consistency of D_{LL} between cavities. Of course this would only be a valid comparison if we assumed the magnetosphere to be in steady state. It may have been displaced inwards, and possibly undergone more refilling after its creation due to magnetospheric conditions which have not affected the deeper signature. Most likely, it is a depletion in electrons of a different energy compared with that of the deeper signature, and was created further in the past but has drifted faster round the planet.

We also try using the estimation for the effective absorbing radius of these moons to narrow the energy range of the penetrators. We use the signatures from the Enceladus data since they are the 'newest' signature and are expected to have undergone the least re-filling. The spatial width of the cavities is calculated assuming the magnetosphere in this region is stationary. Of course, with a single spacecraft we cannot truly resolve spatial and temporal variations. If we assume that this is the true effective width, apply Equation 5.4 and work backwards we find, for the cavities observed on 9 March and 14 July 2005, that the energy of the electrons would need to be ~ 40 MeV, which is unreasonably large. Since any fluxes at this energy would not be sufficient to produce such a noticeable signature this assumption is clearly unrealistic. This therefore suggests that Enceladus presents a larger obstacle to the penetrating particles than a simple inert body. This agrees with the recent findings of Dougherty et al., [2006] who estimate the atmospheric obstacle to be at least ~ 4 R_{EN}. This is still

larger than our estimated cavity widths of ~ 2.5 R_{EN} and indicates that the electrons we are detecting have sufficient energy to penetrate further in to the atmosphere of Enceladus agreeing with the findings of Jones et al., [2006].

Mimas

Observations of two depleted cavities near the L shell of Mimas were also made, at 57° and 26° upstream respectively. We note that the cavity on 14 April 2005 has a greater level of depletion compared with that observed on 15 April 2005 despite being further upstream from the moon. This would be explained if these are downstream travelling signatures, i.e. case a) electrons and the separations were, in fact, 303° and 334° downstream.

For the cavity observed on 14 April 2005 at ~ 57° upstream from the moon we find diffusion coefficients for case a) in the 0.9 MeV electrons of D_{LL} =7.41 ± 0.03 x10^{-12} $R_S^2 s^{-1}$. For case b) and 1.2 MeV electrons, D_{LL} =9.87 ± 0.06 x10^{-11} $R_S^2 s^{-1}$ and for case c) and 2.5 MeV electrons, D_{LL} =6.65 ± 0.06 x10^{-10} $R_S^2 s^{-1}$. Note that in each of these cases, the values of D_{LL} outwards and inwards are equal. This is also apparent from the symmetric profile of the absorption (Figure 5.25) and suggests that the diffusion rates are balanced at the orbit of Mimas unlike the case for any of the other moons.

The second cavity on 15 April 2005 at 00:59 UT gave values for 1.2 MeV of D_{LL}=4.17± 0.05 x10^{-10} $R_S^2 s^{-1}$ (outward) and 3.71 ± 0.05 x10^{-10} $R_S^2 s^{-1}$ (inward) and for 2.5 MeV electrons, D_{LL}=2.81 ± 0.06 x10^{-9} $R_S^2 s^{-1}$ (outward) and 2.50 ± 0.06 x10^{-9} $R_S^2 s^{-1}$ (inward). The inward and outward diffusion rates are not balanced and are, in this case, an order higher than the previous values. The difference in D_{LL} between these two events might indicate that either the fits are not good enough (although the values for the χ^2 of the fit are low), or that the simple geometrical picture we have for these encounters with the moon are not sufficient. However, it may be reflecting the variation in the activity in the magnetosphere that the diffusion rate has changed by almost an order between 14 and 15 April 2005. This would explain why the latter cavity, if we assume an upstream travelling cavity, has a smaller separation from the moon than for the previous case on 14 April, yet has undergone greater refilling. For both of these cavities we find good model fits assuming the initial absorption is caused by a body of the same size as Mimas.

Another way to establish the true 'ages' of these cavities is to take the eccentricity of Mimas into account, as done in Van Allen et al., [1980b]. Their argument was that, due to the orbital eccentricity, Mimas traverses a wide range of radial distances (or L-shells) throughout an orbit. The signature seen at a particular radial distance will therefore have been created only when Mimas was at that exact L-shell (assuming no translation of the signature radially). We have considered this for the two signatures seen on 14 and 15 April 2005. On these two dates Cassini observed depletions centred on L = 3.02 R_S and 3.00 R_S respectively. However, upon inspection of the orbital data, we find that in the two days preceding this observation, Mimas did not venture closer to Saturn than a radial distance of 3.02 R_S. This suggests that the large displacements we observe (compared with most other observations), are due to a combination of the eccentricity and the displacement of the signatures.

General conclusions

Throughout this analysis we have neglected energy and pitch angle dispersion [i.e. Van Allen et al., 1980b]; since we have no information on either of these parameters, but accept that we are effectively seeing a superposition of profiles due to different populations of electrons. As suggested in Van Allen et al., [1980b], and as is seen in the ELS data, the width of the signatures observed is sometimes broader than can be modelled by the diffusion curves with the initial assumption that the absorbing body is the same size as the moon. In fact, we sometimes detect absorption profiles which are apparently generated by a body of ~ twice the moon radius. Of course, depletions that are larger than the moon may arise from other processes, such as energy dispersion of different signatures, which superpose to appear as one cavity in a detector with a broad energy response like the ELS. Of course, for those close flybys, we might not expect the dispersion to result in such a wide signature until more time has passed and greater dispersion has occurred.

In the derivation of the values for the diffusion coefficients we have made the assumption that the diffusion is constant across the depleted region. The presence of asymmetric cavities has allowed us to determine that the diffusion rate is asymmetric inwards and outwards, and not always in the same sense. In general, we calculate a larger diffusion rate outwards through the magnetosphere. At the orbit of Enceladus, however, we also see this reversed with larger radial diffusion inwards. We can estimate the expected profile of electron transport throughout the magnetosphere by considering the phase space density profile which has been analysed in Thomsen et al., [1977],

McKibben and Simpson, [1980] and more recently using data from the Cassini CAPS instrument, Rymer et al., [2006, *submitted*]. These studies indicate a plasma source within L < 4, resulting in a density profile with a negative gradient and thus diffusion would have a tendency to move particles radially outwards [Walt, 1994]. However, as Thomsen et al., [1977] suggest, there is a constantly changing density profile due to the periodic losses of plasma in the inner magnetosphere by the rings and moons, which in turn modifies the dominant direction of diffusion, which we observe at the orbit of Enceladus. This is strongly indicative of the variability of the magnetosphere at the orbit of Enceladus, also inferred in Dougherty et al. [2006], Jones et al. [2006] and Kivelson [2006] among others.

We find that the diffusion rates are faster at Tethys than Mimas, suggesting that D_{LL} does increase with L. We might expect this if the diffusion is driven by magnetic fluctuations, since in the outer magnetosphere the field is weaker, so a disturbance field will be more comparable to the background field and thus the diffusion will be more significant [Walt, 1971].

If there is greater disturbance in the magnetosphere, we may expect an increased rate of diffusion. Thus, we may consider the state of the magnetosphere prior to and after the encounter with the cavity. If we subtract the background magnetic field, the characteristic of the residual fluctuations, such as wave power, will indicate whether we might expect to see fast or slow diffusion acting and thus the state of the magnetosphere in that region.

In addition to the changing width and depth of these cavities, there was a noticeable displacement radially from the L shell of the moon creating the signatures. This could be a gradual drift over the lifetime of the cavity, although in some cases, a displacement is seen very close to the moon, which may suggest that the displacement occurred almost instantaneously. The displacement of signatures may be due to the use of a dipole field model, in the L-shell calculations. However, the field is known to be strongly dipolar within ~ 4 R_S and quasi-dipolar between 4 – 16 R_S [Arridge, 2006, *private communication*] validating our use of a simple field model.

We were not able to detect any local time dependency of note as suggested by Roussos et al., [2005, *private communication*] or any dependence on the age of the signature. Of course, there is a lack of measurements on the dawn side which are required to make a truly global inference from these results.

Since we expect the drift orbits of particles to be circular under steady state conditions, a radial displacement in a drift shell suggests that there is a departure of

these conditions. This may arise from a change in the magnetospheric conditions such as a sudden compression of the magnetosphere by the solar wind. This will result in the inward motion of particles, and, due to conservation of the first adiabatic invariant, the magnetic field strength will increase along with the particle energy. A sudden displacement such as this will be followed by a gradual relaxation of the magnetosphere [Mead and Hess, 1973] which would then cause an outward displacement in these cavities. Of course, if a cavity changes its radial position in the magnetosphere, then the diffusion coefficient may change accordingly. It is also clear that the radial translation of the cavities has a much larger affect than refilling by diffusion.

6 Summary and Conclusions

The work in this thesis has concentrated on the measurements made predominately by the electron spectrometer on the Cassini spacecraft during the first 18 months of its tour of the Saturnian system. In our investigations we focused on two main topics. The first considered the behaviour of electrons at the magnetopause, both a detailed case study of two events and a more general look at the properties of this boundary. As a result of this work, we have been able to infer some properties of the nature of the interaction with the external plasma and fields of the magnetosheath. Such a process is of utmost importance in understanding the global interaction of Saturn's magnetosphere with the solar wind. The second topic concerned the processes behind the generation and re-filling of the cavities carved out in the high energy electrons by the icy moons in the inner magnetosphere. The latter allowed us to make inferences about the internal magnetospheric plasma dynamics.

The magnetosphere of Saturn is a large, fast-rotator containing significant sources of plasma and neutrals in the form of the ring particles and numerous icy satellites. The internal processes are therefore integral in driving the dynamics of the system. It is this fact that made us question what, if any, is the interaction with the external influences of the solar wind? Understanding the balance between these two driving forces will allow us to put the interactions at Saturn in context with those of the magnetospheres of Earth and Saturn.

From our results we were able to make important inferences about reconnection at Saturn, both on a local scale (chapter 3) and a global scale (chapter 4). In chapter 3, we find evidence suggestive of reconnection of the magnetospheric field with the magnetosheath field. This evidence takes the form of the apparent energisation in the electrons and ions, together with a delay between the arrival time of electrons and ions at the spacecraft and a locally magnetically open field. We find that the direction of accelerated ions at the magnetopause broadly agrees with theoretical predictions of the results of reconnection at Earth's magnetopause, further supporting our conclusion. The energisation of the electrons was also important in our investigation, although their already significant thermal velocity in the magnetosheath makes it a difficult task to determine the net velocity increase. Analysis of the high time resolution electron and ion spectra also provided a valuable tool for discerning between different populations. Together with knowledge of the pitch angles of the electrons, this allowed us to make further inferences about the source of, and processes acting on, these particles. The

reconnection electric field was calculated based on our observations of the magnetic field component normal to the magnetopause, and the inferred velocity of the accelerated ions, and found to be small compared with the large corotational electric field of Saturn. This suggests that although reconnection occurs, its effect is small and its effects are not able to penetrate into the magnetosphere significantly before the corotational electric field begins to dominate.

We conclude that the observed reconnection signatures are driven by the external magnetosheath field. We have found no evidence to suggest that the reconnection is triggered internally.

Reconnection was seen clearly at two separate encounters with the dawn and pre-noon magnetopause. Based on the magnetic field orientation and the observed directions of the accelerated ions, we were able to suggest the location of the possible reconnection sites. In the first case (17 April 2005), we inferred that the reconnection site was in the northern hemisphere, anti-Sunwards of the dawn-dusk terminator. For the second event (21 September 2005), conditions for reconnection were favourable along the whole pre-noon magnetopause. Of course, as our sampling is limited to the equatorial, dawn flank of the magnetopause, we are unable to establish any global dependency of reconnection events.

Observations of magnetosheath-like plasma inside the magnetopause indicated that Saturn's magnetopause is open to the magnetosheath flow at times and led us to consider the presence of a permanent boundary layer at Saturn in chapter 4. In addition, we wanted to understand the characteristics of the magnetopause utilising the large number of crossings observed in the first 18 months of the mission. We found a highly variable magnetopause, both in location and characteristics, with evidence of an internal boundary layer for ~ 79% of encounters. This is strikingly similar to values quoted for Earth, and suggests that the entry of magnetosheath plasma into the magnetosphere may not be an insignificant process at Saturn, despite the dominant internal dynamics. At times, the boundary layer was observed extending into the magnetosphere for a duration of nearly two hours following an inbound magnetopause crossing.

Determination of the density in the boundary layer yielded a more complicated story, since we often observed a larger density inside the magnetosphere than in the boundary layer itself, which is not the case at Earth. This led us to conclude that such measurements were excursions into the plasmasheet at Saturn which were skewing the results. Although we did not explicitly find evidence of reconnection being triggered by internal fields and particles in our careful exploration of two magnetopause events in

chapter 3, it is apparent that internal process could significantly impact the population of the boundary layer. The lack of any correlations between the boundary layer and location on the magnetopause suggests that the motion of the magnetopause with respect to the spacecraft significantly affects our determination of the temporal width of the boundary layer, which subsequently affects our identification of any correlations. Bearing this in mind, we also tested for any correlations between the boundary layer and the conditions in the external regions, such as the magnetic field orientation and the pressure of the solar wind. We found the boundary layer width decreased slightly with high magnetic shear between the upstream and downstream fields. This suggests that reconnection reduces the width of the boundary layer. The density ratio in the layer increased with both magnetic shear and dynamic pressure suggesting that this is a controlling factor in the entry of magnetosheath plasma into the magnetosphere, and thus possibly reconnection, agreeing with [Jackman et al., 2004; Cowley et al., 2005].

The presence of plasma depletion layers far from the magnetopause at Saturn under low magnetic shear conditions indicates a slow field pile-up, although the main depletion of plasma is not observed until shortly before the magnetopause crossing. There is also evidence of field build-up close to the magnetopause in high shear cases, indicating that if reconnection is occurring as would be expected for largely anti-parallel fields, it is not removing the flux at a rate to balance the field build up.

Directly-observed signatures of energisation in the electrons show a weak relationship with the dynamic pressure, suggesting that plasma energisation is least likely to be observed when the upstream pressure is low. These observations of the magnetopause have provided us with an insight into the typical processes occurring and their characteristics.

The final science topic concerned the inner magnetosphere and the effects of the icy moons. Analysis of the effect of three of Saturn's moons on the high-energy inner magnetospheric plasma has indicated that there are different rates of electron diffusion inwards and outwards through the magnetosphere. We find, in general, that the latter is greater at the orbits of Tethys and Mimas, indicating a negative radial density gradient and a large source of plasma in the inner magnetosphere, within the orbit of Mimas (~ 3 R_S). This agrees with previous results indicating of a large source of plasma < 4 R_S. At Enceladus, however, we find that, at times, there is a larger inwards diffusion rate, indicating that the opposite is true and the density gradient is positive with radial distance.

We also find that the assumption that the moon is an inert body, carving out a cavity in the high energy electrons, is not sufficient, especially for Enceladus. This indicates that other processes are acting, such as atmospheric and magnetic field interactions, resulting in a larger obstacle than the moon itself being presented to the magnetospheric plasma.

The differences between the depletion signatures of the moons, both their shape and radial displacement away from the moon L shell, shows the variable nature of the magnetosphere at the times of creation of these cavities, and throughout their lifetimes.

6.1 Future work

The magnetopause

The results of the investigations in this thesis have raised just as many questions as they have begun to answer. Reconnection has been shown to occur at the magnetopause, although to better understand the nature of this process at Saturn, more events need to be analysed in detail. Detection of additional reconnection events will allow us to further refine our identification of the magnetic field and plasma conditions required to allow this process to occur, and also the locations at which reconnection is favourable. In particular, we hope to search for reconnection events at the high-latitude magnetopause and on the dusk flank if the extended mission facilitates such encounters. We also hope to carry out a more detailed search of the magnetic signatures of reconnection.

The findings of the survey of magnetopause crossings clearly indicate the need for further investigation. Increased numbers of crossings, particularly at more local times and latitudes, will increase the parameter space and may remove some of the biasing in the results. For example, by characterising the boundary layer at different latitudes we may be able to determine the location of entry of boundary layer plasma, i.e. at the low latitude magnetopause or at the cusps as has been suggested at Earth [Haerendel et al., 1978]. We would also like to consider the properties of the magnetosphere observed just inside the magnetopause and understand better how the internal plasma contributes to the formation of the magnetospheric boundary layer.

We may also try to compare the formation of plasma depletion layers under different upstream conditions such as dynamic pressure. The formation of PDLs will change the conditions adjacent to the Sunward-side of the magnetopause, and thus the

probability of reconnection occurring. Analysis of the effects of PDLs at Saturn with observed reconnection events will prove an interesting comparison if the data allows.

A detailed comparison of electron spectra in the different regions encountered, i.e. magnetosheath, boundary layer, outer magnetosphere and plasmasheet entries, will enable us to better characterise and thus distinguish between these layers. Also key to further work will be the analysis of events in which the ions were better defined. This would allow us to exploit the IMS data to derive velocities and compositional data. This will allow us to infer a source of this boundary layer, particularly whether it is generated by internal or external processes, or both.

Icy satellite absorption cavities

This thesis did not include every absorption signature present in the data; in addition, throughout the rest of the mission, there will be further L shell transits to investigate for absorption cavities, including some at high latitudes. With these additional observations, we will increase the parameter space and may better highlight any global trends or asymmetries of the characteristics of these absorption signatures and the effect of the surrounding magnetospheric plasma.

The absorption cavities carved out by the icy moons in the high energy electrons effectively provide a means of efficiently and accurately correcting for the penetrating radiation in the instrument. This allows us an unimpeded view of the low energy electron (< 26 keV) population in the vicinity of the moons. Since we expect these moons to be a source of low energy plasma, we can analyse the instantaneous and longitudinally-averaged effect of the moons, particularly Enceladus. This would allow us to better understand the interaction processes of the surrounding plasma with the moons themselves and, where relevant, with the atmosphere. Analysis of the density, temperature and pitch angles of the populations at varying positions throughout their orbits around Saturn and under different magnetospheric conditions can be investigated. This will shed light on the characteristics of the moon and the subsequent effect they have on the magnetospheric dynamics.

Acronyms

ASI	Agenzia Spaziale Italiana
AU	Astronomical Unit
CAPS	Cassini Plasma Spectrometer
CEM	Channel Electron Multiplier
CHEMS	Charge-Energy-Mass Spectrometer
CIR	Corotating Interaction Region
dHT	De Hoffman-Teller
DP	Dynamic Pressure
DPU	Data Processing Unit
ELS	Electron Spectrometer
ESA	Electrostatic Analyser
FGM	Fluxgate Magnetometer
FTE	Flux Transfer Event
HEEA	High Energy Electron Analyser
HCS	Heliospheric Current Sheet
HST	Hubble Space Telescope
IBS	Ion Beam Spectrometer
IMF	Interplanetary Magnetic Field
IMS	Ion Mass Spectrometer
INCA	Ion and Neutral Camera
ISEE	International Sun-Earth Explorer
KHI	Kevin Helmholtz Instability
KSM	Kronocentric Solar Magnetospheric
LECP	Low Energy Charged Particle instrument
LEF	Linear Electric Field
LEMMS	Low Energy Magnetospheric Measurement System
LLBL	Low Latitude Boundary Layer
LT	Local Time
MAG	Magnetometer
MAPS	Magnetospheric and Particle Science

MCP	Micro Channel Plate
MHD	Magnetohydrodynamics
MIMI	Magnetospheric Imaging Instrument
MLAT	Magnetic Local Time
MPCL	Magnetopause Current Layer
MSBL	Magnetosheath Boundary Layer
MVA	Minimum Variance Analysis
NASA	National Aeronautics and Space Administration
PEACE	Plasma Electron and Current Experiment
PDL	Plasma Depletion Layer
PLS	Plasma Spectrometer Instrument
PSD	Phase Space Density
TD	Tangential Discontinuity
RD	Rotational Discontinuity
RPWS	Radio and Plasma Wave Science
SEA	Superposed Epoch Analysis
SHM	Scalar Helium Magnetometer
SNG	Singles
SPV	Saturn-Pioneer-Voyager
ST	Straight-Through
TOF	Time-Of-Flight
UT	Universal Time
UV	Ultraviolet
UVIS	Ultraviolet Imaging Spectrograph
VHM	Vector Helium Magnetometer

A Appendix: ELS voltage table and data formats

Table A-1 Sweep table 1 shown with corresponding voltage and electron energy levels

Step Number	Voltage / V	Energy / eV		Step Number	Voltage / V	Energy / eV
0	4,200	26,040		30	44.32	274.8
1	4,200	26,040		31	37.90	235.0
2	3,585	22,227		32	32.41	200.9
3	3,063	18,991		33	27.69	171.7
4	2,622	16,256		34	23.69	146.9
5	2,238	13,876		35	20.18	125.1
6	1,914	11,867		36	17.32	107.4
7	1,636	10,143		37	14.80	91.76
8	1,399	8,674		38	12.61	78.18
9	1,196	7,415		39	10.83	67.15
10	1,022	6,336		40	9.27	57.45
11	873.5	5,416		41	7.90	49.00
12	746.8	4,630		42	6.74	41.81
13	638.0	3,956		43	5.78	35.84
14	545.7	3,383		44	4.92	30.49
15	466.1	2,890		45	4.25	26.34
16	398.6	2,471		46	3.58	22.21
17	340.7	2,112		47	3.11	19.26
18	291.2	1,805		48	2.63	16.33
19	249.0	1,544		49	2.26	13.98
20	212.7	1,319		50	1.88	11.64
21	181.9	1,128		51	1.60	9.89
22	155.5	964.1		52	1.41	8.72
23	132.9	824.0		53	1.22	7.56
24	113.6	704.3		54	1.03	6.39
25	97.07	601.8		55	0.84	5.23
26	83.03	514.8		56	0.75	4.64
27	70.87	439.4		57	0.66	4.06
28	60.63	375.9		58	0.56	3.48
29	51.86	321.5		59	0.47	2.90
				60	0.37	2.32
				61	0.28	1.74
				62	0.19	1.16
				63	0.09	0.58

The ELS energy sweep table is shown in Table A-1. Each step in the voltage sweep is shown along with the corresponding energy.

The final data product is determined by any summing or averaging that takes place. Table A-2 lists the different combination of time resolution and number of energy bins in the final data array for each data format.

Table A-2 Data formats and the associated time and energy resolution

Format ID	Time resolution (s)	Energy resolution (bins)
1	2	63
2	4	63
3	8	63
4	8	32
5	16	32
6	10,10,12*	63
7	32	63
8	32	32

* This format is achieved by averaging over the first 5 sweeps, then the next 5, then the last 6.

B Appendix: Data Analysis

This appendix describes some of the analysis techniques that are used in this thesis.

Calculation of plasma moments

In order to facilitate a good understanding of the plasma environment, the data analysis in this thesis requires information on the density and temperature of the plasma. These parameters are calculated by applying the well documented method of taking integral moments of the distribution in phase space (see Chapter 1). A brief overview of the method is provided here and a full treatment is given in Lewis et al. [2006, *in preparation*].

We must first convert the observed counts to phase space density (PSD), in units of $m^{-6}s^3$ using the derived geometric factor (see Chapter 2). We then need to evaluate the distribution function of the plasma about a volume of velocity space. However, the edges of the field of view (and to some degree the extreme anodes) are affected by spacecraft effects, thus the total useable field of view is only ~ 45 % of the sky. Thus, to completely eliminate these effects we use the data from the central anode only and fill the full 3d velocity space, relying on the assumption that the plasma is isotropic.

The populated distribution function is then evaluated to derive the plasma moments applying the general equation:

$$\underline{M}_r(\underline{x},t) = \int \underline{v}^r f(\underline{v},\underline{x},t) d^3\underline{v}$$

Equation B.1

Where the first few moments ($r = 0,1,2,..$ etc) give the density, the bulk flow velocity and the pressure of the distribution respectively. The latter of these leads to the derivation of the temperature via $P = nk_B T$, where k_B is the Boltzmann constant. The equations thus take the form as derived in Lewis et al., [2006, *submitted*]:

$$n = \frac{4\pi}{3} \sum_{i=1}^{i=63} f_i(\underline{v}) \left(v_i^3 - v_{i-1}^3 \right)$$

Equation B.2

Where n is density, and the summation is carried out over the 63 energy bins, and:

$$T = \frac{4\pi m}{15 k_B} \sum_{i=1}^{i=63} \frac{1}{n_i} f_i(\underline{v}) \left(v_i^5 - v_{i-1}^5 \right)$$

Equation B.3

Where T is the temperature and m is the particle mass. Note that the bulk flow velocity (moment, $r = 1$) is zero, since the velocity of the plasma measured in one direction will be cancelled out by the motion of the plasma in the opposite direction.

Identification of the spacecraft potential

As discussed in Chapter 2, before we calculate these moments the spacecraft photoelectrons must be removed from the raw counts. Note this is only possible for a positive spacecraft potential. Other methods must be employed when the potential is negative and these are briefly discussed in Chapter 2. This is either done manually or by an automated method. The latter method is not a trivial task since in general the form of the distribution doesn't exhibit a clear dip between the photoelectrons and the real population which makes extraction using automated algorithms difficult. Some example 'rules' set into the original code included:

- finding the minima, but there were often multiple minima from the noise and variation inherent in the data;
- limiting the minima to lie within a range of energies;
- fitting a Gaussian to the photoelectron counts and subtracting that from the data. Then assuming that whatever was left was the 'real' population and where that became zero equalled the spacecraft potential. However, the fits were poor since we only had a small number of data points;
- fitting to the photoelectron data in PSD so they can be removed, but this is not a simple straight line.

Often the spectrum was so complex, with additional higher energy populations for example; the code simply discounted much of the data without identifying the potential.

It was thus decided that the only way of obtaining an accurate method is to manually identify the potential. This is carried out using a simple 'point-and-click' tool directly onto close-ups of spectrograms. After the counts are translated into PSD as described above, the data are then shifted along the energy axis by an amount equal to the potential. This corrects for the acceleration of the incoming electrons by the spacecraft potential in accordance with Liouville's theorem.

Minimum Variance Analysis (MVA)

Introduction

We have applied Minimum Variance Analysis (MVA) to the magnetic field data in Chapter 3 in order to derive the normal magnetic field component to the magnetopause. We give a brief description of this method here and a full treatment can be found in Sonnerup and Scheible [1998]. The method aims to identify the dimension of the magnetic field data with the least amount of variance and apply it to a one dimensional current layer. The application of this method to data at the magnetopause was first proposed by Sonnerup and Cahill, [1967]. It derives the direction in space along which the field along the component $\hat{\underline{n}}$ has minimum variance. This can be done through the minimisation of:

$$\sigma^2 = \frac{1}{M}\sum_{m=1}^{M} \left| \left(\underline{B}^{(m)} - \langle \underline{B} \rangle\right) \bullet \hat{\underline{n}} \right|^2$$

Equation B.4

where the average $\langle \underline{B} \rangle$ is defined by:

$$\langle \underline{B} \rangle = \frac{1}{M} \sum_{m=1}^{M} \underline{B}^{(m)}$$

Equation.B.5

where M is the number of vector measurements. The minimisation is subject to the normalisation constraint: $|\hat{\underline{n}}|^2 = 1$ which is implemented using a Lagrange multiplier, λ. The solution to three homogeneous linear equations are then sought:

$$\frac{\partial}{\partial n_{x,y,z}} \left(\sigma^2 - \lambda \left(|\hat{\underline{n}}|^2 - 1 \right) \right) = 0$$

Equation B.6

where $\hat{\underline{n}}$ is in terms of n_x, n_y and n_z in the coordinate system of choice (e.g. KSM) in which the magnetic field data is given. The differentiations are carried out and the three resulting equations are written in matrix form as:

$$\sum_{\nu=1}^{3} M_{\mu\nu}^{B} n_\nu = \lambda n_\mu$$

Equation.B.7

Where μ,ν=1,2,4 denote the components along the X,Y and Z system. The allowed values of λ are the eigenvalues corresponding to the eigenvectors which are orthogonal and represent the direction of maximum, intermediate and minimum variance of the field. We can graphically represent the result in *Hodogram* format, which is a curve in space drawn out by the vectors in maximum, intermediate and minimum space. This is a convenient way of interpreting the results.

MVA confidence and errors

As a first attempt to quantify the success of the MVA, we can take the ratio of the eigenvalues. This allows us to establish the degeneracy in the axis of variance space since the half-length of each axis is $\sqrt{\lambda_{1,2,3}}$. Thus, if the minimum direction and associated eigenvalue are significantly different from the intermediate values, then the minimum is well-defined. So our first measure of the confidence in our results is:

λ_2/λ_3 where λ_2 is the intermediate eigenvalue and λ_3 the minimum. In addition to this we may define uncertainties in the orientations of the eigenvectors x_1, x_2, x_3 due to the statistical errors. Errors associated with violation of the assumptions behind the method, such as lack of stationarity in the normal direction, are more complex and are not considered here.

The angular error in radians (where $i \neq j$) is:

$$|\Delta\varphi_{ij}| = \sqrt{\frac{\lambda_3}{(M-1)}\frac{(\lambda_i + \lambda_j - \lambda_3)}{(\lambda_i - \lambda_j)^2}}$$

Equation B.8

This equation outputs the expected angular uncertainty of eigenvector $\underline{x}_i$ for rotation toward or away from eigenvector $\underline{x}_j$. The statistical error for the normal component of the field, $\langle \underline{B} \rangle \cdot \underline{x}_3$ is:

$$|\Delta\langle \underline{B} \cdot \underline{x}_3 \rangle| = \sqrt{\frac{\lambda_3}{M-1} + (\Delta\varphi_{32}\langle \underline{B} \rangle \cdot \underline{x}_2)^2 + (\Delta\varphi_{31}\langle \underline{B} \rangle \cdot \underline{x}_1)^2}$$

Equation B.9

Similar expressions can be written for the errors on the intermediate and maximum components but the error on the minimum is of most interest for our application.

C Appendix: Coordinate systems

Much of the analysis in space science relies on appropriate use of a coordinate system. Here we describe four coordinate systems used in this thesis. Definitions:

$\underline{K}$ = Unit vector in the direction of the rotation (and hence dipole axes)

$\underline{S}$ = Unit vector pointing from Saturn to the Sun

Kronocentric Solar Magnetospheric (KSM)

This coordinate system is similar to the GSM (Geocentric Solar Magnetospheric) coordinate system used at Earth. It is used frequently throughout the

first two science chapters of this thesis since it is the most suitable system to use when considering the interaction of the solar wind and the magnetospheric field and thus the magnetopause. Because Saturn's rotation axis and magnetic dipole axis are aligned within < 1°, we will do not differentiate them when defining this coordinate system, and we define the frame in terms of the rotation axis. The formal definition [http://mapsview.engin.umich.edu/data_descriptions/coordinate_systems.php, 2006] follows:

$\underline{X} = \underline{S}$	Points from Saturn to the Sun
$\underline{Y} = \underline{K} \times \underline{X}$	Perpendicular to the rotation axis towards dusk
$\underline{Z} = \underline{X} \times \underline{Y}$	Chosen so that the rotation axis lies in the X-Z plane

J2000 Coordinates

Although only referred to briefly when discussing spacecraft position and attitude, we also define J2000 coordinates which is the base system for planetary positions (it is also known as Geocentric Earth Equatorial (GEI_{J2000}) [Hapgood, 1992]). Generally, data in this coordinate frame is transformed into a more useful frame, such as KSM. J2000 has a geocentric origin such that:

$\underline{X}$	First point of Aries (i.e. the intersection of the Earth's equatorial plane with the ecliptic).
$\underline{Z}$	Geographic North pole
$\underline{Y} = \underline{Z} \times \underline{X}$	Completes the set

Saturn-centred Equatorial

This coordinate system is used predominately in the analysis of the magnetospheric interactions with the icy moons since they orbit in the equatorial plane of the planet. These are planet centred where:

$\underline{X}$	In the planet-Sun plane, positive towards the Sun.
$\underline{Z}$	Northward spin axis of the planet.
$\underline{Y} = \underline{Z} \times \underline{X}$	Completes the set

Boundary Normal Coordinates (BNC)

This system is of most use when considering a plane tangential to the magnetopause. We drive such a frame ($\underline{L}, \underline{M}, \underline{N}$) by first determining the normal of the magnetopause, $\underline{N}$ using MVA. We then work out the two tangential components:

$\underline{M} = \underline{N} \times Z$	Where $\underline{Z}$ is the direction of the dipole field, here assumed to be $[0,0,1]$[2] and $\underline{M}$ points in the duskward direction
$\underline{L} = \underline{M} \times \underline{N}$	Where $\underline{L}$ points towards the northern hemisphere.

D Appendix: List of magnetopause crossings

As described in Chapter 2, each magnetopause crossing has been listed. For each crossing we have included: the date and time of the magnetopause encounter, the sense of the crossing, i.e. was Cassini crossing inbound or outbound to the magnetosphere, Saturn-centric distance (R_S), R_X, R_Y, R_Z, magnetic latitude (Mlat) and local time (LT), the magnetic shear in degrees, the boundary layer *temporal* width in hours and minutes, the average density (m^{-3}) and temperature (eV) in the boundary layer, the magnetopause stand-off distance (R_0) as calculated using the Arridge et al., [2006a] magnetopause model and the inferred solar wind dynamic pressure (D_P in nPa) and finally whether or not energised electrons are evident at the magnetopause.

[2] For convenience we assume a northward pointing field for the derivation of the frame despite the southward pointing dipole at Saturn.

Year	Date	Time UT	in/out	Rs	Rx (Rs)	Ry (Rs)	Rz (Rs)	Mlat (°)	LT	Shear (°)	Width (hh:mm)	N (m^{-3})	T (eV)	D_P (nPa)	r0 (Rs)	Energisation?
2004	28-Jun	19:53	in	33.87	16.77	-29.35	-2.17	-15.27	7.99	58.1373	0:07	5.26E+04	164.62	0.0120	27.202	no
2004	28-Jun	20:27	in	33.61	16.67	-29.12	-2.13	-15.26	7.99	11.0404	0:02	1.37E+04	366.56	0.0130	27.016	no
2004	28-Jun	20:44	out	33.51	16.61	-28.98	-2.11	-15.26	8.00	29.8265	0:07	4.67E+04	223.41	0.0130	26.905	no
2004	28-Jun	21:09	in	33.26	16.54	-28.79	-2.08	-15.25	8.00	20.9061	0:01	6.86E+04	140.46	0.0130	26.759	no
2004	28-Jun	21:32	out	33.09	16.47	-28.62	-2.06	-15.24	8.00	1.61786	0:00	4.14E+04	231.15	0.0140	26.62	no
2004	28-Jun	21:56	in	32.90	16.40	-28.45	-2.03	-15.24	8.00	48.5071	0:04	1.90E+04	388.45	0.0140	26.483	no
2004	28-Jun	23:07	out	32.27	16.18	-27.92	-1.95	-15.21	8.02	3.42354	0:14	1.06E+04	464.36	0.0150	26.066	no
2004	29-Jun	2:43	in	30.59	15.52	-26.30	-1.71	-15.14	8.05	6.05291	0:00	3.84E+04	181.91	0.0180	24.781	no
2004	26-Oct	6:58	in	22.77	18.93	-10.33	7.31	-2.19	10.40	8.96532	0:15	3.27E+05	58.47	0.0350	21.37	yes
2004	26-Oct	7:13	out	22.69	18.88	-10.24	7.32	-2.14	10.41	8.96385	0:15	3.27E+05	58.47	0.0350	21.304	yes
2004	26-Oct	7:32	in	22.59	18.82	-10.12	7.32	-2.07	10.43	22.8878	0:16	2.75E+05	61.74	0.0360	21.219	yes
2004	26-Oct	8:21	out	22.32	18.67	-9.82	7.33	-1.91	10.47	18.824	0:00	3.50E+05	42.86	0.0370	21.001	yes
2004	26-Oct	10:42	in	21.57	18.20	-8.95	7.36	-1.41	10.58	102.972	0:33	2.46E+05	73.43	0.0430	20.362	yes
2004	03-Nov	14:34	out	45.42	-9.57	-41.41	-16.00	-13.70	4.67	16.8775	0:11	1.18E+04	486.52	0.0260	22.95	no
2004	03-Nov	18:18	in	46.10	-9.36	-42.17	-16.08	-13.75	4.70	81.1914	0:06	3.91E+04	155.83	0.0240	23.395	no
2004	03-Nov	20:00	out	46.40	-9.26	-42.51	-16.12	-13.75	4.72	3.271	0:42	4.21E+03	656.38	0.0230	23.597	no
2004	04-Nov	1:16	in	47.33	-8.96	-43.54	-16.22	-13.75	4.77	13.0881	0:00	1.60E+04	189.96	0.0200	24.221	no
2004	04-Nov	18:51	out	50.26	-7.83	-47.00	-16.51	-13.72	4.91	82.3802	0:00	1.28E+04	283.06	0.0140	26.398	yes
2004	13-Dec	2:34	in	22.88	18.75	-10.86	7.34	-1.58	10.32	9.16753	0:00	1.80E+05	106.52	0.0350	21.374	yes
2004	13-Dec	3:46	out	22.51	18.54	-10.46	7.32	-1.42	10.37	8.251	0:04	1.55E+05	106.03	0.0370	21.068	yes
2004	13-Dec	5:27	in	21.98	18.23	-9.89	7.30	-1.19	10.44	4.97595	0:14	1.42E+05	91.22	0.0400	20.629	possibly
2005	22-Jan	19:50	out	44.68	-1.20	-44.41	-4.69	-4.95	5.75	8.0283	0:20	4.62E+04	112.35	0.0150	26.034	no
2005	13-Feb	16:38	in	30.49	21.72	-19.82	8.06	-1.68	7.08	98.3994	0:01	2.79E+04	234.47	0.0130	27.123	possibly
2005	23-Feb	22:55	out	28.97	11.85	-39.16	4.93	0.05	5.02	161.656	0:04	1.79E+04	330.73	0.0090	29.504	no
2005	23-Feb	23:07	in	28.92	11.87	-39.17	4.94	0.05	5.04	154.531	0:11	2.34E+04	251.24	0.0090	29.522	no
2005	23-Feb	23:18	out	28.88	11.89	-39.18	4.94	0.05	5.09	154.527	0:11	2.34E+04	251.24	0.0090	29.539	no
2005	06-Mar	21:49	in	25.40	19.57	-14.08	7.99	-0.14	9.96	59.9969	1:41	1.74E+05	78.21	0.0240	23.221	yes
2005	07-Mar	1:23	in	24.51	19.16	-13.14	7.82	-0.15	10.06	11.369	0:20	1.18E+05	98.02	0.0280	22.523	yes
2005	07-Mar	2:05	out	24.33	19.07	-12.95	7.78	-0.15	10.08	48.0493	0:17	9.59E+04	104.37	0.0280	22.382	yes
2005	07-Mar	4:25	in	23.72	18.77	-12.32	7.66	-0.15	10.14	32.5595	0:00	4.39E+04	144.38	0.0310	21.899	yes

Year	Date	Time UT	in/out	Rs	Rx (Rs)	Ry (Rs)	Rz (Rs)	Mlat (°)	LT	Shear (°)	Width (hh:mm)	N (m^{-3})	T (eV)	D_P (nPa)	r0 (Rs)	Energisation?
2005	13-Mar	11:09	out	32.43	3.34	-32.23	1.38	0.02	10.25	19.6419	0:07	8.76E+03	483.04	0.0360	21.147	no
2005	28-Mar	1:24	in	21.23	17.38	-9.96	7.00	-0.20	10.13	72.6811	0:11	2.68E+05	138.49	0.0470	19.858	possibly
2005	28-Mar	1:35	out	21.18	17.36	-9.91	6.99	-0.20	10.14	70.3243	0:11	2.48E+05	142.09	0.0480	19.817	possibly
2005	28-Mar	2:30	in	20.91	17.21	-9.64	6.93	-0.20	10.17	28.2271	0:01	7.58E+04	256.39	0.0500	19.596	yes
2005	28-Mar	3:20	out	20.66	17.07	-9.39	6.87	-0.20	10.20	11.0264	0:01	7.51E+04	285.87	0.0520	19.393	yes
2005	28-Mar	4:04	in	20.44	16.94	-9.17	6.82	-0.20	10.22	60.295	0:00	1.18E+05	227.66	0.0550	19.212	possibly
2005	28-Mar	4:23	out	20.40	16.89	-9.07	6.80	-0.20	10.23	176.025	0:12	4.23E+05	159.57	0.0560	19.133	possibly
2005	28-Mar	12:55	out	17.61	15.22	-6.40	6.12	-0.22	10.58	82.9218	0:02	1.77E+05	267.17	0.0950	16.845	yes
2005	28-Mar	13:06	in	17.55	15.18	-6.34	6.11	-0.22	10.59	21.688	0:02	1.18E+05	240.65	0.0970	16.794	yes
2005	10-Apr	7:36	out	33.49	16.15	-29.11	3.59	-4.69	7.95	116.068	0:10	2.47E+04	270.94	0.0130	26.729	no
2005	10-Apr	10:08	in	33.19	16.21	-28.72	3.61	-4.73	7.98	14.3798	0:12	1.20E+04	434.92	0.0140	26.575	possibly
2005	10-Apr	11:00	out	33.08	16.23	-28.59	3.62	-4.75	7.99	47.3425	0:00	7.49E+04	120.43	0.0140	26.521	possibly
2005	17-Apr	18:12	out	26.43	-0.35	-26.38	-1.74	-3.22	5.86	9.21254	0:03	5.87E+04	211.07	0.0940	16.894	yes
2005	19-Apr	20:42	in	34.89	6.63	-34.19	-2.20	-7.43	6.59	14.2854	0:18	1.05E+05	219.20	0.0220	23.771	no
2005	20-Apr	0:10	in	35.27	7.04	-34.50	-2.21	-7.63	6.63	75.3725	1:15	8.17E+04	348.52	0.0210	24.15	possibly
2005	20-Apr	1:25	out	35.39	7.20	-34.61	-2.22	-7.69	6.64	14.7522	0:15	1.42E+05	147.41	0.0200	24.297	possibly
2005	20-Apr	9:50	out	36.35	8.27	-35.33	-2.26	-8.20	7.73	16.6029	0:05	2.08E+04	946.23	0.0170	25.251	no
2005	27-Apr	19:45	out	35.71	22.18	-27.86	-1.69	-15.97	8.37	26.3109	0:39	7.17E+04	171.04	0.0080	30.403	no
2005	29-Apr	6:19	in	30.78	21.87	-21.62	-1.28	-17.64	8.83	13.9213	0:28	1.12E+05	137.22	0.0120	27.356	no
2005	29-Apr	6:47	out	30.70	21.85	-21.53	-1.27	-17.66	8.84	103.381	0:17	1.39E+05	126.36	0.0120	27.302	no
2005	29-Apr	12:10	in	29.76	21.64	-20.38	-1.20	-17.96	8.93	100.405	0:10	3.55E+04	209.74	0.0140	26.651	no
2005	29-Apr	12:20	out	29.73	21.64	-20.35	-1.20	-17.97	8.93	105.268	0:10	3.76E+04	205.94	0.0140	26.63	no
2005	30-Apr	7:38	in	25.82	20.41	-15.80	-0.92	-19.10	9.31	158.037	0:03	8.00E+04	111.90	0.0220	23.798	no
2005	30-Apr	9:11	out	25.47	20.23	-15.29	-0.89	-19.20	9.35	4.9857	0:28	1.62E+04	365.71	0.0230	23.455	no
2005	30-Apr	12:38	in	26.67	19.95	-14.51	-0.84	-19.42	9.43	161.812	0:00	8.68E+03	580.43	0.0260	22.919	no
2005	01-May	8:15	out	19.45	17.30	-8.87	-0.50	-20.78	10.06	146.256	0:15	4.64E+04	219.94	0.0610	18.71	no
2005	01-May	11:10	in	18.55	16.76	-7.94	-0.44	-20.99	10.18	6.32933	0:20	4.10E+04	488.16	0.0730	17.955	no
2005	06-May	16:30	out	29.98	1.77	-29.86	-1.97	-4.77	6.12	115.816	0:20	1.02E+05	142.83	0.0540	19.293	no
2005	06-May	19:17	in	30.46	2.15	-30.32	-2.00	-5.01	6.16	25.041	0:10	2.47E+04	332.12	0.0490	19.675	no
2005	06-May	21:10	out	30.62	2.42	-30.63	-2.02	-5.09	6.17	164.869	0:01	6.98E+04	158.25	0.0470	19.939	no

Year	Date	Time UT	in/out	Rs	Rx (Rs)	Ry (Rs)	Rz (Rs)	Mlat (°)	LT	Shear (°)	Width (hh:mm)	N (m^{-3})	T (eV)	D_P (nPa)	r0 (Rs)	Energisation?
2005	07-May	4:50	out	32.03	3.46	-31.78	-2.10	-5.80	6.29	103.238	0:12	8.58E+04	216.56	0.0380	20.98	possibly
2005	08-May	1:10	in	34.86	6.16	-34.23	-2.26	-7.23	6.54	151.317	0:02	9.66E+04	217.52	0.0230	23.567	no
2005	08-May	1:55	out	34.95	6.26	-34.31	-2.27	-7.28	6.55	130.718	0:00	4.94E+05	65.92	0.0230	23.657	no
2005	17-May	20:00	in	29.10	21.30	-19.79	-1.33	-18.22	8.95	17.2042	0:25	4.65E+04	209.84	0.0150	26.126	no
2005	25-May	3:43	out	31.17	2.44	-30.99	-2.24	-5.48	6.18	107.362	0:04	2.70E+04	263.19	0.0450	20.145	no
2005	25-May	7:30	in	31.78	2.94	-31.56	-2.28	-5.79	6.23	81.8533	0:00	1.08E+04	530.02	0.0400	20.65	possibly
2005	25-May	13:30	out	32.70	3.75	-32.40	-2.34	-6.24	6.31	102.013	0:24	2.54E+04	369.02	0.0340	21.443	yes
2005	12-Jul	21:24	in	21.56	18.10	-11.67	-1.08	-20.42	9.65	30.4683	0:04	8.92E+04	184.88	0.0430	20.32	possibly
2005	13-Jul	5:50	out	19.11	16.81	-9.04	-0.85	-20.98	9.97	3.18758	0:41	6.29E+04	232.37	0.0670	18.324	possibly
2005	13-Jul	7:00	in	18.75	16.60	-8.67	-0.82	-21.05	10.02	3.87328	0:30	5.48E+04	277.45	0.0720	18.025	no
2005	18-Jul	13:09	out	30.02	0.60	-29.89	-2.72	-5.27	5.95	7.47703	0:12	4.50E+04	265.73	0.0580	18.912	possibly
2005	18-Jul	16:30	in	30.64	1.06	-30.49	-2.78	-5.58	6.00	94.7959	0:38	5.93E+04	313.78	0.0530	19.382	possibly
2005	30-Jul	12:20	in	25.72	19.69	-16.47	-1.64	-19.44	9.15	13.7863	0:07	8.65E+04	148.35	0.0230	23.462	yes
2005	06-Aug	9:30	out	32.15	2.02	-31.93	-3.10	-6.46	6.10	4.76941	0:30	4.76E+04	234.34	0.0410	20.504	yes
2005	07-Aug	21:13	in	36.67	6.48	-35.92	-3.52	-8.78	6.51	100.346	0:12	3.16E+04	265.29	0.0190	24.712	no
2005	07-Aug	21:50	out	36.77	6.56	-35.97	-3.53	-8.82	6.52	62.3209	0:02	4.24E+04	207.28	0.0180	24.778	no
2005	17-Aug	8:40	in	27.67	20.04	-18.96	-2.05	-18.98	8.90	139.741	0:11	2.73E+04	776.00	0.0190	24.771	possibly
2005	25-Aug	14:50	out	34.50	3.25	-34.27	-2.26	-5.42	6.25	86.2647	1:00	2.70E+04	681.80	0.0290	22.233	no
2005	25-Aug	16:00	in	34.62	3.38	-34.38	-2.26	-5.47	6.26	12.6629	0:20	4.17E+04	588.23	0.0290	22.343	no
2005	25-Aug	17:00	out	34.71	3.48	-34.46	-2.26	-5.51	6.27	12.7103	0:30	3.58E+04	566.31	0.0280	22.437	no
2005	27-Aug	10:45	in	37.40	7.69	-36.55	-2.01	-7.04	6.67	68.106	0:00	1.08E+04	1207.48	0.0160	25.61	no
2005	27-Aug	16:00	out	37.57	8.19	-36.61	-1.97	-7.21	6.72	53.3055	0:36	3.07E+04	673.41	0.0150	25.906	possibly
2005	28-Aug	11:00	in	37.84	6.67	-36.29	-2.09	-7.83	6.89	2.07848	0:00	9.71E+04	180.22	0.0180	24.952	no
2005	28-Aug	13:20	out	37.84	6.68	-36.29	-2.09	-7.90	6.91	143.145	0:26	6.67E+04	308.57	0.0180	24.955	possibly
2005	03-Sep	12:10	in	21.57	14.74	-15.74	0.16	-13.44	8.76	127.473	0:14	7.96E+04	426.28	0.0550	19.152	yes
2005	03-Sep	17:50	out	19.98	14.29	-13.97	0.25	-13.81	8.93	146.436	0:08	2.34E+05	165.95	0.0710	18.034	yes
2005	03-Sep	19:50	in	19.39	14.10	-13.31	0.28	-13.95	9.00	179.282	0:00	3.85E+04	394.56	0.0790	17.61	yes
2005	03-Sep	21:55	out	18.76	13.88	-12.61	0.31	-14.10	9.08	118.299	0:04	2.40E+04	623.59	0.0880	17.15	yes
2005	03-Sep	23:30	in	18.26	13.70	-12.06	0.34	-14.22	9.14	62.0945	0:00	2.51E+04	443.92	0.0970	16.788	possibly
2005	08-Sep	20:00	out	29.25	-1.62	-29.20	-0.73	-0.24	5.77	30.9011	0:12	3.51E+04	899.77	0.0750	17.81	possibly

Year	Date	Time UT	in/out	Rs	Rx (Rs)	Ry (Rs)	Rz (Rs)	Mlat (°)	LT	Shear (°)	Width (hh:mm)	N (m^{-3})	T (eV)	D_P (nPa)	r0 (Rs)	Energisation?
2005	08-Sep	23:00	in	29.82	-1.30	-29.79	-0.62	-0.24	5.82	38.645	0:00	1.39E+04	1074.33	0.0690	18.181	possibly
2005	20-Sep	6:20	in	30.64	17.22	-24.57	6.20	-0.32	8.45	18.9021	0:07	5.30E+04	446.29	0.0160	25.471	no
2005	20-Sep	7:30	out	30.43	17.21	-24.32	6.19	-0.15	8.46	13.8465	0:10	4.91E+04	448.79	0.0170	25.34	no
2005	21-Sep	3:55	out	26.27	16.56	-19.49	5.98	-0.31	8.81	2.17987	0:00	6.70E+04	293.22	0.0270	22.621	possibly
2005	21-Sep	9:15	in	25.04	16.27	-18.10	5.88	-0.31	8.92	117.817	1:15	2.68E+04	789.84	0.0320	21.78	no
2005	21-Sep	15:00	out	23.61	15.88	-16.50	5.74	-0.31	9.05	149.505	0:00	1.73E+04	4041.23	0.0390	20.779	yes
2005	21-Sep	17:20	in	22.95	15.68	-15.77	5.67	-0.31	9.11	179.48	1:00	4.68E+04	1029.20	0.0430	20.315	yes
2005	30-Sep	10:37	out	39.08	6.40	-38.48	2.15	-0.28	6.66	112.76	0:00	3.66E+04	357.93	0.0150	26.038	no
2005	30-Sep	13:10	in	39.25	6.63	-38.61	2.24	-0.28	6.68	25.7186	0:08	1.39E+04	1202.24	0.0150	26.227	no
2005	01-Oct	1:10	in	39.98	7.74	-39.13	2.64	-0.28	6.79	26.9277	0:23	2.06E+04	840.28	0.0130	27.102	no
2005	02-Oct	7:15	out	41.07	10.34	-39.58	3.58	-0.29	7.03	40.9075	0:06	1.18E+04	1299.96	0.0100	28.8	no
2005	02-Oct	10:10	in	41.12	10.58	-39.56	3.67	-0.29	7.05	42.5999	0:10	9.27E+03	1653.50	0.0100	28.927	no
2005	02-Oct	18:05	out	41.20	11.21	-39.45	3.90	-0.29	7.12	5.93194	0:38	1.12E+04	1334.83	0.0090	29.236	no
2005	02-Oct	20:00	in	41.21	11.36	-39.41	3.95	-0.29	7.13	15.6591	0:48	1.01E+04	1459.53	0.0090	29.303	no
2005	03-Oct	3:10	out	41.21	11.90	-39.23	4.15	-0.29	7.19	65.5417	0:16	1.57E+04	1288.93	0.0090	29.527	no
2005	03-Oct	9:24	in	41.17	12.37	-39.02	4.32	-0.29	7.24	21.2304	0:00	2.40E+04	832.41	0.0090	29.691	no
2005	03-Oct	17:45	out	41.03	12.95	-38.66	4.53	-0.29	7.03	135.806	1:57	1.72E+04	1365.09	0.0080	29.853	no
2005	10-Oct	2:00	in	21.69	15.17	-14.52	5.43	-0.29	9.20	126.505	0:01	1.87E+05	176.44	0.0530	19.373	yes
2005	10-Oct	4:06	out	21.12	14.98	-13.90	5.37	-0.29	9.26	69.7332	0:06	1.59E+05	169.68	0.0580	18.961	yes
2005	10-Oct	6:10	in	20.49	14.75	-13.21	5.29	-0.29	9.33	117.953	0:04	1.20E+05	236.58	0.0640	18.499	no
2005	10-Oct	6:40	out	20.32	14.68	-13.02	5.26	-0.29	9.34	64.6356	0:04	9.59E+04	301.59	0.0660	18.372	possibly
2005	10-Oct	11:05	in	18.98	14.17	-11.58	5.08	-0.29	9.50	7.62321	0:00	5.40E+05	62.58	0.0830	17.385	no
2005	10-Oct	11:15	out	18.93	14.14	-11.52	5.08	-0.28	9.50	21.4184	0:00	1.43E+05	219.70	0.0840	17.346	possibly
2005	10-Oct	11:40	in	18.80	14.09	-11.38	5.06	-0.28	9.52	3.55699	0:00	1.11E+05	397.95	0.0860	17.246	possibly
2005	15-Oct	5:50	out	28.45	-2.00	-28.36	-0.90	-0.32	5.71	25.4388	0:05	4.12E+04	516.31	0.0850	17.319	possibly
2005	15-Oct	6:25	out	28.56	-1.94	-28.48	-0.88	-0.32	5.72	4.44263	0:05	5.38E+04	382.46	0.0830	17.39	possibly
2005	15-Oct	9:45	in	29.21	-1.60	-29.15	-0.76	-0.32	5.77	123.449	0:00	5.12E+04	330.35	0.0760	17.796	possibly
2005	15-Oct	16:40	in	30.48	-0.89	-30.46	-0.51	-0.33	5.87	32.5153	0:35	7.83E+04	279.04	0.0620	18.635	yes
2005	15-Oct	17:15	out	30.58	-0.83	-30.57	-0.49	-0.33	5.88	32.4848	0:35	7.83E+04	279.04	0.0610	18.705	yes
2005	15-Oct	20:25	in	31.12	-0.51	-31.11	-0.38	-0.33	5.93	30.232	0:00	2.12E+05	77.90	0.0560	19.076	yes

Year	Date	Time UT	in/out	Rs	Rx (Rs)	Ry (Rs)	Rz (Rs)	Mlat (°)	LT	Shear (°)	Width (hh:mm)	N (m^{-3})	T (eV)	D_P (nPa)	r0 (Rs)	Energisation?
2005	16-Oct	20:50	in	34.74	2.02	-34.67	0.52	-0.35	6.23	5.17994	0:04	2.38E+04	623.24	0.0310	21.883	yes
2005	20-Oct	22:15	in	40.74	10.99	-39.05	3.72	-0.37	7.10	124.566	0:00	1.43E+05	140.55	0.0100	28.879	no
2005	20-Oct	23:15	out	40.74	11.07	-39.03	3.74	-0.37	7.11	168.764	0:00	1.79E+04	956.22	0.0100	28.912	no
2005	21-Oct	5:50	in	40.72	11.58	-38.84	3.93	-0.37	7.17	122.091	0:23	3.78E+04	511.51	0.0090	29.11	yes
2005	21-Oct	6:30	out	40.72	11.62	-38.82	3.94	-0.37	7.17	107.927	0:00	2.59E+04	517.55	0.0090	29.125	possibly
2005	24-Oct	23:22	in	35.18	16.36	-30.64	5.69	-0.38	7.97	13.5976	0:05	2.41E+04	761.30	0.0110	27.823	possibly
2005	24-Oct	23:44	out	35.14	16.37	-30.57	5.69	-0.38	7.97	120.979	0:05	2.60E+04	683.98	0.0110	27.794	no
2005	25-Oct	2:05	in	34.86	16.42	-30.22	5.71	-0.38	8.00	70.2739	0:00	2.64E+05	83.41	0.0120	27.651	no
2005	25-Oct	10:30	out	33.74	16.59	-28.82	5.78	-0.38	8.09	0.684713	0:18	1.87E+04	1043.70	0.0130	27.059	yes
2005	25-Oct	22:35	in	31.94	16.70	-26.60	5.83	-0.38	8.24	29.2865	0:20	1.24E+05	159.60	0.0150	26.037	possibly
2005	25-Oct	22:55	out	31.88	16.70	-26.53	5.83	-0.38	8.25	30.2275	0:20	1.23E+05	159.84	0.0150	26.006	possibly
2005	26-Oct	2:20	in	31.32	16.70	-25.86	5.83	-0.38	8.29	56.8497	0:10	5.76E+04	338.23	0.0160	25.675	possibly
2005	26-Oct	3:50	out	31.07	16.69	-25.55	5.83	-0.38	8.31	69.4456	0:08	4.11E+04	529.46	0.0160	25.525	possibly
2005	26-Oct	5:00	in	30.87	16.69	-25.31	5.83	-0.38	8.33	87.4434	1:00	7.73E+04	460.16	0.0170	25.405	yes
2005	26-Oct	11:55	out	29.63	16.62	-23.84	5.82	-0.38	8.43	41.3387	0:10	6.02E+04	389.13	0.0190	24.647	possibly
2005	26-Oct	13:48	in	29.24	16.59	-23.38	5.81	-0.38	8.46	86.4426	0:12	1.08E+05	280.35	0.0200	24.402	no
2005	19-Nov	15:42	in	47.32	12.18	-45.52	4.18	-0.20	7.05	84.6591	0:08	2.55E+04	718.27	0.0050	33.215	no
2005	19-Nov	16:55	out	47.21	12.24	-45.40	4.20	-0.20	7.06	48.7813	0:00	1.10E+04	1175.69	0.0050	33.176	possibly
2005	20-Nov	1:50	in	46.22	12.72	-44.21	4.37	-0.20	7.13	5.25412	0:16	1.55E+04	993.96	0.0060	32.801	no
2005	20-Nov	3:45	out	45.99	12.82	-43.94	4.40	-0.20	7.14	139.794	0:17	3.62E+04	457.28	0.0060	32.714	yes
2005	20-Nov	5:48	in	45.74	12.94	-43.64	4.44	-0.21	7.16	131.104	0:33	1.55E+04	977.11	0.0060	32.614	no
2005	20-Nov	9:11	out	45.37	13.09	-43.20	4.50	-0.21	7.19	37.3486	0:13	1.77E+04	959.97	0.0060	32.465	no
2005	20-Nov	20:40	in	43.90	13.66	-41.45	4.70	-0.21	7.28	5.73651	0:50	1.15E+04	1225.35	0.0060	31.847	no
2005	01-Dec	23:50	out	35.77	-13.23	-32.90	-4.68	0.01	4.46	25.7427	0:11	1.11E+05	157.52	0.0900	17.079	possibly
2005	02-Dec	2:20	in	36.23	-13.13	-33.44	-4.65	0.00	4.49	5.32104	0:10	4.54E+04	548.75	0.0850	17.29	possibly
2005	02-Dec	6:00	out	36.88	-12.99	-34.20	-4.60	0.00	4.54	17.7443	0:10	2.97E+04	593.92	0.0790	17.602	possibly
2005	02-Dec	18:53	in	39.04	-12.41	-36.74	-4.40	-0.02	4.69	8.13699	0:02	1.13E+05	194.13	0.0610	18.726	no
2005	03-Dec	22:40	out	43.05	-10.94	-41.44	-3.90	-0.04	4.96	5.52563	0:03	8.20E+04	342.23	0.0360	21.179	possibly
2005	04-Dec	11:32	in	44.67	-10.16	-43.34	-3.64	-0.06	5.07	73.0126	0:08	6.11E+04	329.03	0.0290	22.316	possibly
2005	04-Dec	14:10	out	44.93	-10.01	-43.67	-3.59	-0.06	5.08	145.197	0:10	4.39E+04	480.35	0.0280	22.523	possibly

Year	Date	Time UT	in/out	Rs	Rx (Rs)	Ry (Rs)	Rz (Rs)	Mlat (°)	LT	Shear (°)	Width (hh:mm)	N (m^{-3})	T (eV)	D_P (nPa)	r0 (Rs)	Energisation?
2005	04-Dec	20:15	in	45.63	-9.64	-44.45	-3.46	-0.06	5.13	142.311	0:00	3.72E+04	411.31	0.0250	23.025	no
2005	04-Dec	22:30	out	45.87	-9.48	-44.78	-3.40	-0.06	5.15	138.819	0:10	3.72E+04	562.13	0.0240	23.242	no
2005	04-Dec	23:37	in	46.01	-9.41	-44.90	-3.38	-0.07	5.16	160.591	0:03	2.93E+04	655.76	0.0240	23.325	no
2005	05-Dec	1:55	out	46.25	-9.27	-45.18	-3.33	-0.07	5.18	41.8718	0:06	1.87E+05	300.05	0.0230	23.512	no
2005	05-Dec	3:30	in	46.41	-9.16	-45.37	-3.30	-0.07	5.19	16.4334	0:00	1.50E+04	1299.76	0.0230	23.643	no
2005	05-Dec	8:58	out	46.97	-8.80	-46.02	-3.17	-0.07	5.23	33.2164	0:58	2.11E+04	1067.76	0.0210	24.093	no
2005	15-Dec	12:30	in	49.97	8.91	-49.09	2.93	-0.21	6.72	33.4519	0:15	5.08E+04	331.91	0.0050	33.382	no
2005	16-Dec	7:45	out	48.45	10.18	-47.25	3.37	-0.23	6.85	76.3097	0:02	3.29E+04	480.13	0.0050	33.033	no
2005	16-Dec	17:47	in	47.56	10.79	-46.18	3.58	-0.23	6.92	7.65086	0:02	2.31E+04	892.02	0.0060	32.777	no
2005	16-Dec	20:42	out	47.29	10.97	-45.86	3.64	-0.23	6.92	117.02	0:10	2.57E+04	750.29	0.0060	32.693	no
2005	16-Dec	21:55	in	47.16	11.05	-45.70	3.67	-0.23	6.95	108.429	0:00	1.09E+04	709.26	0.0060	32.652	no
2005	17-Dec	21:24	in	44.63	12.40	-42.67	4.14	-0.25	7.14	133.109	0:00	2.99E+04	524.19	0.0060	31.747	yes
2005	31-Dec	15:00	out	42.32	-11.58	-40.52	-4.05	-0.04	4.88	107.927	0:09	2.30E+05	84.87	0.0410	20.584	possibly
2005	31-Dec	19:10	in	42.75	-11.34	-41.03	-3.97	-0.04	4.91	76.8214	0:00	3.04E+05	57.15	0.0380	20.881	possibly
2005	24-Feb	0:26	out	39.10	12.00	-39.23	4.99	0.07	7.01	105.054	0:02	5.34E+04	188.93	0.0090	29.639	yes
2005	19-Apr	22:25	out	35.07	6.82	-34.33	-2.20	-7.52	6.61	76.7153	1:05	1.46E+05	151.64	0.0210	23.943	no
2005	20-Apr	2:12	in	35.53	7.30	-34.68	-2.22	-7.76	6.65	2.0421	0:10	3.15E+04	766.02	0.0200	24.388	no
2005	06-May	18:34	in	30.35	2.07	-30.21	-2.00	-4.96	6.15	119.776	0:02	2.16E+05	71.43	0.0500	19.587	no
2005	06-May	18:54	out	30.40	2.11	-30.26	-2.00	-4.98	6.15	5.31762	0:06	8.51E+04	114.12	0.0500	19.626	no
2005	18-Jul	17:30	out	30.81	1.19	-30.66	-2.80	-5.66	6.01	33.7594	0:00	2.65E+04	263.43	0.0510	19.515	no
2005	17-Oct	0:48	out	35.23	2.43	-35.13	0.66	-0.35	6.27	92.2305	0:00	1.50E+05	146.79	0.0290	22.306	possibly
2005	03-Nov	18:30	out	37.32	-13.04	-34.65	-4.67	0.05	4.55	10.157	0:06	2.46E+04	893.43	0.0760	17.772	possibly
2005	17-Dec	9:30	out	45.96	11.74	-44.27	3.91	-0.24	7.04	75.9863	0:18	8.67E+03	1581.57	0.0060	32.246	possibly
2005	17-Dec	11:00	in	45.80	11.82	-44.07	3.94	-0.24	7.05	20.6708	0:01	1.09E+04	1445.92	0.0060	32.188	possibly
2005	17-Dec	11:40	out	45.73	11.86	-43.98	3.95	-0.24	7.06	2.18606	0:04	1.24E+04	1286.35	0.0060	32.162	no
2005	17-Dec	13:00	in	45.58	11.94	-43.81	3.98	-0.24	7.07	173.899	0:01	2.33E+04	581.11	0.0060	32.108	no
2005	17-Dec	15:30	out	45.30	12.08	-43.47	4.03	-0.24	7.09	10.0622	0:10	1.27E+04	1203.26	0.0060	32.005	possibly
2005	31-Dec	8:58	out	41.67	-11.92	-39.71	-4.16	-0.04	4.82	15.2501	0:52	5.82E+04	304.85	0.0450	20.134	possibly
2005	31-Dec	9:40	in	41.75	-11.88	-39.80	-4.15	-0.04	4.83	44.0548	0:00	2.01E+04	772.06	0.0440	20.183	no
2006	01-Jan	14:50	out	44.54	-10.13	-43.23	-3.56	-0.06	5.07	115.928	0:02	2.37E+04	669.11	0.0290	22.268	possibly

Year	Date	Time UT	in/out	Rs	Rx (Rs)	Ry (Rs)	Rz (Rs)	Mlat (°)	LT	Shear (°)	Width (hh:mm)	N (m^{-3})	T (eV)	D_P (nPa)	r0 (Rs)	Energisation?
2006	08-Jan	11:20	in	46.36	2.31	-46.29	0.66	-0.17	6.20	114.128	0:16	3.61E+04	424.30	0.0100	28.468	no
2006	08-Jan	15:55	out	46.08	2.67	-46.00	0.78	-0.17	6.23	136.217	0:01	5.12E+04	284.15	0.0100	28.466	possibly
2006	08-Jan	22:15	in	45.67	3.17	-45.55	0.95	-0.17	6.28	143.987	0:00	1.05E+04	1583.50	0.0100	28.444	no
2006	24-Jan	22:55	out	49.97	-29.70	-38.91	-10.04	0.10	3.41	8.70062	0:55	1.35E+04	1229.29	0.0800	17.574	possibly
2006	26-Jan	3:40	in	53.72	-29.88	-43.49	-10.11	0.08	3.60	149.711	0:02	1.86E+04	931.39	0.0570	19.048	yes
2006	26-Jan	5:55	out	54.00	-29.88	-43.83	-10.11	0.08	3.62	1.74204	0:02	5.99E+04	300.28	0.0550	19.166	possibly
2006	29-Jan	19:10	in	62.16	-28.48	-54.41	-9.64	0.04	4.07	45.3325	0:03	5.77E+04	419.11	0.0220	23.689	possibly
2006	30-Jan	13:05	out	63.40	-27.91	-56.14	-9.46	0.03	4.15	39.5299	0:19	3.18E+04	516.23	0.0190	24.596	yes
2006	31-Jan	1:03	in	64.14	-27.49	-57.20	-9.32	0.02	4.21	85.9451	0:21	1.27E+04	1146.19	0.0170	25.183	possibly
2006	31-Jan	8:15	out	64.56	-27.22	-57.81	-9.22	0.02	4.24	54.9543	0:15	2.04E+04	948.72	0.0160	25.533	possibly
2006	31-Jan	15:58	in	65.00	-26.92	-58.43	-9.12	0.00	4.26	62.5854	0:26	1.45E+04	982.77	0.0150	25.899	possibly

References

Achilleos N., C. S. Arridge, C. Bertucci, M. K. Dougherty, K. K. Khurana, M. E. Burton, C. T. Russell, E. J. Smith, B. T. Tsurutani (2005), Properties of Saturn's magnetopause II: time-dependent morphology and dynamics, *Eos Trans. AGU*, 86(52), Jt. Assem. Suppl., Abstract P43A-0492.

Acuña M. A. and N. F. Ness (1980), The magnetic field of Saturn: Pioneer 11 observations, *Science, 207*, 4429, 444-446.

Acuña, M. A., N. F. Ness, and J. E. P. Connerney (1980), *J. Geophys. Res., 85*, A11, 5675-5678.

Acuña, M. A, J. E. P. Connerney and N. F. Ness (1983), The Z3 zonal harmonic model of Saturn's magnetic field: Analyses and implications, *J. Geophys. Res., 88*, A11, 8771-8778.

Anderson B. J., T.-D. Phan and S. A. Fuselier (1997), Relationships between plasma depletion and subsolar reconnection, *J. Geophys. Res., 102*, A5, 9531-9542.

André, N. et al. (2006), Plasma Dynamics in the Outer Magnetosphere of Saturn, *EGU Geophysical Res. Abstracts,* Vienna, Austria, 8, 05212.

Arridge C. S., N. Achilleos, C. Bertucci, M. K. Dougherty and K. K. Khurana (2006a), Modelling the size and shape of Saturn's magnetopause with variable dynamic pressure, *J. Geophys. Res., 111,* A11, A11227.

Arridge C. S., N Achilleos, M. K. Dougherty, K. K. Khurana, C. T. Russell, D. J. Southwood and the Cassini MAG team (2006b), The Configuration of Saturn's Magnetosphere as Observed by the Cassini Magnetometer, *Eos Trans. AGU*, 87(36), Jt. Assem. Suppl., Abstract P43B-06.

Arridge C. S., C.T. Russell, K.K. Khurana, M.K. Dougherty (2006c), The Mass of Saturn's Magnetodisc, *Geophys. Res. Lett., submitted.*

Badman S. V., E. J. Bunce, J. T. Clarke, S. W. H. Cowley, J-C. Gérard, D. Grodent and S. E. Milan (2005), Open flux estimates in Saturn's magnetosphere during the January 2004 Cassini-HST campaign, and implications for reconnection rates, *J. Geophys. Res., 110*, A11, A11216.

Bagenal, F. (1992), Giant planet magnetospheres, *Ann. Rev. Earth Planet. Sci., 20*, 289-328.

Bame, S. J., J.R. Asbridge, H. E. Felthauser, J.P. Glore, H.L. Hawk, J. Chavez (1978), SEE-C solar wind plasma experiment, *IEE Trans. Geosci. Electron. GE-16,* 216–220.

Baumjohann, W. and R. A. Treumann (1997), *Basic Space Plasma Physics*, Imperial College Press, London.

Bavassano Cattaneo M. B., C. Basile, G. Moreno and J. D. Richardson (1998), Evolution of mirror structures in the magnetosheath of Saturn from the bow shock to the magnetopause, *J. Geophys. Res., 103*, A6, 11,961-11,972.

Behannon K. W., R. P. Lepping and N. F. Ness (1983), Structure and dynamics of Saturn's outer magnetosphere and boundary regions, *J. Geophys. Res., 88*, A11, 8791-8800.

Berchem J. and C. T. Russell (1982), Magnetic field rotation through the magnetopause – ISEE 1 and 2 observations, *J. Geophys. Res., 87* ,8139-8148.

Blanc M. et al. (2002), *Space Science Reviews, 104*, 253–346.

Bogdanova Y. V, C. J. Owen, A. N. Fazakerley, B. Klecker, and H. Rème (2006), Statistical study of the location and size of the electron edge of the Low-Latitude Boundary Layer as observed by Cluster at mid-altitudes, *Annales Geophys.*, 24, 10, 2645-2665

Bridge H.S., J. W. Belcher, R. J. Butler, A. J. Lazarus, A. M. Mavretic, J. D. Sullivan, G. L. Siscoe and V. M. Vasyliunas (1977), The plasma experiment on the 1977 Voyager mission, *Space Science Reviews, 21,* 259.

Bridge, H. S. et al. (1981), Plasma observations near Saturn: Initial results from Voyager 1, *Science, 212,* 4491, 217-224.

Bridge, H. S. et al. (1982), Plasma observations near Saturn: Initial results from Voyager 2, *Science, 215,* 4532, 563-570.

Bryant D. A. and S. Riggs (1989), At the edge of the Earth's magnetosphere, *Phil. Trans. R. Soc. Lond., A*, 328, 43-56.

Bunce E. J., S. W. H. Cowley and J. A. Wild (2003), Azimuthal magnetic fields in Saturn's magnetosphere: effects associated with plasma sub-corotation and the magnetopause-tail current system, *Annales Geophys, 21*, 1-14.

Bunce E. J., S. W. H. Cowley and S. E. Milan (2005), Interplanetary magnetic field control of Saturn's polar cusp aurora, *Annales Geophys.,, 23,* 1405-1431.

Carbary J. F. and S. M. Krimigis (1982), Charged particle periodicity in the Saturnian magnetosphere, *Geophys. Res. Lett., 9,* 1073-1076.

Carbary J. F., S. M. Krimingis and W. –H. Ip (1983), Energetic particles microsiagntures of Saturn's satellites, *J. Geophys. Res., 88,* A11, 8947-8958.

Chapman, S. and V.C.A Ferraro (1931), A new theory of magnetic storms: Part I – The initial phase, *Terr.Magn.Atmos. Electr., 36,* 171, 77-97.

Chenette D. L. and E. C. Stone (1983), The Mimas ghost revisited: An analysis of the electron flux and electron microsignatures observed in the vicinity of Mimas at Saturn, *J. Geophys. Res., 88,* A11, 8755-8764.

Clarke K. E., N. André, D. J. Andrews, A. J. Coates, S. W. H. Cowley, M. K. Dougherty, G. R. Lewis, H. J. McAndrews, J. D. Nichols, T. R Robinson, D. M. Wright (2006), Cassini observations of planetary-period oscillations of Saturn's magnetopause, *Geophys. Res. Lett., 33,* 23, L23104.

Clarke J. T., et al. (2005), Morphological differences between Saturn's ultraviolet aurorae and those of Earth and Jupiter, *Nature, 433,* 717-719.

Coates A. J., C. Alsop, A. J. Coker, D. R. Linder, A. D. Johnstone, R. D. Woodliffe, M. Grande, A. Preece, M. S. Burge, D.S. Hall (1992), The Electron Spectrometer for the Cassini spacecraft, *British Interplanetary Society, 45,* 9, 387-392.

Coates A. J., et al. (2005), Plasma electrons above Saturn's main rings: CAPS observations, *Geophys. Res. Lett, 32,* L14S09.

Connerney J. E. P., M. A. Acuña and N. F. Ness (1983), Currents in Saturn's magnetosphere, *J. Geophys. Res., 88,* A11, 8779-8789.

Connerney, J. E. P (1993), Magnetic fields of the outer planets, *J. Geophys. Res, 98,* E10, 18,659 – 18,679.

Cowley S. W. H. (1976), Comments on the merging of non antiparallel magnetic fields *J. Geophys. Res, 81,* 3455-3458.

Cowley S. W. H (1984), Evidence for the occurrence and importance of reconnection between the Earth's magnetic field and the interplanetary magnetic field, *Magnetic reconnection in space and laboratory plasmas,* Geophysical Monograph 30. E. W. Hones.

Cowley S. W. H. (1995), Theoretical perspectives of the magnetopause: A tutorial review, *Physics of the Magnetopause*, Geophysical Monograph 90, P. Song, B. U. Ö. Sonnerup, M. F. Thomsen., 29-44.

Cowley, S. W. H. (1996), A Beginner's Guide to the Earth's Magnetosphere, *Earth in Space, 8,* 9.

Cowley S.W. H. and C. J. Owen (1989), A simple illustrative model of open flux tube motion over the dayside magnetopause, *Planet. Space Sci., 37,* 11, 1461-1475.

Cowley S. W. H., E. J. Bunce and R. Prangé (2004), Saturn's polar ionospheric flows and their relation to the main auroral oval, *Annales Geophys., 22,* 1379-1394.

Cowley S. W. H., S. V. Badman, E. J. Bunce, J. T. Clarke, J-C. Gérard, D. Grodent, C. M. Jackman, S. E. Milan and T. K. Yeoman (2005), Reconnection in a rotation-dominated magnetosphere and its relation to Saturn's auroral dynamics, *J. Geophys. Res., 110,* A02201.

Crary F. J., et al (2005), Solar wind dynamic pressure and electric field as the main factors controlling Saturn's aurorae, *Nature, 433.*

Crooker N. U, T. E. Eastman and G. S. Stiles (1979), Observations of plasma depletion in the magnetosheath at the dayside magnetopause, *J. Geophys. Res., 84,* A3, 869-874.

Crooker N. U. J. G. Luhmann, C. T. Russell, E. J. Smith, J. R. Spreiter and S. S. Stahara (1985), Magnetic field draping against the dayside magnetopause, *J. Geophys. Res., 90,* A4, 3505-3510.

Davis Jr., L. and E. J. Smith (1990), A model of Saturn's magnetic field based on all available data, *J. Geophys. Res., 95,* A9, 15,257-15,261.

De Hoffmann F. and E. Teller (1950), Magnetohydrodynamic shock, *Phys. Rev, 80,* 4, 692–703.

De Keyser J., et al. (2005), Magnetopause and boundary layer, *Space Sci. Rev., 118,* 231-320.

Dougherty M. K., et al. (2004), The Cassini magnetic field investigation, *Space Science Reviews, 114,* 331-383.

Dougherty M. K. et al. (2005), Cassini magnetometer observations during Saturn orbit insertion, *Science, 307,* 5713, 1266-1270.

Dougherty M. K., K. K. Khurana, F. M. Neubauer, C. T. Russell, J. Saur, J. S Leisner and M. E. Burton (2006), Identification of a dynamic atmosphere at Enceladus with the Cassini Magnetometer, *Science, 311,* 5766, 1406-1409.

Dungey J. W. (1961), Interplanetary magnetic field and the auroral zones, *Phys. Rev. Lett., 6,* 48–49.

Dungey J. W. (1963), The structure of the exosphere or adventures in velocity space, *The Earth's Environment,* edited by C. DeWitt, J. Hieblot, and A. Lebeau, Gordon and Breach, New York, 505–550.

Eastman T. E., E. W. Hones Jr., S. J. Bame and J. R. Asbridge (1976), The magnetospheric boundary layer: Site of plasma, momentum and energy transfer from the magnetosheath into the magnetosphere, *Geophys. Res. Lett., 11,* 685-688.

Eastman T. E. and E. W. Hones Jr. (1979), Characteristics of the magnetopause boundary layer and magnetopause layer as observed by Imp 6, *J. Geophys. Res., 84*, A5, 2019-2028.

Eastman T. E., S. A. Fuselier and J. T.Gosling (1996), Magnetopause crossings without a boundary layer, *J. Geophys. Res., 101*, 49-58.

Espinosa S. A and M. K. Dougherty (2000), Periodic perturbations in Saturn's magnetic field, *Geophys. Res. Lett., 27*, 17, 2785-2788.

Espinosa S. A., D. J. Southward and M. K. Dougherty (2003a), Reanalysis of Saturn's magnetospheric field data view of spin-periodic perturbations, *J. Geophys. Res., 108*, A2.

Espinosa S. A, D. J. Southward and M. K. Dougherty (2003b), How can Saturn impose its rotation period in a noncorotating magnetosphere?, *J. Geophys. Res., 108*, A2.

Espositio L. W., et al. (2005), Ultraviolet imaging spectroscopy shows an active Saturnian system, *Science, 307,* 5713, 1251-1255.

European Space Agency (1993), *The radiation design handbook*, ESA PSS-01-609, Netherlands.

Farrugia C. J., H. K. Biernat and N. V. Erkaev (1998), The effect of the magnetopause shapes of Jupiter and Saturn on magnetosheath parameters, *Planet Space Sci., 46*, 5, 507-514.

Feldman W. C. et al. (1982), Electron heating within the Earth's bow shock, *Phys. Rev. Lett., 49*, 3, 199-201.

Fuselier S. A., B. J. Anderson and T. G. Onsager (1995), Particle signatures of magnetic topology at the magnetopause: AMPTE/CCE observations, *J. Geophys. Res., 100*, A7, 11,805-11,821.

Frank L. A., B. G. Burek, K. L. Ackerson, J. H. Wolfe and J. D. Mihalov (1980), Plasma's in Saturn's magnetosphere, *J. Geophys. Res., 85*, A11, 5696-5708.

Giampieri, G. and M. K. Dougherty (2004), Rotation rate of Saturn's interior from magnetic field observations, *Geophys. Res. Lett., 31*, L16701.

Gombosi T. I. and K. C. Hansen (2005), Saturn's variable magnetosphere, *Science, 307*, 5713, 1224-1226.

Gosling J. T., J. R. Asbridge, S. J. Bame, W. C. Feldman, G. Paschmann, N. Sckopke and C. T. Russell (1982), Evidence for quasi-stationary reconnection at the dayside magnetopause, *J. Geophys. Res., 87*, A4, 2147-2158.

Gosling J. T., M. F. Thomsen, S. J. Bame, T. G. Onsager and C. T. Russell (1990), The electron edge of the low latitude boundary layer during accelerated flow events, *Geophys. Res. Lett., 17*, 11, 1833-1836.

Gurnett D. A., et al. (2004), The Cassini Radio and Plasma Wave Investigation, *Space Science Reviews, 114,* 1, 395 – 463.

Gurnett D.A., et al. (2005), Radio and plasma wave observations at Saturn from Cassini's approach and first orbit, *Science, 207*, 1255-1259.

Haerendel G., G. Paschmann, N. Sckopke, H. Rosenbauer and P. C. Hedgecock (1978), The frontside boundary layer of the magnetopause and the problem of reconnection, *J. Geophys. Res., 83,* A7, 3195-3216.

Hall D. S., C. P. Chaloner, D. A. Bryant, D. R. Lepine and V. P. Tritakis (1991), Electrons in the boundary layers near the dayside magnetopause, *J. Geophys. Res., 96*, A5, 7869-7891.

Hansen K. C., A. J. Ridley, G. B. Hospodarsky, N. Achilleos, M. K. Dougherty, T. I. Gombosi, G. (2005), Global MHD simulations of Saturn's magnetosphere at the time of Cassini approach, *Geophys. Res. Lett., 32*, L20S06.

Hapgood M. A. (1992), Space Physics coordinate transforms: A user guide, *Planet. Space Sci., 40*, 5, 711-717.

Hapgood M. A. and D. A. Bryant (1990), Re-ordered electron data in the low-latitude boundary layer, *Geophys. Res. Lett., 17,* 11, 2043-2046.

Hapgood M. A. and D. A. Bryant (1992), Exploring the magnetospheric boundary layer, *Planet. Space Sci., 40*, 10, 1431-1459.

Hartle, R. E., E. C. Sittler Jr., F.M. Neubauer, R. E. Johnson, H. T. Smith, F. Crary, D. J. McComas, D. T. Young, A. J. Coates, D. Simpson, S. Bolton, D. Reisenfeld, K. Szegö, J.-J. Berthelier, A. M. Rymer, J. Vilppola, J. Steinberg, and N. André (2006), Preliminary interpretation of Titan plasma interaction as observed by the Cassini Plasma Spectrometer: Comparisons with Voyager 1, *Geophys. Res. Lett.* L08201.

Hill T. W., A. J. Dessler, C. K. Goertz (1983), Magnetospheric models (Jovian phenomena), *Physics of Jovian magnetosphere*, edited by A. J. Dessler, 353-394.

Hood L. L. (1983), Radial diffusion in Saturn's radiation belts: a modelling analysis assuming satellite and ring E absorption, *J. Geophys. Res., 88*, A2, 808-818.

Huddleston, D. E., C. T. Russell, G. Le and A. Szabo (1997), Magnetopause structure and the role of reconnection at the outer planets, *J. Geophys. Res., 102*, A11, 24,289-24,302.

Jackman, C.M., N. Achilleos, E. J. Bunce, S. W. H. Cowley, M. K. Dougherty, G. H. Jones, S. E. Milan and E. J. Smith (2004), Interplanetary magnetic field at ~ 9 AU during the declining phase of the solar cycle and its implications for Saturn's magnetospheric dynamics, *J. Geophys. Res., 109,* A11203.

Johnstone A.D., et al. (1997), PEACE: A plasma electron and current experiment, *Space Science Reviews, 79,* 1 - 2, 351 – 398.

Jones G. H., E. Roussos, N. Krupp, C. Paranicas, J. Woch, A. Lagg, D. G. Mitchell, S. M. Krimigis, M. K. Dougherty (2006), Enceladus' Varying Imprint on the Magnetosphere of Saturn, *Science, 311,* 5766, 1412 – 1415.

Khrabrov A. V. and B. U. Ö. Sonnerup (1998), DeHoffmann-Teller analysis, in *Analysis Methods for Multi-Spacecraft Data,* edited by G. Paschmann and P. W. Daly, 241-246.

Kivelson M. G. and C. T. Russell (1995), *Introduction to Space Physics*, Cambridge University Press.

Kivelson M. G. (2006), Does Enceladus Govern Magnetospheric Dynamics at Saturn?, *Science, 311,* 5766, 1391 – 1392.

Kivelson M. G., K. K. Khurana, and R. J. Walker (2002), Sheared magnetic field structure in Jupiter's dusk magnetosphere: Implications for return currents, *J. Geophys. Res., 107,* A7, 1116.

Kivelson M. G. and D. J. Southwood (2005), Dynamical consequences of two modes of centrifugal instability in Jupiter's outer magnetosphere, *J. Geophys. Res. 110,* A12209.

Krimigis S. M., T. P. Armstrong, W. I. Axford, C. O. Bostrom, C. Y. Fan, G. Gloeckler, L. J. Lanzerotti (1977), The Low Energy Charged Particle (LECP) experiment on the Voyager spacecraft, *Space Science Reviews, 21,* 3, 329 – 354.

Krimigis, S. M., T. P., Armstrong, W. I. Axford, C. O Bostrom, G. Gloekler, E. P. Keath, L. J. Lanzerotti, J. F. Carbary, D. C. Hamilton and E. C. Roelof (1981), Low-energy charged particles in Saturn's magnetosphere - Results from Voyager 1, *Science, 212,* 225-231.

Krimigis S. M. et al. (1982), Low-energy hot plasma and particles in Saturn's magnetosphere, *Science, 215*, 4532, 571-577.

Krimigis S. M., J. F. Carbary, E. P Keath, T. P. Armstrong, L. J. Lanzerotti and G. Gloeckler (1983), General characteristics if hot plasma and energetic particle sin the Saturnian magnetosphere: results from the Voyager spacecraft, *J. Geophys. Res., 88,* A11, 8871-8892.

Krimigis S. M. et al. (2004), Magnetosphere Imaging Instrument (MIMI) on the Cassini mission to Saturn/Titan, Space *Science Reviews, 114,* 233–329.

Krupp et al. (2005), The Saturnian plasma sheet as revealed by energetic particle measurements, *Geophys. Res. Lett., 32,* L20S03.

Krupp N., J. Woch, A. Lagg, S. Livi, D. G. Mitchell, S. M. Krimigis, M. K. Dougherty, P. G. Hanlon, T. P. Armstrong, and S. A. Espinosa (2004), Energetic particle observations in the vicinity of Jupiter: Cassini MIMI/LEMMS results, *J. Geophys. Res., 109,* A09S10.

Kurth W. S., A. Lecacheux , T. F. Averkamp , J. B. Groene , and D. A. Gurnett (2006), A Saturnian Longitude System Based on a Variable Kilometric Radiation Period, *Geophys. Res. Lett., in press.*

Lavraud B., M. F. Thomsen, M. G. G. T. Taylor, Y. L. Wang, T. D. Phan, S. J. Schwartz, R, C. Elphic, A. Fazakerley, H. Reme and A. Balogh (2005), Characteristics of the magnetosheath electron boundary layer under northward interplanetary magnetic field,: Implications for high-latitude reconnection, *J. Geophys. Res., 110,* A06209.

Lee L. C. and Z. F. Fu (1985), A theory of magnetic flux transfer at the Earth's magnetopause, *Geophys. Res. Lett., 12,* 105–108.

Lee, L. C. (1995), A review of magnetic reconnection: MHD models, *Physics of the Magnetopause*, Geophysical Monograph 90, P. Song, B. U. Ö. Sonnerup, M. F. Thomsen., 139-153.

Lepping R. P., L. F. Burlaga and L. W Klein (1981), Surface waves on Saturn's magnetopause, *Nature, 292,* 750-753.

Lepping R. P. (1992), Magnetic boundaries of the outer planets: a review, *Adv. Space Res., 12,* 8, 825-842.

Lewis G. R., N. André, A. J. Coates, L. K. Gilbert, D. R. Linder and A. M. Rymer (2006), *Planet. Space Sci., in preparation.*

Linder D. R., A. J. Coates, R. D. Woodliffe, C. Alsop, A. D. Johnstone, M. Grande, A. Preece, B. Narheim, D. T. Young (1998), The Cassini CAPS electron spectrometer, *Measurement techniques in space plasmas: particles,* Geophysical Monograph 102, Edited by R. F. Pfaff, J. E. Borovsky and D. T. Young.

Longmore M., S. J. Schwartz and E. C. Lucek (2006), Rotation of the magnetic field in Earth's magnetosheath by bulk magnetosheath plasma flow, *Annales Geophys., 24,* 339–354.

Maclennan C. G., L. J. Lanzerotti, S. M. Krimigis and R. P. Lepping (1983), Low-energy particles at the bow shock, magnetopause and outer magnetosphere of Saturn, J. *Geophys. Res., 88*, A11, 8817-8830.

Marcucci, M. F., M. B., Bavassano Cattaneo, A. M. di Lellis, P. Cerulli Irelli, L. M. Kistler, T.-D. Phan, G.Haerendel (2001), IMF-By controlled reconnection at the magnetopause, *Memorie della Società Astronomica Italiana, 72,* N. 3, 614 – 617.

Mauk B.H., S. M. Krimigis, D.G. Mitchell, E. C. Roelof, E. P. Keath J. Dandouras (2001), Imaging Saturn's dust rings using energetic neutral atoms, *Planet. Space Sci., 46*, 9, 1349-1362.

Maurice S., I. M. Engle, M. Blanc, M Skubis (1996), Geometry of Saturn's magnetopause model, J. *Geophys. Res, 101*, A12, 27053-27060.

Maynard N. C. et al. (2004), Observed and simulated depletion layers with southward IMF, *Annales Geophys., 22*, 2151-2169.

McComas D. J. et al. (1998), Ulysses' return to the slow solar wind *Geophys. Res. Lett., 25*, 1-4.

McKibben R. B. and J. A. Simpson (1980), Charged particle diffusion and acceleration in Saturn's radiation belts, *J. Geophys. Res., 85*, A11, 5773-5783.

Mead G. D. and W. N. Hess (1973), Jupiter's radiation belts and the sweeping effect of its satellites, *J. Geophys. Res., 78,* 16,2793 – 16,2811.

Mitchell D. G., F. Kutchko, D. J. Williams, T. E. Eastman, L. A Frank and C. T. Russell (1987), An extended study of the low-latitude boundary layer on the dawn and dusk flanks of the magnetosphere, *J. Geophys. Res., 92,* A7, 7394-7404.

Mogro-Campero A. and W. Fillius (1976), The absorption of trapped particles by the inner satellites of Jupiter and the radial diffusion coefficient of particle transport, *J. Geophys. Res., 81,* 7, 1289-1295.

Morrison D., T. V. Johnson, E. M. Shoemaker, L. A. Soderblom, P. Thomas, J. Veverka, and B. A. Smith (1984), *Saturn,* University of Arizona Press, Tom Gehrels, 609-639.

Neugebauer M., D. R. Clay, B. E. Goldstein and B. T. Tsurutani (1984), A reexamination of rotational and tangential discontinuities in the solar wind, J. *Geophys. Res., 89*, A7, 5395-5408.

Ness N. F., M. A. Acuña, R. P. Lepping, J. E. P. Connerney, K. W. Behannon., L. F. Burlaga and F. M. Neubauer (1981), Magnetic field studies by Voyager 1: preliminary results at Saturn, *Science, 212*, 4491, 211-217.

Ness N. F., M. A. Acuña, K. W. Behannon, L. F. Burlaga, J. E. P. Connerney, R. P. Lepping and F. M. Neubauer (1982), Magnetic field studies by Voyager 2: preliminary results at Saturn, *Science, 215*, 4532, 558-563.

Neugebauer M. et al. (1984), A reexamination of rotational and tangential discontinuities in the solar wind, *J. Geophys. Res., 89*(A7), 5395-5408.

Nykyri K., A. Otto, B. Lavraud, C. Mouikis, L.M. Kistler, A Balogh and H. Rème (2006), Cluster observations of reconnection due to the Kelvin-Helmholtz instability at the dawnside magnetospheric flank, *Annales Geophysicae, 24*, 10, 2619-2643.

Ogilvie K. W., J. D. Scudder and M. Sugiura (1971), Magnetic field and electron observations near the dawn magnetopause, *J. Geophys. Res., 76,* 16, 3574-3586.

Ogilvie K. W., J. T. Steinberg, R. J. Fitzenreiter, C. J. Owen, A. J. Lazarus, W. M. Farrell and R. B. Torbert (1996), Observations of the lunar plasma wake from the WIND spacecraft on December 27, 1994, *Geophys. Res. Lett., 23*, 10, 1255-1258.

Onsager T. G., J. D. Scudder, M. Lockwood and C. T. Russell (2001), Reconnection at the high-latitude magnetopause during northward interplanetary magnetic field conditions, *J. Geophys. Res., 106*, A11, 25,467-25,488.

Otto A. and K. Nykyri (2002), Kelvin-Helmholtz Instability and Magnetic Reconnection: Mass Transport at the LLBL, Geophysical Monograph 133, Earth' s Low-Latitude Boundary Layer, 53.

Paoessa M. and A. F. Cheng (1985), A theory of satellite sweeping, *J. Geophys. Res., 90*, A4, 3428-3434.

Paranicas C. and A. F., Cheng (1997), A model of satellite microsignatures for Saturn, *Icarus, 125*, 380-396.

Paranicas C., et al., (2005), Evidence of Enceladus and Tethys microsignatures, *Geophys. Res. Lett., 32,* L20101

Phan T. -D., G. Paschmann, W. Baumjohann, N. Sckopke and H., Lűhr (1994), The magnetosheath region adjacent to the dayside magnetopause: AMPTE/IRM observations, *J. Geophys. Res., 99*, A1, 121-141.

Phan T. –D. and G. Paschmann (1996), Low-latitude dayside magnetopause and boundary layer for high magnetic shear 1. Structure and motion, *J. Geophys. Res., 101*, A4, 7801-7815 .

Phan et al. (1997), Low-latitude dusk flank magnetosheath, magnetopause and boundary layer for low magnetic shear: Wind observations, *J. Geophys. Res., 102*, A9, 19,883-19,895.

Parker, E. N. (1958), Dynamics of the Interplanetary Gas and Magnetic Fields, *Astrophysical Journal, 128*, 664.

Paschmann G., B. U. Ö. Sonnerup, I. Papamastorakis, N. Sckopke, G. Haerendel, S. J. Bame, J. R. Asbridge, J. T. Gosling, C. T. Russell and R. C. Elphic (1979), Plasma acceleration at the Earth's magnetopause: evidence for reconnection, *Nature, 282*, 243.

Paschmann G., I. Papamastorakis, W. Baumjohann, N. Sckopke, C. W. Carlson, B. U. Ö. Sonnerup, and H. Lühr (1986), The magnetopause for large magnetic shear: AMPTE/IRM observations, *J. Geophys. Res., 91*, A10, 11,099-11,115.

Paschmann G., W. Baumjohann, N. Sckopke and T. –D. Phan (1993), Structure of the dayside magnetopause for low magnetic shear, *J. Geophys. Res., 98*, A8, 13,409-13,422.

Paschmann G., S. Haaland, B. U. Ö. Sonnerup, H. Hasegawa, E. Georgescu, B. Klecker, T. D. Phan, H. Réme and A. Vaivads (2005), Characteristics of the near-tail dawn magnetopause and boundary layer, *Annales Geophys., 23*, 1481–1497.

Pontius, D. H. Jr. and T. W. Hill (2006), Enceladus: A significant plasma source for Saturn's magnetosphere, *J. Geophys. Res., 111,* A09214.

Prangé R., L. Pallier, K. C. Hansen, R. Howard, A. Vourlidas, R. Courtin and C. Parkinson (2004), An interplanetary shock traced by planetary auroral storms from the Sun to Saturn, *Nature, 432*, 78-81.

Press W. H., S. A. Teukolsky, W. T. Vettering and B. P. Flannery (1988), *Numerical Recipes in C, The art of scientific computing*, Cambridge University Press.

Rairden R. (1980), Satellite sweeping of electrons and protons in Saturn's inner magnetosphere, *Dept Iowa progress report*, 80-29.

Rijnbeek R. P., S. W. H. Cowley, D. J. Southwood and C. T. Russell (1984), A survey of dayside flux transfer events observed by ISEE 1 and 2 magnetometers, *J. Geophys. Res., 89*, A2, 786-800.

Roussos E. et al. (2005), Low energy electron microsignatures at the orbit of Tethys: Cassini MIMI/LEMMS observations, *Geophys. Res. Lett. 32.*, L24107.

Russell C. T. (1990), The Magnetopause, *Physics of Magnetic Flux Ropes*, edited by C.T. Russell, E.R. Priest and L.C. Lee, 439-453.

Russell C. T. (1991), Planetary Magnetospheres, *Science Progress, 75*, 93-105.

Russell C. T. (1995), A study of flux transfer events at other planets, *Advances in Space Research, 16,* 4159-4163.

Russell, C. T. (2003), The structure of the magnetopause, *Planetary and Space Science, 51*, 731 – 744.

Russell C. T. and R. C Elphic (1978), Initial ISEE magnetometer results: Magnetopause observations, *Space Science Reviews, 22,* 681-715.

Russell C. T. and R. J. Walker (1985), Flux transfer events at Mercury, *J. Geophys. Res., 90*, 11 067–11 074.

Russell C. T., G. Le and H. Kuo (1996), The occurrence rate of flux transfer events, *Advances in Space Research, 18,* 8, 8197-8205.

Russell C. T. and J. G. Luhmann (1997), Saturn: Magnetic field and magnetosphere, *Encyclopaedia of Planetary Sciences*, edited by J. H. Shirley and R. W. Fainbridge, 718-719, Chapman and Hall, New York.

Rymer A. M., A. J. Coates, K. Svenes, G. A. Abel, D. R. Linder, B. Narheim, M. F. Thomsen, D. T. Young (2001), Cassini plasma spectrometer electron spectrometer measurements during the Earth swing-by on August 18, 1999, *J. Geophys. Res., 106,* A12, 30,177-30,198.

Rymer A. M. et al. (2006), Electron sources in Saturn's magnetosphere, *J. Geophys. Res., submitted.*

Scarf F. L., L. A. Frank, D. A. Gurnett, L. J. Lanzerotti, A. Lazarus and E. C. Sittler (1984), Measurements of plasma, plasma waves, and suprathermal charged particles in Saturn's inner magnetosphere, *Saturn,* University of Arizona Press, Tom Gehrels, 318-353.

Schardt A. W., K. W. Behannon, R. P. Lepping, J. F. Carbary, A. Eviatar and G. L. Siscoe (1984), The outer magnetosphere, *Saturn,* University of Arizona Press, Tom Gehrels, 416-459.

Scholer M., F. M. Ipavich, G. Gloecker, D. Hovestadt and B. Klecker (1981), Leakage of magnetospheric ions into the magnetosheath along reconnected field lines at the dayside magnetopause, *J. Geophys. Res., 86*, A3, 1299-1304.

Scholer M. (1988), Magnetic flux transfer at the magnetopause based on single X-line bursty reconnection, *Geophys. Res. Lett., 15*, 291–294.

Sckopke N., G. Paschmann, G. Haerendel, B. U. Ö. Sonnerup, S. J. Bame., T. G. Forbes, E. W. Hones Jr. and C. T. Russell (1981), Structure of the low latitude boundary layer, *J. Geophys. Res., 86*, A4, 2099-2110.

Scudder J. D., D. L. Lind and K. W. Ogilvie (1973), Electron observations in the solar wind and magnetosheath, *Geophys. Res. Lett., 78*, 28, 6536-6548.

Selesnick R. S. (1993), Micro- and macro-signatures of energetic charged particles in planetary magnetospheres, *Adv. Space Re., 13,* 10 10,221-10230.

Shue J. –H., J. Chao, H. Fu, C. T. Russell, P. Song, K. Khurana and H. Singer (1997), A new functional form to study the solar wind control of the magnetopause size and shape, *J. Geophys. Res., 102,* A5, 9497-9511.

Shue J. –H., C. T. Russell and P. Song (2000), Shape of the low-latitude magnetopause: Comparison of models, *Adv. Space Res., 25,* 718, 1471-1484.

Sibeck D. G. (1994), Magnetosheath magnetic field variability, *Adv. Space Res. 14*, 7, 791-794.

Sibeck D. G. et al. (1989), The magnetospheric response to 8-minute period strong-amplitude upstream pressure variations, *J. Geophys. Res., 94*, 2505–2519.

Sibeck D. G., R. E. Lopez and E. C. Roelof (1991), Solar wind control of the magnetopause shape, location, and motion, *J. Geophys. Res.*, *96*, 5489–5495.

Sibeck, D. G. et al. (1999), Plasma transfer processes at the magnetopause, *Space Sci. Rev., 88*, edited by B. Hultqvist, M. Oieroset, G. Paschmann, and R. Treumann, Kluwer Academic Publisher, 207-283.

Simpson, J. A., D. C Hamilton, R. B. McKibben, A. Mogro-Campero, K. R. Pyle and A. J. Tuzzolino (1974), The protons and electrons trapped in the Jovian dipole magnetic field region and their interaction with Io, *J. Geophys. Res., 79*, 25, 3522-3544.

Simpson, J. A., T. S Bastian, D. L. Chenette, G. A. Lentz, R. B. McKibben, K. R. Pyle and A. J. Tuzzolino (1980a), Saturnian trapped radiations and its absorption by satellites and rings: The first results from Pioneer 11, *Science, 207,* 4429, 411-415.

Simpson, J. A., T. S Bastian, D. L. Chenette, R. B. McKibben, K. R. Pyle (1980b), The trapped radiations of Saturn and their absorption by satellites and rings, *J. Geophys. Res., 85*, A11, 5731-5762.

Sittler Jr. E. C., K. W. Ogilvie and J. D. Scudder (1983), Survey of low-energy plasma electrons in Saturn's magnetosphere: Voyagers 1 and 2, *J. Geophys. Res., 88*, A11, 8847-8870.

Sittler Jr. E. C. et al. (2003), Energetic Nitrogen Ions within the Inner Magnetosphere of Saturn, *American Astronomical Society, DPS meeting #35,* 40.23.

Sittler et al. (2006), Energetic nitrogen ions within the inner magnetosphere of Saturn, *J. Geophys. Res., 111*, A09223.

Slavin J. A., E. J., Smith, P.R., Gazis and J. D. Mihalov (1983), A Pioneer-Voyager study of the solar wind interaction with Saturn, *Geophys. Res. Lett., 10*, 1, 9-12.

Slavin J. A., E. J. Smith, J. R. Spreiter and S. S. Stahara (1985), Solar wind flow about the outer planets: gas dynamic modelling of the Jupiter and Saturn bow shocks, *J. Geophys. Res.*, *90*, A7, 6275-6286.

Smith E. J., L. Davis Jr., D. E. Jones, P. J. Coleman Jr., D. S. Colburn., P. Dyal and C. P. Sonett (1980), Saturn's magnetic field and magnetosphere, *J. Geophys. Res.*, *85*, A11, 5655-5674.

Smith H. T., M. Shappirio, E. C. Sittler, D. Reisenfeld, R. E. Johnson, R.A. Baragiola, F. J. Crary, D. J. McComas and D. T. Young (2005), Discovery of nitrogen in Saturn's inner magnetosphere, *Geophys. Res. Lett.*, *32*, L14S03.

Song P., R. C. Elphic, C. T. Russell, J. T. Gosling and C. A. Cattell (1990), Structure and properties of the subsolar magnetopause for northward IMF: ISEE observations, *J. Geophys. Res.* 95, 6375.

Song P. and C. T. Russell (1992), Model of the formation of the low-latitude boundary layer for strongly northward interplanetary magnetic field, *J. Geophys. Res.*, *97*, A2, 1411-1420.

Sonnerup B.U.Ö. and L.J. Cahill.Jr. (1967), Magnetopause structure and attitude from Explorer 12 observations, *J. Geophys. Res.*, *72*, 171.

Sonnerup B.U.Ö. (1976), Magnetopause and boundary layer (review), Physics of solar planetary environments, *Proceedings of the International Symposium on Solar-Terrestrial Physics*, Boulder, United States, 541-557.

Sonnerup B. U. Ö., G. Paschmann, I. Papamastorakis, N. Sckopke, G. Haerendel, S. J. Bame, J. R. Asbridge, J. T. Gosling and C. T. Russell (1981), Evidence for magnetic reconnection at the Earth's magnetopause, *J. Geophys. Res.*, *86*, A12, 10,049-10,067.

Sonnerup B. U. Ö. and B. G. Ledley (1979), Ogo 5 magnetopause structure and classical reconnection, *J. Geophys. Res.*, *84*, A2, 399-405.

Sonnerup, B. U. Ö and M. Scheible (1998), Minimum and maximum variance analysis, in *Analysis Methods for Multi-Spacecraft Data, ISSI Scientific Report, SR-001*, edited by Paschmann and P.W Daley, 185.

Southwood D. J., Farrugia C. J. and Saunders M. A (1988), What are flux transfer events?, *Planet. Space Sci.*, *36*, 503–508.

Southwood D. J. and M. G. Kivelson (2005), Saturnian magnetosphere dynamics, *MIST meeting*, London, 25 November.

Stern. D. P. (1995), Modelling the field of the global magnetopause, *Physics of the Magnetopause*, Geophysical Monograph 90, P. Song, B. U. Ö. Sonnerup, M. F. Thomsen., 45-51.

Stevenson, D. J. (1983), Planetary magnetic fields, *Rep. Prog. Phys., 46,* 555-620.

Stone E.C., A.M. Frandsen, R.A. Mewaldt, E.R. Christian, D. Margolies, J.F. Ormes and F. Snow (1998), The Advanced Composition Explorer, *Space Sci. Rev., 86*, 1, 1-22.

Thomsen M. F. T., C. K. Goertz and J. A. Van Allen (1977), On determining magnetospheric diffusion coefficients from the observed effects of Jupiter's satellite Io, *J. Geophys. Res., vol. 82*, 35, 5541-5550.

Thomsen M. F. and J. A. Van Allen (1980), Motion of trapped electrons and protons in Saturn's Inner magnetosphere, *J. Geophys. Res., 85,* A11, 5831-5834.

Tokar R. L. et al. (2005), Cassini observations of the thermal plasma in the vicinity of Saturn's main rings and the F and G rings, *Geophys. Res. Lett., 32*, L14S04.

Tokar R. L. et al. (2006), The interaction of Saturn's plasma with the atmosphere of Enceladus: Cassini observations, *Science, 311,* 5766, 1409-1412.

Walker R. J. and C. T. Russell (1985), Flux transfer events at the Jovian magnetopause, *J. Geophys. Res., 90*, A8, 7397-7404.

Wolfe J. H., J. D. Mihalov, H. R. Collard, D. D. McKibbin, L. A. Frank, D. S. Intriligator (1980), Preliminary results on the plasma environment of Saturn from the Pioneer 11 Plasma Analyser Experiment, *Science, 207*, 4429, 403-407.

Van Allen J.A. and L.A. Frank (1959), Radiation around the Earth to a radial distance of 107,400 km, *Nature, 183*, 430-434.

Van Allen J. A., M. F. Thomsen, B. A. Randall, R. L. Rairden and C. L., Grosskreutz (1980a), Saturn's magnetosphere, rings, and inner satellites, *Science, 207,* 4429, 415-421.

Van Allen J. A., M. F. Thomsen, B. A. Randall (1980b), The energetic charged particle absorption signature of Mimas, *J. Geophys. Res., 85,* A11, 5709-5718.

Van Allen J. A. (1982), Findings on rings and inner satellites of Saturn by Pioneer 11, *Icarus, 51,* 509-527.

Van Allen, J. A. (1984), Energetic particles in the inner magnetosphere of Saturn, *Saturn,* University of Arizona Press, Tom Gehrels, 281-317.

Vasyliunas V. M. (1983), Plasma distribution and flow', *Physics of the Jovian magnetosphere, Cambridge planetary science series*, A. J. Dessler (Editor), 395-451

Violante L., M. B. Bavassano Cattaneo, G. Moreno and J. D. Richardson (1995), Observations of mirror waves and plasma depletion layer upstream of Saturn's magnetopause, *J. Geophys. Res., 100*, A7, 12,047-12,055.

Vogt R. E et al. (1982), Energetic charged particles in Saturn's magnetosphere: Voyager *Science, 215,* 4532, 577-582.

Walt, M. (1971), The radial diffusion of trapped particles induced by fluctuating magnetospheric fields, *Space Sci. Rev, 12*, 4, 446-485.

Walt M. (1994), *Introduction to geomagnetically trapped radiation*, Cambridge atmospheric and space science series.

Young, D. T. et al. (2004), The Cassini plasma spectrometer investigation, *Space Science Reviews*, *114*, 1-112.

Young D. T. et al. (2005), Composition and dynamics of plasma in Saturn's magnetosphere, *Science, 307*, 5713, 1262-1266.

Zwan B. J and R. A Wolf (1976), Depletion of solar wind plasma near a planetary boundary, *J. Geophys. Res.*, *81*, 10, 1636-1648.